



**HAL**  
open science

# A new approach to stellar occultations in the Gaia era

Joao Ferreira

► **To cite this version:**

Joao Ferreira. A new approach to stellar occultations in the Gaia era. Astrophysics [astro-ph]. Université Côte d'Azur; Universidade de Lisboa. Faculdade de ciências (Lisboa, Portugal), 2020. English. NNT : 2020COAZ4084 . tel-03185433

**HAL Id: tel-03185433**

**<https://theses.hal.science/tel-03185433>**

Submitted on 30 Mar 2021

**HAL** is a multi-disciplinary open access archive for the deposit and dissemination of scientific research documents, whether they are published or not. The documents may come from teaching and research institutions in France or abroad, or from public or private research centers.

L'archive ouverte pluridisciplinaire **HAL**, est destinée au dépôt et à la diffusion de documents scientifiques de niveau recherche, publiés ou non, émanant des établissements d'enseignement et de recherche français ou étrangers, des laboratoires publics ou privés.



# THÈSE DE DOCTORAT

## Occultations stellaires: une nouvelle approche grâce à la mission Gaia

**João FERREIRA**

Laboratoire J-L. Lagrange – Observatoire de la Côte d'Azur ; Instituto de  
Astrofísica e Ciências do Espaço, Lisboa

**Présentée en vue de l'obtention**

**du grade de docteur en** Sciences de la Planète  
et de l'Univers

d'Université Côte d'Azur

et de Faculdade de Ciências da Universidade de  
Lisboa

**Dirigée par :** Paolo Tanga

**Co-encadrée par :** Pedro Machado

**Soutenue le :** 2020-12-15

**Devant le jury, composé de :**

Felipe BRAGA-RIBAS (Universidade Tecnológica Federal do  
Paraná)

René DUFFARD (Instituto de Astrofísica de Andalucía)

Guy LIBOUREL (Université Côte d'Azur)

Pedro MACHADO (Instituto de Astrofísica e Ciências do  
Espaço)

Françoise ROQUES (Observatoire de Paris)

Pablo SANTOS-SANZ (Instituto de Astrofísica de Andalucía)

Paolo TANGA (Observatoire de la Côte d'Azur)

Kleomenis TSIGANIS (Aristotle University of Thessaloniki)



# **Occultations stellaires: une nouvelle approche grâce à la mission Gaia**

## **A new approach to stellar occultations in the Gaia era**

Jury:

Président du jury :

Guy LIBOUREL, Professeur, Université Côte d'Azur

Rapporteurs :

Felipe BRAGA-RIBAS, Professeur Associé, Universidade Tecnológica Federal do Paraná

Pablo SANTOS-SANZ, Maître des Conférences, Instituto de Astrofísica de Andalucía

Examineurs:

René DUFFARD, Professeur Associé, Instituto de Astrofísica de Andalucía

Françoise ROQUES, Astronome, Observatoire de Paris

Kleomenis TSIGANIS, Professeur Associé, Aristotle University of Thessaloniki

Directeur de thèse:

Paolo TANGA, Astronome, Observatoire de la Côte d'Azur

Co-Directeur de thèse:

Pedro MACHADO, Professeur, Instituto de Astrofísica e Ciências do Espaço

# Resumé en Français

Les astéroïdes participent à la compréhension de plusieurs problèmes clés liés à la science du système solaire et à l'environnement spatial de notre planète, tels que les conditions du système solaire lors de sa formation, l'apport d'eau et de molécules organiques sur la Terre, le danger potentiel des astéroïdes proches de la Terre ("Near Earth Asteroids" - NEA) et leur rôle dans l'influence du climat de la Terre.

Les occultations stellaires sont une occasion unique d'obtenir du sol une astrométrie astéroïde très précise, proche de la performance de Gaia, ainsi que des formes / tailles pour les astéroïdes. Lorsqu'un astéroïde cache la lumière d'une étoile, l'incertitude de sa position instantanée peut être similaire à celle de l'étoile cible. En exploitant la précision de Gaia DR2 sur les astéroïdes et les étoiles, la prédiction et l'exploitation des occultations stellaires deviennent une méthode efficace pour collecter systématiquement l'astrométrie des astéroïdes.

L'amélioration des prévisions via Gaia DR2 est prouvée par des statistiques de prévisions réelles et une comparaison entre les prédictions d'occultations stellaires avec Gaia DR2 pour les astéroïdes et autres données, comme Astorb et MPCORB, afin de vérifier lesquelles correspondent le mieux aux cordes observées d'occultations passées.

En même temps, les occultations d'astéroïdes peuvent offrir la possibilité de confirmer ou de découvrir des étoiles doubles, dans une gamme de petites séparations angulaires très complémentaires de la résolution accessible à Gaia elle-même. Nous présenterons des statistiques et des simulations montrant l'amélioration attendue de la prédiction des occultations d'astéroïdes grâce à l'astrométrie de Gaia, en particulier en ce qui concerne les incertitudes plus petites sur le mouvement propre des étoiles cibles.

Par une approche bayésienne, le Modèle d'Inférence bayésienne (Bayesian Inference Method - BIM) nous déterminons dans l'espace des paramètres (durée; époque du centre; chute du flux; luminosité de l'étoile) le domaine des événements détectables à partir d'un site unique. Notre étude prépare l'exploitation du télescope robotique de 0,5 m UniversCity dans le "Plateau de Calern" (sud de la France), pour lequel nous déterminons l'étendue de la

taille de l'astéroïde et de la luminosité de l'étoile que nous espérons atteindre. Cette installation ne sera pas opérationnelle qu'après le fin de ce travail. Les résultats obtenus concernant la performance du système sont comparés avec la méthode utilisée avant (Moindres Carrés), avec des signaux faux positifs, pour déterminer quand ils sont plus probables, et avec des observations réelles, pour vérifier la viabilité de de nouveau méthode.

Après ce travail de simulation des performances attendues d'UniversCity avec le matériel disponible, notre objectif a été d'appliquer ces limitations aux événements prévus et de maximiser l'efficacité de l'utilisation du télescope. Pour cela, et en tenant compte de tous ces facteurs, nous avons estimé le nombre d'événements pouvant être observés avec un télescope robotique sur une période d'un an avec les catalogues actuels d'étoiles et d'astéroïdes. Pour prendre en compte l'amélioration des incertitudes sur les astéroïdes obtenus grâce à Gaia pour chaque événement, nous avons vérifié quel serait l'impact sur la probabilité si l'astéroïde avait une incertitude 2, 5, 10 ou 20 fois plus petite, et les résultats pour chaque régime ont été compilés.

Nous avons aussi analysé les données de DR2 pour les 14 099 astéroïdes sur le catalogue, comment cela impacte leur incertitude du demi-axe majeur ( $a$ ), et comment cela change les prévisions d'occultations stellaires. Ce travail a été réalisé pour 2 méthodes de pondération, ce qui est utilisé dans AstDyS (Farnocchia et al.) et un autre développé par l'équipe de Nice. En utilisant des résidus d'observation et occultations archivées, nous avons vérifié si cette nouvelle méthode améliorait les orbites.

Grâce à des collaborations avec plusieurs astronomes, 16 observations ont été réalisées au cours de ce travail. Parmi ces observations, 3 occultations positives ont été analysées par la méthode bayésienne qui a été utilisé pour d'autres observations lorsque les données photométriques étaient disponibles.

**Mots clés:** occultations – planètes mineures, astéroïdes: général – astrométrie – techniques: photométrie – méthodes: numériques

---

A new approach to stellar occultations in the Gaia era

**Abstract:** Asteroids are involved in understanding several key issues in Solar System science and the space environment of our planet, such as the conditions of the Solar System during its formation, the delivery of water and organic molecules to Earth, the potential danger of NEA and their role in affecting Earth's climate.

Stellar occultation events are a unique opportunity to obtain from the ground very accurate asteroid astrometry, close to the performance of Gaia, and shapes/sizes. When an asteroid hides the light of a star, the uncertainty of its instantaneous position can be similar to that of the target star. By exploiting the accuracy of Gaia DR2 on both asteroids and stars, stellar occultation prediction and exploitation becomes an effective method to systematically collect asteroid astrometry.

The improvement of predictions through Gaia DR2 is proven via statistics of real predictions and comparison between stellar occultation predictions with Gaia DR2 for asteroids and other, such as Astorb and MPCORB, to verify which fit better to observed chords of past occultations.

At the same time, asteroid occultations can offer the possibility to confirm or discover double stars, in a range of small angular separations very complementary to the resolution accessible to Gaia itself. We will present statistics and simulations showing the improvement expected in the prediction of asteroid occultations thanks to Gaia astrometry, in particular regarding the smaller uncertainties on the proper motion of target stars.

Through a bayesian approach, the Bayesian Inference Method (BIM), we determine in the parameter space (duration; centre epoch; flux drop; star brightness) the domain of detectable events from a single site. Our study prepares the exploitation of the 0.5-m robotic telescope at "Plateau de Calern" (Southern France) UniversCity, for which we determine the range of asteroid size and star brightness that we expect to reach. This facility will start operations after this work is over. The results obtained regarding the performance were compared with the previously used method to deriving all the relevant parameters (Least Squares Fit), with false positive signals to determine when these are most likely, and with several real observations, to verify the viability of this new method.

After this work simulating the expected performance of UniversCity with

---

the available equipment, the plan is to apply these limitations to predicted events and maximize the efficiency of the telescope's use. For that end, and accounting for all these factors, a survey was made to estimate how many events would be observable with a robotic telescope in a 1-year period with the current star and asteroid catalogues. To account for improvements in the asteroid uncertainties thanks to Gaia, for each event we checked what the impact on the likelihood would be if the asteroid had an uncertainty 2, 5, 10 or 20 times smaller, and results for each regime were compiled.

We also analyzed the data of the 14 099 asteroids present DR2, how this impacted the semi-major axis ( $a$ ) uncertainty, and how that would translate into improvements on stellar occultation predictions. This was made for two different weighting schemes, the one used for AstDyS (Farnocchia et al.) and one developed by the team, using observation residuals and occultations from the past to verify that the new weighting scheme would bring an improvement.

Thanks to the collaboration with several astronomers, 16 observations were made throughout this work, with the three positives being analyzed with the new bayesian approach, which was also used for a few other observations where the photometric data was shared.

**Keywords:** occultations – minor planets, asteroids: general – astrometry – techniques: photometric – methods: numerical

---



# Resumo em Português

Os asteroides são uma parte essencial de vários elementos-chave do estudo do Sistema Solar, bem como do estudo do espaço à volta do nosso planeta, das condições do Sistema Solar durante a sua formação, do transporte de água e matéria orgânica para a Terra, do possível perigo de Asteroides Próximos da Terra ("Near Earth Asteroids" - NEA) e do seu impacto no clima da Terra.

As ocultações estelares apresentam uma oportunidade única de obter a partir de telescópios no solo astrometria de asteroides muito precisa, ao nível do telescópio espacial Gaia, bem como a determinação do tamanho e formato destes corpos. Quando um asteroide atravessa o caminho de luz de uma estrela, fazendo com que o brilho desta desapareça, a incerteza na sua posição nesse preciso momento é da mesma ordem da incerteza na posição da estrela. Se aproveitarmos a precisão da segunda divulgação de dados do Gaia ("Gaia Data Release 2 - Gaia DR2 ou GDR2), tanto para estrelas como para asteroides, as previsões e observações de ocultações estelares tornar-se-ão um método eficaz de obter sistematicamente dados astrométricos de asteroides.

As melhorias nas previsões obtidas graças ao Gaia DR2 são comprovadas a partir de estatísticas de previsões reais bem como da comparação entre previsões com dados do Gaia para asteróides com outras bases de dados mais completas, como Astorb e MPCORB, para verificar qual destas bases se ajusta melhor às observações feitas no passado.

Além disto, as ocultações estelares podem também oferecer a possibilidade de confirmar sistemas binários de estrelas, numa pequena gama de separações angulares complementar aos limites de resolução permitidos pelo Gaia. Apresentamos estatísticas e simulações que comprovam as melhorias esperadas na previsões de ocultações estelares graças à astrometria fornecida pelo Gaia, em particular no que toca à diminuição das incertezas no movimento próprio das estrelas-alvo.

Através de um método de inferência bayesiana ("Bayesian Inference Method" - BIM), determinamos o intervalo de parâmetros (duração do evento, época central, queda de fluxo, fluxo original) no qual podemos detectar eventos a partir de um local específico - o Observatório de Calern, em Nice, França. Este

estudo foi feito tendo em conta a preparação para a instalação do telescópio UniversCity, um telescópio robótico com 50 cm de diâmetro, neste Observatório. Um dos objectivos deste trabalho era determinar, antes da sua estreia, quais os limites deste telescópio em termos de tamanho do asteroide a observar, fluxo da estrela e duração do evento. Este telescópio poderá começar a ser usado apenas após o final deste trabalho. Os resultados obtidos em relação ao desempenho do UniversCity foram comparados com o que se pode obter utilizando o método anterior (Mínimos Quadrados), com o uso de falsos positivos enquanto sinais, para averiguar quando estes se podem tornar problemáticos, e com várias observações reais partilhadas nos arquivos existentes, para verificar a viabilidade deste novo método.

Depois desta tarefa de simular os resultados esperados do UniversCity com o equipamento disponível, o plano é aplicar estas limitações do telescópio à previsão e planeação de eventos, maximizando a eficiência do seu uso. Com esse propósito, e tendo em conta todos os factores relevantes, foi feita uma sondagem para averiguar quantas observações se poderiam fazer no espaço de 1 ano com os catálogos de estrelas e asteroides atuais. Para ter em conta as melhorias esperadas nas incertezas dos asteroides graças aos dados do Gaia, verificámos, para cada evento, qual o impacto na sua probabilidade se a incerteza do asteroide fosse cortada por um factor de 2, 5, 10 ou 20, e os resultados de cada grupo foram compilados.

Também analisámos os dados do DR2 para os 14 099 asteroides presentes na sua lista de objetos, e ver como estes dados alteram a incerteza do parâmetro semi-eixo maior ( $a$ ), e como essa alteração se reflecte como melhorias nas previsões de ocultações. Isto foi feito com dois esquemas diferentes de pesar as observações, aquele actualmente em vigor no AstDyS (Farnocchia et al.), e um desenvolvido pela equipa de Nice. Usámos os resíduos das observações e a concordância com ocultações do passado para verificar se este novo esquema traz melhorias.

Grças à colaboração com vários astrónomos, 16 observações foram feitas ao longo deste trabalho, com as três ocultações positivas analisadas com o novo método bayesiano, que também foi usado noutras observações, em que os dados fotométricos foram partilhados.

**Palavras-chave:** ocultações – planetas menores, asteroides: geral – astrometria – técnicas: fotometria – métodos: numéricos

## Dedication

To all my family, for their continuous support throughout my life. They have made all of this work possible.

## Acknowledgments

Federica Spoto helped develop and explained how to use the OrbFit software tool, actively discussing the results brought through its use.

Enrico Corsaro, who taught me how to use the DIAMONDS software tool he developed, and adapted it to the specific peculiarities of stellar occultation functions. His work laid the foundation for the paper in Appendix D.

Everyone who developed the tools publicly available to exploit stellar occultations. In particular, Dave Herald for the development of Occult, Andrey Plekhanov for Linoccul, Hristo Pavlov for Tangra and OccultWatcher. Observation predictions and archives also played an important role, for which I thank in particular Steve Preston, for his personal predictions page, and Eric Frappa, for the maintenance of the Euraster archive.

Several amateur and professional astronomers gave their time to the observations described in Chapter 4. My thanks to Matthieu Conjat (AIMA Development), Erick Bondoux and Jean-Pierre Rivet (OCA), Rui Gonçalves (Instituto Politécnico de Tomar), Joana Oliveira (Observatoire de Paris), Diogo Pereira and Hugo Martins (Faculty of Sciences of the University of Lisbon) and Máximo Ferreira (Centro Ciência Viva Constância).

Finally, to the reviewers and the jury if this thesis for the time they dedicated to discussing and improving the work presented.

# Contents

<b>1</b>	<b>Introduction</b>	<b>37</b>
1.1	Asteroids History . . . . .	37
1.1.1	How have they been observed? . . . . .	37
1.1.2	Observation Methods and Missions . . . . .	43
1.2	Stellar Occultations . . . . .	45
1.2.1	General properties . . . . .	45
1.2.2	Why are they important? . . . . .	54
1.3	The Gaia Mission . . . . .	60
1.4	Goals and Structure of this Thesis . . . . .	68
<b>2</b>	<b>Extending the occultations sample with Gaia</b>	<b>73</b>
2.1	Context . . . . .	73
2.2	UniversCity Telescope . . . . .	74
2.3	Limitations to account for in DR2 . . . . .	78
2.4	Set-up . . . . .	79
2.5	Star and Asteroid Uncertainties . . . . .	80
2.6	Orbit improvements with Gaia . . . . .	86
2.7	Statistics on events per size . . . . .	90
<b>3</b>	<b>Simulations</b>	<b>93</b>
3.1	Context . . . . .	93
3.2	Least Squares and Bayes' Theorem . . . . .	94
3.2.1	Least Squares Fit Method . . . . .	94
3.2.2	Bayes' Theorem and Bayesian Analysis . . . . .	95
3.3	Setup . . . . .	96
3.4	Results . . . . .	106
3.4.1	Gaussian and Uniform priors . . . . .	110
3.4.2	False positives . . . . .	111
3.4.3	Comparison of BIM to LSF . . . . .	113
3.4.4	DIAMONDS vs PyOTE . . . . .	114
3.4.5	BIM vs Real Cases . . . . .	116

---

<b>4</b>	<b>Observations</b>	<b>119</b>
4.1	Context . . . . .	120
4.2	Positives . . . . .	121
4.2.1	Triton . . . . .	121
4.2.2	Aemilia . . . . .	122
4.2.3	Phaethon . . . . .	125
4.2.4	Millman . . . . .	126
4.3	Negatives . . . . .	129
4.3.1	2000 HD22 . . . . .	129
4.3.2	Gezelle . . . . .	130
4.3.3	Sveta . . . . .	130
4.3.4	Paijanne . . . . .	131
4.3.5	Nolde . . . . .	131
4.3.6	Modestia . . . . .	132
4.3.7	1993 FE48 . . . . .	132
4.3.8	Deikoon . . . . .	132
4.3.9	Elektra . . . . .	133
4.3.10	Phaethon . . . . .	134
4.3.11	Europa . . . . .	134
4.3.12	Alfaterna . . . . .	135
4.3.13	2002 MS4 . . . . .	135
4.4	Analysis to other observations . . . . .	136
4.4.1	Europa event - RIO team . . . . .	136
4.4.2	Galatea . . . . .	140
4.4.3	Euphrosyne . . . . .	140
<b>5</b>	<b>Exploiting Occultation Astrometry</b>	<b>143</b>
5.1	Context . . . . .	143
5.1.1	Debiasing . . . . .	144
5.1.2	Error Models . . . . .	146
5.2	Setup . . . . .	150
5.3	Testing error models with occultations . . . . .	154
5.3.1	Best occultations . . . . .	154
5.3.2	Full Scale Runs on Occultations . . . . .	159
5.4	Orbital Elements with Gaia . . . . .	166

---

5.4.1	Full Scale Run on DR2 Asteroids . . . . .	173
<b>6</b>	<b>Conclusions and Future Work</b>	<b>177</b>
6.1	UnivCity and Robotic Telescopes . . . . .	177
6.2	Simulation of events . . . . .	178
6.3	Comparing astrometry: occultations and other sources . . . . .	179
6.4	Future Work . . . . .	180
6.4.1	Gaia DR3 and beyond . . . . .	180
6.4.2	Exploiting Single Chord Occultations . . . . .	181
6.4.3	NEA Events . . . . .	182
	<b>Bibliography</b>	<b>185</b>
<b>A</b>	<b>Asteroid Orbital Improvement</b>	<b>199</b>
A.1	OrbFit . . . . .	201
A.1.1	Software description . . . . .	201
A.1.2	Orbital elements and required data . . . . .	203
<b>B</b>	<b>Code snippets</b>	<b>207</b>
B.1	UnivCity and Linocult . . . . .	207
B.2	Simulations . . . . .	208
B.3	Gaia Star Query . . . . .	210
B.4	Gaia Asteroid Query and OrbFit files . . . . .	212
B.5	Photometry . . . . .	213
<b>C</b>	<b>Abbreviations Used</b>	<b>217</b>
<b>D</b>	<b>Paper Published</b>	<b>219</b>



# List of Figures

1.1	(1) Ceres, the first asteroid discovered and largest object of the Main Belt. Image by NASA. Image from <a href="#">Baer et al. [2011]</a> . . .	38
1.2	Diameter distribution of numbered asteroids, according to the NEOWISE survey. Diameters smaller than 5km are assumed to be heavily under-represented due to the biases introduced by the limitations of the most typical observation methods. . . .	39
1.3	Number of known asteroids by year in the last 2 decades. Image from Minor Planet Center. . . . .	41
1.4	Amount of known NEA by year in the last 4 decades. From the scarce growth, it is considered that the population of NEA larger than 1 km is well-known and almost completely catalogued, but the smaller sizes are still under-represented. Image from Minor Planet Center. . . . .	42
1.5	Mass distribution of the Main Belt, with the pie chart sections in the same order of the legend, in clockwise direction. . . . .	42
1.6	Example of Prediction from "call4obs", originally made by Steve Preston. . . . .	46
1.7	Representation of the first ever occultation by an asteroid: (2) Pallas, 1961/10/02, by D. Evans and J. van Lourens. The blue line is the chord registered during the observation, and the sphere is the model of Pallas at the time, with the chord assumed to be central, or close to it. Image by Occult. . . . .	47
1.8	First reliable multi-chord event by any object other than the Moon, according to Occult: Venus, 1959/07/07. The sphere is the model of Venus, and each line represents a distinct observation recorded. Image by Occult. . . . .	48
1.9	First ever multi-chord event by an asteroid, according to Occult: (433) Eros, 1975/01/24. Green and red lines represent beginning and end of chords (chords are nearly vertical in this image). Image by Occult. . . . .	48

1.10	Positive events, per year, according to Occult. Also labelled are some of the main catalogues used for occultation predictions at the year of their release. . . . .	51
1.11	Number of events with at least one positive occultation, per year, according to Occult. . . . .	51
1.12	Number of events with at least two positive occultations (allowing more accurate astrometry and possibly diameter determination or shape modelling), per year, according to Occult. . . . .	52
1.13	Magnitude Distribution of stars used for reported positive occultations, according to Occult. First column represents stars with $V < 2$ and last represents $V > 15$ . Given the typically small telescopes used, there is a bias against fainter stars, as these are far more numerous. Data from Occult. . . . .	52
1.14	Reported observations by aperture from 1997 to 2006. Small telescopes (less than 30cm of diameter) are the most used. Image by Eric Frappa. . . . .	53
1.15	Same plot, but cumulative data from 2009 to 2018. Source is also Euraster. . . . .	53
1.16	(345) Tercidina observed by several dozens of astronomers in September 17 <sup>th</sup> 2002. Shape becomes much simpler to model with multiple observations, as well as the correction of systematic errors in each individual observation. Image by Euraster. . . . .	54
1.17	Occultation by Neptune's moon, Triton, the first one using DR2 data (Chord 11 was observed in Nice). This event actually pre-dated DR2, with this data being released ahead of time specifically for this occultation. Image by Euraster. . . . .	55
1.18	Bessel Fundamental Plane. This allows us to use observations made on different sections of Earth's surface in a single plane, in order to combine those observations' data. Image by G. Pieper, published in Wikipedia. . . . .	56

---

1.19	Correction to the orbit of (95 626) 2002 GZ32, which was made possible due to the several positive and negative reports. Green points are sites with positive reports, and red have negative reports. Original image from Steve Preston’s predictions, edited by Jean Lecacheux (LESIA, Paris Observatory). . . . .	56
1.20	Example of an atmosphere, in this case Triton, visible during the occultation thanks to a central flash. Result obtained by Rui Gonçalves in Constância, Portugal. Similar result obtained in Nice shown in Figure 4.1 . . . . .	57
1.21	Example of a ring system being detected thanks to stellar occultations, in this case the centaur (10 199) Chariklo. Discovery made in 2014 [Braga-Ribas et al., 2014]. . . . .	58
1.22	Example of a multiple asteroid system detected via occultations: (87) Sylvia (main body) and its satellites Romulus (far left) and Remus (bottom centre). This observation was a European campaign that included 36 detected chords and 14 negative observations. Sylvia has a radius of 277 km, Romulus 22 km and Remus 11 km, with a separation of several Sylvia radii between them. Image by Euraster. . . . .	58
1.23	Example of the light of a star changing with time because of an occulting object with an atmosphere and rings. Image by J. L. Elliot [Elliot, 1979] . . . . .	59
1.24	Gaia satellite (image by ESA). . . . .	61
1.25	Trajectory of Gaia from Earth to the L2 point, image courtesy of ESA. . . . .	62
1.26	Historical progression of astrometry precision until Gaia, with some of the most important catalogues of their time and their size. Image from [Høg, 2011] . . . . .	64
1.27	Distribution of star Uncertainty (position + proper motion for RA and Dec) with Gaia DR2 for stars of magnitude 14 or below. A random sample of 3 million stars was chosen within the Gaia data. Vast majority has sub-mas uncertainty. . . . .	64

1.28	Projection of how Gaia will increase precision in orbital uncertainties of MBA. This is taken from [Gaia Collaboration et al., 2018a], where the orange points represent the expected astrometry quality from DR2, the black points the current state-of-the-art results from other methods, and the red and blue points represent the expected improvement with 5 and 10 years of Gaia data, respectively. We can see that, for a five-year mission, the state-of-the-art orbital uncertainties can be improved by a factor of up to 10, and since the mission has been extended to 9 years, the 10 year projection is more likely to be the scenario with the final catalogue, bringing an improvement of up to 2 orders of magnitude. These values will be used in Chapter 2 . . . . .	66
1.29	DR2 data vs other methods combined for Asteroids. Image by [Gaia Collaboration et al., 2018a]. . . . .	67
1.30	Schematic of how occultations are prepared and what their contributions help with. . . . .	69
2.1	UnivCity Telescope. Image by Eric Bondoux (OCA). . . . .	74
2.2	Expected Noise distribution for UnivCity and exposure time of 0.1 s, star at zenith, as function of V magnitude. Line description: black continuous line is the total expected flux, red continuous line scintillation noise, horizontal long dashed green line is the static noise brought by the background, readout and dark current sources, blue short dashed line is photon noise and yellow short dashed line is the total noise, adding the previously mentioned sources. We can see that scintillation dominates for magnitudes smaller than 9 and the static noise dominates starting from magnitude 11. This means that, for fainter stars, improving the available equipment, within reason, to minimize readout and dark current noise should allow a bigger improvement than changing the exposure time. . . . .	76
2.3	Same as previous figure, but with exposure time of 0.5 s. . . . .	77

- 
- 2.4 SNR Distribution, exposure time of 0.1 s, as function of V magnitude. Line description: black, continuous line is the expected SNR at each magnitude step, and the horizontal lines, from highest to lowest, represent SNR of 10, 5, 3 and 1 for comparison. We can see that for 0.1 s, we reach an SNR of 3 at around magnitude 13, meaning from this point forward detecting the target star should be difficult, and a SNR of 1 just beyond magnitude 14, meaning from this point the source is mixed in the background, theoretically remaining undetected. . . . . 77
- 2.5 Same as previous figure, but with  $dt = 0.5$  s. Now, SNR of 3 is reached around magnitude 14.5 and SNR of 1 around magnitude 16, showcasing how much further we can push the target star brightness if a larger exposure time is possible. . . . . 78
- 2.6 Path predicted for the Pluto event mentioned in Chapter 1 before DR2 data for the star was available. Central line crosses centre of France, southern limit crosses northern African countries and there is no north limit, as the shadow went all the way to the North Pole. Image by Josselin Desmars, Lucky Star Project. . . . . 79
- 2.7 Pluto shadow path once DR2 data for the star was used. Massive shift towards south, with the central line now crossing the northern African countries, the southern limit crossing some central African countries and the northern limit now below the North Pole, excluding a few stations in Nordic territory. Overall, shift towards South was of over 1 000 km, and while not visible on this image, the uncertainties also decreased massively, giving great confidence to all stations in the new shadow path that they would detect the event. Image by Josselin Desmars, Lucky Star Project. . . . . 80
- 2.8 Star Magnitude distribution, with an expected behaviour of more events for fainter stars, which are more numerous. . . . . 81
- 2.9 Magnitude Drop distribution, showing that usually the drop is very large, as even a 1 magnitude drop corresponds to a flux shift of approximately 60%. . . . . 81

2.10 Asteroid Diameter distribution, again with an expected behaviour, as small asteroids are more frequent than large ones. . . . .	82
2.11 Max Duration distribution, with durations smaller than 1 second dominating this survey. . . . .	82
2.12 Star uncertainty from Gaia, with position and proper motion, stars with magnitude 13.5 to 14. Errors below 1 mas clearly dominate. . . . .	83
2.13 Similar analysis, but magnitudes 11 to 12.5. . . . .	83
2.14 Asteroid Uncertainty Distribution, in mas, for all events visible from Calern analyzed. . . . .	84
2.15 Same analysis, also in mas, but for star uncertainty. . . . .	85
2.16 Star/Asteroid uncertainty ratio for all events. The peak is around 0.1, meaning the star's uncertainty is 1 order of magnitude below the asteroid's, with only a small minority of events having such a poor star precision that it became relevant in the overall event uncertainty. There is, however, a large distribution, meaning we can not always neglect the star's contribution.	85
2.17 Star/Asteroid uncertainty ratio comparison between UCAC4 and DR2. Only stars that were present in both UCAC4 and DR2 and had a 5-parameter solution in DR2 were included, hence the difference from Figure 2.16. There is an average increase of 2 orders of magnitude and, while before, with UCAC4, the star and the asteroid had, on average, comparable uncertainties, now the star's contribution is almost always negligible.	86
2.18 Representation of the effect on an asteroid's occultation probability as a function of a normalized distance from its centre in units of object diameter, for several uncertainty proportions. A distance of 0 means the site is at the shadow path's centre, and 0.5 Diameters corresponds to the predicted shadow path limit.	87
2.19 Shift in Magnitude distribution, depending on asteroid orbital quality. We can notice that, the further we decrease the asteroid's uncertainty, the more weight we give to long events, filtering out shorter events, which are typically associated with big error margins. . . . .	89

2.20	Shift in Diameter distribution, depending on asteroid orbital quality. Big diameters become more and more important, not only because of the bigger shadow area they cover, but because these events typically have lower error margins to begin with.	89
2.21	Shift in Event Probability distribution, depending on asteroid orbital quality. As expected, events with low probabilities tend to disappear, either because they became too unlikely in the new run, or because their probability is now much higher. Bigger efficiency in observations to be expected. . . . .	90
3.1	DNR distribution for the simulations used, which depends on combined star+asteroid magnitude and the expected magnitude drop. Since higher DNR imply an easier event to track, we prioritised low DNR combinations of magnitude and drop.	98
3.2	Distribution of Diameter value and uncertainty in WISE survey (122 594 asteroids). Colour plot is the precision, Uncertainty/Size, for easier reading. Two main trends exist, of precision 5% and 25%. . . . .	100
3.3	Discrepancies in Diameter values of IRAS [Ryan and Woodward, 2010] and WISE [Masiero et al., 2011] surveys (2 141 common asteroids). In some extreme causes, we can get disparities of over 50%, and a difference of 20% or more can be found for $\sim 20\%$ of the sample. . . . .	100
3.4	Example of case with high DNR (12.0): Magnitude 11.5, drop 1.0 and 10 points inside occultation. . . . .	102
3.5	Example of case with middle-of-the-road DNR (4.9): Magnitude 12.5, drop of 0.4 and 8 points inside occultation. . . . .	102
3.6	Example of case with low DNR (2.1): Magnitude 13.5, drop 0.7 and 2 points inside occultation. . . . .	103
3.7	Prior vs Posterior Distribution of Flux for Intermediate example. Vertical lines represent medians. . . . .	103
3.8	Same, but for drop. . . . .	104
3.9	Same, but for duration. . . . .	104
3.10	Same, but for Centre Epoch. . . . .	104

- 
- 3.11 Example of correlation check between Duration and Drop for the "Easy" case. . . . . 105
- 3.12 Same, but between Duration and Centre Epoch. . . . . 106
- 3.13 Distribution of the significant (left, green peak) and non-significant (right, blue peak) solutions found by the BIM as a function of the uncertainty on the centre epoch  $t_0$ , expressed in percentage of the sampling time. At around 100% uncertainty, the frequency of the two situations is about the same. This results are for the Gaussian priors. . . . . 107
- 3.14 The figure represents the expected uncertainty resulting from the BIM fit (Gaussian priors) on the duration  $L$  (left) and the center epoch  $t_0$  of the occultation, as a function of the DNR. The dots represent each result obtained from a simulated occultation. The continuous black line is the smoothed average value, while the shaded areas enclose the quantiles equivalent to  $1-\sigma$  and  $2-\sigma$ . The expected trend  $\sim 1/DNR$  (red dashed line) is visible in both plots. The uncertainty is expressed, respectively, as percentage of duration and of sampling time. . . 109
- 3.15 Distribution of the Bayesian detection probability obtained by the BIM, for the false positives (blue population rising towards the left) and the true events (red population rising towards the right). For the true events the distribution is strongly dominated by the peaked around the significance threshold of 99%. For the false positives the detection probability remains always very small. The probability of false positives is  $\sim 10^{-4}$  for significant events. . . . . 110
- 3.16 Comparison of the performance on the centre epoch as a function of the DNR, for the Gaussian (blue curve) and Uniform priors (red). Here, only the average value is shown. Despite the relatively small difference, the Gaussian prior has a better performance for more difficult events. . . . . 111

- 
- 3.17 Expected distribution of the astrometric uncertainty on the single chord estimated by our accuracy model, applied to a large set of predictions. Only the component of the uncertainty relative to the fit of each light curve by the BIM is taken into account. The colour corresponds to the chord length, expressed as the number of data points within the light curve minimum. 112
- 3.18 Uncertainty including the AT error as derived from a simple model (half of the asteroid apparent radius, computed for each event) for a single-chord event, meaning there would be no other observation to this occultation besides ours. For  $D < 10$  km and occultation duration  $< 5$  samples, the uncertainty due to asteroid size no longer dominates and the two error distributions overlap. . . . . 112
- 3.19 Tests made with the LSF as a function of whether they were rejected or not vs DNR. Rejected means not fitting the curve, not being able to estimate parameter uncertainties or estimating these uncertainties as being several orders of magnitude above the nominal values. Only 48% of cases were accepted. . 113
- 3.20 PyOTE's estimate of the duration of the Daphne occultation. This was the case with the largest DNR among the analyzed ( $\sim 7.8$ ). . . . . 114
- 3.21 PyOTE's estimate of the duration of the Victoria occultation. Centre line is best fit, other lines are separated by 1-sigma in flux and duration. This was the case with the lowest DNR among the analyzed ( $\sim 1.4$ ). . . . . 115

3.22	DNR and uncertainty on central epoch for a number of observed events similar to those adopted for the simulation. The colour of the circles is associated to the number of data points in the occultation minimum, indicated by the scale at the right of the plot. Red line represents the average expected uncertainty for the event, and the green areas represent 1 (dark green) and 2 (light green) sigma intervals. Note that the points represent the uncertainty in time obtained through the BIM, NOT the times reported. For the performance comparison between reported uncertainties and the ones obtained through the BIM, check Table 3.2 . . . . .	118
4.1	Triton light curve. Central flash observed, which can be used to study Triton's atmosphere. . . . .	122
4.2	Triton occultation analyzed by the Paris team (Bruno Sicardy et. al). Blue line is Neptune's flux, red line the occulted star's flux. Black is the ratio between the two, normalised to 1 for the average outside the occultation. . . . .	123
4.3	Fit of some observed chords of Triton during this event. Our observation is close to the centre. Image by Euraster. An image with all the used chords will be provided in a future publication by the Lucky Star collaboration. . . . .	124
4.4	Aemilia occultation, seen with AOTA ( <b>A</b> steroidal <b>O</b> ccultation <b>T</b> iming <b>A</b> nalyzer), a tool present in Occult. The blue dots represent the samples, with their 1-sigma uncertainties, and red lines represent the flux inside and outside the occultation, as well as the slope seen in one and another direction with a 1-sampling time interval. Ingress and egress times in local unites (+2 UTC). . . . .	125
4.5	Occultation of (3200) Phaethon as seen with a 1 meter telescope in Nice. Observing team: Jean-Pierre Rivet, Paolo Tanga, Erick Bondoux, David Vernet. . . . .	127

- 
- 4.6 Shape of (3200) Phaethon fit to the three observed chords: Baba Aissa from Algeria (blue), Christian Weber from Germany (red) and our observation (purple). Dashed green and red lines represent uncertainties in disappearance and reappearance moments for each chord, which shows the Nice observation was far more precise than the others. Fit made by Eric Frappa. . . 128
- 4.7 Millman occultation, as analyzed with Tangra. Blue is the light curve of the occulted star and yellow the light curve of a reference star in the Field Of View. . . . . 129
- 4.8 Occultation of (5638) Deikoon, fitted for the 2 positive chords (Lionel Rousselot, Vierzon, France, and Alain Figer, Paris, France). Dashed lines represent timing uncertainties by each user, and their large size does not exclude a spherical model for the asteroid. Our observation is represented by the purple line, numbered 11, meaning that we missed the event by a little over 1 object radius ( $\sim 50$  km). Fit made by Eric Frappa, shared in Euraster. . . . . 133
- 4.9 European results of (307 261) 2002MS4 campaign. Our observation is the first negative chord to the north. Results will be published by the LESIA team in the future. Image by Euraster. 137
- 4.10 DIAMONDS applied to the OBSPA Europa observation. Reported duration was  $104.66 \pm 1.25$  s. Obtained duration with DIAMONDS was  $115.9 \pm 5.8$  s. A difference of 11.3 s that corresponds to a 2-sigma discrepancy. . . . . 138
- 4.11 DIAMONDS applied to the FOZ Europa observation. Reported duration was  $115.52 \pm 1.32$  s. Obtained duration with DIAMONDS was  $114.3 \pm 2.4$  s. A difference of only 0.8 s, so good agreement between both results. . . . . 139
- 4.12 Galatea plot. Red line represents light curve from BIM, while Green lightcurve represents the first approximation found by Rui Gonçalves. Blue points represent the obtained photometry. 140

4.13	Light curve of Euphrosyne. Results reported were duration of $18.56 \pm 0.04$ s and mid epoch at 00:43:10.30. Results with DIAMONDS were duration of $18.4 \pm 0.05$ s and mid epoch at 00:43:10.20. Results were compatible within 1-sigma. . . . .	141
5.1	A single chord occultation is ambiguous. The chord can always fit two different positions for the object, here assumed to be a sphere of Diameter D, usually extracted from WISE. The distance between the observed chord and the two possible solutions can be defined as in Equation 6.1 . . . . .	148
5.2	Idealised scheme of the uncertainties involved in the astrometry derived from single chord observations of stellar occultations. We adopt as an example a very elongated ellipsoidal asteroid, projected on the fundamental plane in which the asteroid is at rest and the occulted star moves along the dashed arrows. The AC and AT axes represent the across and along-track directions, respectively. In (a) the observed chord duration (black segment) is the same as for the surface-equivalent sphere in (b). The mid-chord point corresponds to the barycentre position in (b), but not in (a), where the error on the derived astrometry $e_{AT}$ cannot be estimated without a precise knowledge of the shape. Points (c) and (d) represent the ambiguity on the AC position of the observed chord, which can be on opposite sides of the barycentre. . . . .	149
5.3	There are 4 clear trends, all relating to the rules of AC and AL uncertainty for poor chords, a majority of the archive. Here, we can see that events with 3 or more chords tend to stay out of these trends, as they usually provide good enough astrometry for a particular solution. The rest are distributed across AL being 2, 4 or 8 times smaller, depending on chord length. . . .	151
5.4	Some events with 3 or more chords still fell on the trends, likely due to poor distribution of chords, or poor chord precision, like visual observations or observations with an NTP server with bad synchronization rather than observations timed by a precise system such as GPS. . . . .	151

- 
- 5.5 Example of an outlier that fell in the trendline. One of the chords was visual, and therefore left out of the fit, and the other 3 chords were too close to provide a good constraint on the object's position. . . . . 152
- 5.6 AL uncertainty in mas as a function of the number of chords of an event. The transition from 2 to 3 chords seems to be when there is a major improvement in the fit, telling us which should be our cutoff on the number of chords for this work. This is to be expected as, with few exceptions, three chords is when an unambiguous fit to the asteroid becomes possible. Since most occultations correlate Along and Across Track uncertainties, a similar plot with Across Track has a similar distribution, with higher uncertainties. . . . . 152
- 5.7 Sky-projected distance from both ephemeris to the centre epoch astrometric solution of (51) Nemausa for its 1983/09/11 occultation. TS20 clearly approaches the published position, having it almost within a 1-sigma distance. Asteroid had apparent size of 125 mas, putting the FV15 fit outside the body in the AL direction. Both models are compatible in AC direction. . . . . 156
- 5.8 Despite the general improvement brought by the TS20, FV15 still usually provides good solutions, with the best case being that of (1 263) Varsavia, an event from 2003/07/08. Asteroid had apparent size of 25 mas, putting the TS20 fit outside the body for the AL direction, though it remains compatible in AC direction. . . . . 157
- 5.9 One of the best improvements, that of (212) Medea's event, on 2011/01/08. Asteroid had apparent size of 92 mas, putting the FV15 fit outside the body. . . . . 157

5.10	Anomalous (472) Roma event, on 2010/07/08. The star was particularly bright (Vmag. 2.5), with several of the observations having large timing errors, in the order of seconds, likely due to unconventional equipment, such as non-fast moving cameras, being used, or in some cases visual reports instead. Saturation issues may have also played a role on the unreliability of some results. . . . .	158
5.11	Example of event where TS20 greatly outperformed FV15, an occultation by (41) Daphne on 2012/02/23. . . . .	162
5.12	Example of event where TS20 greatly outperformed FV15, an occultation by (8 931) Hirokimatsuo on 2017/11/15. . . . .	163
5.13	Example of event where TS20 greatly outperformed FV15, an occultation by (521) Brixia on 2011/05/27. . . . .	164
5.14	Correlation between Across and Along Track Differences (in units of diameter) and H0 magnitude of asteroid. There is a positive correlation, suggesting that the differences tend to be larger for larger magnitude asteroids, which correspond to smaller diameters. . . . .	165
5.15	Same plot, but with Observations available for fit as auxiliary colour. There seems to be a negative correlation, as less observations can bring up the error, which is to be expected. . . . .	165
5.16	Density distribution of AC distance as a function of asteroid radius vs asteroid size, showing a negative correlation. Red means low density and green/blue high density. . . . .	166
5.17	Distribution of difference to occultation solution in AC difference, in units of asteroid diameter. Both are centred on 0, and seem to display gaussian behaviour. Gaussian line is for illustration purposes. . . . .	166
5.18	Similar plot to Figure 5.17, but for differences in AL direction. Once again, gaussian distributions centred in 0, meaning no biases are noticeable. . . . .	167

- 
- 5.19 Astrometric solutions of (145) Adeona at the moment of its occultation. The origin of the plot is the position derived from the occultation, in blue. The ellipse is exaggerated, and corresponds to a 10-sigma region, and the arrow represents the velocity vector. To the left, in orange, is the fit with MPC data only. To the right, in green, the fit with MPC and Gaia combined. 168
- 5.20 Plot similar to Figure 5.19 for (13 244) Dannymeyer, an asteroid with a single chord occultation on November 7<sup>th</sup> 2019. The discrepancy between the solutions is larger now, as this asteroid has not been observed as many times as (145) Adeona. . . . . 168
- 5.21 Shape solutions obtained with OrbFit for the (50) Virginia occultation. Adding Gaia data improves the agreement between orbital fit and occultation. Chords for MPC+Gaia solution show in green, to better illustrate what was observed. . . . . 169
- 5.22 Shape solutions for (145) Adeona occultation. The orbital solution does not depend heavily on the Gaia observations, likely due to already good constraints prior to adding them, and so the results are similar. . . . . 170
- 5.23 Shape solutions for (163) Erigone occultation. Once again, the orbit is relatively unchanged, with a noticeable deviation in RA from the occultation's solution. . . . . 171
- 5.24 Shape solutions for (118) Peitho occultation. The most drastic change, in favour of adding Gaia data, with the difference going from almost 100 mas to less than 10 mas. . . . . 172
- 5.25 Prediction of occultation by (100) Hekate on March 13<sup>th</sup> 2020. The cross represents the site of observation at OCA. Using all MPC observations, but not Gaia, the across axis uncertainty is 37 mas, slightly smaller, but comparable, to the diameter of the object. The probability of a positive detection at our site was calculated at 33%. There were 3 009 observations to this asteroid in total, ranging from 1871 to 2020. . . . . 173

5.26	113 observations by Gaia to (100) Hekate were added to the orbital fit. This causes a decrease on the across axis from 37 to 3 mas, our site is now inside the shadow path, and the probability raised to 91%. . . . .	174
5.27	Comparison of semi-major axis uncertainty (in au) for the 14 099 asteroids in DR2 with and without Gaia data. Despite the limited number of observations (a few hundred among thousands, on average) and the small time frame of DR2 (22 months vs tens of years with other methods), there is a clear tendency for a drop of $\sigma_a$ , with an average drop of $\sim 17\%$ . . . . .	174
5.28	Zoomed in version of Figure 5.27, showing us that larger distances result in greater decreases, likely because these objects (Centaur) have less observations than MBA, giving Gaia a greater weight. . . . .	175
5.29	Smoothed average of semi-major axis uncertainty as a function of asteroid Diameter. We see that the uncertainty distribution lowers slightly when adding Gaia data across all sizes. For better visualization, TNO were excluded, due to their big size and semi-major axis uncertainty skewing the plot. . . . .	175
6.1	Example of occultation short term prediction of (65 803) Didymos obtained using Occult with the Gaia15.5 catalogue built for this work. . . . .	183
6.2	Another example, with one of the best NEA in terms of orbital precision, (68 950) 2002 QF15, theoretically visible at Calern. AC uncertainty of 15 mas. . . . .	183
6.3	Example of event found for (65 803) Didymos in the time frame until the launch of ESA's HERA spacecraft (2024). AC uncertainty of 10 mas. . . . .	184
A.1	Example from Veres et al. (2017) of dependence of the residuals to the year of observation for a specific site (code 691 - Spacewatch). Different observatories have different trends, so each needs its own rule. This also applies to other parameters. . . . .	199

A.2	Same analysis, also from Veres et al. (2017), but with dependence on object brightness (code 699 - LONEOS). . . . .	200
A.3	Same analysis, also from Veres et al. (2017), but with dependence on object projected velocity in the sky (code 699 - LONEOS). . . . .	200
A.4	Trend of residuals as a function of catalogue for RA and Dec. "No catalogue" tends to have larger residuals, Gaia DR1 and DR2 smaller, and a large scatter is seen with UCAC catalogues, especially UCAC2. . . . .	201
A.5	Same analysis, for asteroid magnitude. "No mag" means that no magnitude is given for a certain observation, focusing only on astrometry. Observations that don't allow a magnitude estimate tend to be difficult, so these result in larger residuals. Then, there is a clear trend for larger residuals associated to larger magnitudes, similar to what was verified in FV15. . . .	202
B.1	Setup file for mandatory global run of events, readable by Linoccult. Dates of run are from 01/01/2018 to 31/12/2018, so one full year. "MinDiameter" is the minimum diameter of an asteroid, meaning any diameter smaller excludes the object from this run. "MaxDiameter" does the same with an upper bound, but is left unused. Results are output in a .bin file which will then be used to extract local events. . . . .	207
B.2	User sites file, that Linoccult reads together with the .bin global file to assess events visible in specific locations. . . . .	207
B.3	Local Linoccult file. "SitesFilePath" indicates where Linoccult must read the site file, "InputEventsFilePath" where to read the .bin file and "Calculation Mode 0" ensures Linoccult does not compute globally every event again, just for the local sites. . . . .	209
B.4	Setting up all relevant variables for the simulation. . . . .	209
B.5	Flux calculation for specific event. . . . .	210
B.6	Getting every star within a certain Declination band that follows all of our restrictions. . . . .	211
B.7	Section in Occult which builds the Gaia star catalogue from our output files. . . . .	212

B.8	Getting every observation from a specific asteroid made by Gaia. This example shows the query for the lowest numbered asteroid in the catalogue, (8) Flora. . . . .	213
B.9	File that queries AstDyS for the initial values of orbital parameters of every asteroid in DR2, whose MPC numbers are extracted from a source file made previously. . . . .	213
B.10	File that queries MPC for all available observations of each asteroid present in DR2. . . . .	214
B.11	Example of a setup file to be read by OrbFit, in this case for (1566) Icarus. Main difference between runs is whether the error model used for the observations is the previously established one (Farnocchia - fcct14) or the new one built by Federica Spoto (gaiaDR2). . . . .	214
B.12	Example of application of photutils to a stellar occultation. Target was Pluto, for an occultation on 2016/07/14 in Constância. By using a FITS file for each frame (1024 x 1024 pixels), photutils analyzes searches for sources above noise level by a certain threshold (signal 5x larger than noise in this example). Then, it lists the (x;y) pixel coordinates of each target that surpasses this threshold, and by using a first approach, we attempt to manually identify in the first frame which of these targets is the occulted star, doing aperture photometry of 3.5 pixels radius around it, the value found to have the best SNR for targets that are not very bright. Other stars, should they be above the threshold for the entire video, can be used as reference later. Once the occulted star has been found, we search its surroundings in the following frame for it. If it is not found, then we assume it remains in the same coordinates, which should be the case for stable images. This is necessary in case the drop caused by the occultation is large enough to remove the star from the list of objects above the threshold. A different approach is to use relative positions by taking a few reference stars, and using their positions to estimate the position of the lost target. . . . .	215

# List of Tables

1.1	Average precision in star precision for different magnitudes in DR2. $G < 15$ is the most relevant group for this work. . . . .	65
1.2	Stars with 2 or 5 parameter analysis in each DR, as well as number of objects with an estimated $G$ magnitude. Number of objects with 5-parameter analysis grew by 3 orders of magnitude between DR1 and DR2. Such jumps will not be seen in DR3 or any future releases for the stars, but there is still a growth of events with good star astrometry to be expected with the newer catalogue, and a lot more asteroids in DR3 and beyond, this new version representing for Solar System Objects what DR2 was for the stars. . . . .	68
2.1	Expected efficiency for specific site, depending on asteroid uncertainty improvement. . . . .	88
2.2	Table listing, for each asteroid uncertainty improvement factor and for each asteroid size category, how many events have probabilities above 1% (minimum for observation planning), 25%, 50% and 75%. Clear trend of less unreliable events is found, as should be expected. . . . .	91
3.1	Performance comparison between PyOTE and DIAMONDS, the two bayesian tools available. Centre epoch precision is shown to be of comparable size most of the time, with DIAMONDS benefiting from being more versatile in the choices made and more user friendly for mass use. . . . .	116

3.2	Observed occultation chords chosen for comparison to our model for observation accuracy. Their photometric light curves data have been fitted by the model, with the same procedure adopted for the simulations. For the (3 200) Phaethon observation in particular, since our uncertainty was the one published, the "author" uncertainty is the one obtained by Jean-Pierre Rivet, another member of the observation, through a different method. For the other observations, the uncertainties were obtained from various sources, namely the Planoccult mailing list where the observers shared their reports, Euraster and the Occult archive. $\sigma_{t_0}$ R is the reported uncertainty, $\sigma_{t_0}$ B (s) the uncertainty obtained with the BIM and dt the exposure time. . . .	117
5.1	Rule applied by [Vereš et al., 2017] to the epoch of each asteroid observation. . . . .	146
5.2	Rule applied by [Vereš et al., 2017] to the method of each asteroid observation. . . . .	147
5.3	Rule applied by [Vereš et al., 2017] to the reference star catalogue of each asteroid observation, for RA and Dec coordinates separately. . . . .	147
5.4	Table of every asteroid occultation with 20 or more positive chords reported, sorted by ascending asteroid number. Distance to astrometric solution of occultation by FV15 and TS20 error models are shown, with a clear trend of better solutions under TS20. . . . .	155
5.5	Comparison between the error models FV15 and TS20 by using OrbFit. We analyze average and $\sigma$ of AC, AL and total differences. We can see that using the current database for each asteroid provides better results, as is to be expected, as more modern observations tend to be more precise. We also see a tendency for differences to become smaller by adopting the TS20 model rather than FV15. . . . .	159

- 
- 5.6 Same as Table 5.5, but as ratio of difference and apparent diameter at moment of occultation, along with percentage of events that fell within one diameter of difference to the occultation. This percentage means how many events would have been confirmed by the occultations, barring issues regarding irregular shapes or bad chord distribution. Like in Table 5.5, current knowledge improves results compared to "postdictions" and TS20 outperforms FV15. . . . . 160
- 5.7 Same as Table 5.5, but only for events with 5 or more chords, which are typically the most precise. About 8% of events ( $\sim 370$ ) fall under this category. Results tend to be slightly further away on average, but the progression by using current knowledge vs "postidction" and TS20 vs FV15 is still present. 160
- 5.8 Same as Table 5.6, but only for events with 5 or more chords. 160
- 5.9 Determining which model is better or whether they are similar. Here, we adopt the convention that they are similar if their distances to the occultation's astrometric solution are within 10% of the larger distance. If not, then whichever model is the closest is considered to be better. We can see that, for the non-similar results, TS20 was better more than twice the amount of cases than FV15. . . . . 161
- 5.10 Distribution of events in different regions of AC difference: " $d < R$ ", where the difference is smaller than the asteroid's radius, "1-sigma", where the difference is between  $R$  and  $R + \sigma_{occ} + \sigma_{model}$ , "3-sigma", where difference is between  $R + \sigma_{occ} + \sigma_{model}$  and  $R + 3 * (\sigma_{occ} + \sigma_{model})$  and "incompatibility", where the difference is even larger. We also separate the data set between stars with known issues from DR2 that the rest, showing that, if these issues were to be treated, results would improve. Only the runs with the best current knowledge were used for this analysis, and once again TS20 outperforms FV15. . . . . 161

- 6.1 All 11 NEA with  $\sigma_a < 10^{-9}$  au, in ascending order. Full list of "interesting" targets included the 70 best NEA in terms of semi-major axis uncertainty, plus (65 803) Didymos for the HERA mission. . . . . 184

# Introduction

---

## Contents

---

<b>1.1 Asteroids History</b> . . . . .	<b>37</b>
1.1.1 How have they been observed? . . . . .	37
1.1.2 Observation Methods and Missions . . . . .	43
<b>1.2 Stellar Occultations</b> . . . . .	<b>45</b>
1.2.1 General properties . . . . .	45
1.2.2 Why are they important? . . . . .	54
<b>1.3 The Gaia Mission</b> . . . . .	<b>60</b>
<b>1.4 Goals and Structure of this Thesis</b> . . . . .	<b>68</b>

---

## 1.1 Asteroids History

### 1.1.1 How have they been observed?

Asteroids are small bodies of our Solar System that have been known since the early 19<sup>th</sup> century. The very first one to be discovered is also the biggest known object of the Main Belt, (1) Ceres (Figure 1.1), with a diameter of 945 km, discovered in 1801 by Italian astronomer Giuseppe Piazzi.

Its existence was hinted at by an empirical law derived by Johann Elert Bode in the 18<sup>th</sup> century, who, through a geometric distribution of the known planets at the time (Mercury to Saturn), stated that there should be a planet between Mars and Jupiter. However, in the following decades more objects were discovered in this region, such as (2) Pallas, (3) Juno, (4) Vesta and (5) Astraea, until in 1846 the discovery of Neptune rendered this Law discredited.

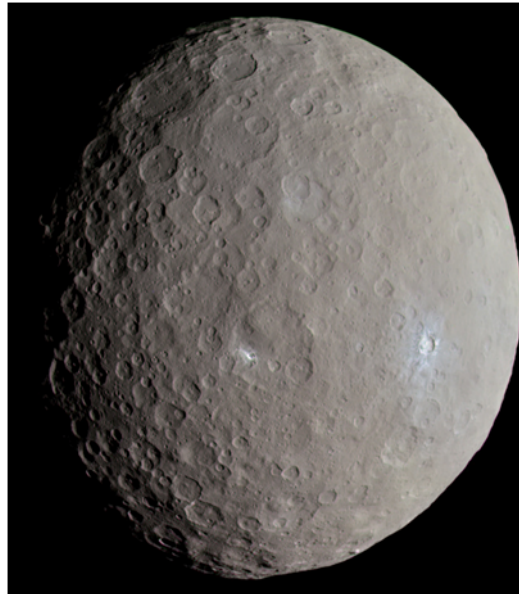


Figure 1.1: (1) Ceres, the first asteroid discovered and largest object of the Main Belt. Image by NASA. Image from [Baer et al. \[2011\]](#)

Astronomers kept looking for new objects between Mars and Jupiter, as well as beyond Neptune, reaching 1 000 numbered asteroids in the 20s, 10 000 in 1989, 100 000 in 2005 [[Tichá et al., 2007](#)] and over 540 000 nowadays, to which we can add another 450 000 unnumbered asteroids [[DeMeo et al., 2015](#)]. The recent evolution of numbered asteroids, as well as Near Earth Asteroids in particular, can be found in [Figures 1.3 and 1.4](#).

The known population of asteroids can be considered to be known with reasonable completeness down to diameters of 5 km, with smaller sizes being under-represented due to the biases imposed by the observation methods, which usually favour larger and/or brighter objects. You can see the distribution in [Figure 1.2](#)

Asteroids are important because they are the remnants of the formation period of our Solar System's formation. Their composition and distribution allows us to peek into those early days, and study how our system evolved from then until now. Another useful reason to study them is for our own defense, since we are constantly being bombarded with small objects, and on occasion large bodies hit the Earth, which may cause permanent changes to our landscape and considerable losses. Studying asteroids can help prevent

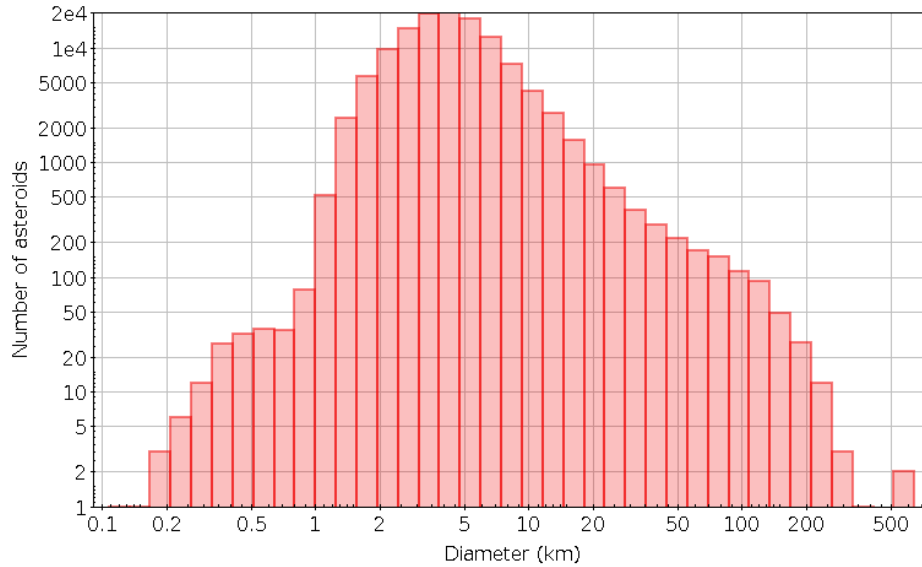


Figure 1.2: Diameter distribution of numbered asteroids, according to the NEOWISE survey. Diameters smaller than 5km are assumed to be heavily under-represented due to the biases introduced by the limitations of the most typical observation methods.

this from happening in our future. Finally, nearby asteroids may also be interesting to study as an exploitable resource, depending on their composition, though for now missions to asteroids remain very costly.

Nowadays, the small bodies of the Solar System are split into different categories, depending on their semi-major axis, composition and interaction with other objects. Some examples are listed.

- **MBA: Main Belt Asteroids**, objects whose semi-major axis is between Mars (1.5 au) and Jupiter (5.2 au), being by far the largest known subgroup of asteroids;
- **TNO: TransNeptunian Objects**, objects whose semi-major axis is bigger than Neptune's (>30 Astronomical Units, au), with Pluto being the most well-known example;
- **NEA: Near-Earth Asteroids** (also known as NEO - Near Earth Objects), whose closest approach to the Sun (perihelion) is smaller than 1.3 au;

- Centaurs: Semi-major axis between Jupiter (5.2 au) and Neptune (30 au);
- Trojans: Asteroids that share an orbit with a planet, usually Jupiter. These asteroids are in one of the Lagrange points of the Sun-planet system;
- Amor: NEA whose perihelion is larger than Earth's aphelion, named after (1 221) Amor;
- Apollo: NEA whose perihelion is smaller than Earth's aphelion, named after (1 862) Apollo;
- Aten: NEA whose semi-major axis is smaller than 1 au, named after (2 062) Aten;
- Atira: NEA whose aphelion is smaller than Earth's perihelion, named after (163 693) Atira;
- PHA: **P**otentially **H**azardous **A**steroids, whose orbits make close approaches to Earth and represent a risk of impact.

Throughout the decades, the method of detecting asteroids has changed. While at first astronomers had to compare plates with sky images to look for objects with noticeable movements nowadays, this process is computerized, and accepted sets of observations allow astronomers to estimate orbital parameters and include a new object in the catalogues.

The current preliminary designation method for new objects follows a standard, enumerated.

1. The year of discovery of the object;
2. A first letter ranging A-Y representing the half-month in which the object was discovered within that year (letter I is not used);
3. A second letter ranging A-Z representing the order of discovery within that half-month;
4. If necessary, a complementary number with the cycle of the 2<sup>nd</sup> letter.

The asteroid gets a permanent catalogue number once its orbit is accurate enough to predict its position at the next opposition with a precision sufficient for its recovery (typically a few arcminutes).

Later, an object's name can be changed to reference a person, group, place or historical figure, as long as its catalogue number remains the same.

We stress here that, for occultations, we will only be referring to numbered asteroids, as good orbits are usually required for reliable predictions.

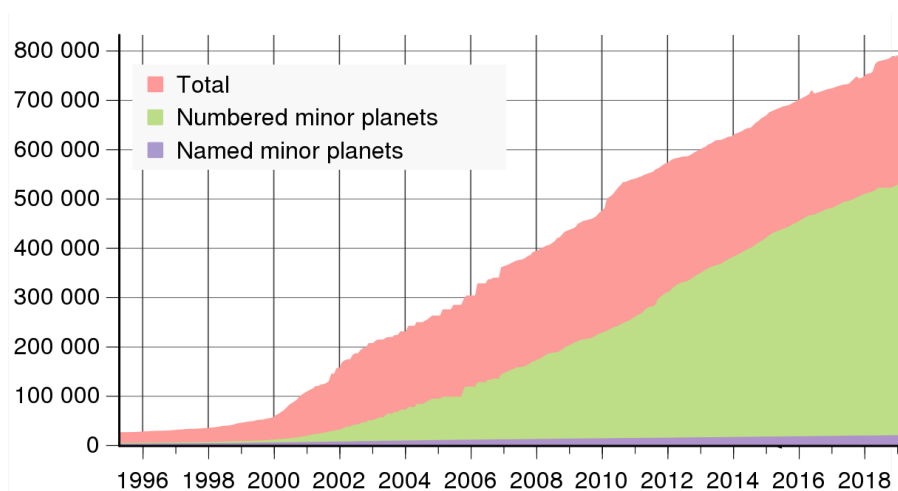


Figure 1.3: Number of known asteroids by year in the last 2 decades. Image from Minor Planet Center.

Asteroids are thought to be, along with comets, primordial objects of the Solar System, retaining properties from the planetesimal stage, making their study vital to study the origins of our system. The most complete databases as of right now are Astorb<sup>1</sup>, MPC<sup>2</sup> (**Minor Planet Center**), AstDyS-2<sup>3</sup> (**Asteroids Dynamic Site**) and JPL Horizons<sup>4</sup> (**Jet Propulsion Lab**). While all four are used, there are differences between them: MPC is the official database of the International Astronomical Union, and is the group in charge of the provisional and definitive identifiers of small bodies. It updates its observations archive monthly, and details epoch, observatory, method and RA/Dec coordinates for each asteroid observation. Meanwhile, the other 3

<sup>1</sup> <ftp://ftp.lowell.edu/pub/elgb/>

<sup>2</sup> <https://minorplanetcenter.net/iau/MPCORB.html>

<sup>3</sup> <http://hamilton.dm.unipi.it/astdys/>

<sup>4</sup> <https://ssd.jpl.nasa.gov/horizons.cgi>

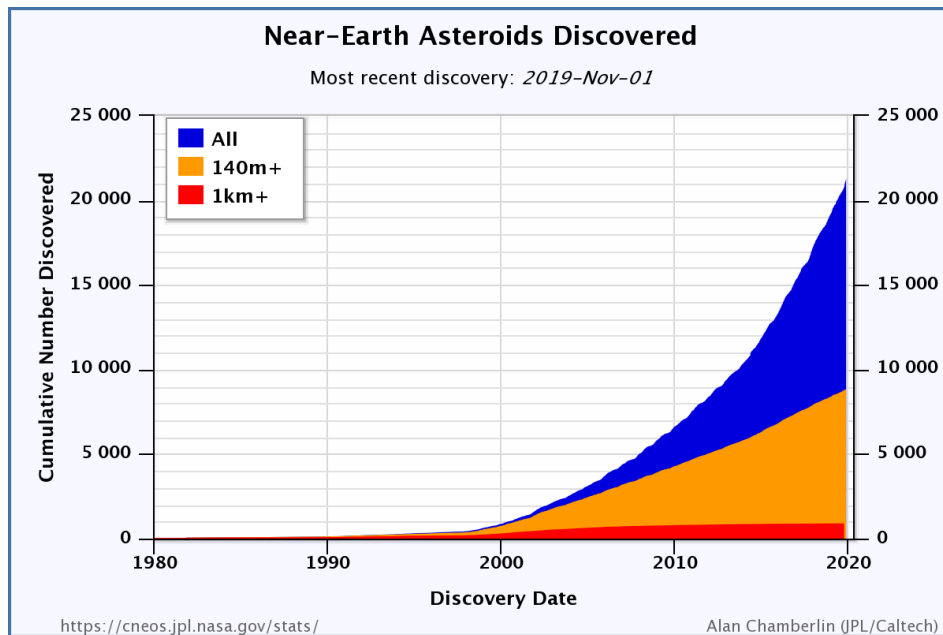


Figure 1.4: Amount of known NEA by year in the last 4 decades. From the scarce growth, it is considered that the population of NEA larger than 1 km is well-known and almost completely catalogued, but the smaller sizes are still under-represented. Image from Minor Planet Center.

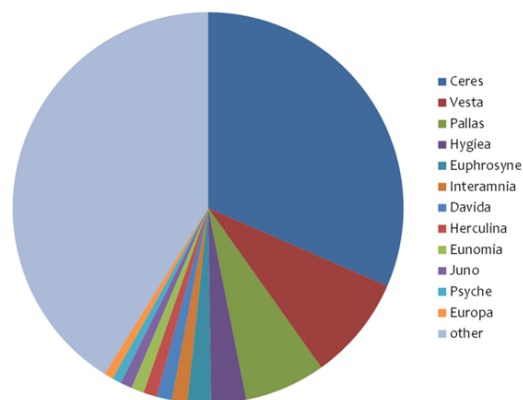


Figure 1.5: Mass distribution of the Main Belt, with the pie chart sections in the same order of the legend, in clockwise direction.

sources use the MPC database of observations, but apply their own data selection rules to refine the orbits by rejecting some of the least precise data points (see Appendix A for the rules applied to Astorb and JPL).

### 1.1.2 Observation Methods and Missions

While this work focuses on stellar occultations and the Gaia space mission, there are several other methods that have been historically used to obtain the astrometry of asteroids, with varying degrees of availability and precision. The following is a list of the most commonly used methods, with the average accuracy taken from [Desmars et al., 2015], and some current or future missions that apply to each category:

- Radar observations: mostly used for close targets, to assess their shape. The rapid decay of the photon flux in this regime makes it so the current set of radar observations is heavily biased towards NEA. It allows to study the size, shape and spin of each body, and can reach kilometer-sized precision in the measurements;
- Thermal radiometry: observations in the micrometer range, to measure the thermal flux of an asteroid. One of the most reliable methods to estimate an asteroid's size and its geometric albedo.
- Ground-based direct imaging through the use of photographic plates or CCD, which allows relative astrometry, using reference objects around the asteroid to determine its position and apparent velocity, and photometry, the measurement of the flux of the asteroid, helping build shape models. At the time of the paper reference, these accounted for almost 95% of all observations, almost entirely due to CCD imaging in the most recent decades. The average astrometric precision of this method is 300 mas. It should be noted that photometry is one of the methods that allows the build of shape models;
- Space observations, carried out by probes outside of Earth's atmosphere. This is useful to increase the quality of the image, as it is no longer necessary to account for distortions caused to the light signal by the air molecules. Due to the expensive nature of space missions, this is

not as frequent as ground-based observations, but several space probes, mentioned later in this chapter, have been used for this purpose, with an especially sizeable contribution by the WISE telescope, accounting for  $\sim 4\%$  of all observations. The average astrometric precision from this method is 600 mas. Some highlights for this method are:

- Gaia, analyzed in detail in Section 1.3;
  - NEOWISE<sup>5</sup> [Masiero et al., 2011], NASA mission. All-sky survey that discovered thousands of asteroids and provided the most complete asteroid diameter table to date, with over 120 000 measurements, and is currently focusing on NEA;
  - Euclid<sup>6</sup>, future ESA mission. Despite focusing on topics such as the expansion of the universe and the identity of dark matter, it is also expected to greatly increase the available information on spectral classification of asteroids. See [Carry, 2018];
- "In-situ" observations, when space probes target a specific asteroid either to study it at the surface, or to return samples to Earth. Some examples of such missions are:
    - Hayabusa<sup>7</sup> [Kawaguchi et al., 2008] and Hayabusa2<sup>8</sup> [Tsuda et al., 2013], a completed and an on-going JAXA missions (Japan). Hayabusa landed on (25143) Itokawa, recovered samples from it, and returned to Earth, being the first of this kind of missions to return. Hayabusa2 had a similar task to study (162173) Ryugu, and is expected to return in December 2020;
    - OSIRIS-REx<sup>9</sup> [Lauretta, 2015]: On-going NASA mission. Orbiting the asteroid (101 955) Bennu, and with the goal of return samples from this object to Earth;
    - Lucy<sup>10</sup>: Future NASA mission. Planned to cross several trojan asteroids, most notably (11 351) Leucus [Buie et al., 2018];

---

<sup>5</sup> [https://www.nasa.gov/mission\\_pages/neowise/mainindex.html](https://www.nasa.gov/mission_pages/neowise/mainindex.html)

<sup>6</sup> <https://sci.esa.int/web/euclid>

<sup>7</sup> <http://www.isas.jaxa.jp/en/missions/spacecraft/past/hayabusa.html>

<sup>8</sup> <http://www.hayabusa2.jaxa.jp/en/>

<sup>9</sup> <https://www.nasa.gov/osiris-rex/>

<sup>10</sup> <https://www.nasa.gov/content/goddard/lucy-overview>

- DART (Double Asteroid Redirection Test)<sup>11</sup> [Cheng et al., 2018]: Future NASA mission. Planetary defense test on the binary system of (65803) Didymos. By directly crashing a satellite into the moon of Didymos, which is only 160 m in size, scientists will be able to study the shift caused on its orbit. This is connected to HERA<sup>12</sup> [Sears et al., 2004], an ESA mission, that will help measure the consequences of the DART's impact;
- DESTINY+<sup>13</sup> [Sarli et al., 2018]: Future JAXA mission, planned to flyby (3200) Phaethon, to understand the origin of its meteor shower;
- Psyche<sup>14</sup> [Maurel et al., 2020]: Future NASA mission, designed to orbit its namesake, (16) Psyche, and study its composition.

Finally, stellar occultations, explained in detail in the next section.

## 1.2 Stellar Occultations

### 1.2.1 General properties

A stellar occultation is an event in which a certain object crosses the trajectory of a star's light from the observer's perspective. Because of the apparent size of stars and asteroids, this event can only be visible in certain "shadow" areas that the asteroid produces on the planet's surface when passing in front of a star. The smaller the object, the smaller the size of this shadowed region is, making the event much more difficult to observe, and needing great precision on the position of both star and asteroid better than arc-second size. For that reason, it was not feasible to observe stellar occultations of small bodies for a long time, because their orbits were not precise enough and because until recently even the star catalogues had uncertainties too large to make mass predictions, only applying this method to the Moon and the planets, not only because of their bigger angular size, but because we know their orbits with

---

<sup>11</sup> <https://www.nasa.gov/planetarydefense/dart>

<sup>12</sup> [https://www.esa.int/Safety\\_Security/Hera](https://www.esa.int/Safety_Security/Hera)

<sup>13</sup> <https://destiny.isas.jaxa.jp/>

<sup>14</sup> <https://www.jpl.nasa.gov/missions/psyche/>

much greater precision than other bodies. These have been happening since the end of the 19<sup>th</sup> century, with Venus providing the first event by a planet with multiple observers. Details in Figure 1.8

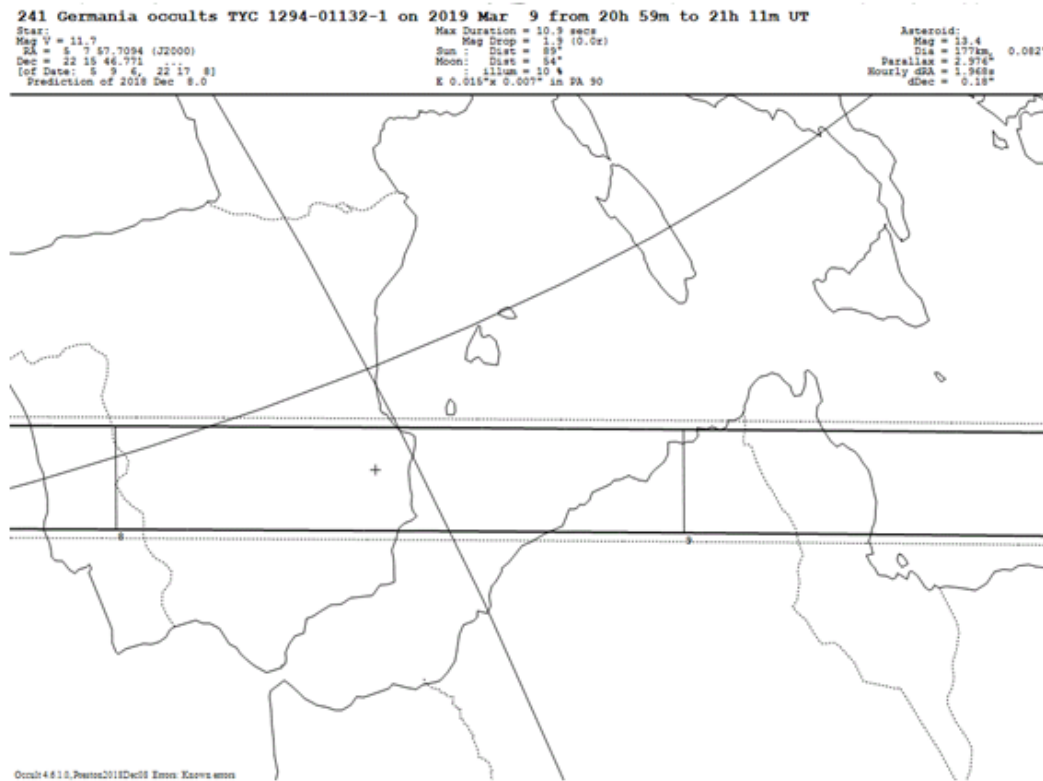


Figure 1.6: Example of Prediction from "call4obs", originally made by Steve Preston.

What we can extract from stellar occultations are disappearance/reappearance times, which tell us when the asteroid was in front of the star, the RA/Dec coordinates of the star to place the event in the sky and the magnitude drop, to estimate the brightness of the asteroid during this period. If well exploited, this can result in an astrometric solution to the asteroid as precise as that of the star during the occultation, typically a precision better than other methods.

The first recorded paper on stellar occultations by small bodies (not the Moon or a major planet) was in 1952 [Taylor, 1952], regarding the prediction of an occultation by (3) Juno, while the first reported positive observation of an occultation by a small body was in 1961 [Evans and Lourens, 1961],

describing the observation of (2) Pallas occulting a star, officially inaugurating a new method of observing the small bodies of the Solar System. A sketch of the observed chord can be seen in Figure 1.7

Several years would still have to pass before an event by an asteroid was observed in multiple sites, namely (433) Eros in 1975 [Weston et al., 1975] (Figure 1.9). This means that, from this moment, it became possible to study the shape of asteroids through this method.

Note: Figures 1.7, 1.8 and 1.9 are taken from an archive, and the respective chord uncertainties are not provided.

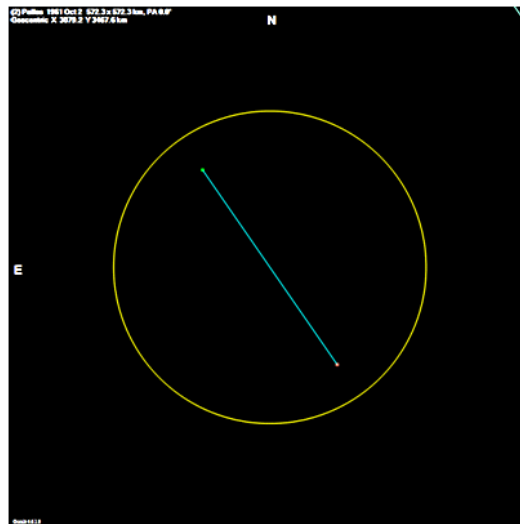


Figure 1.7: Representation of the first ever occultation by an asteroid: (2) Pallas, 1961/10/02, by D. Evans and J. van Lourens. The blue line is the chord registered during the observation, and the sphere is the model of Pallas at the time, with the chord assumed to be central, or close to it. Image by Occult.

The amount of observations every year by astronomers to such type of events has greatly increased due to several factors: improvement of star catalogues (UCAC, Tycho, Hipparcos [Perryman, 2012, Colas et al., 2011, Dunham et al., 2002] and now Gaia<sup>15</sup>) [Tanga and Delbo, 2007], as well as asteroid catalogues (currently over 500 000 numbered asteroids compared to less than 10 000 in 1990), faster devices to compute events while cross-matching these two

<sup>15</sup> <http://sci.esa.int/gaia/>

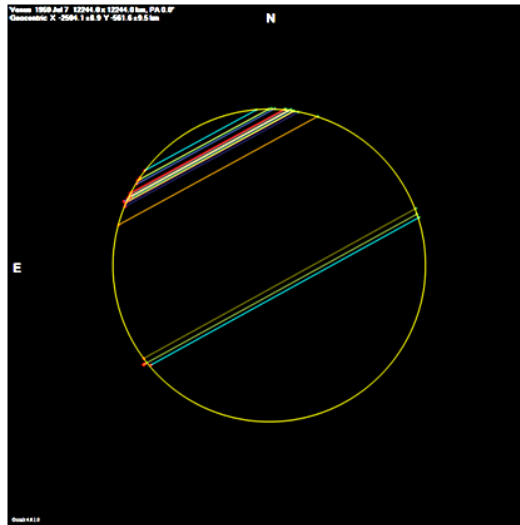


Figure 1.8: First reliable multi-chord event by any object other than the Moon, according to Occult: Venus, 1959/07/07. The sphere is the model of Venus, and each line represents a distinct observation recorded. Image by Occult.

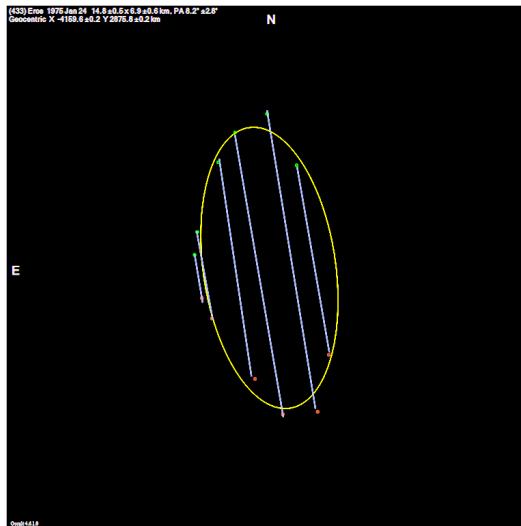


Figure 1.9: First ever multi-chord event by an asteroid, according to Occult: (433) Eros, 1975/01/24. Green and red lines represent beginning and end of chords (chords are nearly vertical in this image). Image by Occult.

catalogues and an overall increase on the number of astronomers involved in stellar occultations.

Today, there are several databases and tools worldwide dedicated to occultations, which can be used for predictions, observation archives, data reduction and gathering of astrometric results. The main used during this work were:

- Occult, also known as winOccult<sup>16</sup>: software tool developed by Dave Herald (Murrumbateman, Australia) with several different uses throughout this work: predictions based on asteroid and star catalogues, upload of user catalogues besides the ones already implemented in it; complete archive of every event observed with at least one positive report since the very first occultation in 1961; lightcurves of some of those events, if the observers shared their photometry data; statistics on the asteroids observed and the stars used, as well as results per year and per observer; and detailed descriptions of the error models used and the uncertainties sent to MPC;
- Euraster<sup>17</sup>: online network focused on European observers, managed by Eric Frappa (Faycelles, France). It contains an archive of every reported occultation in Europe from 1997 to 2018, as well as every event with at least one positive report starting from 2019. Eric Frappa also made several statistics on the observations made, including telescope diameter distribution, as can be seen in Figure 1.14, number of events, positive reports, events with multiple positives, etc., and gathered some of the campaigns which yielded the best astrometric results and best allowed for shape measurements of the respective objects. One other helpful section is a summary of the results obtained with two robotic telescopes named TAROT<sup>18</sup>, one at Calern and the other at La Silla (Chile).
- Linocult<sup>19</sup>: software tool developed by Andrey Plekhanov (Moscow, Russia), mostly focused on the prediction of events. This is an open-source tool, giving us access to the code used, most notably the formula applied to calculate the probability of an event being positive based on

<sup>16</sup> <http://www.lunar-occultations.com/iota/occult4.htm>

<sup>17</sup> <https://www.euraster.net/>

<sup>18</sup> <https://grandma.lal.in2p3.fr/observatories/tarot/>

<sup>19</sup> <http://andyplekhanov.narod.ru/occult/occult.htm>

the distance from the observer to the nearest shadow-centre point and the uncertainty associated to the observation. It also allows the use of several observing sites at once for the predictions.

- Lucky Star<sup>20</sup>: collaboration project created by teams at LESIA (Paris Observatory), RIO (Observatório Nacional, Rio de Janeiro, Brazil) and Instituto Astrofísico de Andalucía (Granada, Spain), managed by Bruno Sicardy (LESIA). Heavily focused on the study of distant minor bodies, such as TNOs and Centaurs, members from this team were the first to find a ring system around a Centaur, publishing this result in 2014 [Braga-Ribas et al., 2014]. Another object with a known ring system is Haumea [Ortiz et al., 2017]. Campaigns are made for these objects, with the predictions being made by the LESIA team using their own orbital elements, from a method named NIMA, the Numerical Integration of the Motion of an Asteroid [Desmars et al., 2015].
- "Asteroid Occultations"<sup>21</sup>, by Steve Preston (US), the global go-to website of occultation predictions, with the highlight events compiled in IOTA-ES's (International Occultation Timing Association - European Section) "call4obs" webpage<sup>22</sup>

According to Euraster, a network managed by Eric Frappa for European observations, and Occult, a tool developed by Dave Herald for global results, recently there has been a sort of “boom”, likely thanks to Gaia, as can be seen in the subsequent chapter. Figures 1.10, 1.11 and 1.12 are complete up to mid-2020, and it should be noted that the right-most bar represents an incomplete year. Figure 1.13 shows the magnitudes of stars observed in reported events with at least one positive chord. For simplicity, the left-most bar represents all stars with magnitude below 2, and the right-most bar every star with magnitude lower than 15.

A peculiarity of this field is that big telescopes are usually not required, unless a special observation is being planned. For the most part, small telescopes can obtain very accurate results and are the most used for stellar occultations.

<sup>20</sup> <http://lesia.obspm.fr/lucky-star/>

<sup>21</sup> <https://www.asteroidoccultation.com/>

<sup>22</sup> <https://call4obs.iota-es.de/>

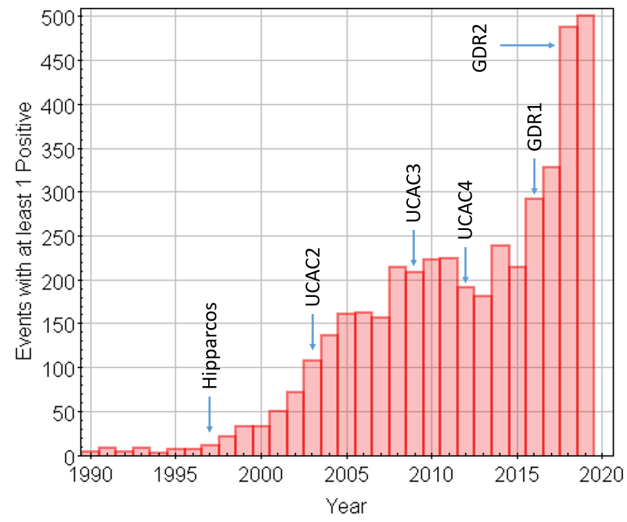


Figure 1.10: Positive events, per year, according to Occult. Also labelled are some of the main catalogues used for occultation predictions at the year of their release.

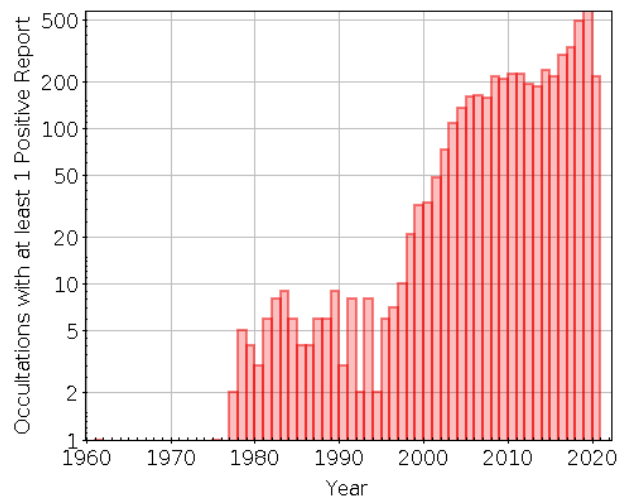


Figure 1.11: Number of events with at least one positive occultation, per year, according to Occult.

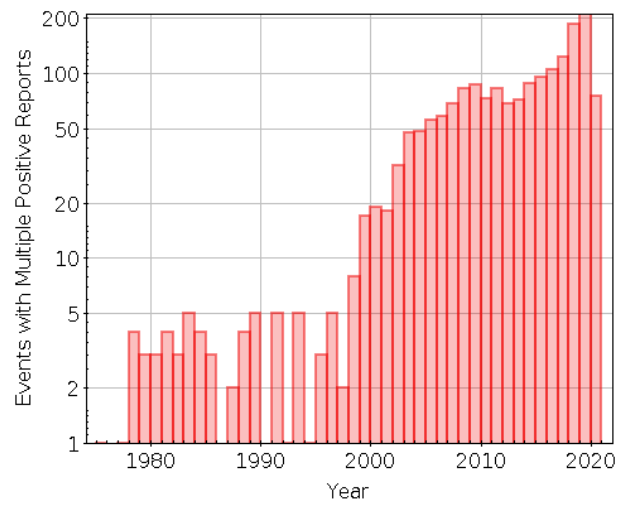


Figure 1.12: Number of events with at least two positive occultations (allowing more accurate astrometry and possibly diameter determination or shape modelling), per year, according to Occult.

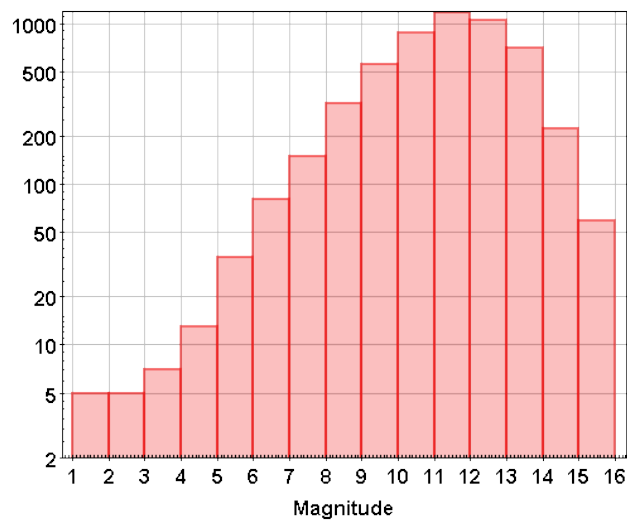


Figure 1.13: Magnitude Distribution of stars used for reported positive occultations, according to Occult. First column represents stars with  $V < 2$  and last represents  $V > 15$ . Given the typically small telescopes used, there is a bias against fainter stars, as these are far more numerous. Data from Occult.

Figure 1.14 shows the aperture distribution of telescopes used in Europe for occultations, between 1997 and 2006. Figure 1.15 is a simplified version of the same distribution between 2009 and 2018.

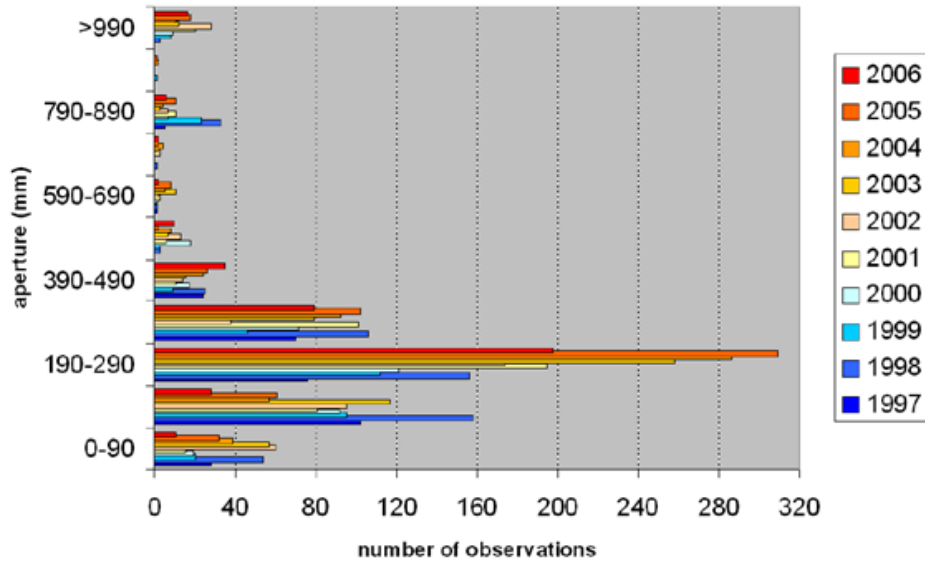


Figure 1.14: Reported observations by aperture from 1997 to 2006. Small telescopes (less than 30cm of diameter) are the most used. Image by Eric Frappa.

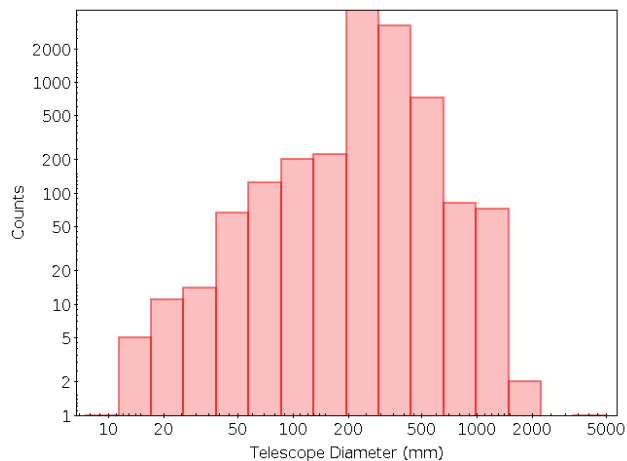


Figure 1.15: Same plot, but cumulative data from 2009 to 2018. Source is also Euraster.

When several astronomers observe the same event, it becomes possible to

model the 2D projected shape of the asteroid at the moment of the occultation, as there will be several chords from which to draw data [Durech et al., 2015]. Campaigns may be made to observe particular objects, which can result in dozens of registered chord, such as in the examples in Figure 1.16, where the shape could be determined, and Figure 1.17, where the shape was not the objective, but rather the study of the atmosphere at different latitudes and altitudes of Triton.

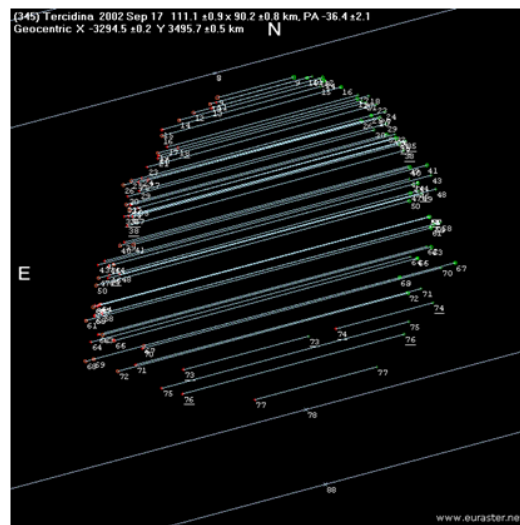


Figure 1.16: (345) Tercidina observed by several dozens of astronomers in September 17<sup>th</sup> 2002. Shape becomes much simpler to model with multiple observations, as well as the correction of systematic errors in each individual observation. Image by Euraster.

### 1.2.2 Why are they important?

In the earlier decades, occultations provided the most precise ground-based method of deriving astrometry for the asteroids. Occultations have an average historical precision of  $\sim 20$  mas. Thanks to the improvements by Gaia, as can be seen in the Gaia space mission section, this uncertainty is much smaller now, with occultations providing mas-level precision in its measurements, which can translate to kilometer-level precision for most MBA.

If many observations in different points of the globe are made to the same occultation, we may obtain several chords, which can help derive the projected

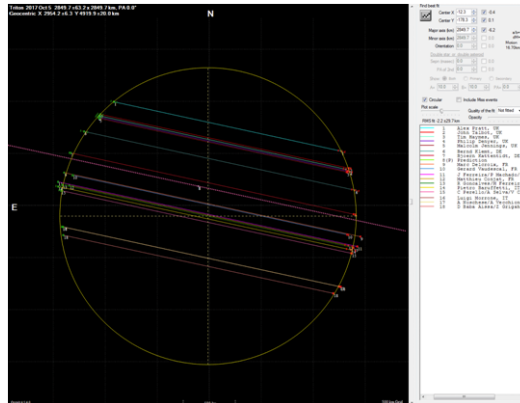


Figure 1.17: Occultation by Neptune’s moon, Triton, the first one using DR2 data (Chord 11 was observed in Nice). This event actually pre-dated DR2, with this data being released ahead of time specifically for this occultation. Image by Euraster.

shape of the asteroid during the observation and its absolute size, one of the parameters necessary to finalize a 3D shape model. This can help study its shape and spin.

In order to combine different observations to the same object, we need to use what is known as the Bessel Fundamental Plane, illustrated in Figure 1.18

After merging every observation in a single plane, it is then possible to not only construct the asteroid’s size and shape, as seen before, but also enhance our knowledge of its orbit, constraining where the asteroid was, as exemplified in Figure 1.19

The chord combination determines the position of the asteroid’s centre of mass. The method to determine said position is to measure the asteroid’s angular distance to the star from a geocentric perspective for each chord, and the chord’s distribution and size will determine the likely centre of the object when using circular or elliptical shapes, unless prior knowledge suggests that more complex forms are necessary.

In multi-chord occultations, we may also be able to estimate other parameters, such as the object’s density (in case of a known mass, typically available for binary or multiple systems), internal structure through the density and external structure through the albedo. In other cases, some interesting features may be found, such as the signature of an atmosphere, studied through

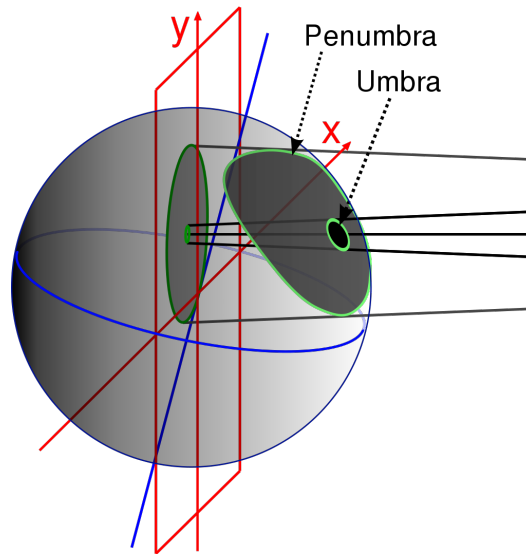


Figure 1.18: Bessel Fundamental Plane. This allows us to use observations made on different sections of Earth's surface in a single plane, in order to combine those observations' data. Image by G. Pieper, published in Wikipedia.

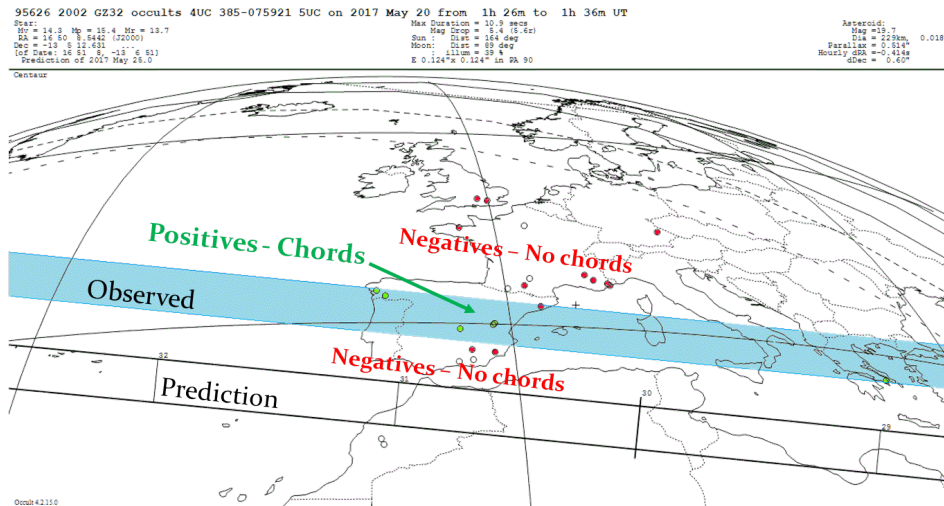


Figure 1.19: Correction to the orbit of (95 626) 2002 GZ32, which was made possible due to the several positive and negative reports. Green points are sites with positive reports, and red have negative reports. Original image from Steve Preston's predictions, edited by Jean Lecacheux (LESIA, Paris Observatory).

occultations for Triton and Pluto [Sicardy et al., 2003] and even rings, like (10 199) Chariklo [Braga-Ribas et al., 2014] and Haumea [Ortiz et al., 2017]! A compilation of every effect possibly observable through a stellar occultation is made in Figure 1.23

The atmosphere can be detected by the gradual signal transition and, in central chords, by a “central flash”, which is a noticeable spike in the flux in the middle of the occultation. This happens because light is refracted by the object’s atmosphere, and therefore, at the moment the object is centered on the star, its light, focused by the atmosphere, causes a spike. The upper atmosphere can also be studied via spikes smaller than the central flash throughout the occultation.

The rings, should they cross the star’s light path as well, shall be detected with abrupt but very brief drops in flux, both before and after the occultation.

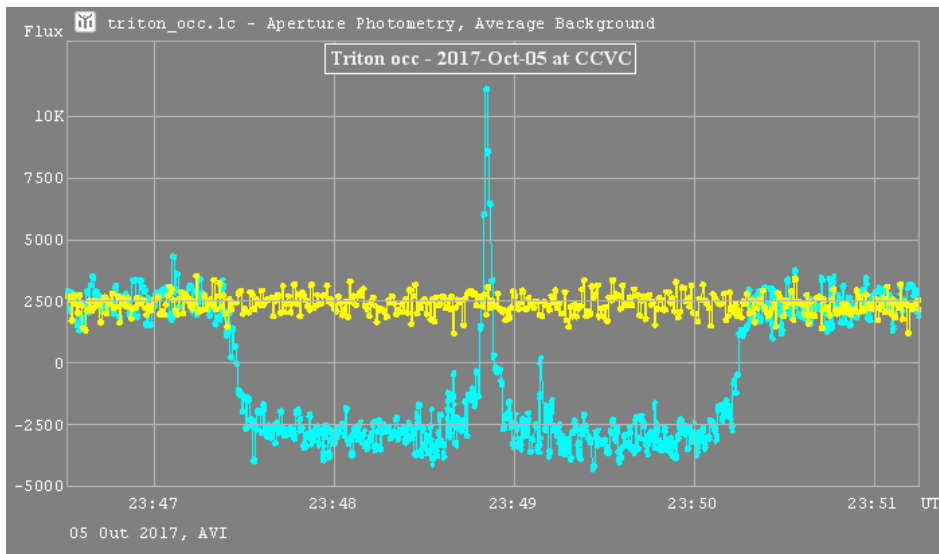


Figure 1.20: Example of an atmosphere, in this case Triton, visible during the occultation thanks to a central flash. Result obtained by Rui Gonçalves in Constância, Portugal. Similar result obtained in Nice shown in Figure 4.1

An example of the immediate usefulness of occultation astrometry is refining the trajectories of NEO, helping us determine which of these are potentially more dangerous in our near future. For small asteroids, constraining their orbits may allow to study non-gravitational effects such as Yarkovsky. The Yarkovsky effect is a force acting on a body that rotates, due to the un-

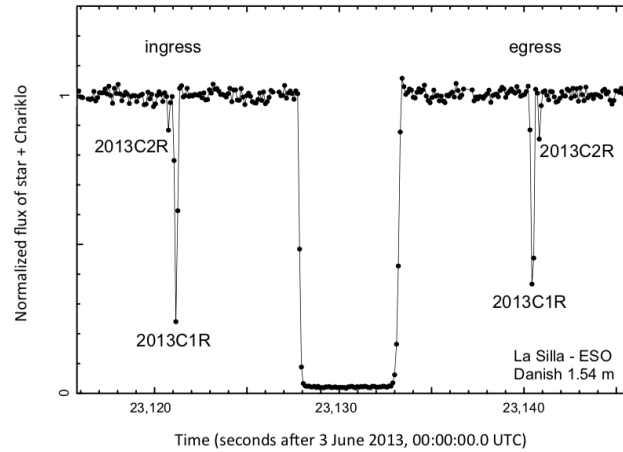


Figure 1.21: Example of a ring system being detected thanks to stellar occultations, in this case the centaur (10 199) Chariklo. Discovery made in 2014 [Braga-Ribas et al., 2014].

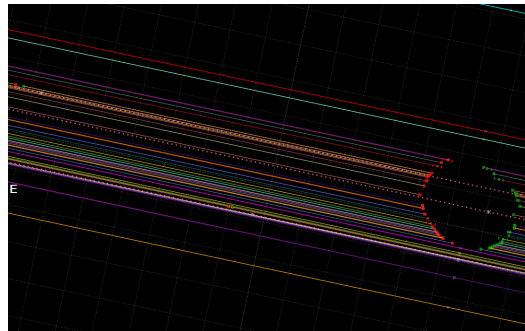


Figure 1.22: Example of a multiple asteroid system detected via occultations: (87) Sylvia (main body) and its satellites Romulus (far left) and Remus (bottom centre). This observation was a European campaign that included 36 detected chords and 14 negative observations. Sylvia has a radius of 277 km, Romulus 22 km and Remus 11 km, with a separation of several Sylvia radii between them. Image by Euraster.

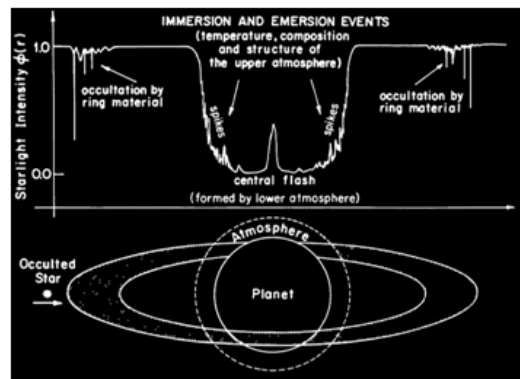


Figure 1.23: Example of the light of a star changing with time because of an occulting object with an atmosphere and rings. Image by J. L. Elliot [Elliot, 1979]

even distribution of thermal photons emitted from the surface of the object. This can cause slight shifts in the orbit, which are inversely proportional to the size of the asteroid [Farnocchia et al., 2013] and noticeable with big observation arcs with precise astrometry. This effect contributes to the dispersion of families of asteroids [Spoto et al., 2015].

Occultations have already contributed to some important results. Here are a few examples of their importance for the current knowledge of TNO and Centaurs [Ortiz et al., 2019]:

- Determining the radius and albedo of Eris [Sicardy et al., 2011];
- Characterizing the atmosphere of Pluto [Sicardy et al., 2003, Meza et al., 2019, Sicardy et al., 2016];
- Several physical properties of Makemake [Ortiz et al., 2012];
- Discovery of ring system around the Chariklo Centaur [Braga-Ribas et al., 2014];
- Discovery of ring system around the TNO and dwarf planet Haumea [Ortiz et al., 2017].

There have also been some advances in the study of MBA:

- The detection of Yarkovsky Effect on Near Earth Asteroids (NEA) [Farnocchia et al., 2013, Durech et al., 2015];
- The non-convex shape of (234) Barbara, which has its own family of asteroids (Barbarians) [Tanga et al., 2015];
- Shape modelling of several objects [Shepard et al., 2018, Satō et al., 2014];
- Spin and rotation determination [Devogèle et al., 2017, Wang et al., 2015, Merline et al., 2013].

So far, according to [Herald et al., 2020], astronomers have observed just over 4 000 occultation events and 16 000 chords in total, with more than half of these events happening in the last 10 years.

In terms of the astrometry, each occultation manages to obtain better precision than other typical methods of observation, such as CCD Imaging of direct observations to asteroids, observations by Space Telescopes or Photography and Radio Imaging [Desmars et al., 2015]. Thanks to Gaia, as is explained in the following section, we now have a bigger than ever star catalogue with precision in the micro-arcsecond level, which allow good predictions, and soon data on asteroid observations by Gaia will be public as well. So, in the near future we expect not only an increase in the number of observations, but also an increase in efficiency and quality of results.

The star and asteroid catalogues, when combined, result in predictions and by using refining parameters, such as date windows, diameter and duration restrictions, etc, it is possible to discuss whether the observation of a certain occultation is viable.

### 1.3 The Gaia Mission

The Gaia mission by ESA with has primary goal of creating a precise 3D map of our galaxy. This will be achieved via unprecedented results in parameters such as position, proper motion, parallax, radial velocity and temperature of stars. This mission is studying over  $1.7 * 10^9$  objects, representing over 1% of all stars in the Milky Way.

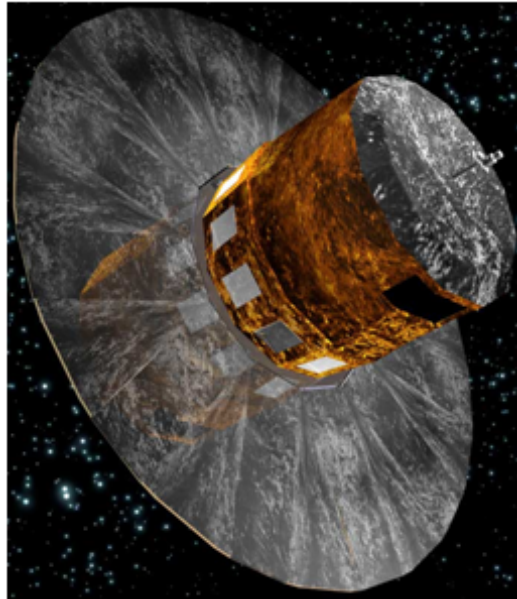


Figure 1.24: Gaia satellite (image by ESA).

Gaia was launched in 2013 and started observations in 2014 with a predicted mission end in 2019, which has since been extended to 2022 and may be extended to 2024, the maximum possible limit for the spacecraft until its fuel is completely consumed. It orbits in the Sun-Earth L2 (Lagrangian) point, roughly 1.5 million km away from Earth. This is a commonly used spot for space missions, as it allows for a stable orbit of the spacecraft and thermal stability of the equipment. It also allows observations uninterrupted by Earth eclipses. Other space telescopes in this region include, for example, Herschel<sup>23</sup>, WMAP<sup>24</sup> and Planck<sup>25</sup>, with the James Webb Space Telescope (JWST)<sup>26</sup>, Euclid<sup>27</sup>, PLATO<sup>28</sup>, SPICA<sup>29</sup>, WFIRST, now the Nancy Grace Roman Telescope<sup>30</sup> and ATHENA<sup>31</sup> are also planned to launch towards that region.

<sup>23</sup> <https://sci.esa.int/web/herschel>

<sup>24</sup> <https://map.gsfc.nasa.gov/>

<sup>25</sup> <https://sci.esa.int/web/planck>

<sup>26</sup> <https://www.jwst.nasa.gov/>

<sup>27</sup> <https://sci.esa.int/web/euclid>

<sup>28</sup> <https://sci.esa.int/web/plato>

<sup>29</sup> <https://spica-mission.org/>

<sup>30</sup> <https://roman.gsfc.nasa.gov/>

<sup>31</sup> <https://sci.esa.int/web/athena/-/59896-mission-summary>

Gaia is a successor of a similar mission, Hipparcos, launched by ESA in 1989, which, at the time, also managed to obtain some of the best astrometric results at the time, at milliarcsecond (mas) level. This mission managed to reach that level of precision for about 120 000 stars [Perryman, 2012, Colas et al., 2011, Dunham et al., 2002], a big improvement at the time, but a far more limited number than that provided by Gaia today.

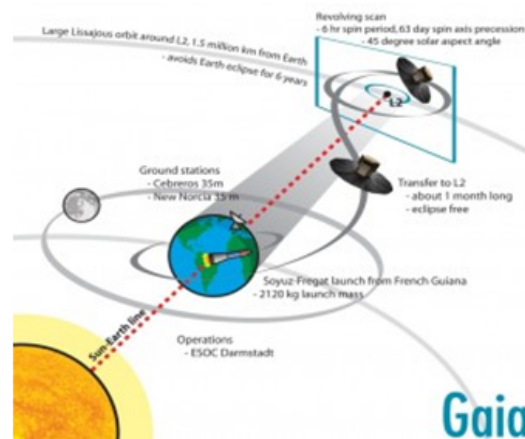


Figure 1.25: Trajectory of Gaia from Earth to the L2 point, image courtesy of ESA.

The following is the payload of Gaia:

- A dual telescope concept, with a common structure and a common focal plane. Both telescopes are based on a three-mirror anastigmat (TMA) design. Beam combination is achieved in image space with a small beam combiner;
- Silicon-carbide (SiC) ultra-stable material is used for mirrors and telescope structure;
- A highly robust measurement system for the Basic Angle between the two telescopes' pointing directions;
- A large common focal plane with an array of 106 CCDs. The large focal plane also includes areas dedicated to the spacecraft's metrology and alignment measurements.

These instruments obtain astrometry, photometry and spectroscopy for the observed sources. A full description of the spacecraft and its scientific goals can be found in [Gaia Collaboration et al., 2016].

The first Data Release of Gaia was made public in September 2016<sup>32</sup>, with the publication of 2-parameter solutions and magnitudes of over  $10^9$  stars, the first step towards the end goal of making a map of the local zone of the Milky Way. While for contemporary observations, this was already a step up from previous catalogues, the stars did not yet have proper motion measurements, meaning they couldn't be propagated to far epochs, so for occultations these stars would be useful for short term predictions only. A compromise solution were the temporary catalogues TGAS<sup>33</sup> (Tycho-Gaia Astrometric Solution) and HSOY<sup>34</sup> (Hot Stuff for One Year), a combination of Hipparcos and Gaia star positions to attribute proper motions to  $\sim 100\,000$  stars. This was exclusive to DR1, as from DR2 forward most targets had proper motion values calculated.

In April 2018, Gaia's Data Release 2 (DR2)<sup>35</sup> [Gaia Collaboration et al., 2018a,b] was published, now with more targets ( $1.7 * 10^9$ ), 5-parameter astrometric solutions (position, proper motion and parallax) rather than 2-parameter (position only) for most of them (except the stars present in TGAS) and data for many fields such as variable stars, quasars and, of our interest, 14 099 objects of our Solar System, mostly MBA. The distribution of uncertainties associated to DR2 stars can be seen in Figures 1.27 and Table 1.1

Spoto et al. [2017] have tested the use of Gaia stellar astrometry as a reference for observed occultations as astrometric measurements, having the accuracy comparable to that of the target star. Such an approach, if systematically applied, can give access to ground based observers ultra-precise astrometry at the level of Gaia, even after the mission has concluded its operations, with the uncertainty on proper motions as the only degrading factor for the measurement precision.

By the end of its mission, Gaia will have achieved a precision never before

---

<sup>32</sup> <http://sci.esa.int/gaia/58275-data-release-1/>

<sup>33</sup> [https://gea.esac.esa.int/archive/documentation/GDR1/Data\\_processing/chap\\_cu3tyc/](https://gea.esac.esa.int/archive/documentation/GDR1/Data_processing/chap_cu3tyc/)

<sup>34</sup> <http://dc.zah.uni-heidelberg.de/hsoy/q/q/form>

<sup>35</sup> <http://sci.esa.int/gaia/60243-data-release-2/>

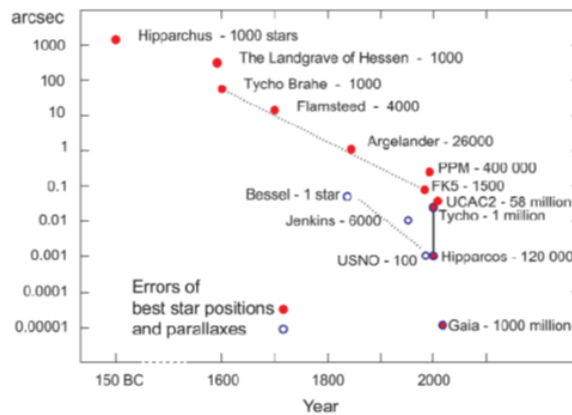


Figure 1.26: Historical progression of astrometry precision until Gaia, with some of the most important catalogues of their time and their size. Image from [Høg, 2011]

seen in the position and proper motion of stars eligible to be observed with small telescopes, as can be seen in Figure 1.27

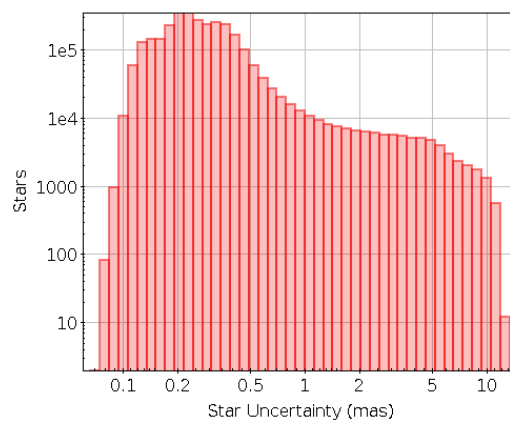


Figure 1.27: Distribution of star Uncertainty (position + proper motion for RA and Dec) with Gaia DR2 for stars of magnitude 14 or below. A random sample of 3 million stars was chosen within the Gaia data. Vast majority has sub-mas uncertainty.

With so many stars now having errors below 1 mas (see Table 1.1), occultation predictions became far better, with smaller error bars, which are now dominated by the asteroid's ephemeris uncertainty rather than the star's

position.

By grouping asteroid Gaia data with star Gaia data, we will be able to constrain the shadow path of an occultation to a much higher degree, with the prospect of several high-quality predictions in the near future. By the end of the mission, Gaia should have data on 350 000 objects of our Solar System, which represents almost half of the current catalogues. Figure 1.28 shows the state of the art for asteroids compared to what is obtained with DR2 and the improvements expected by the end of the nominal (5 years) and extended (10 years) mission. A comparison is also made in Figure 1.29 between the semi-major axis uncertainty attributed to asteroids present in DR2 just with the DR2 observations and the uncertainty obtained by combining all other methods, including ground based and satellite observations. We can see that for some cases, just 22 months of data with Gaia already rivals decades of observations with other methods (Figure 1.28).

Data product or source type	Typical uncertainty
Five-parameter astrometry (position & parallax)	0.02–0.04 mas at $G < 15$ 0.1 mas at $G = 17$ 0.7 mas at $G = 20$ 2 mas at $G = 21$
Five-parameter astrometry (proper motion)	0.07 mas yr <sup>-1</sup> at $G < 15$ 0.2 mas yr <sup>-1</sup> at $G = 17$ 1.2 mas yr <sup>-1</sup> at $G = 20$ 3 mas yr <sup>-1</sup> at $G = 21$
Two-parameter astrometry (position only)	1–4 mas

Table 1.1: Average precision in star precision for different magnitudes in DR2.  $G < 15$  is the most relevant group for this work.

Further Data Releases of Gaia include:

1. Early DR3 (EDR3) on December 3<sup>rd</sup> 2020, which will not include new data on asteroids, but rather improved data on astrometry and photometry of stars and quasars, with 34 months of observations;
2. Full DR3, in the first half of 2022, including new data on  $\sim 150\,000$  Solar System objects;

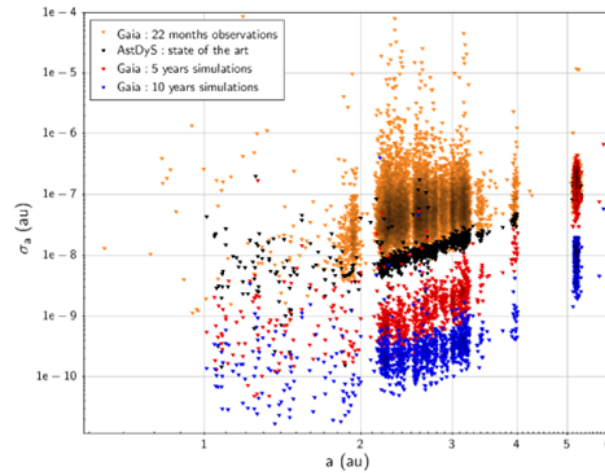


Figure 1.28: Projection of how Gaia will increase precision in orbital uncertainties of MBA. This is taken from [Gaia Collaboration et al., 2018a], where the orange points represent the expected astrometry quality from DR2, the black points the current state-of-the-art results from other methods, and the red and blue points represent the expected improvement with 5 and 10 years of Gaia data, respectively. We can see that, for a five-year mission, the state-of-the-art orbital uncertainties can be improved by a factor of up to 10, and since the mission has been extended to 9 years, the 10 year projection is more likely to be the scenario with the final catalogue, bringing an improvement of up to 2 orders of magnitude. These values will be used in Chapter 2

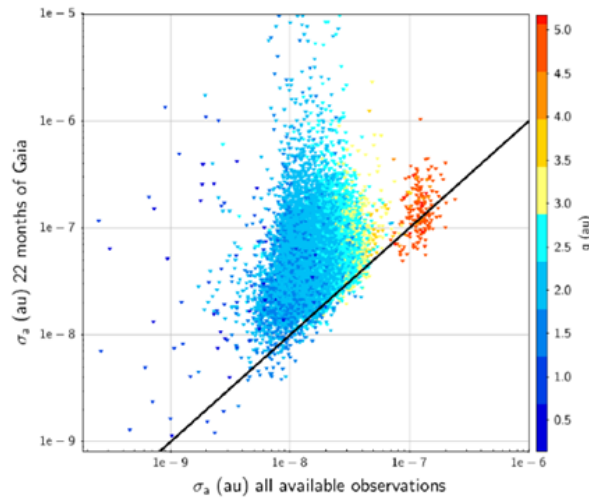


Figure 1.29: DR2 data vs other methods combined for Asteroids. Image by [Gaia Collaboration et al., 2018a].

3. DR4 in a later date, to be determined, which will encompass the nominal observational period of 5.5 years;
4. The final catalogue, date to be determined, after the mission's end.

Table 1.2 lists the approximate number of sources predicted for DR3 compared with DR2 and DR1 and their astrometric quality<sup>36</sup>.

The full DR3 will have more data compared to EDR3, but this will mostly apply to other parameters, such as sources with radial velocities, variable sources, temperature measurements, extinction and reddening and, most importantly for us, asteroids. But when it comes to astrometry, EDR3 and DR3 will be equivalent. While the number of stars with 5-parameter estimates will not increase as dramatically as it did between DR1 and DR2, there is still an almost 40% increase in this population, which can once again impact the amount of viable events, although most of this increase will come in the fainter magnitudes. The quality of the astrometry is also expected to increase thanks to the extra year of measurements between the two catalogues, an increase which will be quantified upon release. The current expectations for the

<sup>36</sup> <https://www.cosmos.esa.int/web/gaia/release>

Data Type	DR3	DR2	DR1
5-parameter	$1.8 * 10^9$	$1.3 * 10^9$	$2.1 * 10^6$
2-parameter	$0.3 * 10^9$	$0.4 * 10^9$	$1.1 * 10^9$
G magnitude	$1.8 * 10^9$	$1.7 * 10^9$	$1.1 * 10^9$
Asteroid Astrometry	$\sim 150\ 000$	14 099	None

Comparison of Early DR3, DR2 and DR1

Table 1.2: Stars with 2 or 5 parameter analysis in each DR, as well as number of objects with an estimated G magnitude. Number of objects with 5-parameter analysis grew by 3 orders of magnitude between DR1 and DR2. Such jumps will not be seen in DR3 or any future releases for the stars, but there is still a growth of events with good star astrometry to be expected with the newer catalogue, and a lot more asteroids in DR3 and beyond, this new version representing for Solar System Objects what DR2 was for the stars.

average astrometric parameter improvements are as follows:

- A decrease by a factor of 2 on the proper motion uncertainties;
- A decrease by 20% for parallax uncertainties;
- An overall, unquantified, reduction on some systematic errors, such as the parallax zero point, issues with bright stars and double sources at resolution limit.

## 1.4 Goals and Structure of this Thesis

Figure 1.30, explained after, shows the typical processing of occultations, both before and after the event happens.

- The blue boxes represent catalogues that exist prior to the observation: Gaia DR2 is the star catalogue most used nowadays, Astorb and MPC are, alongside AstDyS, the asteroid catalogues, with the orbital elements and uncertainties of each body, DAMIT<sup>37</sup> [Durech et al., 2010] and ISAM<sup>38</sup> [Marciniak et al., 2012] are shape model databases, with one or multiple models for about 2 400 asteroids ( $\sim 0.4\%$  of all numbered asteroids) and WISE is the asteroid diameter database previously mentioned as NEOWISE;

<sup>37</sup> <https://astro.troja.mff.cuni.cz/projects/damit/>

<sup>38</sup> <http://isam.astro.amu.edu.pl/>

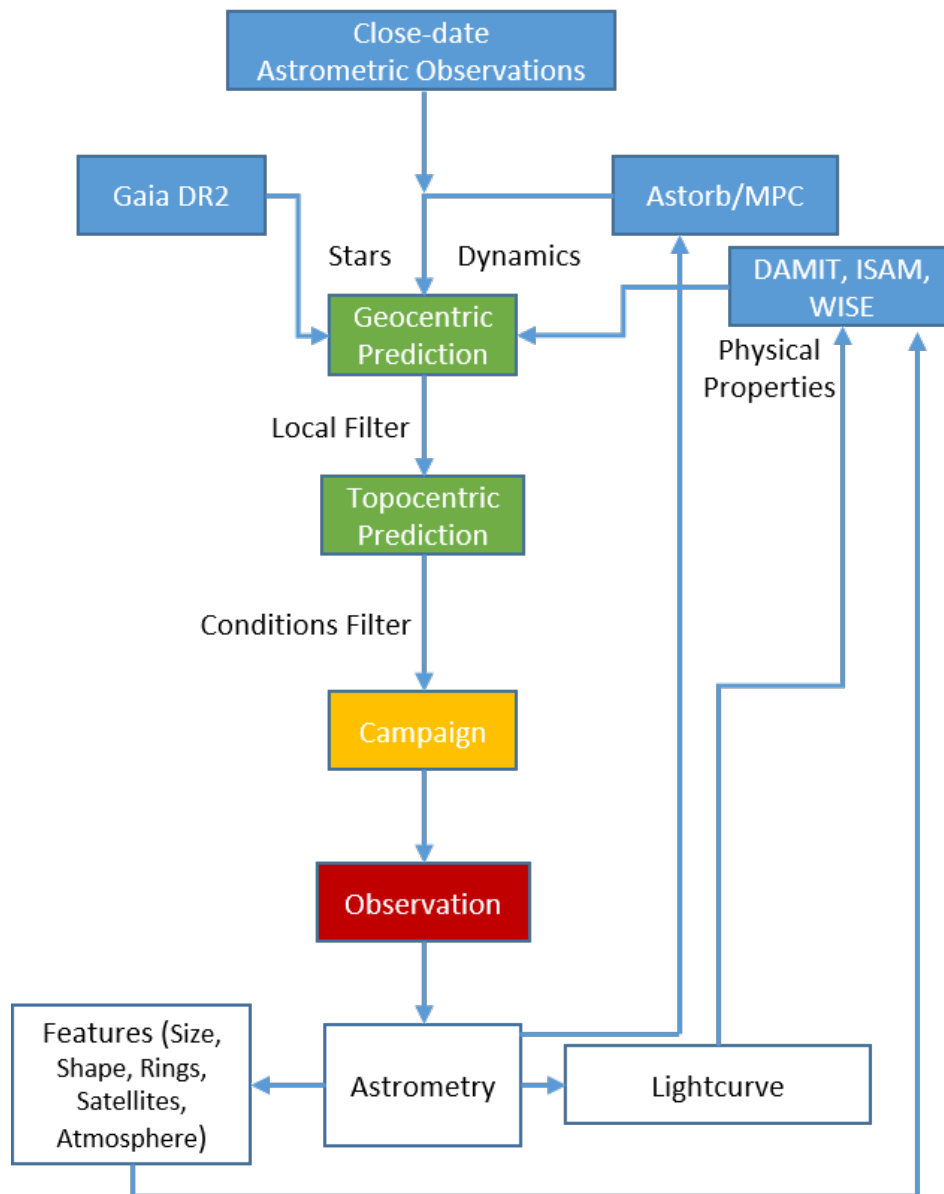


Figure 1.30: Schematic of how occultations are prepared and what their contributions help with.

- Green boxes represent the generated predictions. By using all of the previously mentioned catalogues, a first step is made by cross-matching stars and asteroids from a geocentric perspective, to create a global set of predictions. Afterwards, each observer applies their own filters, to account both for location (latitude/longitude/altitude and local hour) and limitations (star magnitude, magnitude drop, duration, minimum star altitude, among others). This way, each of them can have a fine-tuned set of viable occultations observable;
- The yellow and red boxes represent the observation. This may either be a single observer, the most typical case, or, as in the yellow box, a "campaign", where several observers target a specific event. This is not always possible, but whenever possible, campaigns are suggested in mailing lists or prediction websites;
- The white boxes represent the results of the observation: the astrometry obtained from the position of the star and whether the occultation was positive or negative, a light curve of the event for each observer and, with several observers and depending on the target, possible special features. All of these results will then be incorporated in the existing databases, refining the relevant information accordingly.

In this work, we address several aspects of this process; we exploited the DR2 star catalogue, both from software tools (Occult, Linoccult with all DR2 stars up to magnitude 14) and by building our own from querying the Gaia archive (stars up to magnitude 15.5); used the available asteroid databases, mainly Astorb, to get predictions for the Calern site, to determine the viability of a 50 cm telescope with Gaia data on stars and asteroids, aiming for smaller targets (meaning shorter events) and for a systematic observation plan (robotic telescope); made observations to recover the astrometry and lightcurve data of several occultation events, both independently and as part of campaign projects; measured the improvement to orbits by adding Gaia asteroid data and by using an updated debiasing and error weighting models.

Following the introduction to the main topics addressed in this work, here is an overview to the thesis and its structure:

In Chapter 2, the focus was on checking the improvements verified and the ones expected through the application of Gaia data to stellar occultations, analysing the improvements on both the star catalogue and the asteroid orbits. Some statistics are presented on how this impacts the use of a 50 cm telescope.

Chapter 3 features all of the work done on the creation of a routine that simulated thousands of light curves under limit conditions for that 50 cm telescope, to assess its expected performance. A description is made to the method of building these light curves to be as close to real observations as possible, the bayesian inference method applied to fit the occultations, how this compares to other tools and how real observations in the recent past behaved compared to our simulated results. Most of this work was published as an article, as can be seen in Appendix D.

A summary of every observation made throughout this work is presented in Chapter 4, with special focus to the positives, where an occultation was detected, but a general description of negatives, where we missed the occultation, as well. The BIM used in Chapter 3 was applied to our own observations to check the uncertainties, and we also used it on photometry data from other observations, as a collaboration.

Chapter 5 features the work made towards the improvement of asteroid orbits by exploiting the data from Gaia present in DR2 for all 14 099 asteroids there featured. A comparison between the standard debiasing and weighting schemes and the ones developed by the team, and a comparison was made between the resulting predictions for real events by OrbFit from this work and from other sources.

Finally, Chapter 6 has the conclusions of this thesis, as well as the plans for future work.

The main body of the thesis is then followed by the appendices:

- A: Theoretical work on orbital improvement of asteroids, used for the respective chapter;
- B: Important snippets of code used throughout this work;
- C: Most commonly used abbreviations. All of them are explained within the work, but this short list helps the reader find their meaning more easily;

- D: Accepted paper where I was first author. This paper was accepted by the *Astronomy & Astrophysics* journal on 2020/06/30 and published on 2020/09/11, Volume 641, A81.

# Extending the occultations sample with Gaia

---

## Contents

---

<b>2.1</b>	<b>Context</b>	<b>73</b>
<b>2.2</b>	<b>UniversCity Telescope</b>	<b>74</b>
<b>2.3</b>	<b>Limitations to account for in DR2</b>	<b>78</b>
<b>2.4</b>	<b>Set-up</b>	<b>79</b>
<b>2.5</b>	<b>Star and Asteroid Uncertainties</b>	<b>80</b>
<b>2.6</b>	<b>Orbit improvements with Gaia</b>	<b>86</b>
<b>2.7</b>	<b>Statistics on events per size</b>	<b>90</b>

---

## 2.1 Context

As mentioned in the Introduction, Gaia has had and will have a noticeable impact in occultations and the general study of minor bodies of the Solar System [Tanga and Delbo, 2007], thanks to the precision obtained on the position and proper motion of most stars available for small telescope observations, as well as with observations by Gaia to the asteroids themselves. This chapter focuses on the impact by Gaia, studying how the work rate of a single site will change based on stellar precision improvements alone.

We considered a telescope with an aperture of 50 cm, because one with such size, UniversCity, is being built in Nice specifically for occultations, and because it's the high-end limit of accessibility for amateur astronomers. We also use UniversCity as an example because, with the mass increase of viable

events on a specific location a fixed, automated instrument can become an efficient approach. Our goal is to compute the sample of occultations that would be observable with such a system, and to analyze how much Gaia has shifted the paradigm towards a new strategy of observations.

## 2.2 UniversCity Telescope

A robotic telescope named UniversCity is being built at the Calern site of OCA, with one of its goals being the regular observation of stellar occultations. Figure 2.1 shows the model of the telescope.

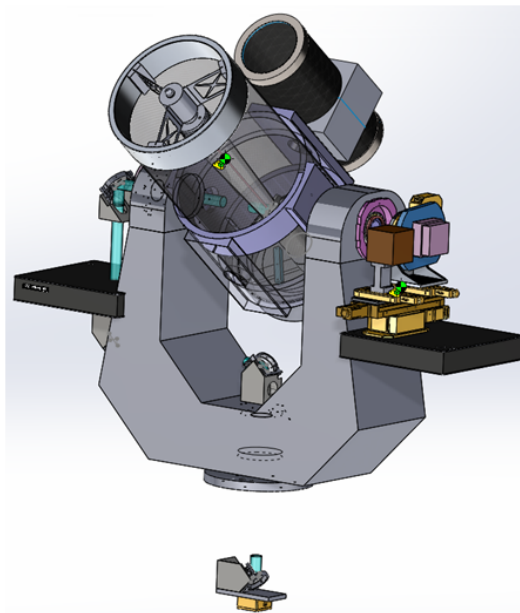


Figure 2.1: UniversCity Telescope. Image by Eric Bondoux (OCA).

This 50 cm robotic telescope will start to operate in 2021 at the Calern observing station. A robotic telescope is a device that makes observations without the input of a human user, be it in preparing or operating it. Software with Artificial Intelligence (AI) characteristics can be used to optimize an automatic schedule planned several days in advance, and is built to make the presence of an operator during an event unnecessary. [Tsapras et al., 2009] There are already some robotic telescopes that sometimes serve the purpose of observing stellar occultations, most notably TAROT (**T** éléscopes à **A**ction

Rapide pour les Objets Transitoires), a french project that has three such telescopes, one in France<sup>1</sup>, another one in Chile<sup>2</sup> and one in the Réunion island [Klotz and Thierry, 2019]. This project has so far resulted in over 120 positive occultation reports in 15 years, but it should be noted that TAROT is mostly used for a multitude of other fields, and its aperture is 25 cm, thus having a smaller limiting magnitude.

All of the work in Chapter 3 was made accounting for the expected performance of UniversCity, given its properties. For this purpose, we built a code to simulate the signal of potential targets (see more in Appendix B):

- The flux depends on the telescope’s size (50 cm), the camera/filter system being used (iXON 888, used for the Triton event analyzed in Chapter 4, estimated efficiency of 30% with no filter), the gain factor ( $5.24 e^-$  with the camera used for tests), the altitude of the site (to account for airmass, 1 260 m used for Calern), exposure time used and the combined magnitude of star and asteroid;
- The signal noise at each step is a gaussian with its standard deviation depending on [Mary, 2006]:
  - Poisson photon noise: intrinsic to any light source, the square root of the average flux;
  - Scintillation noise: caused by the atmosphere, depends on exposure time, telescope size, site’s altitude and average flux. See Equation 2.1 for details, where  $D$  is the telescope’s diameter in meters,  $Z$  the complementary angle of the object’s sky altitude,  $h$  the site altitude compared to sea level and  $h_0$  a reference height of 8 km,  $T_{int}$  the exposure time and  $F$  the flux;
  - Static noise sources: independent from the target, being a function of the exposure time: readout noise, associated with the electron analog-to-digital conversion, dark current noise, associated with photo electrons generated by thermal effects inside the detector (negligible with small durations) and the sky’s background.

<sup>1</sup><https://grandma.lal.in2p3.fr/observatories/tarot/>

<sup>2</sup><https://www.eso.org/public/images/esopia-tarot-5395/>

$$\delta n_{sc} = 0.09 * D^{-\frac{2}{3}} * \sec(Z)^{1.75} * e^{-\frac{h}{h_0}} * (2 * T_{int})^{-0.5} * F \quad (2.1)$$

Figures 2.2 and 2.3 show the expected flux noise as a function of the targets' combined magnitude for two different, typical exposure times (0.1 and 0.5 s). Figures 2.4 and 2.5 translate these values into SNR, showing us the expected magnitude limits for different source detection cut-off criteria. From these results, we extracted the parameters for the simulations used in Chapter 3.

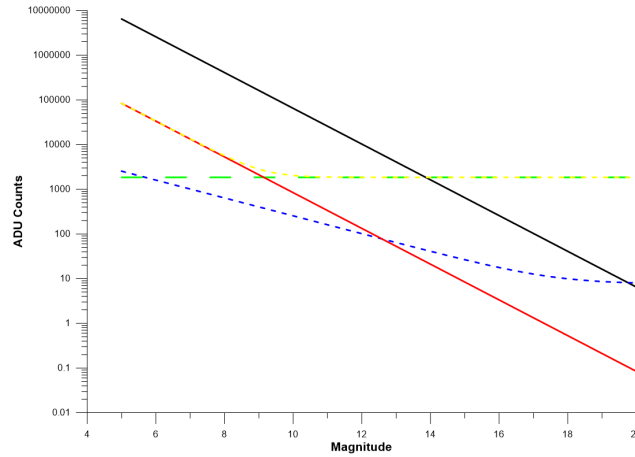


Figure 2.2: Expected Noise distribution for UniversCity and exposure time of 0.1 s, star at zenith, as function of V magnitude. Line description: black continuous line is the total expected flux, red continuous line scintillation noise, horizontal long dashed green line is the static noise brought by the background, readout and dark current sources, blue short dashed line is photon noise and yellow short dashed line is the total noise, adding the previously mentioned sources. We can see that scintillation dominates for magnitudes smaller than 9 and the static noise dominates starting from magnitude 11. This means that, for fainter stars, improving the available equipment, within reason, to minimize readout and dark current noise should allow a bigger improvement than changing the exposure time.

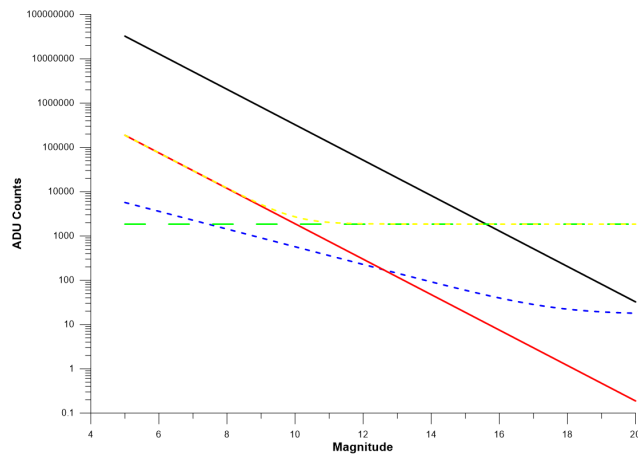


Figure 2.3: Same as previous figure, but with exposure time of 0.5 s.

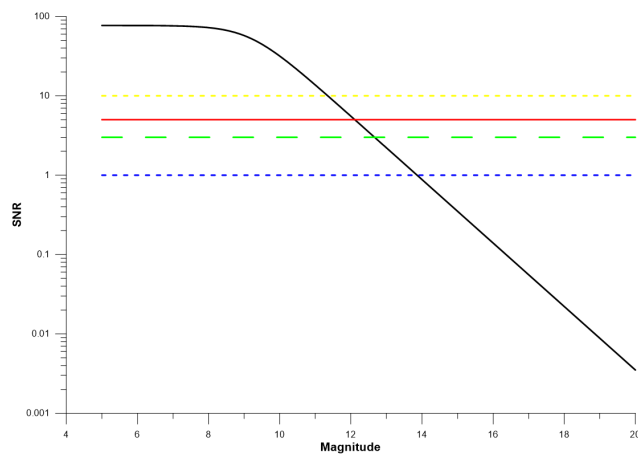


Figure 2.4: SNR Distribution, exposure time of 0.1 s, as function of V magnitude. Line description: black, continuous line is the expected SNR at each magnitude step, and the horizontal lines, from highest to lowest, represent SNR of 10, 5, 3 and 1 for comparison. We can see that for 0.1 s, we reach an SNR of 3 at around magnitude 13, meaning from this point forward detecting the target star should be difficult, and a SNR of 1 just beyond magnitude 14, meaning from this point the source is mixed in the background, theoretically remaining undetected.

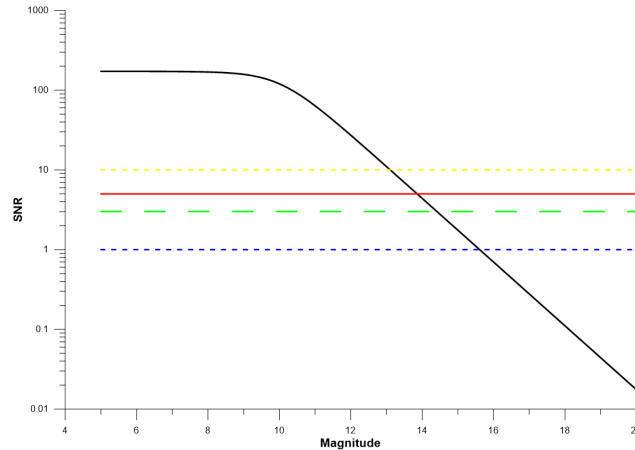


Figure 2.5: Same as previous figure, but with  $dt = 0.5$  s. Now, SNR of 3 is reached around magnitude 14.5 and SNR of 1 around magnitude 16, showcasing how much further we can push the target star brightness if a larger exposure time is possible.

## 2.3 Limitations to account for in DR2

Some considerations have been made regarding the limitations<sup>3</sup> present in the DR2 catalogue, most notably:

- Incompleteness at  $G < 12$  and  $G > 20$ ;
- Incompleteness of fast moving stars, with velocities above 600 mas/year;
- Problems processing binary sources at the limit of resolution, which can affect up to 30% of the sources;
- About 20% of the stars only have a 2-parameter astrometric solution rather than 5-parameter, limiting their usefulness for long term predictions due to propagation issues;
- Systematic errors on parallax of bright stars, of  $G$  smaller than 5.

Other known issues of DR2 can be found in the source listed above, but these are the main concerns for the stellar occultation predictions. Any issue on the astrometric precision can affect the overall uncertainty of an event,

<sup>3</sup><https://www.cosmos.esa.int/web/gaia/dr2-known-issues>

and photometric issues can affect both the predicted star magnitude and drop caused by the event, as well as mislead observers once the observation is attempted.

## 2.4 Set-up

After Gaia’s DR2 was released, some of the predictions tools, such as winOccult and Linoccult, started using it as a catalogue for the stars, specifically up to magnitude 14.

With the drastic improvements on both position and proper motion, most stars had such well defined coordinates that their uncertainties no longer played a significant role in the overall error margin of the predictions, which now depended almost exclusively on the ephemeris errors of the asteroids. This was tested for a large sample of events. An example is shown in Figures 2.6 and 2.7.

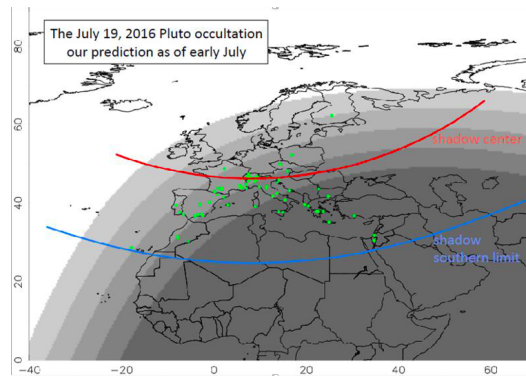


Figure 2.6: Path predicted for the Pluto event mentioned in Chapter 1 before DR2 data for the star was available. Central line crosses centre of France, southern limit crosses northern African countries and there is no north limit, as the shadow went all the way to the North Pole. Image by Josselin Desmars, Lucky Star Project.

A run was made in Linoccult with the most recent version of Astorb at the time (December 5<sup>th</sup> 2018), filtering on asteroids with diameters  $D \geq 5\text{km}$ , and Gaia DR2 used as the star catalogue. The conditions were as follows:

- June 5<sup>th</sup> 2018 to June 5<sup>th</sup> 2019, a 1-year run centred on the date of astorb

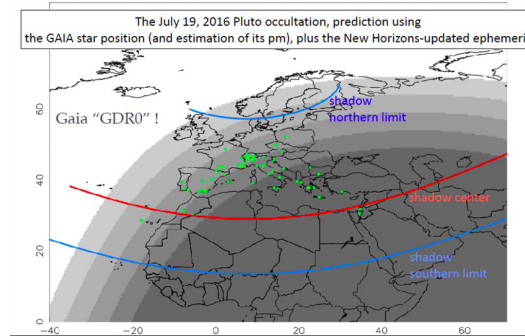


Figure 2.7: Pluto shadow path once DR2 data for the star was used. Massive shift towards south, with the central line now crossing the northern African countries, the southern limit crossing some central African countries and the northern limit now below the North Pole, excluding a few stations in Nordic territory. Overall, shift towards South was of over 1 000 km, and while not visible on this image, the uncertainties also decreased massively, giving great confidence to all stations in the new shadow path that they would detect the event. Image by Josselin Desmars, Lucky Star Project.

to minimize ephemeris uncertainties and biases regarding the time of the year and amount of hours per night;

- Maximum star magnitude of 14;
- Minimum drop of 0.1 magnitudes;
- Minimum Max Duration of 0.1s.

This run yielded over 600 000 events for about 50 000 objects, from which we could extract some statistics, including the expected magnitude distribution of stars (Figure 2.8), magnitude drops (Figure 2.9), diameters of involved asteroids (Figure 2.10) and expected duration, which in Linoccult is expressed down to tenths of second (Figure 2.11). The durations were dominated by small values due to the fact that small asteroids are far more common.

## 2.5 Star and Asteroid Uncertainties

Before going any further, we also analyzed the typical position and proper motion uncertainties of stars in this magnitude range ( $G \leq 14$ ) with Gaia

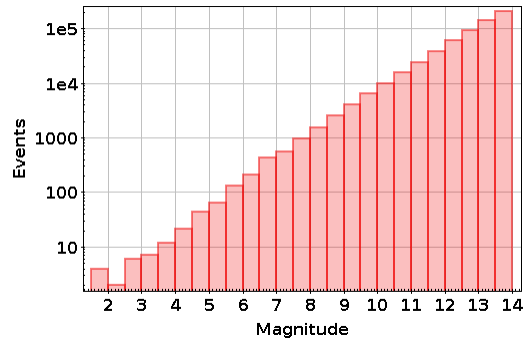


Figure 2.8: Star Magnitude distribution, with an expected behaviour of more events for fainter stars, which are more numerous.

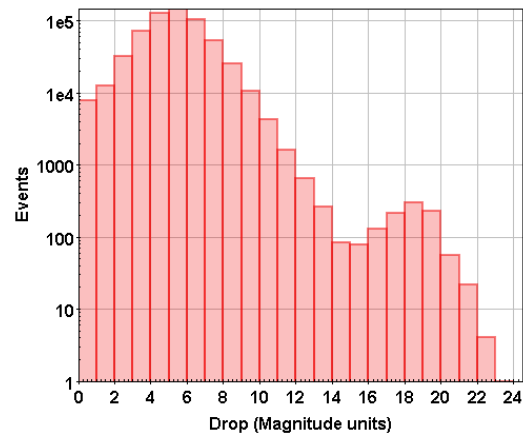


Figure 2.9: Magnitude Drop distribution, showing that usually the drop is very large, as even a 1 magnitude drop corresponds to a flux shift of approximately 60%.

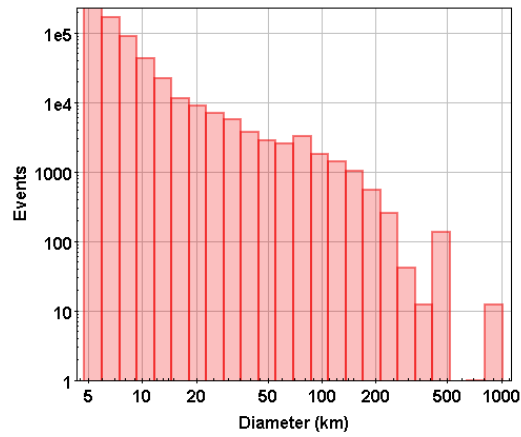


Figure 2.10: Asteroid Diameter distribution, again with an expected behaviour, as small asteroids are more frequent than large ones.

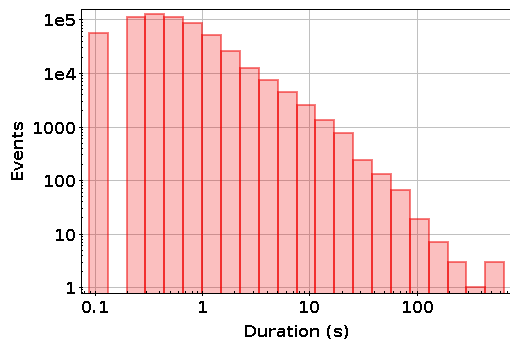


Figure 2.11: Max Duration distribution, with durations smaller than 1 second dominating this survey.

DR2. By making a query to this database restricting stars on their magnitude, we found the uncertainty distributions displayed in Figures 2.12 and 2.13, for which we made a quadratic sum of RA and Dec uncertainties.

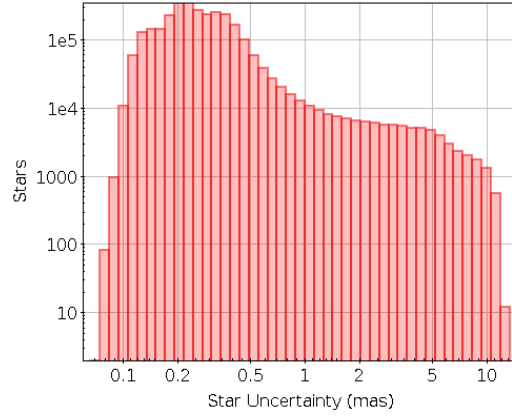


Figure 2.12: Star uncertainty from Gaia, with position and proper motion, stars with magnitude 13.5 to 14. Errors below 1 mas clearly dominate.

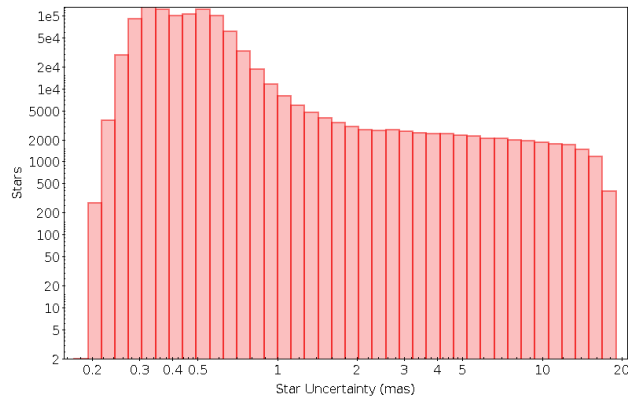


Figure 2.13: Similar analysis, but magnitudes 11 to 12.5.

Afterwards, a constraint made on a specific geographical location lets us look at actual predictions with given probabilities and realistic prospects of being observed. For this, we used the Calern Observatory as our location ( $43^{\circ} 45' 16.92''$  N,  $6^{\circ} 55' 14.16''$  E), restricted the star's altitude to at least  $5^{\circ}$  to avoid being very affected by air mass. We also constrained to events with at least 1% of probability of being observed, to leave out the ones that were too

far away to be realistically seen, but still include enough events to have relevant statistics to use. In the end, 11 864 events followed these criteria. Distance here is important to know how far away we are of the asteroid's shadow with relation to its size, with distances at least 3x larger usually meaning a 0% chance of observing the event.

Of all the remaining events, we extracted the asteroids involved and checked their ephemeris uncertainties through a query to JPL Horizons, where we could extract the RA and Dec uncertainty on the ephemeris of asteroids. By approximating RA and Dec as the main axes of the asteroid's orbital uncertainty, we can approximate the total uncertainty through a quadratic sum.

Now that we had the uncertainties on the asteroids, a cross-match was made between our table and Gaia DR2 using the star's RA, Dec and magnitude. All of the events with a good match were then analyzed to compare the uncertainties of star and asteroid and check which dominates.

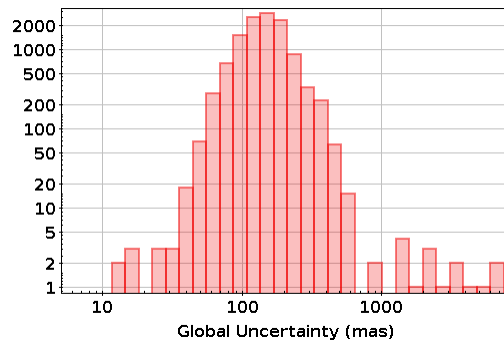


Figure 2.14: Asteroid Uncertainty Distribution, in mas, for all events visible from Calern analyzed.

With this work, we confirm that in most cases, the star's uncertainty is indeed no longer relevant when compared to the asteroid's, as it will be typically an order of magnitude below (see Figures 2.14, 2.15 and 2.16). And we can also show that this was not the case prior to Gaia. The most common catalogue used for occultation predictions prior to Gaia DR2 was UCAC4<sup>4</sup> (UCAC - U.S. Naval Observatory CCD Astrograph Catalog). Using the same set of events, we can compare the star/asteroid uncertainty ratio using DR2 with the obtained using UCAC4. For this, we further had to restrict

<sup>4</sup><http://cdsarc.u-strasbg.fr/viz-bin/cat/I/322A>

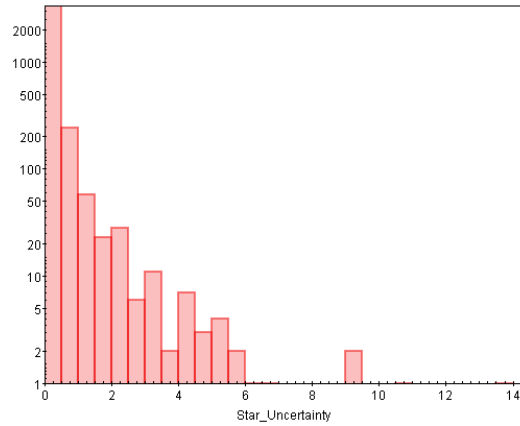


Figure 2.15: Same analysis, also in mas, but for star uncertainty.

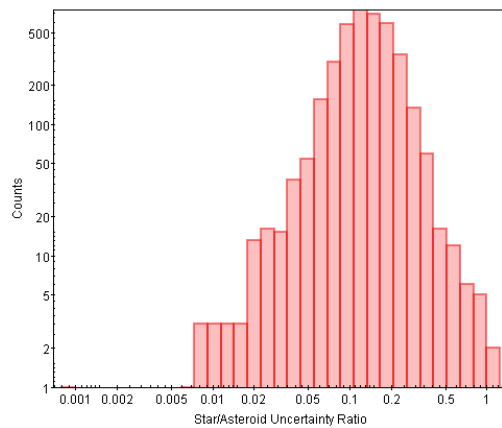


Figure 2.16: Star/Asteroid uncertainty ratio for all events. The peak is around 0.1, meaning the star's uncertainty is 1 order of magnitude below the asteroid's, with only a small minority of events having such a poor star precision that it became relevant in the overall event uncertainty. There is, however, a large distribution, meaning we can not always neglect the star's contribution.

to stars that have position and proper motion uncertainty estimates on both catalogues. The results were as seen in Figure 2.17

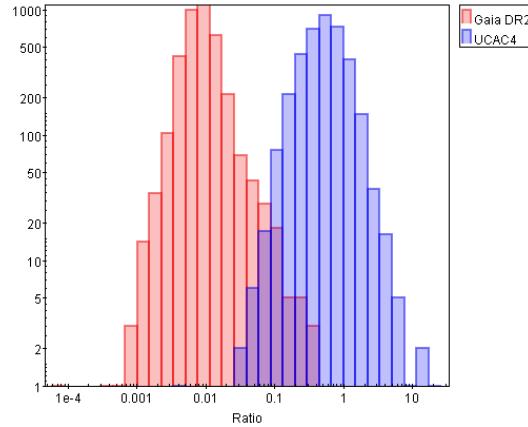


Figure 2.17: Star/Asteroid uncertainty ratio comparison between UCAC4 and DR2. Only stars that were present in both UCAC4 and DR2 and had a 5-parameter solution in DR2 were included, hence the difference from Figure 2.16. There is an average increase of 2 orders of magnitude and, while before, with UCAC4, the star and the asteroid had, on average, comparable uncertainties, now the star’s contribution is almost always negligible.

We see an average improvement on this ratio of almost 2 orders of magnitude! This means that using UCAC4, the star’s uncertainties would most of the time be relevant for the error propagation, often even surpassing the asteroid’s own uncertainties, which will no longer be the case, turning the focus of improving predictions towards the asteroid catalogues and their uncertainties.

## 2.6 Orbit improvements with Gaia

As mentioned in the Introduction, and shown with Figure 1.28, we expect Gaia to improve the orbits of asteroids compared to the current state-of-the-art results. Depending on the mission duration and the semi-major axis of the object, this can vary between 1 and 2 orders of magnitude. To have a glimpse on how that will affect event predictions, we used the same set of 600 000 events to see how many would be flagged for observation at Calern and how many positives we would expect by reducing the asteroid’s orbital uncertainty

by factors of 2, 5, 10, 20, 50 and 100, improvements to be expected from Gaia, as shown in Figure 1.28.

Figure 2.18 shows how these variations affect the probability distribution as a function of distance to shadow centre and uncertainty.

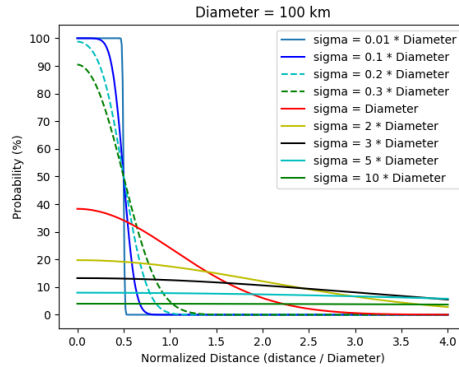


Figure 2.18: Representation of the effect on an asteroid's occultation probability as a function of a normalized distance from its centre in units of object diameter, for several uncertainty proportions. A distance of 0 means the site is at the shadow path's centre, and 0.5 Diameters corresponds to the predicted shadow path limit.

The formula to calculate these probabilities was extracted from Linoccult's code and confirmed with the LESIA team responsible for the NIMA method. The probability density function is a Gaussian, and the probability at a site corresponds to the integral of that function over the space where the occultation would be positive, meaning the location  $\pm$  the radius of the object, as written in Equation 2.6, where  $D$  is the distance from the site to the shadow path centre,  $R$  the asteroid's radius and  $\sigma$  the across-path uncertainty.

$$p = \int_{\frac{D-R}{\sigma}}^{\frac{D+R}{\sigma}} N(x) dx$$

As we would expect, through reducing the uncertainty of the asteroid, we would be making it so that the shadow-path area's probability increases, while the outside areas become less and less likely to see the occultation. The limits would be a uniform nearly 0% probability distribution in case of no knowledge (the event can happen anywhere) and 100% on the shadow and 0% outside in case of perfect determination of the orbit.

Another thing to expect, and which was verified through this experiment, was a great increase in the efficiency of observations, namely the positives/observations ratio. This value was obtained by adding the probabilities of all events to get the expected number of positives for 1 year, and dividing it by all events that passed the aforementioned filters. This value started out at a ratio of 2% with the current asteroid uncertainties. A number that might seem low, but is explained by the fact that we accept events with as little as 1% of probability of being positive, and these are far more common than high-probability events, not only due to distances, but also due to how big the uncertainties of most asteroids are compared to their sizes. The efficiency evolution can be seen in Table 2.1

Improvement Factor	Expected Positives	Events	Efficiency
1	228	11 864	1.9%
2	232	7 533	3.1%
5	215	3 592	6.0%
10	191	1 918	10.0%
20	159	985	16.1%
50	126	433	29.1%
100	117	287	40.8%

Statistics on orbital improvement

Table 2.1: Expected efficiency for specific site, depending on asteroid uncertainty improvement.

The amount of expected positives (not accounting for bad weather conditions), in case we observed every event with at least 1% of probability, should not vary much in this analysis in a first approximation. That is because, while many small probability events would disappear with better constraints, some events would become far more likely, more or less cancelling out. The amount of expected positives would only decrease after a strong improvement on the uncertainties, because the amount of far-away low probability events would actually out-weigh the amount events that became very likely. The amount of expected positives with the current uncertainty distribution was 228 (out of a total of 11 864 events). Following the same order on the factor of decrease thanks to Gaia, this number went to 232, 216, 191, 159, 126 and 117.

This shows just how much Gaia's data would help improve the efficiency on the use of our equipment. We can also notice some patterns on the type

of events that become more likely, as seen in Figures 2.19, 2.20 and 2.21

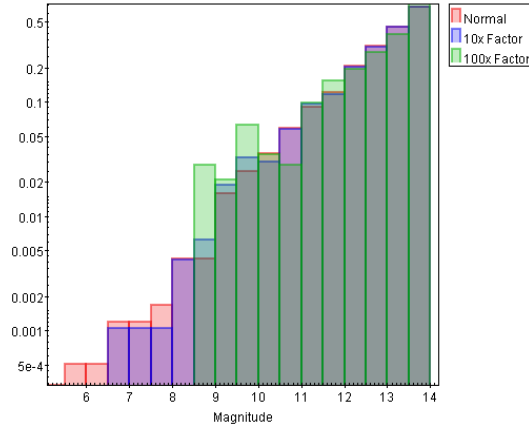


Figure 2.19: Shift in Magnitude distribution, depending on asteroid orbital quality. We can notice that, the further we decrease the asteroid's uncertainty, the more weight we give to long events, filtering out shorter events, which are typically associated with big error margins.

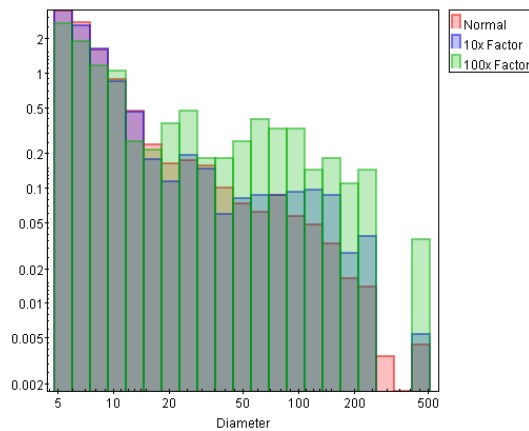


Figure 2.20: Shift in Diameter distribution, depending on asteroid orbital quality. Big diameters become more and more important, not only because of the bigger shadow area they cover, but because these events typically have lower error margins to begin with.

It should be noted that the biggest improvements, x50 and x100, might be too optimistic for early results with asteroids and Gaia. This is an improvement that might be verified after 5-10 years of data are reduced, which will not happen before at least DR4.

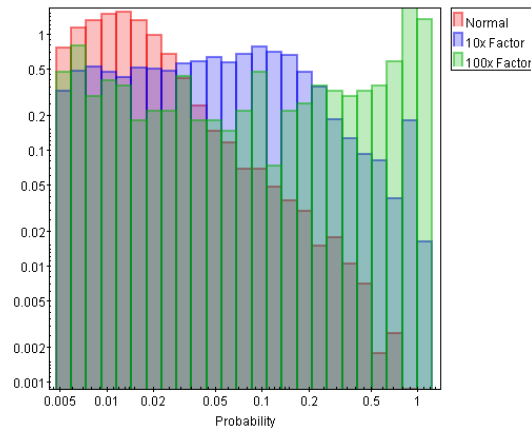


Figure 2.21: Shift in Event Probability distribution, depending on asteroid orbital quality. As expected, events with low probabilities tend to disappear, either because they became too unlikely in the new run, or because their probability is now much higher. Bigger efficiency in observations to be expected.

## 2.7 Statistics on events per size

For this section, we discarded the data on orbital improvements by a factor of 50 or 100, looking at the more realistic values of orbital improvement, and because these two regimes did not have enough events for the following analysis. The goal was to check, for different sizes, what the impact was on improving the asteroid orbits in terms of amount of viable observations, as well as efficiency of predictions. For this, the following steps were made:

1. Separate the asteroids in four size groups: 5 to 10 km, 10 to 20 km, 20 to 40 km and over 40 km;
2. Filter, for each improvement factor, the amount of events with a probability of positive observation at Calern of over 20%, 50% and 75%;
3. Analyze how many positives were expected, and how many events passed each probability filter.

As can be seen from these size groups, asteroids smaller than 5 km were left out of this analysis. While going smaller on the size limit would exponentially increase the number of available events, their corresponding orbital improvement with Gaia would be more delicate.

With all of this set up, Table 2.2 was obtained.

Improvement Factor	Size Category	Total	Above 25	Above 50	Above 75
1	5	9403	0	0	0
1	10	1411	2	0	0
1	20	550	0	0	0
1	40	500	65	7	2
2	5	6115	0	0	0
2	10	818	4	1	0
2	20	290	14	0	0
2	40	310	77	25	8
5	5	2881	11	0	0
5	10	401	19	2	0
5	20	141	46	6	0
5	40	169	63	39	21
10	5	1515	79	0	0
10	10	209	40	4	1
10	20	80	39	13	6
10	40	114	54	42	29
20	5	746	143	6	0
20	10	104	33	8	2
20	20	51	30	22	11
20	40	84	48	42	34

Statistics on orbital improvement

Table 2.2: Table listing, for each asteroid uncertainty improvement factor and for each asteroid size category, how many events have probabilities above 1% (minimum for observation planning), 25%, 50% and 75%. Clear trend of less unreliable events is found, as should be expected.

As would be expected, at first the largest bodies, which have on average the best orbital precision, are the ones that give the most reliable events, while the smallest bodies, due to how many they are, dominate the total number of events. This tells us that the orbital improvements brought by Gaia will not represent a major breakthrough for large bodies, but rather for smaller ones.

For all sizes, as we progress in the uncertainty factor, the number of events decreases, while the number of reliable events increases, leaving the total amount of expected positive events even throughout.

For bodies with 5 to 10 km, there is no reliable event (probability above

20%) at first, despite the huge number of predictions included. This is a reflection of the poorer precision within this range, which would only get worse at even smaller sizes. However, an improvement on the orbit of 10-20x, within reason for Gaia observations, sees this group delivering several reliable events, even if they still do not surpass the 50% probability threshold, with few exceptions. And even with an improvement of 20x, this group does not give any event with a probability above 75%.

These data led to the creation of a set of simulations that would represent the events expected to be at the limits of this telescope's efficiency. The work shown in Chapter 3 was developed specifically for the expected performance of UniversCity, and all of the results should be adjusted for telescopes in other conditions, such as different diameter, camera-filter system and location.

# Simulations

---

## Contents

---

<b>3.1</b>	<b>Context</b>	<b>93</b>
<b>3.2</b>	<b>Least Squares and Bayes' Theorem</b>	<b>94</b>
3.2.1	Least Squares Fit Method	94
3.2.2	Bayes' Theorem and Bayesian Analysis	95
<b>3.3</b>	<b>Setup</b>	<b>96</b>
<b>3.4</b>	<b>Results</b>	<b>106</b>
3.4.1	Gaussian and Uniform priors	110
3.4.2	False positives	111
3.4.3	Comparison of BIM to LSF	113
3.4.4	DIAMONDS vs PyOTE	114
3.4.5	BIM vs Real Cases	116

---

## 3.1 Context

The initial goal of this work was to predict the performance of the UniversCity telescope, and then apply our findings to the observations. Due to its debut happening only after the end of this work, this section was limited to the use of simulations to predict how many observations would be viable given the typical conditions of the telescope-camera system and the site where it has been built. The expected results associated to UniversCity will be verified with the future use of the telescope.

Besides testing out the potential of this robotic telescope, a performance comparison was also carried out to verify that the method being used, the

Bayesian Inference Method (BIM), provided better results than usual Least Squares Fit (LSF), as well as one of the most common tools, PyOTE<sup>1</sup>, a public domain software tool that applies the more general OTE<sup>2</sup> (OTE - Occultation Timing Extractor) light curve analysis with Python.

## 3.2 Least Squares and Bayes' Theorem

### 3.2.1 Least Squares Fit Method

The most commonly used method for regression of points is known as the Least Squares Fit (LSF). A method inherently connected to the field of Astronomy through parts of its origin, the LSF was ultimately put together by Carl Friedrich Gauss in the 19<sup>th</sup> century to calculate the orbits of celestial bodies as the first use of this method in astrometry.

The main objective of the LSF is to ensure that we can adjust a set of (typically) independent parameters to a dataset in the most optimal way possible. Whatever the fit, there are differences between the model and the results, known as the "residuals", and the LSF fits the model that minimizes the sum of the squares of the residuals in our dataset, as show in Equations 3.1 and 3.2

$$r_i = y_i - f(x_i, \beta) \quad (3.1)$$

Here,  $r$  is the residual,  $y$  the data point and  $f$  the function of the parameters vector  $\beta$ .

$$S = \sum_{i=1}^n r_i^2 \quad (3.2)$$

Here,  $S$  is the sum of the squares of residuals, which we want to minimize.

<sup>1</sup> <https://pypi.org/project/pyote/>

<sup>2</sup> <http://occultations.org/observing/software/ote/>

### 3.2.2 Bayes' Theorem and Bayesian Analysis

Bayesian analysis consists of a statistical procedure to estimate one or more parameters of an underlying distribution based on an observed distribution, following Bayes' Theorem, a probability theory based on prior knowledge of events [Corsaro and De Ridder, 2014a,b]. It follows Equation 3.3

$$P(\theta|D, M) = \frac{L(\theta|D, M) \pi(\theta, M)}{P(D|M)} \quad (3.3)$$

Here:

- $\theta$  is the free parameters vector that we use in a model  $M$ . The flux detected, the drop during the occultation, the centre epoch of the event, the duration and, possibly, the transition time between outside and inside the event can all be present;
- $D$  stands for the dataset used, namely the sampled flux for the whole observation;
- $L$  is the likelihood function, which indicates the compatibility of the evidence with the given model  $M$ ;
- $\pi$  is our prior knowledge on the parameters, the estimate of the probability of the model  $M$  before the dataset  $D$  is taken into account. This step incorporates prior knowledge one might have on the event, or other events similar to it, and can assume any shape, with the most common being uniform and gaussian priors, explained further ahead.
- $P(D|M)$  is also known as the "Bayesian evidence",  $\varepsilon$ , which can help us compare different models.  $\varepsilon$  depends not only on how well our model fits the dataset, but also on how many free parameters are being used, which means that we can compare an occultation model with 4 parameters to a flat signal model with no occultation with just 1 parameter, and determine which fits better to the data thanks to  $\varepsilon$ . In our particular case, this can vary from 1 (flat signal, meaning no occultation, where we just measure the average Flux) to 4 (Flux, Drop, Duration, Centre

Epoch) or even 5 or 6 ( $\sigma$ , to have a gradual transition of flux, rather than instantaneous, with the possibility of different values on each side). The more complex models should, in theory, always fit better than the simplest one, but the addition of 3 or 4 additional parameters might not be justified. We decide by making a ratio of the bayesian evidences, and introducing a cut-off from which we reject the more complex model in favour of the simpler one.

- Our result, on the left-hand side, is the posterior probability density function, the probability of the model M given the dataset D.

### 3.3 Setup

For this section, a code was built in C++ to accurately simulate the light curves that we would expect to observe from UniversCity. The flux and noise values were calculated based on the sources mentioned in the Noise Budget section of Chapter 2.

We fed our simulated data set into both the LSF and BIM codes, for fitting them with a simple light curve model. This model assumes a flat signal outside the occultation, and a sharp transition at the beginning and end of the event. Extremely variable sky absorption conditions or other effects that could induce fast signal variations on the duration along the light curve are neglected at this stage. With such assumptions, our model is described by the following free parameters:

- $F_0$ : The average combined flux from the asteroid and the target star, before and after the occultation;
- $A$ : The flux drop, with  $F_0 - A$  representing the signal received during the occultation;
- $dt$ : Duration of the occultation;
- $t_0$ : Central Epoch of the occultation.

We can completely neglect the apparent star size in this context, as for all stars with  $V > 11$  it is well below 1 mas. We have verified this assumption

by using the stellar radii and parallaxes published in Gaia DR2, that show a maximum apparent diameter of 0.2 mas at  $V = 11$ . This means that there is no need to account for Fresnel Diffraction [Roques et al., 2008, Pass et al., 2018] for the purposes of this simulation. Fresnel scale (see Equation 3.4) for MBA is 0.2 km, while asteroids considered for this project have a diameter  $D \geq 5km$ . This effect would cause a wave-like behaviour on the light curve, which is not detectable if the object occulting the star has a much larger apparent diameter. Another way of showing that the Fresnel scale is not detectable for this work is to see that the typical main belt asteroid has an orbital velocity of at least 5 km/s, meaning that for the 0.2 km to correspond to a single sampling point, we would need an exposure time of at most 0.04 s, lower than the exposure time considered.

$$F = \sqrt{\lambda * D/2} \quad (3.4)$$

F is the Fresnel number,  $\lambda$  stands for the wavelength used and D is the distance between the occulter and observer. If we apply visible light ( $\sim 500$  nm) and a distance of 1 au (opposition distance for some of the closer MBA), we arrive to a Fresnel number of 0.2 km.

We also note that the flux  $F_0$  can be measured, in general, with very high accuracy before and after the occultation, by accumulating the signal on a time interval (for instance, a few minutes) much longer than the occultation event itself (which lasts seconds). Also, reference stars can be used to minimise fluctuations in the flux, a method now as "differential" photometry. Assuming that this procedure is validated for a specific setup, the uncertainty on  $F_0$  can be considered to be negligible.

We can expect that two factors dominate the efficiency of any attempt to model the occultation event as a discontinuity in the time-sampled star flux. We distinguish them as:

1. The number of samples  $N_{occ}$  measured within the duration of the occultation. For a given total flux and flux drop, the larger this number, the better is defined the duration of the event. In our simulations,  $N_{occ}$  can assume a fractional value;
2. The signal-to-noise budget of the occultation signal, expressed as the

ratio between the flux drop and its total uncertainty.

Hereinafter, we call this last factor the drop-to-noise ratio (DNR) expressed as in Equation 3.5

$$DNR = \frac{F_0 - A}{\sqrt{(\sigma_{F_0})^2 + (\sigma_A)^2}} \quad (3.5)$$

Where  $\sigma_{F_0}$  and  $\sigma_A$  are the noise of the signal outside and inside the occultation.

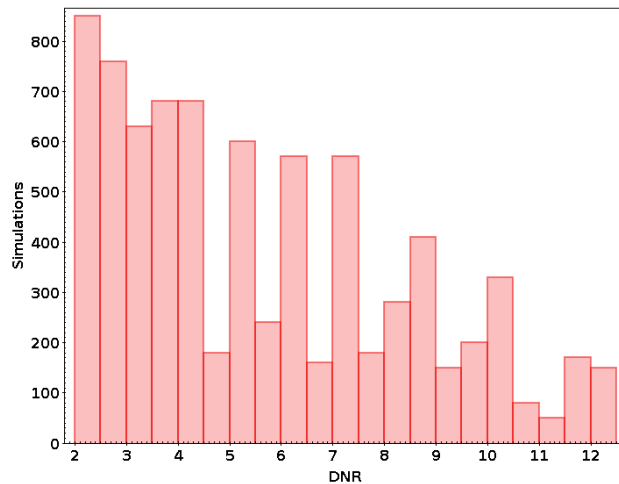


Figure 3.1: DNR distribution for the simulations used, which depends on combined star+asteroid magnitude and the expected magnitude drop. Since higher DNR imply an easier event to track, we prioritised low DNR combinations of magnitude and drop.

The DNR and  $N_{occ}$  thus become the two main parameters characterising the "difficulty" of the data reduction for each light curve and they are fully complementary. For instance, a very difficult signal with  $DNR \sim 1$  (see Figure 3.1 for DNR distribution) can still be detectable and measurable if the occultation is sampled over a sufficiently large number of points  $N_{occ}$ . We will show that our occultation detection methods are in fact very sensitive to these two parameters.

Another test we made was False Positives runs for both Asteroids and TNO, where we fed the same priors to DIAMONDS<sup>3</sup> [Corsaro and De Ridder, 2014a,b] (high-Dimensional And multi-MODal NesterD Sampling), but used a flat, constant signal light curve instead of an occultation, to see how many times it would consider to detect an event, and how often this happened as a function of magnitude, drop and duration.

Efficient Bayesian methods are a powerful approach to fit models in multi-dimensional spaces, and to chose the best model among different alternatives [Sivia and Skilling, 2006].

A critical part of the BIM is the definition of the priors, related to the information available on the free parameters. One should note that, in practice, for the occultation events the definition on the priors relies on the information produced by the prediction, which can provide a first estimate of the parameters. The total flux  $F_0$  can be estimated from the brightness of the target star and the asteroid, by taking into account properties of the instrument and the observing conditions. The flux drop  $F_0 - A$  can be guessed, although the theoretical brightness of the asteroid can be affected by a rather large error (several tenths of magnitude) due both to the absolute magnitude  $H_0$  errors [Jurić et al., 2002] [Pravec et al., 2012] and to the viewing/illumination geometry of a possibly irregular shape.  $H_0$  is the absolute magnitude of an asteroid in the V band, defined as its brightness at 1 au from the Sun and observer, observed at a 0 deg phase angle.

The maximum duration  $L_{Max}$  is computed in general by the prediction, but can be affected by a large uncertainty, depending both upon the error on the average object size (see Figures 3.2 and 3.3), and on the projection of its shape at the epoch of the event.

Normally, the knowledge of the absolute occultation epoch  $t_0$  is dominated by the uncertainty on the orbit and the star position. For typical multi-opposition MBA, this is close to a few seconds.

In practical situations, several additional factors can introduce large discrepancies in the predictions, such as absorption due to poor sky conditions, errors in the star or asteroid magnitude or large uncertainties in the asteroid ephemerides.

---

<sup>3</sup><https://github.com/EnricoCorsaro/DIAMONDS>

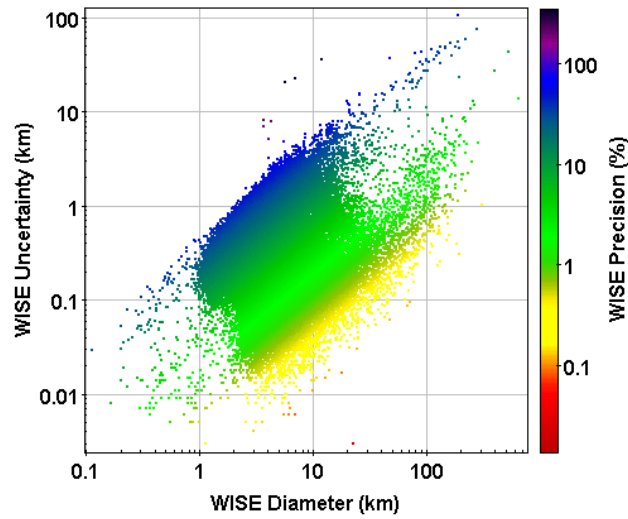


Figure 3.2: Distribution of Diameter value and uncertainty in WISE survey (122 594 asteroids). Colour plot is the precision,  $\text{Uncertainty}/\text{Size}$ , for easier reading. Two main trends exist, of precision 5% and 25%.

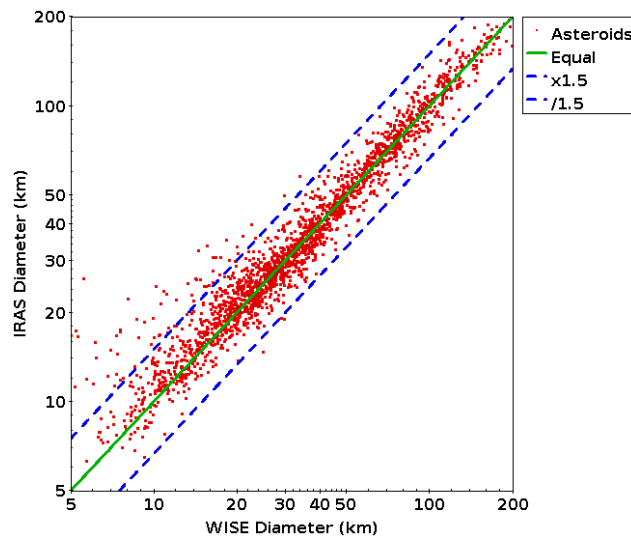


Figure 3.3: Discrepancies in Diameter values of IRAS [Ryan and Woodward, 2010] and WISE [Masiero et al., 2011] surveys (2 141 common asteroids). In some extreme causes, we can get disparities of over 50%, and a difference of 20% or more can be found for  $\sim 20\%$  of the sample.

On the base of these considerations, we compared two approaches: uniform priors with rather large intervals and gaussian priors more closely tuned on the predicted values. They are intended to represent two rather extreme situations, associated to rather poor and good predictions of the parameters, respectively.

In the case of the uniform priors, we simply assume a possible interval of 0.5-1.5x the nominal value of each parameter.

Gaussian priors are more strictly adhering to the prediction, and are defined by the following standard deviations values:

- Flux ( $F_0$ ): 0.5 magnitudes, 37% in flux;
- Drop (A): 0.3 mag, 24% in flux;
- Duration ( $L_{Max}$ ): 0.2x  $L_{Max}$ ;
- Centre Epoch ( $t_0$ ): 2s.

For the BIM, we used the package DIAMONDS. Figures 3.4, 3.5 and 3.6 show 3 examples of occultations simulated, presenting three different categories that could be considered of "easy", "intermediate" or "hard" difficulty for the package to analyze. All plots were made using matplotlib [Hunter, 2007].

The "easy" example shows the occultation with the highest DNR and longest duration, with the other examples getting progressively harder. Among other things, DIAMONDS outputs the marginal distribution of each free parameter. In the case of the uniform priors, the range of this marginal distribution is the one given in the priors, while for the gaussian priors, an interval is selected by DIAMONDS according to the result. Figures 3.7, 3.8, 3.9 and 3.10 are the marginal distributions (in blue) obtained in the "intermediate" example. The x-axis shows the parameter-range and the y-distribution is an adimensional value useful to determine the most likely range of correct values. In each image, the gaussian prior for the example is shown (in red) for comparison, and each distribution has a vertical line showing its median value, to better visualise how far apart the two are.

We draw two conclusions from the marginal distribution figures. First, the posterior function is narrower than the prior, meaning that our prior is not

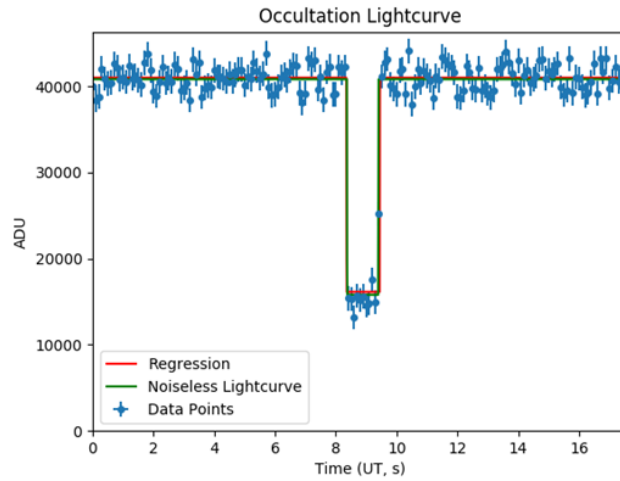


Figure 3.4: Example of case with high DNR (12.0): Magnitude 11.5, drop 1.0 and 10 points inside occultation.

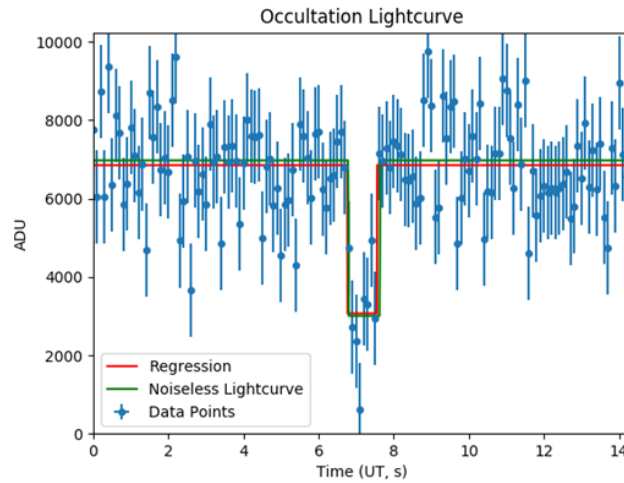


Figure 3.5: Example of case with middle-of-the-road DNR (4.9): Magnitude 12.5, drop of 0.4 and 8 points inside occultation.

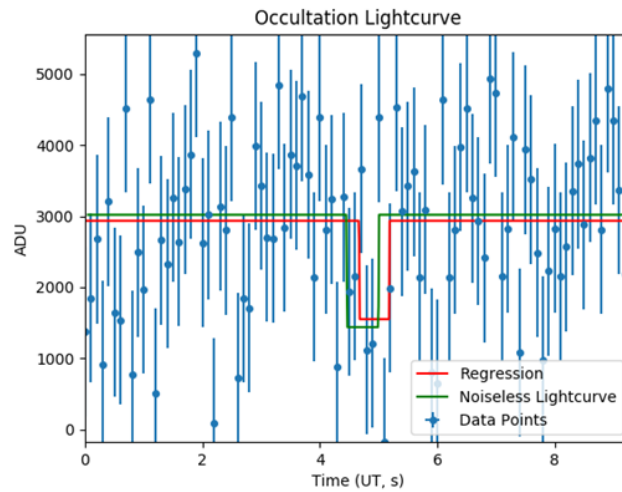


Figure 3.6: Example of case with low DNR (2.1): Magnitude 13.5, drop 0.7 and 2 points inside occultation.

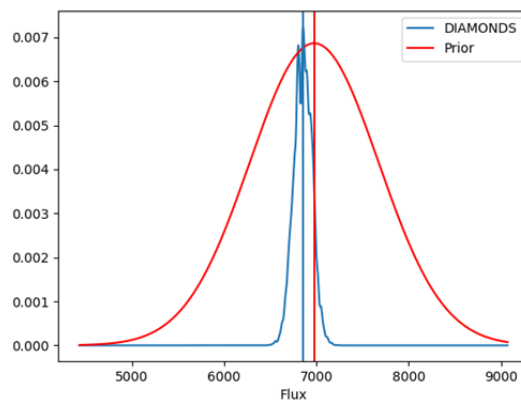


Figure 3.7: Prior vs Posterior Distribution of Flux for Intermediate example. Vertical lines represent medians.

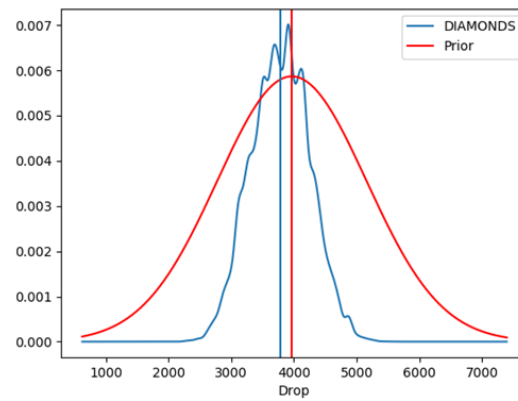


Figure 3.8: Same, but for drop.

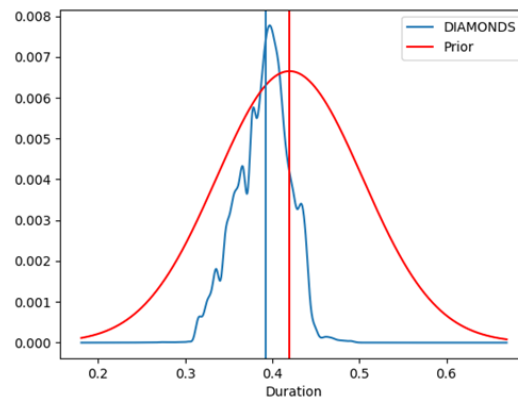


Figure 3.9: Same, but for duration.

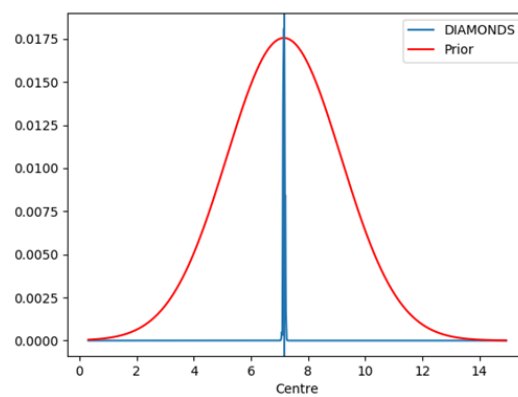


Figure 3.10: Same, but for Centre Epoch.

too optimistic and is not guiding the code to the right value beyond what's reasonable (in which case, this analysis would be moot). This is especially evident for the Centre Epoch marginalization. And second, it lets us check for any unintentional biases in any of the parameters, which were corrected before the runs analyzed in this chapter.

One other utility of the marginal distributions is to check for correlations between the four parameters during DIAMONDS's performance. Since there are four free parameters, there is a total of six parameter pairs that must be analyzed, to ensure that no correlation exists that might affect the performance of DIAMONDS. Two examples are shown in Figures 3.11 and 3.12, where no clear correlation was found. This applied to all pairs for the examples shown above.

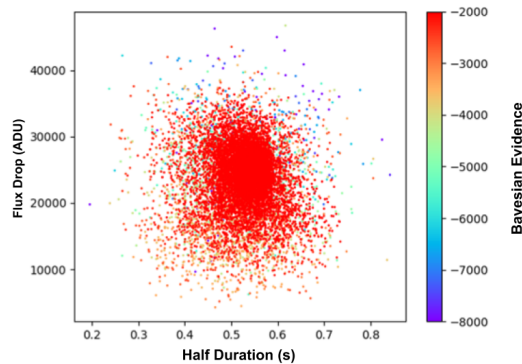


Figure 3.11: Example of correlation check between Duration and Drop for the "Easy" case.

Now that the BIM was set, the simulations could be used in mass. The conditions for the simulations were the following:

- Exposure time of 0.1 s, a typical value in occultations;
- Magnitude 11.5 to 13.5, steps of 0.2;
- Drop of 0.3 to 1.0 magnitudes, steps of 0.1;
- Maximum Duration of 0.2 s to 1 s, steps of 0.1 s, corresponding to 2 to 10 sampling points;
- 10 tests for each combination.

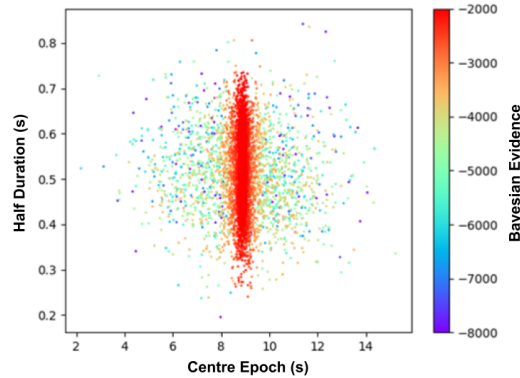


Figure 3.12: Same, but between Duration and Centre Epoch.

This gave us a total of  $11 \times 10 \times 9 \times 8 = 7920$  light curves, representing 792 different combinations of flux, drop and duration. The highest magnitude is close to the expected limit of the telescope and the star is considered to be at the zenith. The magnitude drop values are usually higher, but this would translate to near total flux drops, which would be easier to detect, so they were discarded, and the interesting limit values were considered instead. The duration is also typical for medium-sized asteroids.

These 7 920 light curves were analyzed with both uniform and gaussian priors, and 7 920 flat signal light curves with the same parameter distribution on the priors was made as well, which were used for the False Positives test, to determine how the BIM would react when we gave priors expecting an occultation that did not occur. Each cycle of light curves lasted  $\sim 2.5$  days, with several cycles serving the purpose of refining the initial parameters before the final results for the occultations and the false positives.

### 3.4 Results

An example of the marginal distributions provided by the BIM is shown in Figure 3.7

We checked, for a number of representative cases, the correlation of the parameters by pairs. No pairs of parameters exhibit any significant correlation.

The significance of the occultation can then be evaluated by computing

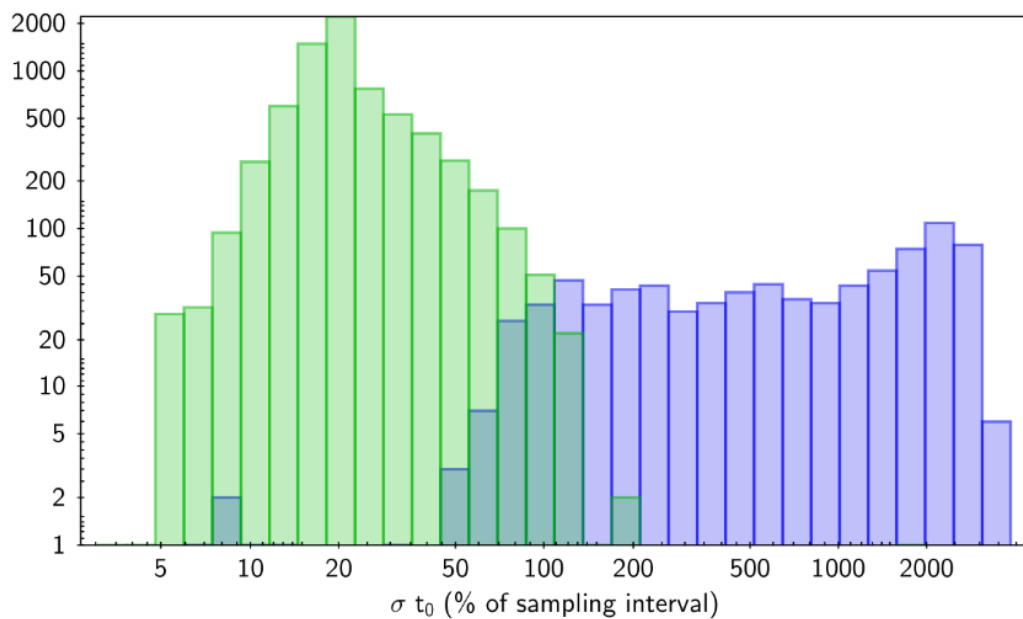


Figure 3.13: Distribution of the significant (left, green peak) and non-significant (right, blue peak) solutions found by the BIM as a function of the uncertainty on the centre epoch  $t_0$ , expressed in percentage of the sampling time. At around 100% uncertainty, the frequency of the two situations is about the same. This results are for the Gaussian priors.

the Bayesian evidence of the model containing the occultation signal and of a model of flat (no occultation) light curve. The result is the detection probability of the occultation, in percentage.

$$C(\%) = \frac{100}{1 + \frac{E_{flat}}{E_{occ}}}$$

Where  $E_{occ}$  is the Bayesian evidence of the occultation model and  $E_{flat}$  stands for the flat signal. In general it is considered that the model is significant with respect to another if the Bayesian evidence of the former model is at least 5 orders of magnitude larger than that of the latter model. This corresponds to  $C_{crit} \sim 99.3\%$ . We thus classify as "non significant" all results with  $C < C_{crit}$ . [Trotta et al., 2008]

In the following, we characterize the results on the base of the uncertainty (standard deviation) of the marginal distribution for the duration and the centre epoch ( $\sigma_L$  and  $\sigma_{t_0}$ ), which are the two fundamental parameters determining the observed chord length and the position of the asteroid relative to the star, in the direction of its motion. While the first quantity is related to the physical properties of the object, the second directly defines the quality of the occultation astrometry, the seminal parameter that motivates our study.

Hereinafter,  $\sigma_L$  is expressed in percentage of the total duration, while  $\sigma_{t_0}$  is in percentage of the sampling time. As the occultation signature is obtained through several samples, we expect in general a sub-sample time uncertainty for a high DNR.

The frequency of failed convergence to a solution of the BIM, and the fraction of false positives, are additional quality indicators of the performance for a given DNR. These quantities are clearly related. We can observe in Figure 3.13 that at  $\sigma_{t_0} > 100\%$  non-significant solutions start to dominate the population. Such threshold for high uncertainties define a domain of model results that should be discarded in practical applications.

By considering only significant solutions we obtain the main results on the occultation accuracy, illustrated in Figure 3.14

Based on our simulations, they represent what can be obtained from the observed events. The plots show that a trend  $\sim 1/DNR$  appears both for

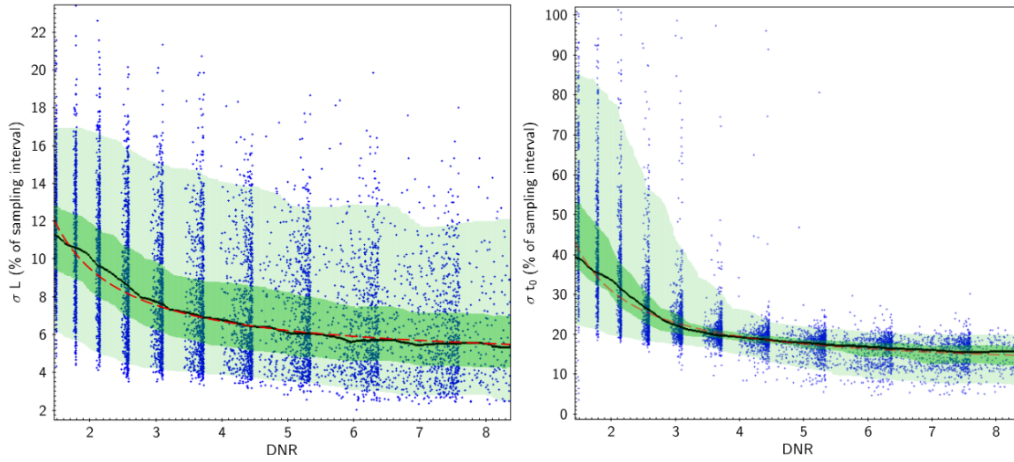


Figure 3.14: The figure represents the expected uncertainty resulting from the BIM fit (Gaussian priors) on the duration  $L$  (left) and the center epoch  $t_0$  of the occultation, as a function of the DNR. The dots represent each result obtained from a simulated occultation. The continuous black line is the smoothed average value, while the shaded areas enclose the quantiles equivalent to  $1\text{-}\sigma$  and  $2\text{-}\sigma$ . The expected trend  $\sim 1/DNR$  (red dashed line) is visible in both plots. The uncertainty is expressed, respectively, as percentage of duration and of sampling time.

$\sigma_L$  and  $\sigma_{t_0}$ , similar to the generic behavior of the photometric precision of a stellar source as a function of the SNR.

The same plots also clearly show that the average precision of  $\sigma_{t_0}$  is well below the sampling time, although the dispersion of the precision increases dramatically for  $DNR < 4$ . In the same range of low DNR, most of the non-significant solutions can be found (they are not represented in Figure 3.14 and fall in a higher range of precision values).

By having more points inside the occultation, it also becomes easier for the BIM to determine the drop, and the duration precision should also increase due to the uncertainty being compared to a larger quantity than when there are only a few points. With more points to sample from, the centre epoch determination also becomes more robust, which should increase its precision as well.

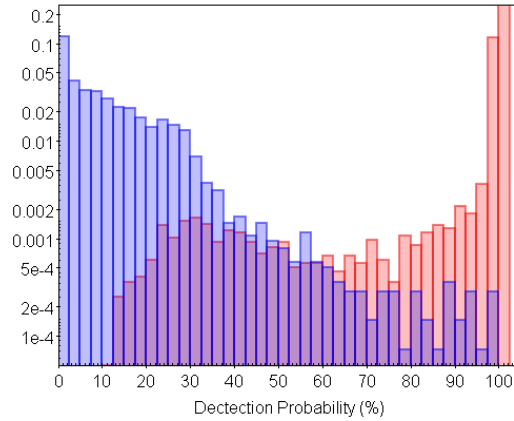


Figure 3.15: Distribution of the Bayesian detection probability obtained by the BIM, for the false positives (blue population rising towards the left) and the true events (red population rising towards the right). For the true events the distribution is strongly dominated by the peaked around the significance threshold of 99%. For the false positives the detection probability remains always very small. The probability of false positives is  $\sim 10^{-4}$  for significant events.

### 3.4.1 Gaussian and Uniform priors

Since the simulated occultation signals for both sets of priors (Gaussian and Uniform) were exactly the same, their results are directly comparable.

In terms of general performance, we observe a slightly better behavior of the Gaussian priors, as shown in Figure 3.16

The plot is equivalent to the right panel of Figure 3.14, but only the lines representing the average precision values are shown.

In addition, it must be taken into account that, while the Gaussian priors always produce a final fit, the BIM with Uniform priors does not converge for 6% of the time, especially for low DNR values. Despite the similarity of the curves in Figure 3.16, we can thus conclude that the performance of the Uniform priors is worse. The computational time is similar for both sets, averaging on 15 seconds per case.

Figures 3.17 and 3.18 show the expected results on the astrometric uncertainty using DIAMONDS for the set of predictions in Chapter 2. These are obtained by calculating the DNR and number of sampling points expected for each event and checking the corresponding centre epoch precision when using

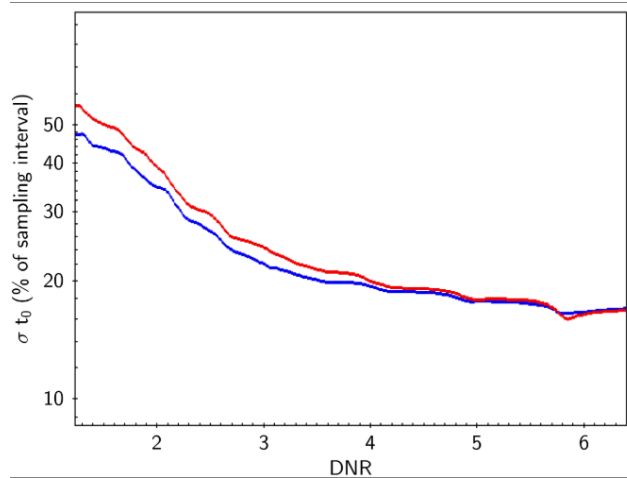


Figure 3.16: Comparison of the performance on the centre epoch as a function of the DNR, for the Gaussian (blue curve) and Uniform priors (red). Here, only the average value is shown. Despite the relatively small difference, the Gaussian prior has a better performance for more difficult events.

the 0.1 s exposure time. Then, from the asteroid’s apparent velocity in mas/s, the uncertainty was converted to mas.

Figure 3.17 shows almost no dependence on asteroid size, but some dependence on duration for smaller objects, for which large samples are unavailable due to our limitations. Figure 3.18 adds the Along Track uncertainty (see Appendix D for more details). In both Figures, the continuous lines are the smoothed averages.

### 3.4.2 False positives

The set of test corresponding to false positives, after BIM analysis, results in very large uncertainties (for instance, of the order of  $\sim 200\%$  or more on  $t_0$ ).

The distribution of the detection probability values for real and false events (Figure 3.15) is particularly illuminating. In fact, it shows that false positives are systematically characterized by a low detection probability, that does not reach  $C_{crit}$ .

In practice, when evaluating the BIM results on real light curves, without knowing *a priori* the reality of a detection, only solutions with  $C > C_{crit}$  will be selected. Figure 3.15 shows that in the corresponding range, the probability

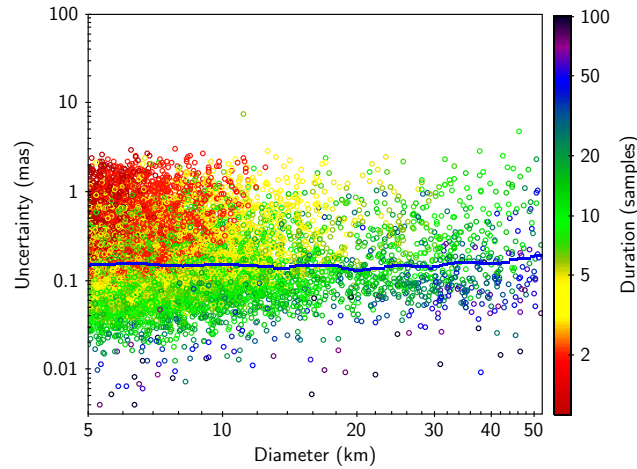


Figure 3.17: Expected distribution of the astrometric uncertainty on the single chord estimated by our accuracy model, applied to a large set of predictions. Only the component of the uncertainty relative to the fit of each light curve by the BIM is taken into account. The colour corresponds to the chord length, expressed as the number of data points within the light curve minimum.

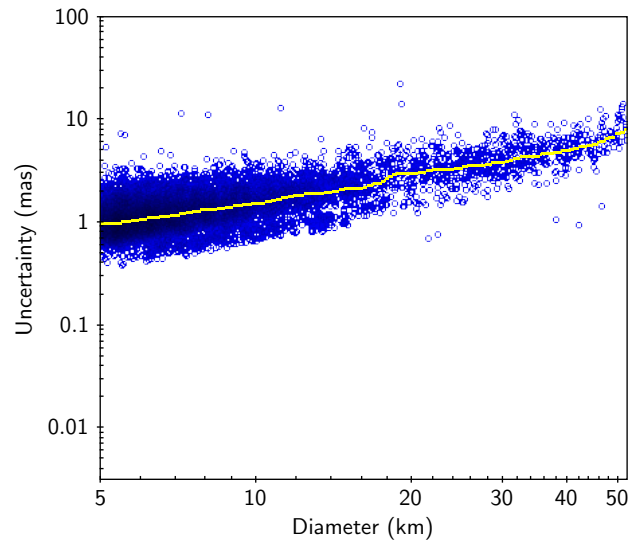


Figure 3.18: Uncertainty including the AT error as derived from a simple model (half of the asteroid apparent radius, computed for each event) for a single-chord event, meaning there would be no other observation to this occultation besides ours. For  $D < 10$  km and occultation duration  $< 5$  samples, the uncertainty due to asteroid size no longer dominates and the two error distributions overlap.

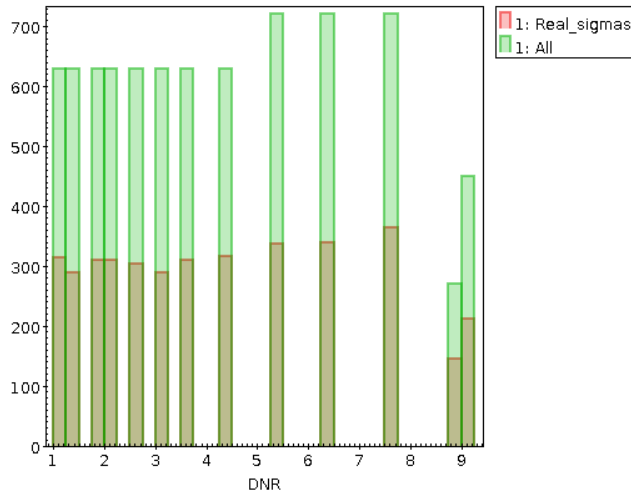


Figure 3.19: Tests made with the LSF as a function of whether they were rejected or not vs DNR. Rejected means not fitting the curve, not being able to estimate parameter uncertainties or estimating these uncertainties as being several orders of magnitude above the nominal values. Only 48% of cases were accepted.

of a false positive is  $< 5 \times 10^{-4}$ .

### 3.4.3 Comparison of BIM to LSF

Although we did not expect a better performance by the simple (or simplistic) LSF approach, for sake of completeness we compared the performance of BIM and LSF for similar conditions.

The LSF code was setup in Python with a rectangular light curve model, and the initial parameter guess was set to the expected values, just like with the gaussian priors for the BIM. The tests were made to the same light curves.

As expected the LSF cannot be considered a good candidate for practical applications in critical cases. In particular, and somewhat counter-intuitively, the LSF had more trouble automatically fitting an easier light curve, likely due to the dimension of the jump compared to the data noise. Within the sets we tested, while the BIM with Gaussian priors always fit a solution to the data, the LSF either failed to fit the curve, estimate the parameter uncertainties or it successfully estimated uncertainties, but these turned out to have nonsensical values (e.g. the duration being 0.5 s and having uncertainty

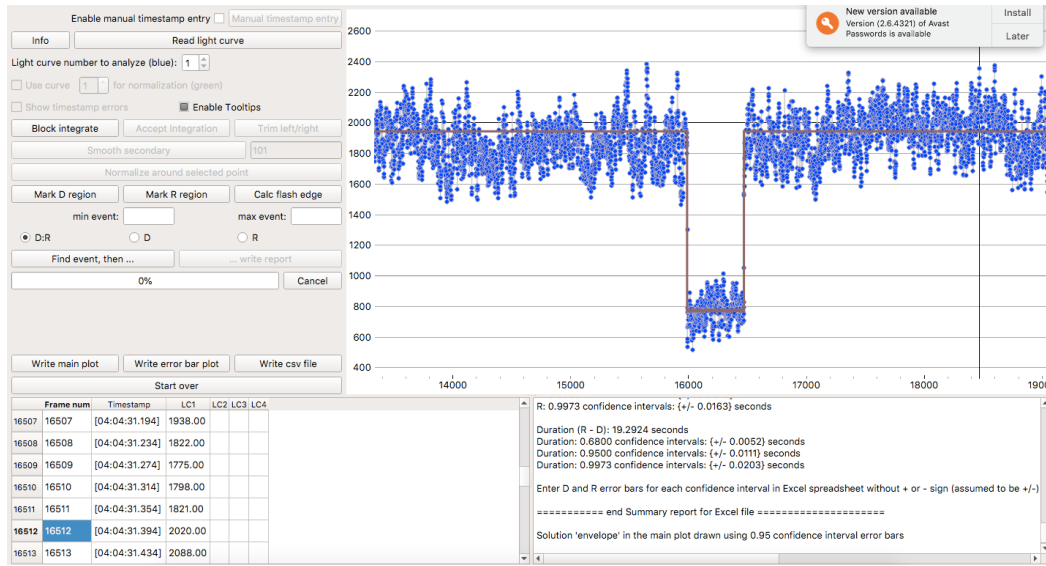


Figure 3.20: PyOTE’s estimate of the duration of the Daphne occultation. This was the case with the largest DNR among the analyzed ( $\sim 7.8$ ).

of  $10^{12}$  s) for just over half of the cases (52%). This proves that the LSF is far more unreliable, and even within the acceptable results the distributions of accuracy and precision of the parameters were worse.

### 3.4.4 DIAMONDS vs PyOTE

There is a multitude of tools and packages to help reduce data of stellar occultations. Among these, a well-known one is called "R-OTE", based on R coding language. Recently, a simplified version has been made available in Python, called "PyOTE" (view same source link). Much like DIAMONDS, PyOTE also uses a Bayesian Inference Method to constrain the parameters of an occultation. While it requires a bigger input from the user than DIAMONDS, a performance comparison is useful, and so a few events were chosen. Simulations could not be used, because PyOTE specifically requires file formats obtained from Data Reduction tools (.csv with specific column order and identifiers). An "easy" event was chosen (Daphne), as well as a few "hard" ones, with low DNR.

With Daphne, the exposure time was 0.04s (25 FPS recording) an uncertainty of 0.0052s on the duration (19.292s) corresponds to only 13% of the

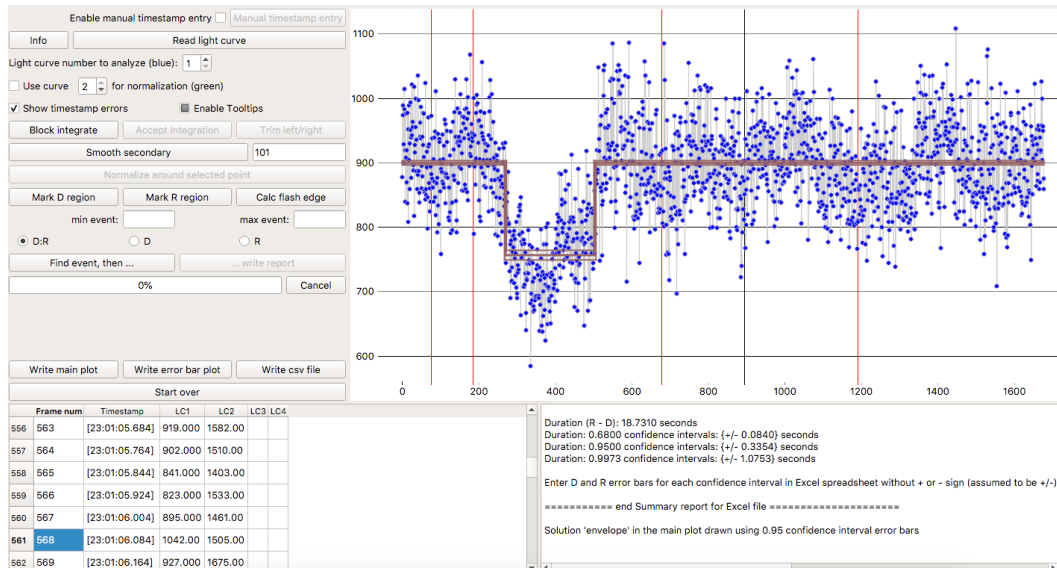


Figure 3.21: PyOTE’s estimate of the duration of the Victoria occultation. Centre line is best fit, other lines are separated by 1-sigma in flux and duration. This was the case with the lowest DNR among the analyzed ( $\sim 1.4$ ).

exposure time. For the same event, DIAMONDS calculated a duration of 19.302s and an uncertainty of 0.0055s (14% of exposure time). So this means the two tools had a similar performance, and the durations are matched within 2 sigma of either PyOTE’s or DIAMONDS’s calculations, and we can consider them consistent. But the more interesting analysis is how each behaves for difficult events. Five events observed within the previous were used: (146) Aemilia on 2019/05/15, (476) Hedwig on 2019/02/12, (12) Victoria and (181 145) 2005 QC178 on 2019/01/17 and (586) Thekla on 2018/05/17. This events were observed by Matthieu Conjat and Rui Gonalves.

For PyOTE, the duration of the Victoria event was 18.73 seconds with a 1-sigma uncertainty of 0.084 s (105% of exposure of 0.08 s). For DIAMONDS, the duration was 18.67 s with a 1-sigma uncertainty of 0.14 s (181%). The results are consistent, as with Daphne. This uncertainty is larger due to the fact that we do not account in our occultation model for long transitions, assuming a sharp one.

Table 3.1 shows the results obtained as function of the DNR and the precision of PyOTE and DIAMONDS as a percentage of the exposure time.

Asteroid	Number	DNR	PyOTE (%)	DIAMONDS (%)
Daphne	41	7.82	13	14
2005 QC178	181 145	3.62	33	19
Hedwig	476	2.98	21	22
Thekla	586	2.76	97	33
Aemilia	159	1.84	54	51
Victoria	12	1.42	105	181

Duration Precision results

Table 3.1: Performance comparison between PyOTE and DIAMONDS, the two bayesian tools available. Centre epoch precision is shown to be of comparable size most of the time, with DIAMONDS benefiting from being more versatile in the choices made and more user friendly for mass use.

Every event had duration values consistent between the two tools within 2-sigma from the worst performing one. We can conclude that the two codes are similar in performance, alternating the best fit. PyOTE is better for prolonged transitions, while DIAMONDS is better for sharp ones. Overall, the two tools are evenly matched, with DIAMONDS being more versatile on the set-up. This is the case because PyOTE is a point-and-click tool that works with one event at a time, while DIAMONDS is a command line tool, more easily scriptable. DIAMONDS's performance can also be improved regarding long transitions if we include a fifth free parameter to account for the slopes. This will decrease the chances of the occultation being deemed significant, but might improve the overall results in cases where these slopes are noticeably non-vertical.

### 3.4.5 BIM vs Real Cases

We analyzed light curves of occultations obtained by our group (see Chapter 4) and other observers, whose light curves are available at the Occult archive. While not every positive observation comes with the obtained photometry (some users, for example, only provide a report stating their results), this archive is still complete enough to provide several interesting cases to analyze with DIAMONDS and compare our results with the ones reported by each observer. To keep this analysis close to what was analyzed, we looked for events with a DNR within the ranges shown in Figure 3.1, and we also made

a filter on the number of points inside the occultation by excluding light curves with more than 25 sample points inside the event. A total of 25 events of the past 10 years were found, and are shown in the Table 3.2 by ascending order of DNR.

Asteroid	Y	M	D	Observer	DNR	$\sigma_{t_0}$ R (s)	$\sigma_{t_0}$ B (s)	dt (s)
Hygiea	2015	5	14	Dunford	1.5	0.35	0.15	0.25
Cybele	2015	10	28	Kattendidit	1.5	1.3	1.8	2.5
Phocaea	2017	3	3	Dunford	1.7	0.01	0.015	0.04
Elisabetha	2016	6	20	Dunford	1.9	0.5	0.24	0.5
Lutetia	2016	8	13	Perello	2.0	0.53	0.26	0.65
Hedwig	2019	2	12	Conjat	2.0	0.06	0.02	0.1
Selene	2019	7	22	Haymes	2.3	0.16	0.08	0.16
Vala	2016	1	2	Perello	2.8	0.25	0.12	0.65
Tchaikovsky	2019	1	17	Conjat	2.9	0.07	0.01	0.07
Unitas	2015	4	30	Bardecker	3.0	0.3	0.05	0.53
Lotis	2016	3	1	Gault	3.5	0.5	0.12	0.53
Caprera	2017	5	4	Hooper	3.9	0.48	0.14	0.65
Lucina	2016	11	30	Frappa	4.3	0.21	0.03	0.3
Lomia	2011	5	26	Gault	4.3	0.26	0.1	0.7
Hertha	2015	9	25	Perello	4.3	0.53	0.9	1.5
Anahita	2017	3	26	Hooper	4.5	0.12	0.008	0.15
Phaethon	2019	10	15	Tanga	5.8	0.004	0.002	0.01
Eos	2015	9	26	Perello	7.0	0.85	0.38	1.7

Table 3.2: Observed occultation chords chosen for comparison to our model for observation accuracy. Their photometric light curves data have been fitted by the model, with the same procedure adopted for the simulations. For the (3 200) Phaethon observation in particular, since our uncertainty was the one published, the "author" uncertainty is the one obtained by Jean-Pierre Rivet, another member of the observation, through a different method. For the other observations, the uncertainties were obtained from various sources, namely the Planoccult mailing list where the observers shared their reports, Euraster and the Occult archive.  $\sigma_{t_0}$  R is the reported uncertainty,  $\sigma_{t_0}$  B (s) the uncertainty obtained with the BIM and dt the exposure time.

The BIM outperforms the reported uncertainties in 85% of the cases, but it should be noted that it is common practice to state the sampling time as the uncertainty, which would put these at a disadvantage against our method. To combat this practice would be another reason to implement the BIM as

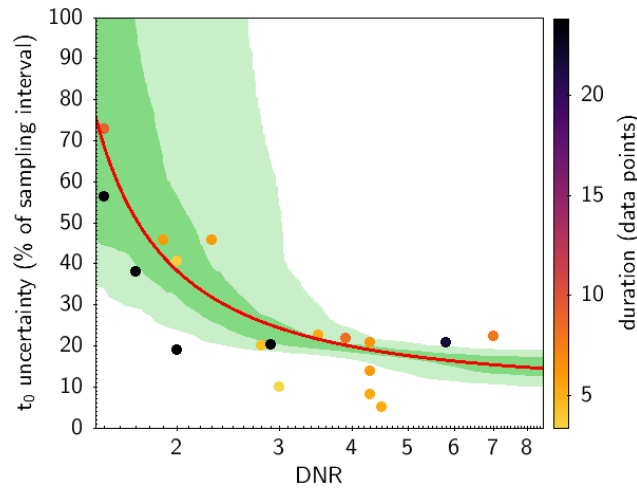


Figure 3.22: DNR and uncertainty on central epoch for a number of observed events similar to those adopted for the simulation. The colour of the circles is associated to the number of data points in the occultation minimum, indicated by the scale at the right of the plot. Red line represents the average expected uncertainty for the event, and the green areas represent 1 (dark green) and 2 (light green) sigma intervals. Note that the points represent the uncertainty in time obtained through the BIM, NOT the times reported. For the performance comparison between reported uncertainties and the ones obtained through the BIM, check Table 3.2

standard procedure.

These results were published as an article in *Astronomy & Astrophysics* [Ferreira, J. F. et al. \[2020\]](#), seen in Appendix D of this work.

Figure 3.22 shows that the expected behaviour of the timing uncertainty with the DNR falls within the uncertainties reported by each observer, showing a good approximation between simulations and real astrometry. Most of the cases that had many points (20 or more) fall below the expected behaviour, but with more sample points inside the occultation, we also expect DIAMONDS to improve the  $t_0$  precision.

The knowledge gained on how to optimize the BIM allowed the use of DIAMONDS for real observations, which can be seen in Chapter 4, as well as a comparison between the uncertainties obtained by other observers and this method in some collaborations.

# Observations

---

## Contents

---

<b>4.1</b>	<b>Context</b>	<b>120</b>
<b>4.2</b>	<b>Positives</b>	<b>121</b>
4.2.1	Triton	121
4.2.2	Aemilia	122
4.2.3	Phaethon	125
4.2.4	Millman	126
<b>4.3</b>	<b>Negatives</b>	<b>129</b>
4.3.1	2000 HD22	129
4.3.2	Gezelle	130
4.3.3	Sveta	130
4.3.4	Paijanne	131
4.3.5	Nolde	131
4.3.6	Modestia	132
4.3.7	1993 FE48	132
4.3.8	Deikoon	132
4.3.9	Elektra	133
4.3.10	Phaethon	134
4.3.11	Europa	134
4.3.12	Alfaterna	135
4.3.13	2002 MS4	135
<b>4.4</b>	<b>Analysis to other observations</b>	<b>136</b>
4.4.1	Europa event - RIO team	136

---

4.4.2	Galatea . . . . .	140
4.4.3	Euphrosyne . . . . .	140

---

## 4.1 Context

Here, we have a list of all observations of stellar occultations in which I participated throughout my PhD. For most of them, the telescope used was the 40 cm at Coupole Schaumasse<sup>1</sup>, operated by Matthieu Conjat (AIMA). Here are some details:

- **Size:** 40 cm;
- **Altitude:** 350 m;
- **Location:** OCA;
- **Coordinates:** 43°43' 32.9" N, 07°17' 59.4" E;
- **Time source:** NTP Time Server Monitor synchronisation - Windows 7 Pro;
- **Type:** Reflector;
- **Mount:** Equatorial;
- **Sensor:** Asi 174mm (CMOS);
- **Filter:** None.

Unless specified otherwise, this was the equipment used. Other observers and fits to shape models are shown if applicable, and all images are extracted from Euraster. It should be noted that, until 2018, all reports, be them positive, negative or doubtful, were published in the public page, but since 2019 only events with at least one positive chord are shown, so if no reports are seen for the events listed in 2019 and 2020, that may not necessarily mean that our observation was the only one made to that specific event, only that no positive chords were obtained. All of the stars have their J2000 coordinates listed, propagated from Gaia DR2.

For the positive events, we used the BIM developed during Chapter 3 to obtain the uncertainties for the results.

---

<sup>1</sup> <https://www.oca.eu/fr/conferences/1904-le-telescope-schaumasse-de-l-observatoire-de-nice, inFrench>

Whenever necessary, the photometry of these events was made using either a program I built for this purpose (see Appendix B) or Tangra<sup>2</sup> [Pavlov and Mallama, 2015], a manual software tool built for this purpose.

## 4.2 Positives

### 4.2.1 Triton

- **Date:** 2017/10/05-06;
- **Location:** Calern Observatory, Nice;
- **Coordinates:** 43°45' 13.18" N, 06°55' 22.43" E;
- **Telescope:** Omicron, C2PU;
- **Altitude:** 1 268 m;
- **Diameter:** 1.040 m;
- **Sensor:** iXON 888 (CCD);
- **Filter:** SDSS i', bandpass from 700 to 850 nm;
- **Frame Rate:** 9.567 per second.

Other members participating in the observation:

- Jean-Pierre Rivet;
- Pedro Machado;
- Paolo Tanga;

Details:

- Occulted Star: 4UC 410-143659;
- Magnitude: 12.7;
- Right Ascension: 22h 54m 18.4314s;
- Declination: -8°0' 8.312";
- Maximum Duration: 161 s;
- Magnitude drop: 1.2;
- Distance to Sun: 149°;
- Distance to Moon (100%): 34°.
- **Duration:**  $172.3 \pm 0.2$  s
- **D:**  $23:46:25.9 \pm 0.1$  s
- **R:**  $23:49:18.2 \pm 0.1$  s

---

<sup>2</sup> <http://www.hristopavlov.net/Tangra3/>

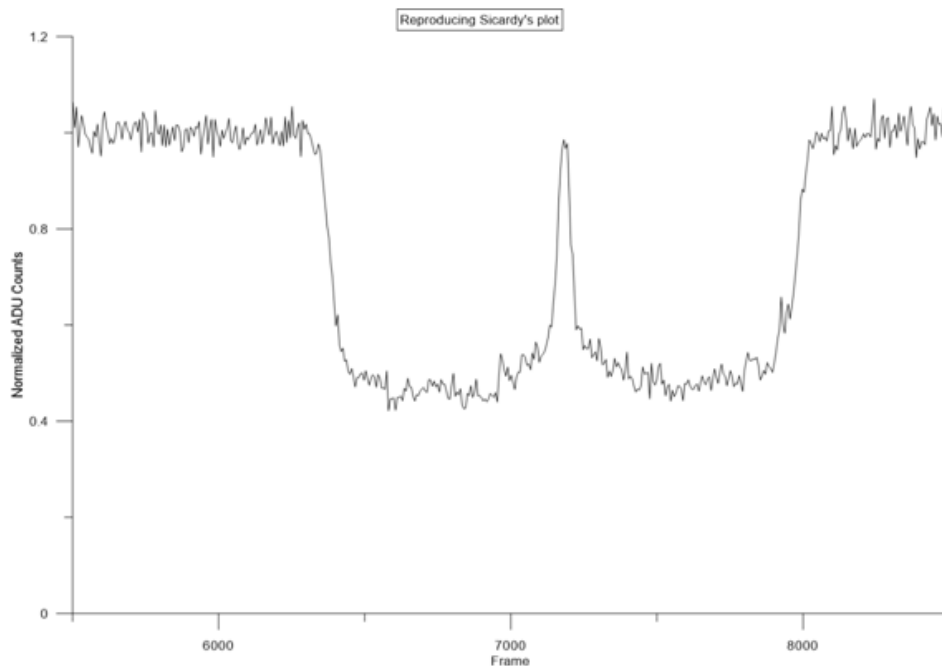


Figure 4.1: Triton light curve. Central flash observed, which can be used to study Triton's atmosphere.

- **Drop:** N/A
- **Other chords?** Yes, over 80 positive chords! The detection and characterization of Triton's atmosphere was the primary goal, with the astrometric solution having uncertainties in the order of 20 mas for Across Track (AC) and 50 mas for Along Track (AL).

#### 4.2.2 Aemilia

- **Date:** 2019/05/15-16;
- **Frame Rate:** 3.33 per second;
- **BIM uncertainty:** 0.18 s;
- **PyOTE uncertainty:** 0.3 s.

Details:

- UCAC4 545-047842;
- Magnitude: 13.5;
- Right Ascension: 9h 4m 47.984s;
- Declination: 18°48' 43.364'';

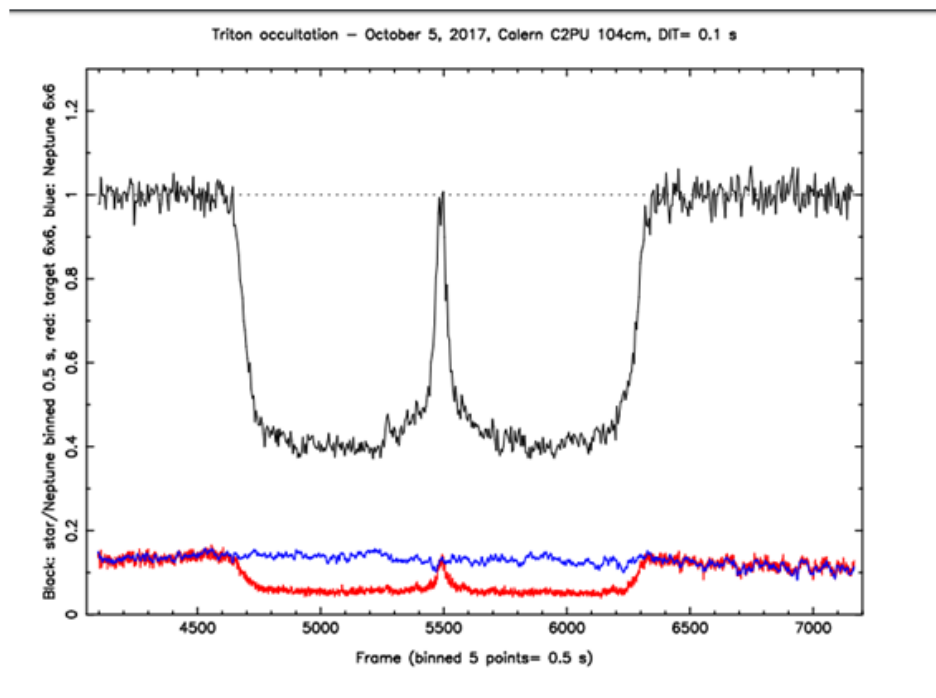


Figure 4.2: Triton occultation analyzed by the Paris team (Bruno Sicardy et. al). Blue line is Neptune's flux, red line the occulted star's flux. Black is the ratio between the two, normalised to 1 for the average outside the occultation.

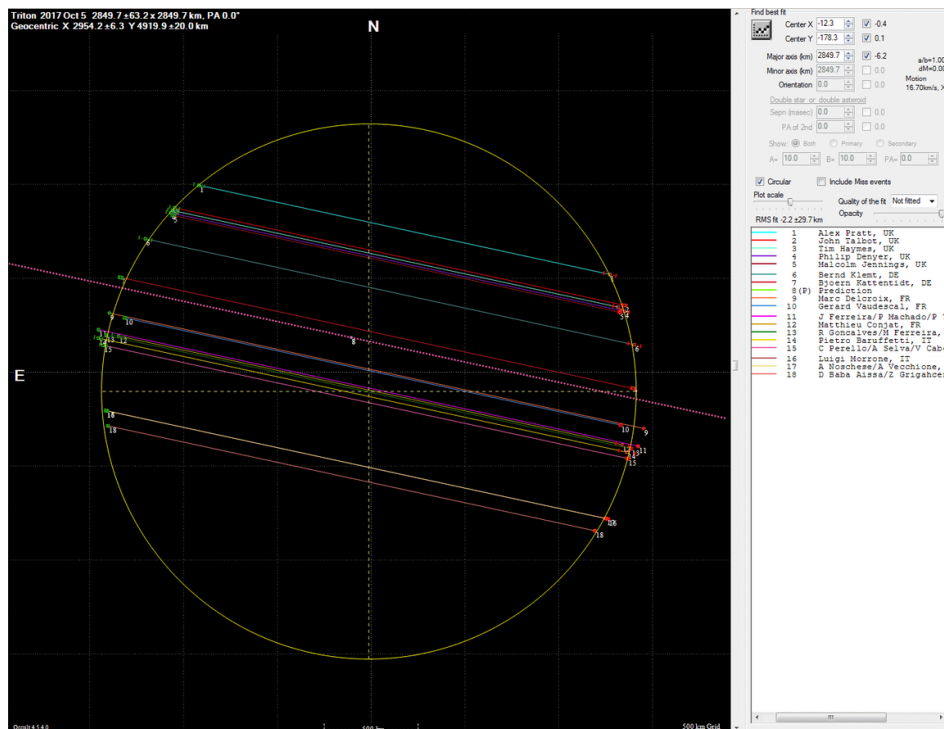


Figure 4.3: Fit of some observed chords of Triton during this event. Our observation is close to the centre. Image by Euraster. An image with all the used chords will be provided in a future publication by the Lucky Star collaboration.

- Maximum Duration: 5.6 s;
- Magnitude drop: 0.9;
- Distance to Sun: 78°;
- Distance to Moon (89%): 63°.

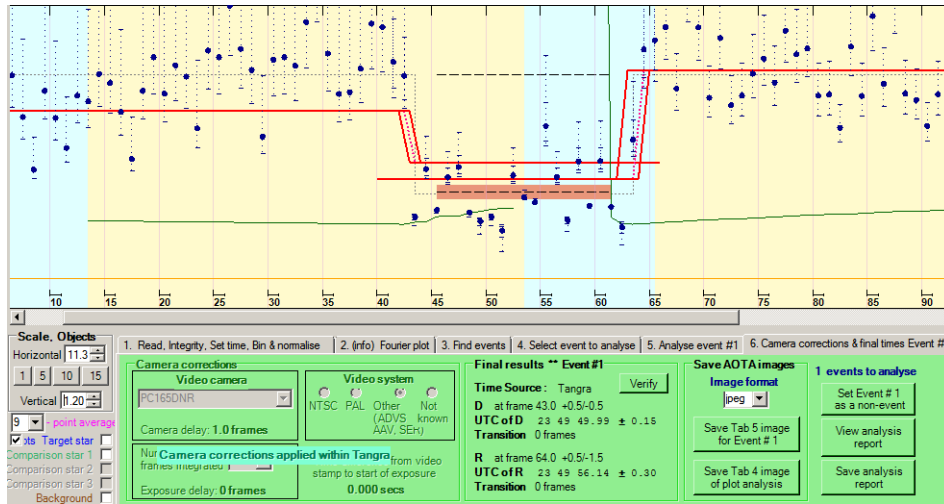


Figure 4.4: Aemilia occultation, seen with AOTA (Asteroidal Occultation Timing Analyzer), a tool present in Occult. The blue dots represent the samples, with their 1-sigma uncertainties, and red lines represent the flux inside and outside the occultation, as well as the slope seen in one and another direction with a 1-sampling time interval. Ingress and egress times in local unites (+2 UTC).

Results:

- **Duration:**  $6.15 \pm 0.45$  s
- **D:** 21:49:49.99  $\pm 0.15$  s
- **R:** 21:49:56.14  $\pm 0.30$  s
- **Drop:** 60%
- **Other chords?** Yes, 1, by Pierre Le Cam, from Le Grand Pressigny. Astrometric uncertainties of 3.5 mas for AC and 28.9 mas for AL.

### 4.2.3 Phaethon

- **Date:** 2019/10/15-16;
- **Frame Rate:** 20 per second.
- **BIM uncertainty:** 0.002 s;

- **PyOTE uncertainty:** 0.004 s.

Other members participating in the observation (in a different site, still in Nice, while I was at Couple Schaumasse with Matthieu Conjat):

- Jean-Pierre Rivet;
- David Vernet;
- Erick Bondoux
- Paolo Tanga;

Details:

- Occulted Star: UCAC4 707-014626
- Magnitude: 11.1;
- Right Ascension: 1h 57m 50.6930s;
- Declination:  $51^{\circ}17' 46.087''$ ;
- Maximum Duration: 0.2 s;
- Magnitude drop: 5.7;
- Distance to Sun:  $137^{\circ}$ ;
- Distance to Moon (96%):  $41^{\circ}$ ;
- Other observers: 2 positive chords (Christian Weber, Berlin, Germany and Baba Aissa, Algeria) and 2 negatives, one of which also by this team. Astrometric uncertainties of 0.1 mas for AC and AL.

This observation was part of a campaign. Results were as follows:

Parameters obtained from DIAMONDS:

- Duration:  $0.218 \pm 0.002$  s
- Centre epoch (UT): 19h 47m 9.8358s
- Chord length:  $4.982 \pm 0.048$  km

#### 4.2.4 Millman

- **Date:** 2020/03/07-08;
- **Frame Rate:** 11.11 per second.
- **BIM uncertainty:** 0.1 s;
- **PyOTE uncertainty:** 0.08 s.

Details:

- UCAC4 612-021900;
- Magnitude: 12.7;
- Right Ascension: 5h 32m 35.586s;

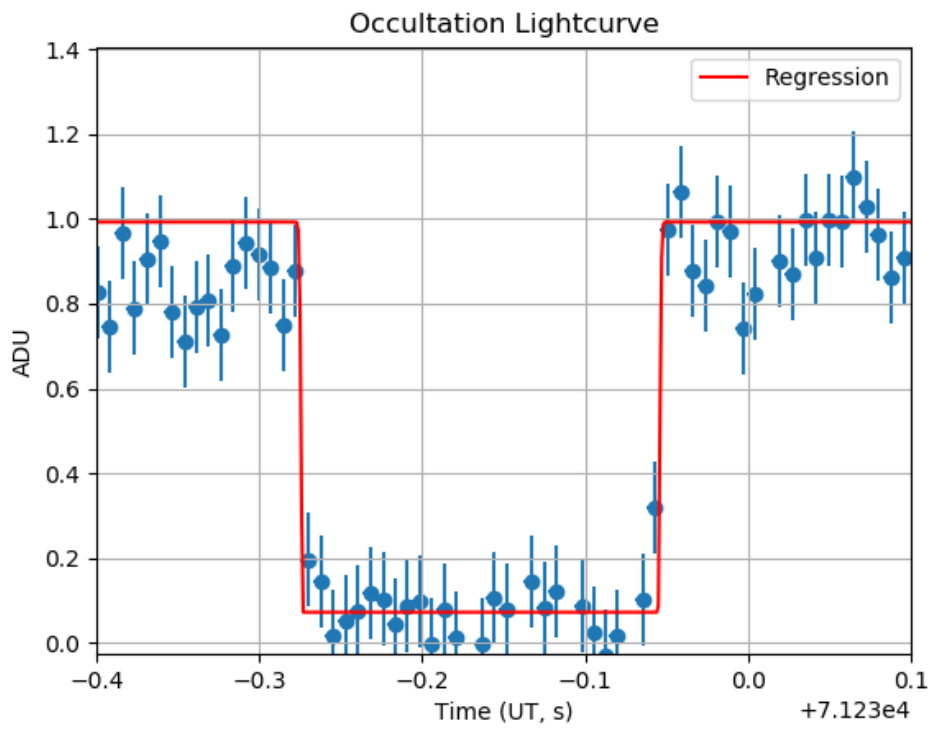


Figure 4.5: Occultation of (3200) Phaethon as seen with a 1 meter telescope in Nice. Observing team: Jean-Pierre Rivet, Paolo Tanga, Erick Bondoux, David Vernet.

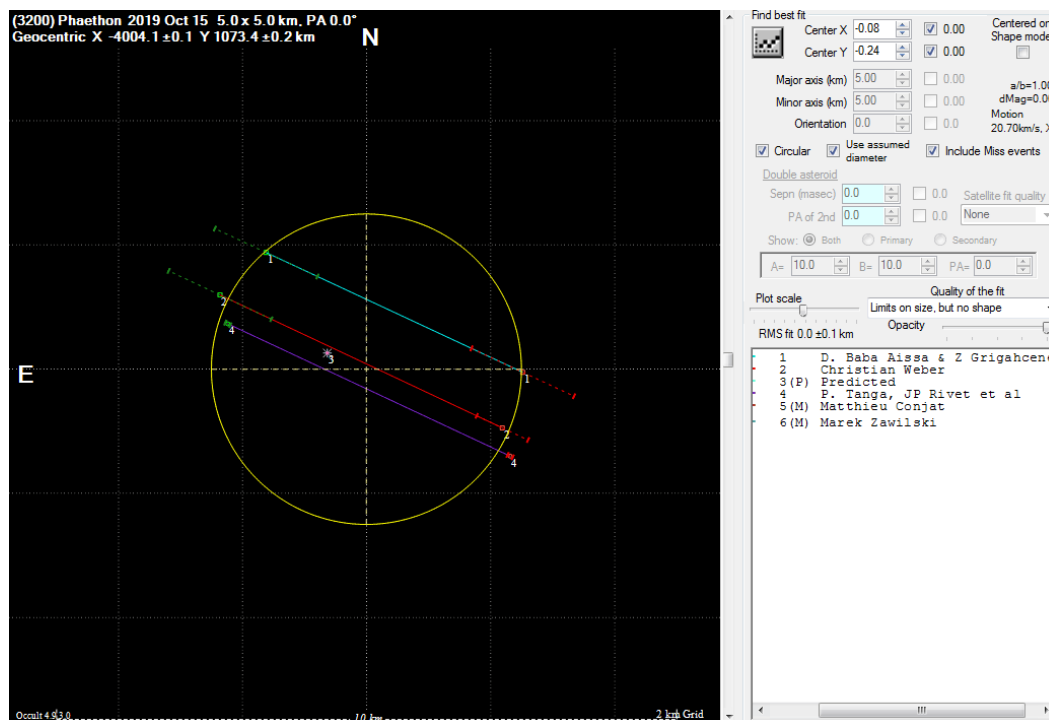


Figure 4.6: Shape of (3200) Phaethon fit to the three observed chords: Baba Aissa from Algeria (blue), Christian Weber from Germany (red) and our observation (purple). Dashed green and red lines represent uncertainties in disappearance and reappearance moments for each chord, which shows the Nice observation was far more precise than the others. Fit made by Eric Frappa.

- Declination:  $32^{\circ}13' 53.082''$ ;
- Maximum Duration: 1.0 s;
- Magnitude drop: 3.7;
- Distance to Sun:  $96^{\circ}$ ;
- Distance to Moon:  $56^{\circ}$ .



Figure 4.7: Millman occultation, as analyzed with Tangra. Blue is the light curve of the occulted star and yellow the light curve of a reference star in the Field Of View.

Results:

- **Duration:**  $1.40 \pm 0.27$  s
- **D:**  $19:30:42.76 \pm 0.18$  s
- **R:**  $19:30:44.16 \pm 0.09$  s
- **Drop:** 67%
- **Other chords?** Yes, 1 by Florian Signoret from Calern. Astrometric uncertainties of 0.5 mas for AC and 4.1 mas for AL.

## 4.3 Negatives

### 4.3.1 2000 HD22

- **Date:** 2018/07/04-05;
- **Frame Rate:** 5 per second.

Details:

- UCAC4 376-110513;
- Magnitude: 13.2;
- Right Ascension: 18h 14m 57.409s;
- Declination:  $-14^{\circ}49' 41.825''$ ;
- Maximum Duration: 0.9 s;
- Magnitude drop: 4.0;
- Distance to Sun:  $169^{\circ}$ ;
- Distance to Moon (26%):  $63^{\circ}$ ;
- Other observers: None reported.

### 4.3.2 Gezelle

- **Date:** 2018/07/13-14;
- **Frame Rate:** 5 per second.

Details:

- Occulted Star: UCAC4 350-180841;
- Magnitude: 13.7;
- Right Ascension: 19h 38m 45.217s;
- Declination:  $-20^{\circ}07' 18.388''$ ;
- Maximum Duration: 1.2 s;
- Magnitude drop: 2.6;
- Distance to Sun:  $178^{\circ}$ ;
- Distance to Moon (1%):  $171^{\circ}$ ;
- Other observers: None reported.

### 4.3.3 Sveta

- **Date:** 2018/09/29-30;
- **Frame Rate:** 2 per second.

Details:

- Occulted Star: UCAC4 358-198864;
- Magnitude: 11.9;
- Right Ascension: 20h 01m 41.363s;
- Declination:  $-18^{\circ}26' 16.327''$ ;
- Maximum Duration: 2.4 s;

- Magnitude drop: 5.1;
- Distance to Sun: 112°;
- Distance to Moon (77%): 124°;
- Other observers: 3 negative reports.

#### 4.3.4 Paijanne

- **Date:** 2018/12/01-02;
- **Frame Rate:** 5 per second.

Details:

- Occulted Star: UCAC5 570-009915
- Magnitude: 12.1;
- Right Ascension: 4h 16m 27.655s;
- Declination: 23°54' 59.200";
- Maximum Duration: 1.7 s;
- Magnitude drop: 4.1;
- Distance to Sun: 176°;
- Distance to Moon (29%): 118°;
- Other observers: 1 negative report.

#### 4.3.5 Nolde

- **Date:** 2018/12/10-11;
- **Frame Rate:** 5 per second.

Details:

- Occulted Star: UCAC4 566-014034
- Magnitude: 10.5;
- Right Ascension: 5h 7m 45.495s;
- Declination: 23°2' 58.057";
- Maximum Duration: 1.2 s;
- Magnitude drop: 6.8;
- Distance to Sun: 179°;
- Distance to Moon (11%): 140°;
- None reported.

### 4.3.6 Modestia

- **Date:** 2019/02/17-18;
- **Frame Rate:** 14 per second.

Details:

- Occulted Star: UCAC4 559-032482
- Magnitude: 12.4;
- Right Ascension: 6h 40m 52.144s;
- Declination: 21°45' 9.591";
- Maximum Duration: 14.5 s;
- Magnitude drop: 2.3;
- Distance to Sun: 130°;
- Distance to Moon (96%): 26°;
- Other observers: None reported.

### 4.3.7 1993 FE48

- **Date:** 2019/02/17-18;
- **Frame Rate:** 25 per second.

Details:

- Occulted Star: UCAC4 531-047225
- Magnitude: 10.6;
- Right Ascension: 8h 43m 34.540s;
- Declination: 16°8' 19.161";
- Maximum Duration: 1.4 s;
- Magnitude drop: 6.7;
- Distance to Sun: 145°;
- Distance to Moon (96%): 5°;
- Other observers: None reported.

### 4.3.8 Deikoon

- **Date:** 2019/02/23-24;
- **Frame Rate:** 12.5 per second.

Details:

- Occulted Star: UCAC4 487-051992

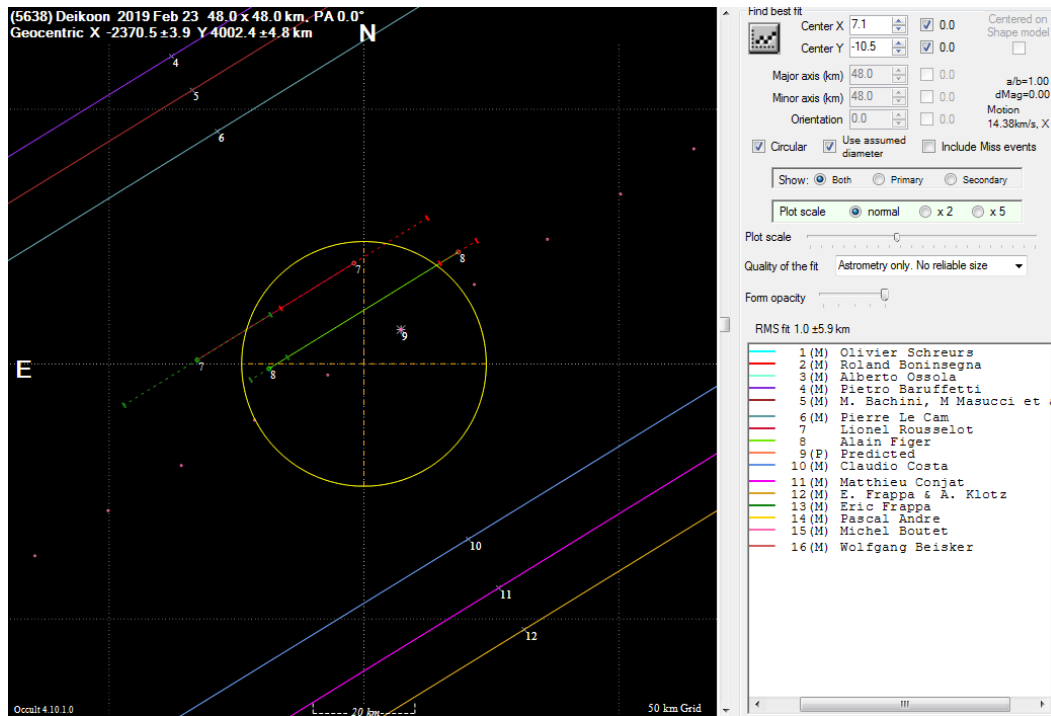


Figure 4.8: Occultation of (5638) Deikoon, fitted for the 2 positive chords (Lionel Rousselot, Vierzon, France, and Alain Figer, Paris, France). Dashed lines represent timing uncertainties by each user, and their large size does not exclude a spherical model for the asteroid. Our observation is represented by the purple line, numbered 11, meaning that we missed the event by a little over 1 object radius ( $\sim 50$  km). Fit made by Eric Frappa, shared in Euraster.

- Magnitude: 11.5;
- Right Ascension: 11h 10m 16.709s;
- Declination:  $7^{\circ}17' 24.657''$ ;
- Maximum Duration: 2.8 s;
- Magnitude drop: 5.9;
- Distance to Sun:  $169^{\circ}$ ;
- Distance to Moon (76%):  $48^{\circ}$ ;
- Other observers: 2 positive and 11 negative reports. Astrometric uncertainties of 1.3 mas for AC and 6.4 mas for AL.

#### 4.3.9 Elektra

- **Date:** 2019/06/28-29;

- **Location:** Nice Observatory;
- **Frame Rate:** 10 per second.

Details:

- Occulted Star: UCAC4 423-140215
- Magnitude: 12.4;
- Right Ascension: 22h 41m 21.0093s;
- Declination:  $-5^{\circ}33' 45.272''$ ;
- Maximum Duration: 23.2 s;
- Magnitude drop: 0.49;
- Distance to Sun:  $117^{\circ}$ ;
- Distance to Moon (17%):  $68^{\circ}$ ;
- Other observers: 1 positive report (Lionel Rousselot) and 1 negative. Because only 1 chord was obtained, no shape fit could be made. Astrometric uncertainties of 5.8 mas for AC and 46.0 for AL.

#### 4.3.10 Phaethon

This refers only to the observation at Coupole Schaumasse, made simultaneously with the observation mentioned in the Positives section.

- **Date:** 2019/10/15-16;
- **Frame Rate:** 20 per second.

Details:

- Occulted Star: UCAC4 707-014626
- Magnitude: 11.1;
- Right Ascension: 1h 57m 50.6930s;
- Declination:  $51^{\circ}17' 46.087''$ ;
- Maximum Duration: 0.2 s;
- Magnitude drop: 5.7;
- Distance to Sun:  $137^{\circ}$ ;
- Distance to Moon (96%):  $41^{\circ}$ .

#### 4.3.11 Europa

- **Date:** 2020/06/21-22;
- **Frame Rate:** 10 per second.

Details:

- Occulted Star: UCAC4 343-195279
- Magnitude: 11.6;
- Right Ascension: 19h 47m 1.3432s;
- Declination:  $-21^{\circ}26' 3.732''$ ;
- Maximum Duration: 119.7 s;
- Magnitude drop: 0.1;
- Distance to Sun:  $156^{\circ}$ ;
- Distance to Moon (5%):  $166^{\circ}$ ;
- Other observers: None reported.

#### 4.3.12 Alfaterna

- **Date:** 2020/06/30-2020/07/01;
- **Frame Rate:** 8.33 per second.

Details:

- Occulted Star: UCAC4 519-054243
- Magnitude: 12.5;
- Right Ascension: 13h 14m 45.4252s;
- Declination:  $13^{\circ}43' 38.379''$ ;
- Maximum Duration: 2.7 s;
- Magnitude drop: 3.5;
- Distance to Sun:  $92^{\circ}$ ;
- Distance to Moon (30%):  $35^{\circ}$ ;
- Other observers: None reported.

#### 4.3.13 2002 MS4

- **Date:** 2020/08/08-09;
- **Location:** Centro Ciência Viva (CCV) Constância, Portugal;
- **Coordinates:**  $39^{\circ}29' 41.6''$  N,  $08^{\circ}19' 25.2''$  W;
- **Telescope:** RC;
- **Altitude:** 170 m;
- **Diameter:** 0.508 m;
- **Filter:** None;

- **Frame Rate:** 1.56 per second.

Other members participating in the observation:

- Miguel Bento;
- Rui Gonçalves.

Details:

- Occulted Star: Gaia DR2 4253248324549054464;
- Magnitude: 13.6;
- Right Ascension: 18h 47m 29.9638s;
- Declination:  $-6^{\circ}16' 31.473''$ ;
- Maximum Duration: 38 s;
- Magnitude drop: 5.7;
- Distance to Sun:  $90^{\circ}$ ;
- Distance to Moon (76%):  $94^{\circ}$ .

Results: Part of a campaign by the Lucky Star collaboration, as object is a TNO. The team was looking for peculiar characteristics, like rings, satellites asteroids or an atmosphere. As a result, several observers attempted this event, with over 30 other negatives and at least 60 positives! A record at the time of this observation for TNO. Astrometric uncertainties to be determined.

## 4.4 Analysis to other observations

While most of the astrometric analysis done with DIAMONDS was applied to our own observations, on occasion a collaboration was made to use it on the results of other published observations. Here, a compilation of those cases is made:

### 4.4.1 Europa event - RIO team

An occultation by the Galilean moon Europa was observed by the RIO team on 2017-03-31, and subsequently published [Morgado et al., 2019]. This involved a magnitude 9.5 star, but because the Galilean moons are bright, the predicted drop was only 0.03 mag. This campaign included three positive reports:

- OBSPA - Observatory in Atacama, Chile, with exposure time of 0.4 s and cycle time of 1.41 s, using a 40 cm telescope and a ProLine/PL16803 CCD camera;

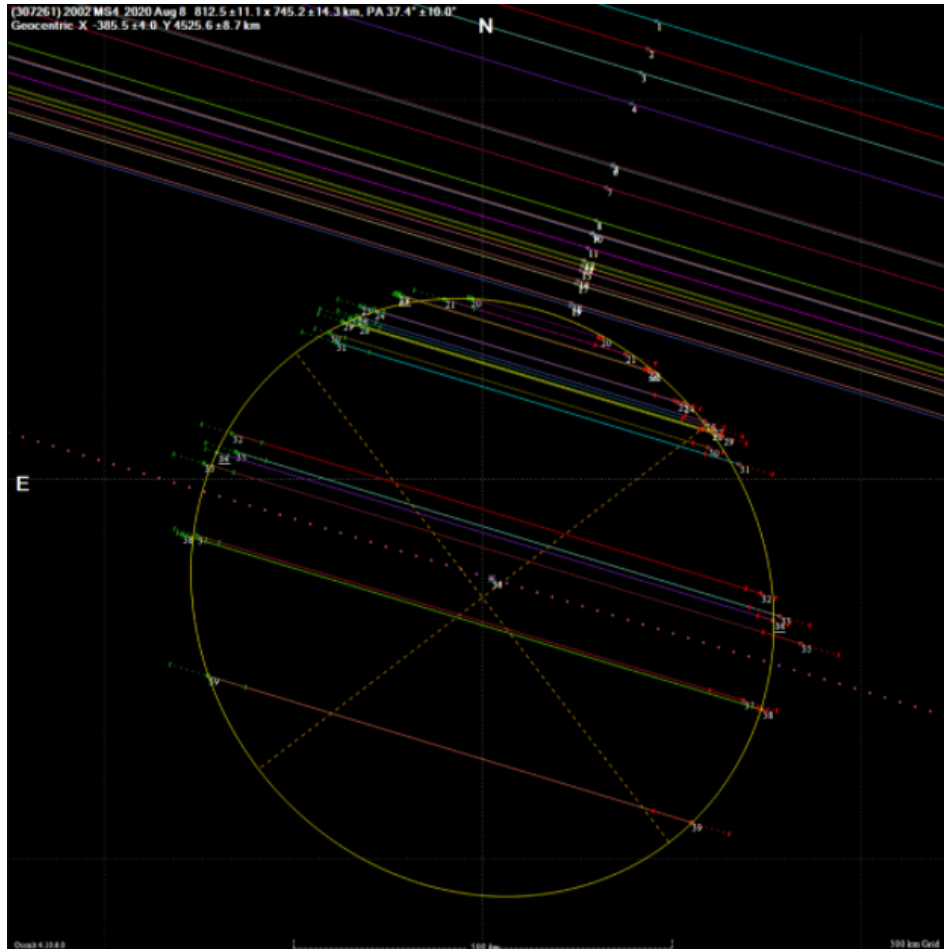


Figure 4.9: European results of (307 261) 2002MS4 campaign. Our observation is the first negative chord to the north. Results will be published by the LESIA team in the future. Image by Euraster.

- FOZ - Observatory in Foz do Iguacu, Brazil, with exposure time 1 s and no dead time, using a 28 cm telescope and a Raptor/Merlin CCD camera;
- OPD - Observatory in Itajubá, Brazil, with exposure time of 0.6 s and a cycle time of 0.63 s, using a 60 cm telescope and a ASCOM/KAF16803 CCD camera.

A collaboration was made with the RIO team to analyze their results with DIAMONDS, and check if there would be any discrepancy. Fits to the lightcurves shown in Figures 4.10 and 4.11

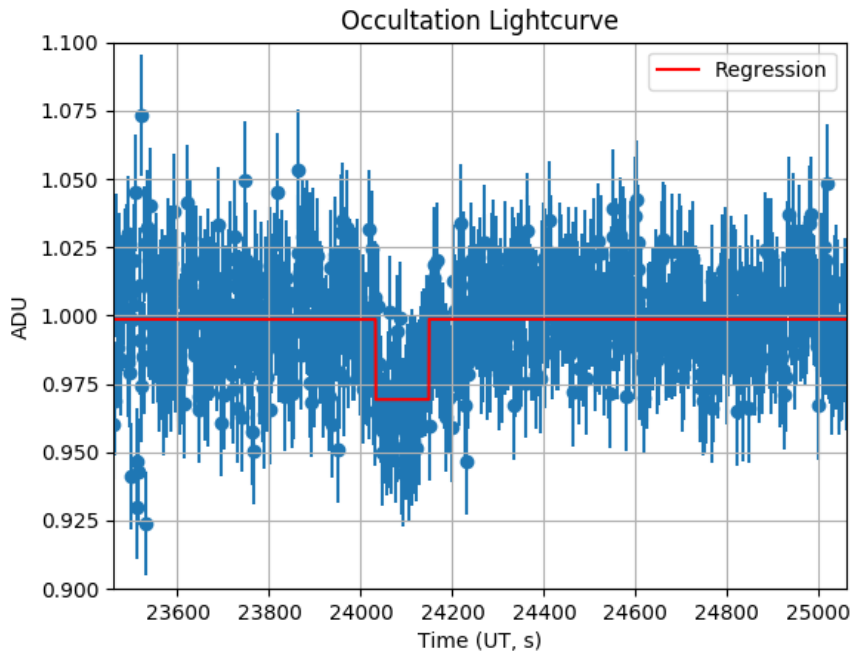


Figure 4.10: DIAMONDS applied to the OBSPA Europa observation. Reported duration was  $104.66 \pm 1.25$  s. Obtained duration with DIAMONDS was  $115.9 \pm 5.8$  s. A difference of 11.3 s that corresponds to a 2-sigma discrepancy.

The results were not considered to be incompatible, as they were within 1-sigma of each other, after a revision by the authors suggested that they had underestimated the uncertainty on their results.

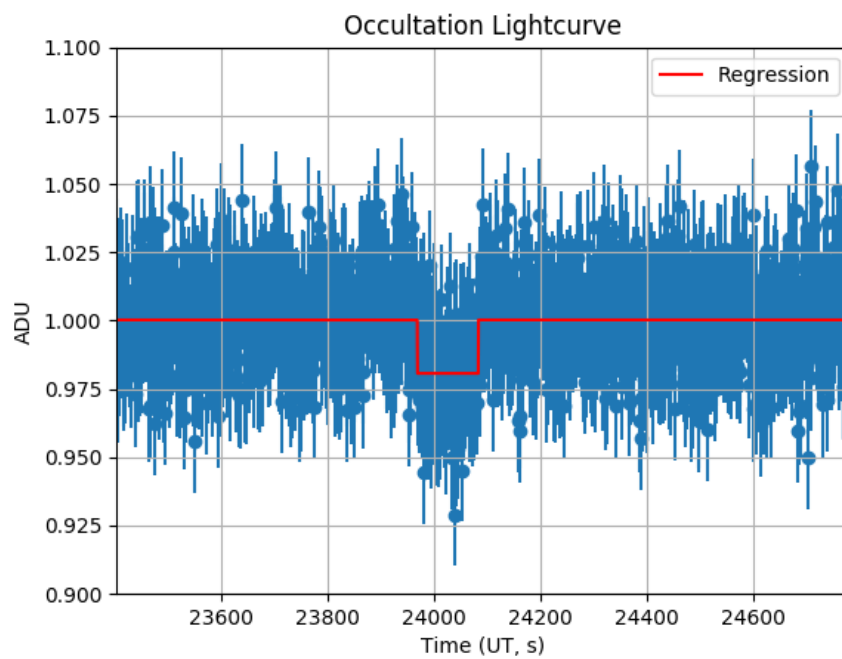


Figure 4.11: DIAMONDS applied to the FOZ Europa observation. Reported duration was  $115.52 \pm 1.32$  s. Obtained duration with DIAMONDS was  $114.3 \pm 2.4$  s. A difference of only 0.8 s, so good agreement between both results.

### 4.4.2 Galatea

This was an observation made by Rui Gonçalves in Tomar, Portugal, to the asteroid (74) Galatea on 2019-10-20 (see Figure 4.12). He reported an uncertainty of 0.24 s on the duration and 0.16 on the timing. However, DIAMONDS provided compatible values for start and end with uncertainties of 0.04 s for each parameter, cutting these by a factor of 4.

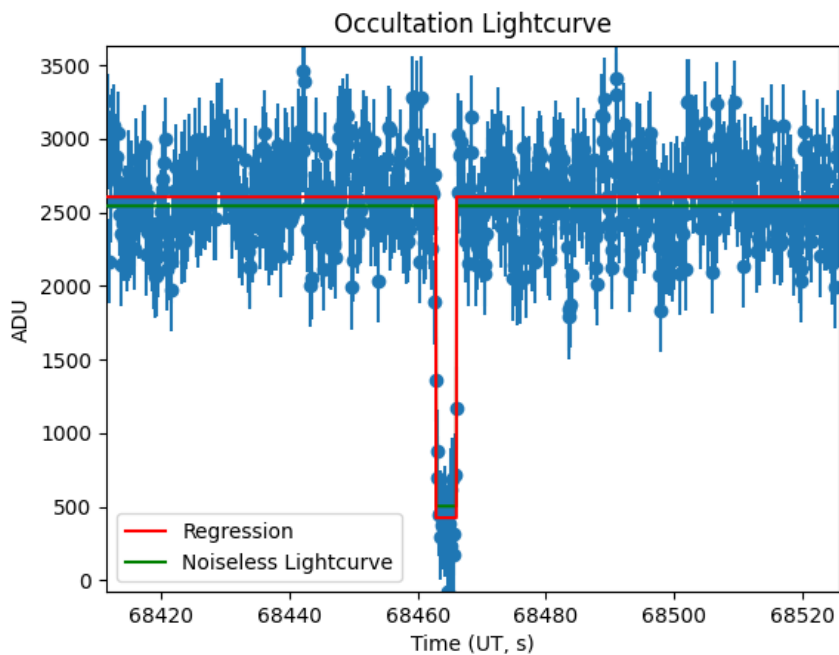


Figure 4.12: Galatea plot. Red line represents light curve from BIM, while Green lightcurve represents the first approximation found by Rui Gonçalves. Blue points represent the obtained photometry.

### 4.4.3 Euphrosyne

On 2018-02-13, several observers reported an occultation by (31) Euphrosyne, with 2 positive chords (Roland Boninsegna, Dourbes, Belgium and Jan-Maarten Winkel, Zeddum, the Netherlands). Roland Boninsegna shared his photometric data with us (see Figure 4.13), allowing a comparison of results.

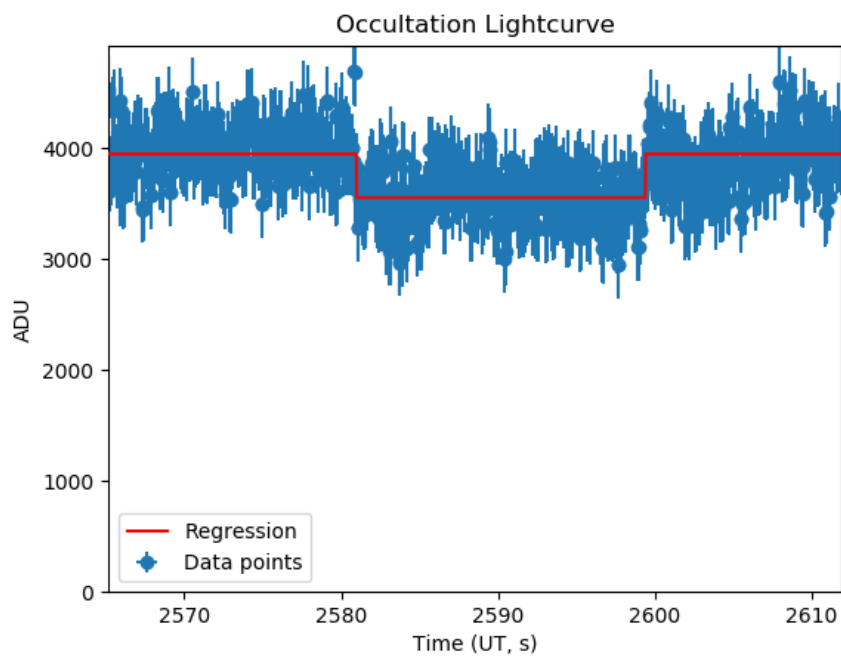


Figure 4.13: Light curve of Euphrosyne. Results reported were duration of  $18.56 \pm 0.04$  s and mid epoch at 00:43:10.30. Results with DIAMONDS were duration of  $18.4 \pm 0.05$  s and mid epoch at 00:43:10.20. Results were compatible within 1-sigma.



# Exploiting Occultation Astrometry

---

## Contents

---

<b>5.1</b>	<b>Context</b>	<b>143</b>
5.1.1	Debiasing	144
5.1.2	Error Models	146
<b>5.2</b>	<b>Setup</b>	<b>150</b>
<b>5.3</b>	<b>Testing error models with occultations</b>	<b>154</b>
5.3.1	Best occultations	154
5.3.2	Full Scale Runs on Occultations	159
<b>5.4</b>	<b>Orbital Elements with Gaia</b>	<b>166</b>
5.4.1	Full Scale Run on DR2 Asteroids	173

---

## 5.1 Context

In this chapter, we tackle issues related to orbital fitting using data from different sources, and check the improvement brought to the results by using a new combination of debiasing and data weighting. Different sources have different structures and different information, making their combination a complex topic. There is also the matter of addressing the possible biases and how reliable each source is.

Debiasing involves the correction of past observations by using modern star catalogues as a standard to find local or global biases that influenced their astrometric results. The Gaia DR2 catalogue, thanks to its proper motion

solutions, has allowed a revision of past works on the topic, such as [Farnocchia et al., 2015].

Data weighting, on the other hand, is necessary because not every asteroid observation has the same accuracy. New methods, new equipment and new reference catalogues have allowed a general improvement of the results' precision. Because the MPC observations archive does not provide the observation uncertainty, it is a complex task to analyze each branch that affects this value in order to properly determine which observations should be prioritised when fitting an orbit [Vereš et al., 2017].

MPC has an 80-character-per-line format for each file of asteroid observations. This format allows the indication of epoch, method, observer, reference star catalogue, RA/Dec coordinates and magnitude measurements, if these are provided by the observers. Orbits computed by MPC assume 1 arcsec uncertainty for each observation. These files include ground and space-based observations, but not Gaia data as of the time of this work. Occultations are included, but an occultation archive by Dave Herald [Herald et al., 2020] provides their astrometric uncertainties, being preferable to use, if we can make it compatible with MPC observations. Meanwhile, Gaia also has a public archive of its own, with its own structure, and so, once again, combining it with the rest requires compatibility, which is brought by a widely used software tool named OrbFit<sup>1</sup>, that was also adopted in the frame of this study. This tool was used for the Gaia DR2 astrometry [Gaia Collaboration et al., 2018a]. One issue to tackle when combining Gaia and MPC data is that they have considerably different uncertainties, and Gaia has a very short time-frame in comparison, meaning that Gaia observations may be given such a strong weight that the fit rejects a large amount of other observations.

### 5.1.1 Debiasing

Debiasing means using current catalogues to correct local or global biases in older ones, and retroactively correcting the observations made while using these catalogues accordingly.

In [Farnocchia et al., 2015], the reference catalogue used is pre-Gaia, and therefore the main issue it tackles, namely the correction to proper motions of

---

<sup>1</sup> <http://adams.dm.unipi.it/orbfit/>

stars (and, to a smaller degree, their positions as well) has undergone a major shift, thanks to DR2. This data release not only presented proper motions that had a higher precision than ever before, but it is also a highly dense catalogue, which adds to the statistical confidence of future corrections to be made.

For this paper, a survey was made to assess which catalogues were used the most in asteroid observations up until that point, the most frequent being USNO (A1.0<sup>2</sup>, A2.0<sup>3</sup>, B1.0<sup>4</sup> and SA2.0<sup>5</sup>), UCAC (2<sup>6</sup>, 3<sup>7</sup> and 4<sup>8</sup>, meanwhile updated to UCAC 5<sup>9</sup>) and 2MASS<sup>10</sup>, which amassed about 85% of all observations.

Since none of these catalogues had a reliable measurement of proper motions for most of their stars, the authors used as a reference the PPMXL<sup>11</sup> catalogue. This is a merger of 2MASS and USNO-B1.0, with added proper motions, and it was considered the best reference available, as 2MASS had good position measurements.

Once the reference catalogue was chosen, the process to determine how good other catalogues are is to divide the sky in small sections, about 50 000 in [Farnocchia et al., 2015]. In each section, a cross-match was made between PPMXL and each of the other catalogues (except 2MASS, due to its redundancy). Based on the average corrections necessary, each catalogue was assigned a certain weight. UCAC4, for example, was a good match, because on average the corrections were small (2 arcseconds in position and about 2 mas/year in proper motion for both RA and Dec) and the sky coverage was complete. An example of a bad catalogue was USNO-A1.0 (about 0.5 arcseconds in position and 6 mas/year in proper motions had to be corrected).

The new approach by [Tanga et al., 2020] uses Gaia DR2 as a reference, and instead of splitting the sky in regions, it focuses on each individual aster-

---

<sup>2</sup> <http://tdc-www.harvard.edu/catalogs/ua1.html>

<sup>3</sup> <http://tdc-www.harvard.edu/catalogs/ua2.html>

<sup>4</sup> <http://tdc-www.harvard.edu/catalogs/ub1.html>

<sup>5</sup> <http://tdc-www.harvard.edu/software/catalogs/usnosa2.html>

<sup>6</sup> <http://tdc-www.harvard.edu/software/catalogs/ucac2.html>

<sup>7</sup> <http://tdc-www.harvard.edu/software/catalogs/ucac3.html>

<sup>8</sup> <https://irsa.ipac.caltech.edu/data/UCAC4/ucac4.html>

<sup>9</sup> <http://tdc-www.harvard.edu/software/catalogs/ucac5.html>

<sup>10</sup> <https://irsa.ipac.caltech.edu/Missions/2mass.html>

<sup>11</sup> <https://irsa.ipac.caltech.edu/Missions/ppmx1.html>

oid observation, trying to only use specifically the reference stars in the field of view. This version is fine-tuned for almost 40 different observatories and 20 reference star catalogues. It also eliminates issues brought by potential transition between different fields during an observation that could be brought with the previous method. However, the trade-off is that this method requires more computational time, and if it finds a set of observer/catalogue not accounted for, it defaults to the coordinates given by MPC, not making any corrections.

### 5.1.2 Error Models

Observations can have different uncertainties depending on a multitude of factors, the main being the reference catalogue used, the epoch and observer associated to the observation and physical parameters of the asteroids, such as brightness and rate of motion. Since MPC does not publish uncertainties, these have to be estimated in order to weigh how important an observation should during an orbital fit.

The model introduced by [Vereš et al., 2017] makes a hierarchy of the factors to take into account, prioritising the observer, then the reference star catalogue, observation and epoch, and finally the method. By estimating the uncertainty  $\sigma$  of the observation, in arcseconds, they then attribute a weight based on Equation 5.1

$$\omega = 1/\sigma^2 \quad (5.1)$$

Tables 5.1, 5.2 and 5.3 show relative weights of epoch, method and catalogue used, respectively, where the weakest elements are given a weight of 1.

Year	Relative Weight $\omega$
1801-1890	1
1891-1950	2.25
1951-Present	4

Weight attributed to different observation epochs

Table 5.1: Rule applied by [Vereš et al., 2017] to the epoch of each asteroid observation.

Method	Relative Weight $\omega$
Micrometre	1
CCD Imaging	9
Satellite	9
Meridian	45
Hipparcos	56.25
Occultations	225

Weight attributed to different observation methods

Table 5.2: Rule applied by [Vereš et al., 2017] to the method of each asteroid observation.

Star Catalogue	Relative Weight $\omega_{RA}$	Relative Weight, $\omega_{Dec}$
GSC-ACT	1	1
USNO-SA	0.9	1.25
USNO-B	1.25	1.93
USNO-A	1.25	2.03
GSC	1.55	1.68
CMC	1.62	2.51
UCAC	2.88	3.61
2MASS	5.02	5.20

Weight attributed to different reference star catalogues

Table 5.3: Rule applied by [Vereš et al., 2017] to the reference star catalogue of each asteroid observation, for RA and Dec coordinates separately.

The full error model combines all of these rules, in order to give each observation its final weight to be used in the orbital fitting.

The new error model, by Spoto et al. (in prep.) adds asteroid brightness, and combines all parameters in a multi-dimensional analysis. When an observation does not meet any of the parameter combinations in the error model, it defaults to an uncertainty of 1 arcsec.

Stellar occultations have their own uncertainty determination [Herald et al., 2020], depending on the quality of the astrometry provided by each observation. This quality will depend mostly on the uncertainties provided with each chord and how many an observation has:

- If the quality is considered good, then an attempt is made to fit a known shape model, and the astrometric solution provided refers to the centre of the shape model, which should coincide most of the time with the

centre of mass of the asteroid. Uncertainty is typically set to 2% of the asteroid's diameter;

- Events with a good distribution of chords across the body are fit through a least-squares fit that will locate the centre of an ellipse that fits all chords, defining its major and minor axes, and the uncertainties are not set to any amount, instead depending on the fit;
- Events with a small or uneven distribution of chords do not fit any shape, even an ellipse, rather just estimating the diameter of the circular body that would best fit each chord. In this case, the uncertainty estimation depends on the length of the chord, with the criteria explained in the following paragraph.

Single chord occultations, the most common type, represent  $\sim 60\%$  of the archive.

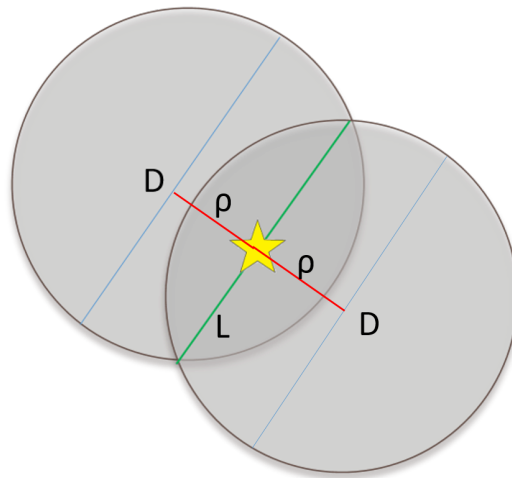


Figure 5.1: A single chord occultation is ambiguous. The chord can always fit two different positions for the object, here assumed to be a sphere of Diameter  $D$ , usually extracted from WISE. The distance between the observed chord and the two possible solutions can be defined as in Equation 6.1

As of right now, the method chosen to fit a single chord occultation to the orbit of an asteroid involves one single possibility, where the centre of the object is assumed to be at the chord level, and the uncertainty must scale to fit both possibilities at once, with a set uncertainty of 40% of the asteroid's

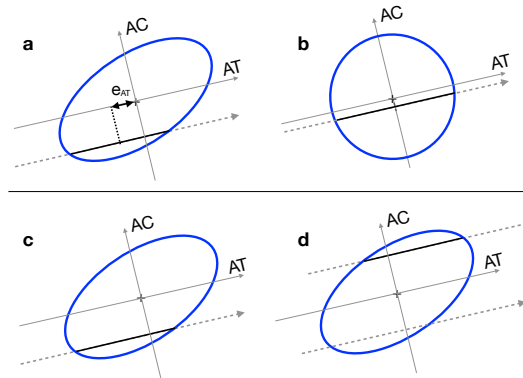


Figure 5.2: Idealised scheme of the uncertainties involved in the astrometry derived from single chord observations of stellar occultations. We adopt as an example a very elongated ellipsoidal asteroid, projected on the fundamental plane in which the asteroid is at rest and the occulted star moves along the dashed arrows. The AC and AT axes represent the across and along-track directions, respectively. In (a) the observed chord duration (black segment) is the same as for the surface-equivalent sphere in (b). The mid-chord point corresponds to the barycentre position in (b), but not in (a), where the error on the derived astrometry  $e_{AT}$  cannot be estimated without a precise knowledge of the shape. Points (c) and (d) represent the ambiguity on the AC position of the observed chord, which can be on opposite sides of the barycentre.

diameter for the Across direction (AC). This is to cover the two possible solutions that fit the observation in one single result. The Along direction (AL) has a branched rule for determining its uncertainty:

- 5% of Duration, if the observed chord is  $\geq 80\%$  of the maximum expected duration;
- 10% of Duration, if the observed chord is 60-80% of the maximum expected duration;
- 20% of Duration, if the observed chord is  $< 60\%$  of the maximum expected duration.

Particularly long asteroids, such as (216) Kleopatra, (433) Eros and (25143) Itokawa, have uncertainties of 20% of Diameter, and cases where the timing uncertainty supersedes this rule, its value is taken instead. This creates sets of trends regarding the AC and AL uncertainties, which can be seen in 5.3 and 5.4.

In addition, it should be considered that even when the shape of an asteroid is well known, there is an ambiguity that persists for single chords (Figure 5.1 shows the case of a spherical asteroid and Figure 5.2 the case of an elliptical asteroid).

For more information on these topics, see Appendix A.

Using OrbFit, we analyzed the impact of adding Gaia data to the orbital fitting and the improvements brought by new debiasing (Tanga et al., in prep.) and data weighting (Spoto et al., in prep.) models by exploiting the occultation's astrometry archive.

## 5.2 Setup

Two major files were used for the setup, both extracted from Occult's archives. The first one had the following information for each event, in a total of over 3 000 events:

- Asteroid number (or PXMYY for planets and satellites, M00 corresponding to the planet);

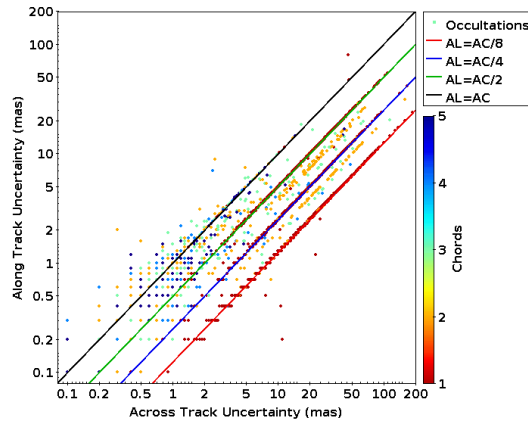


Figure 5.3: There are 4 clear trends, all relating to the rules of AC and AL uncertainty for poor chords, a majority of the archive. Here, we can see that events with 3 or more chords tend to stay out of these trends, as they usually provide good enough astrometry for a particular solution. The rest are distributed across AL being 2, 4 or 8 times smaller, depending on chord length.

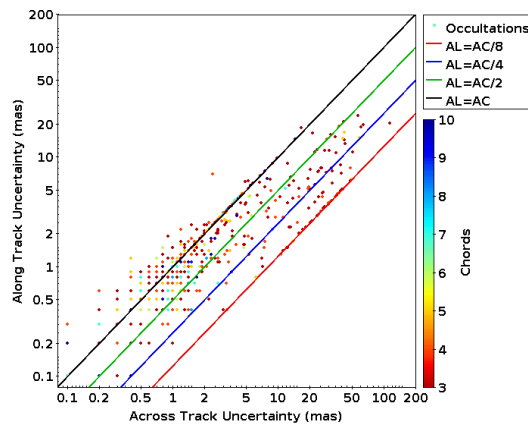


Figure 5.4: Some events with 3 or more chords still fell on the trends, likely due to poor distribution of chords, or poor chord precision, like visual observations or observations with an NTP server with bad synchronization rather than observations timed by a precise system such as GPS.

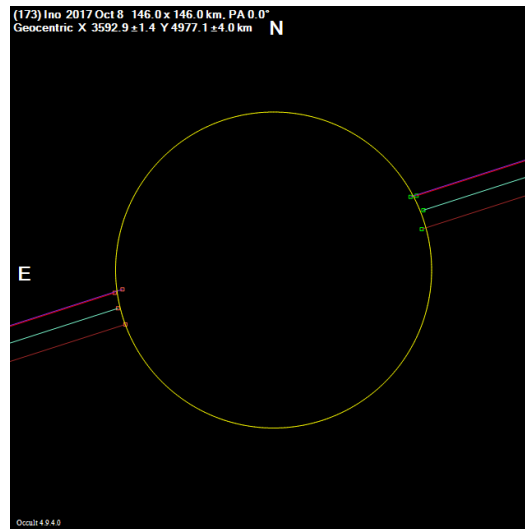


Figure 5.5: Example of an outlier that fell in the trendline. One of the chords was visual, and therefore left out of the fit, and the other 3 chords were too close to provide a good constraint on the object's position.

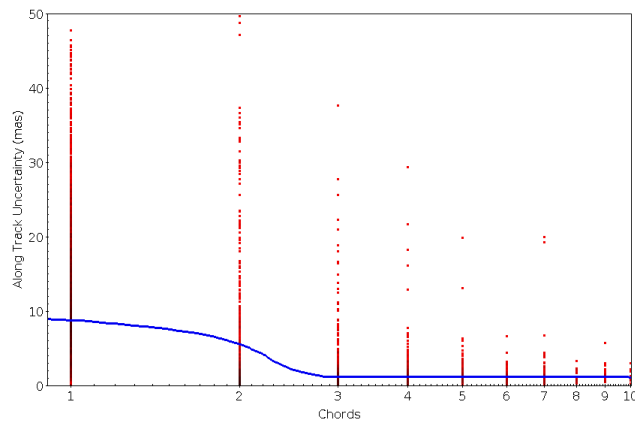


Figure 5.6: AL uncertainty in mas as a function of the number of chords of an event. The transition from 2 to 3 chords seems to be when there is a major improvement in the fit, telling us which should be our cutoff on the number of chords for this work. This is to be expected as, with few exceptions, three chords is when an unambiguous fit to the asteroid becomes possible. Since most occultations correlate Along and Across Track uncertainties, a similar plot with Across Track has a similar distribution, with higher uncertainties.

- Asteroid name;
- Event's centre epoch year, month and day (day written in decimal value to account for exact time);
- Centre epoch uncertainty, in mas;
- Minimum distance from geometric centre observer to line of path ( $\rho$ ), in arc seconds;
- $\rho$  uncertainty, in mas;
- Phase angle, to convert to RA and Dec, in degrees;
- Star RA and Dec;
- Best available star catalogue, usually Gaia DR2;
- Number of chords registered.

This historical file includes every occultation from the very first, in 1961, to midway 2020.

A second file is available, in .xml format, with details for each chord. From this, we extracted for matching purposes asteroid number and name, as well as chord centre epoch date. We also extracted the disappearance (D) and reappearance (R) times, which would give us the chord duration.

For the goals of this work, further information was necessary:

- Asteroid diameter and its uncertainty from WISE, assuming always a spherical shape;
- JPL ephemeris to obtain distance to object at moment of event, in order to obtain the object's apparent angular diameter, in mas;
- Also from the ephemeris, the apparent angular velocity, to convert the duration to the distance travelled in that interval, in mas as well.

We do not consider occultations by planets and satellites, as this work was focused on asteroids. That left us with 3 034 events.

## 5.3 Testing error models with occultations

We tested the performances of two different approaches to data weighting and debiasing, described in Appendix A: the standard one from the literature [Farnocchia et al., 2015], labelled "FV15" (Farnocchia et al. [2015] + Vereš et al. [2017]) for brevity, and the new, labelled "TS20" in OrbFit (Tanga + Spoto, in prep.). To verify that TS20 can outperform FV15, we need to see which can fit better an orbit to accurate observations. And, as mentioned before, occultations provide some of the most accurate measurements for asteroids. Therefore, two different scenarios were made to test both models, each involving checking all occultations we can get data from, and how far each model's astrometric solution is from the one published for the event:

- Using every observation up to the moment of the event, including Gaia DR2 when applicable, which would be the best available set at the epoch of observation, providing a retroactive prediction, "postdiction";
- Using every observation available currently, except the occultation itself, to use the best knowledge on each orbit.

### 5.3.1 Best occultations

A trial run was made before attempting to study every occultation at once. For that, we chose events that we expected to have good precision. All occultations with at least 20 positive chords were grabbed from Occult's archive, a total of 21. Each occultation was tested with the observations known at the time, which would give us a hindsight view on how accurate each model would have been. Table 5.4 presents the distance between the occultation and each model's solution for the centre epoch date of the event.

We can see that, out of 21 events, there was a similar distance, within 10% of each other, for 7, a better performance by FV15 in another 5 and finally a better result by TS20 in 9 of them.

One event in particular, by (472) Roma, yielded bad results with both error models. Trying independent tools, like JPL Horizons and AstDyS, similar large distances to the occultation's solution were found. This is due to issues

Number	Date	FV15 AC	TS20 AC	FV15 AL	TS20 AL
2	29-05-1983	77.2	67.2	76.2	66.4
9	12-09-2008	6.3	6.1	28.6	28.0
9	07-03-2014	2.2	4.1	9.8	18.0
51	11-09-1983	104.5	43.9	106.3	46.0
87	29-10-2019	8.9	10.9	43.8	53.6
90	19-07-2011	43.5	43.5	49.2	49.2
130	21-04-2018	14.0	11.8	7.2	6.1
135	11-12-2008	28.7	16.0	64.6	35.3
212	08-01-2011	1.7	1.7	3.9	3.9
216	12-03-2015	3.6	3.6	5.5	5.5
234	21-11-2009	5.4	3.2	16.6	10.0
345	17-09-2002	3.1	1.5	11.4	5.7
372	26-01-2007	30.2	18.0	68.0	40.6
381	13-01-1991	10.6	11.9	32.8	36.7
420	26-08-2003	6.0	5.1	16.2	13.7
451	05-10-2016	2.2	2.1	36.8	34.6
472	08-07-2010	546.1	539.2	497.8	491.5
498	17-02-2004	12.6	12.6	4.2	4.2
704	23-03-2003	9.5	10.3	50.0	65.8
925	22-12-2003	60.8	11.3	83.6	15.6
1263	18-07-2003	28.6	12.5	25.8	11.2

Error model distance, in mas, for precise events

Table 5.4: Table of every asteroid occultation with 20 or more positive chords reported, sorted by ascending asteroid number. Distance to astrometric solution of occultation by FV15 and TS20 error models are shown, with a clear trend of better solutions under TS20.

related to the event itself, namely the star used<sup>12</sup>: a Hipparcos star with a high proper motion left unchecked by Gaia. So, using its Gaia solution, as is standard today, the star's movement is unaccounted for, introducing issues that are not seen in other such events.

Figures 5.7, 5.8 and 5.9 show some of the results. In these Figures, blue represents the occultation, orange FV15 and green TS20. The dot represents the astrometric solution for the occultation and the ephemeris for each model, and the ellipses represent their respective 1-sigma uncertainty. Finally, the arrow represents the movement direction. For all of these, the precision of the occultation is sub-mas, due to the high number of chords, so its uncertainty ellipse is not visible.

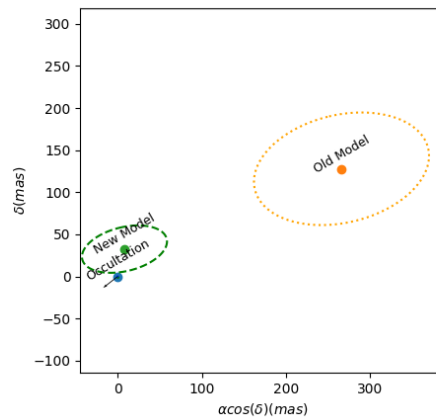


Figure 5.7: Sky-projected distance from both ephemeris to the centre epoch astrometric solution of (51) Nemausa for its 1983/09/11 occultation. TS20 clearly approaches the published position, having it almost within a 1-sigma distance. Asteroid had apparent size of 125 mas, putting the FV15 fit outside the body in the AL direction. Both models are compatible in AC direction.

With a first glimpse indicating that TS20 had the potential to improve the general results over the standard one, two full runs were made to every occultation in the archive (planets and satellites excluded, like before).

<sup>12</sup> <https://www.euraster.net/results/2010/index.html#0708-472>

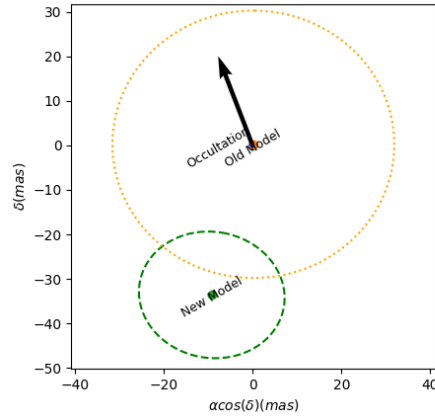


Figure 5.8: Despite the general improvement brought by the TS20, FV15 still usually provides good solutions, with the best case being that of (1 263) Varsavia, an event from 2003/07/08. Asteroid had apparent size of 25 mas, putting the TS20 fit outside the body for the AL direction, though it remains compatible in AC direction.

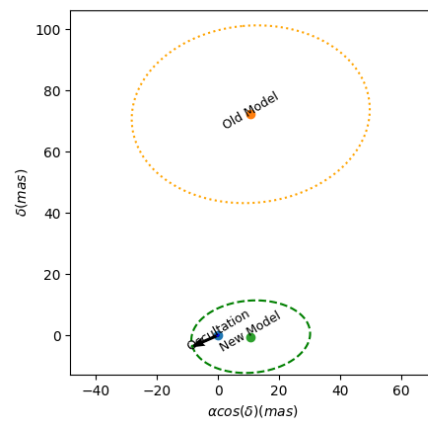


Figure 5.9: One of the best improvements, that of (212) Medea's event, on 2011/01/08. Asteroid had apparent size of 92 mas, putting the FV15 fit outside the body.

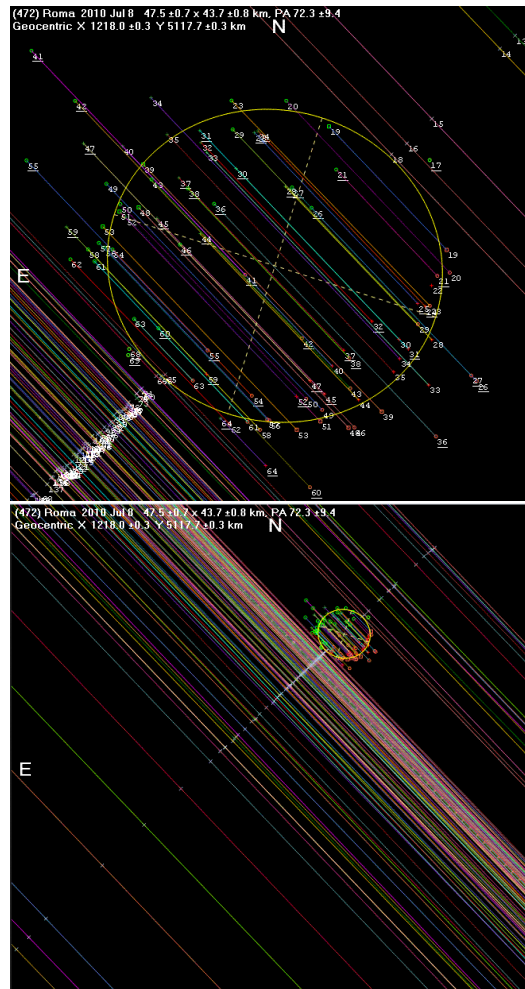


Figure 5.10: Anomalous (472) Roma event, on 2010/07/08. The star was particularly bright ( $V_{\text{mag.}} 2.5$ ), with several of the observations having large timing errors, in the order of seconds, likely due to unconventional equipment, such as non-fast moving cameras, being used, or in some cases visual reports instead. Saturation issues may have also played a role on the unreliability of some results.

### 5.3.2 Full Scale Runs on Occultations

Four different runs were made, with "postdiction" or best current knowledge vs FV15 or TS20. In each of these runs, OrbFit was run in order to obtain the ephemeris of the asteroid propagated to the epoch of each occultation, and then we computed the difference of the position projected on the sky plane to the astrometric solution provided by the occultations archive. Runs under the same database regime ("postdiction" or current knowledge) were also plotted, to verify which model had the shortest distance and shorter uncertainty ellipse. Tables 5.5 to 5.10 provide some statistics of the obtained results. Dist stands for total, AC for Across Track and AL for Along Track differences in position on the local plane of the sky. We also analyzed the set of events with 5 or more chords, as those tend to fall under the best astrometric categories of the occultations archive, and therefore should have the most reliable positions to compare the ephemeris of each model with.

Run Used	Diff. average	Dist $\sigma$	AC Average	AC $\sigma$	AL Average	AL $\sigma$
FV15, At time	40	49	15	26	35	44
FV15, All	37	46	14	24	32	41
TS20, At time	32	38	12	22	27	33
TS20, All	29	35	11	21	25	30

Debiasing and Data Weight comparison, absolute differences in mas

Table 5.5: Comparison between the error models FV15 and TS20 by using OrbFit. We analyze average and  $\sigma$  of AC, AL and total differences. We can see that using the current database for each asteroid provides better results, as is to be expected, as more modern observations tend to be more precise. We also see a tendency for differences to become smaller by adopting the TS20 model rather than FV15.

There is a clear trend of improvement when using all available observations, which is to be expected, as more observations should in theory give us a more accurate orbit. It is also noticeable that the change between the models provides consistently better results, showing the new error model, TS20, brings an improvement to the accuracy of fitting the occultation observations.

We should address why, most of the time, the solutions are very close to each other, as can be seen in Table 5.9. There are several possible explanations, the most likely being:

Run Used	Diff avg.	Dist $\sigma$	AC avg.	AC $\sigma$	AL avg.	AL $\sigma$	< Diam
FV15, At time	0.77	0.85	0.27	0.43	0.67	0.78	74%
FV15, All	0.73	0.81	0.26	0.43	0.63	0.74	76%
TS20, At time	0.62	0.70	0.22	0.38	0.54	0.63	82%
TS20, All	0.58	0.64	0.21	0.34	0.50	0.58	84%

Debiasing and Data Weight comparison, in Diameter units

Table 5.6: Same as Table 5.5, but as ratio of difference and apparent diameter at moment of occultation, along with percentage of events that fell within one diameter of difference to the occultation. This percentage means how many events would have been confirmed by the occultations, barring issues regarding irregular shapes or bad chord distribution. Like in Table 5.5, current knowledge improves results compared to "postdictions" and TS20 outperforms FV15.

Run Used	Dist average	Dist $\sigma$	AC Average	AC $\sigma$	AL Average	AL $\sigma$
FV15, At time	45	55	18	30	38	49
FV15, All	40	47	15	25	34	43
TS20, At time	34	43	13	24	28	38
TS20, All	31	40	12	24	26	33

Debiasing and Data Weight comparison, absolute differences in mas

Table 5.7: Same as Table 5.5, but only for events with 5 or more chords, which are typically the most precise. About 8% of events ( $\sim 370$ ) fall under this category. Results tend to be slightly further away on average, but the progression by using current knowledge vs "postidction" and TS20 vs FV15 is still present.

Run Used	Dist avg.	Dist $\sigma$	AC avg.	AC $\sigma$	AL avg.	AL $\sigma$	< Diam
FV15, At time	0.56	0.60	0.22	0.33	0.48	0.54	83%
FV15, All	0.55	0.63	0.21	0.33	0.47	0.57	85%
TS20, At time	0.47	0.58	0.18	0.31	0.39	0.52	88%
TS20, All	0.43	0.52	0.17	0.30	0.36	0.45	90%

Debiasing and Data Weight comparison, in Diameter units

Table 5.8: Same as Table 5.6, but only for events with 5 or more chords.

- Star coordinates in the occultations archive are mostly taken from DR2 (only 9 have other sources due to not being present in DR2), and  $\sim 20\%$

Group	At Time of Event	All Observations
FV15 was better	16%	16%
Similar within 10% of each other	45%	44%
TS20 was better	39%	40%

Qualitative assessment of how many times each model was better

Table 5.9: Determining which model is better or whether they are similar. Here, we adopt the convention that they are similar if their distances to the occultation's astrometric solution are within 10% of the larger distance. If not, then whichever model is the closest is considered to be better. We can see that, for the non-similar results, TS20 was better more than twice the amount of cases than FV15.

Run	$d < R$	1-sigma tolerance	3-sigma tolerance	Incompatibility
FV15, Bad Stars	78.7%	5.1%	4.1%	12.1%
TS20, Bad Stars	85.4%	4.5%	3.5%	7.6%
FV15, Good Stars	85.6%	4.2%	2.8%	7.4%
TS20, Good Stars	90.6%	2.4%	2.5%	4.5%

Distribution of occultations by AC difference to solution

Table 5.10: Distribution of events in different regions of AC difference: " $d < R$ ", where the difference is smaller than the asteroid's radius, "1-sigma", where the difference is between  $R$  and  $R + \sigma_{occ} + \sigma_{model}$ , "3-sigma", where difference is between  $R + \sigma_{occ} + \sigma_{model}$  and  $R + 3 * (\sigma_{occ} + \sigma_{model})$  and "incompatibility", where the difference is even larger. We also separate the data set between stars with known issues from DR2 that the rest, showing that, if these issues were to be treated, results would improve. Only the runs with the best current knowledge were used for this analysis, and once again TS20 outperforms FV15.

have a duplicate<sup>13</sup> and/or bad astrometry<sup>14</sup> flag, contributing to the error budget. A duplicate source flag is used when there are observational, cross-matching or processing issues or stellar multiplicity, which may lead to problems in the object's astrometry. Meanwhile, a parameter named RUWE, which stands for "Renormalised Unit Weight Error", assesses the quality of the astrometric solution of a star to a single star model. Its value is expected to be around 1.0, and a threshold for "bad" solutions is usually recommended at 1.4. Both of these flags

<sup>13</sup> [https://gea.esac.esa.int/archive/documentation/GDR2/Catalogue\\_consolidation/chap\\_cu9val\\_cu9val/sec\\_cu9val\\_942/ssec\\_cu9val\\_942\\_dupl.html](https://gea.esac.esa.int/archive/documentation/GDR2/Catalogue_consolidation/chap_cu9val_cu9val/sec_cu9val_942/ssec_cu9val_942_dupl.html)

<sup>14</sup> <https://www.cosmos.esa.int/web/gaia/dr2-known-issues>, Astrometry Considerations section

are biased towards bright stars, and, due to the frequent use of small telescopes, occultation observers tend to favour these. The separation between problematic and non-problematic stars has clear effects on the difference distributions, as can be seen in Table 5.10;

- Most of the asteroid orbits may already be so well defined, that the subtle differences in the error models bring only small changes in the position for the time of event;
- Even within 10%, differences can be substantial, namely if both distances to the asteroid are quite large. This may hint at a problem with the astrometric solution of the occultation itself, rather than the models being used.

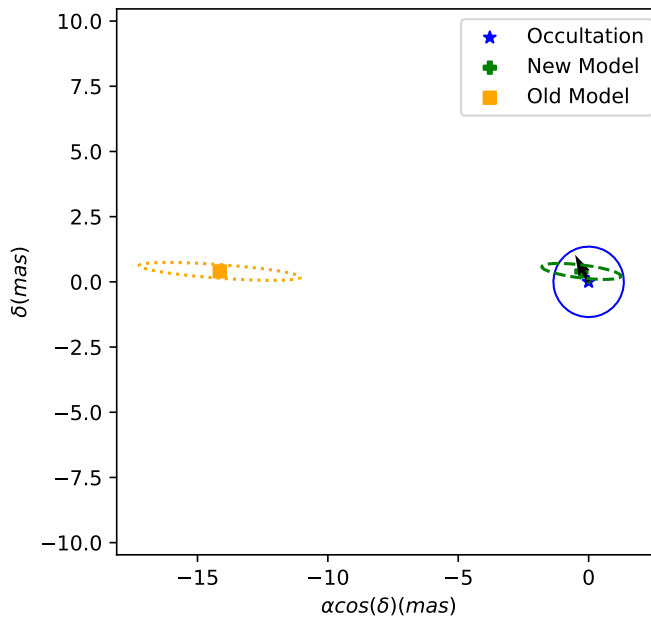


Figure 5.11: Example of event where TS20 greatly outperformed FV15, an occultation by (41) Daphne on 2012/02/23.

We also found some correlations between the differences and the asteroid's  $H_0$  magnitude, as well as the number of observations available and how the distance varies as a function of the diameter, seen in Figures 5.14, 5.15 and

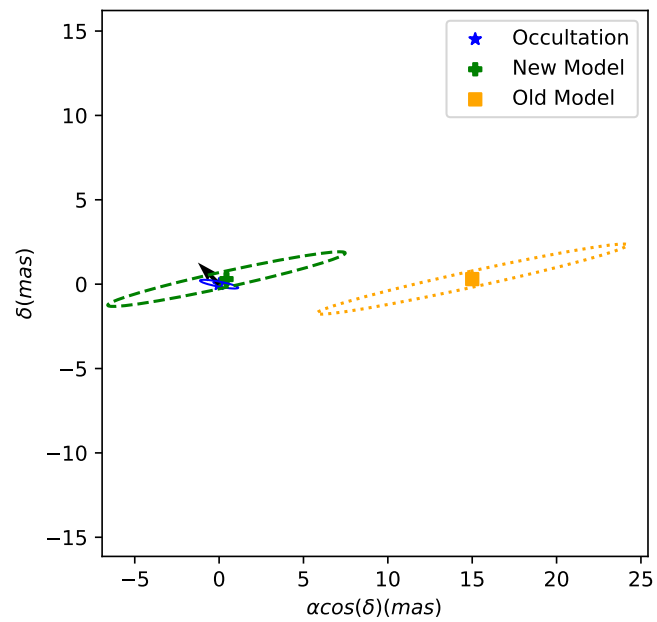


Figure 5.12: Example of event where TS20 greatly outperformed FV15, an occultation by (8 931) Hirokimatsuo on 2017/11/15.

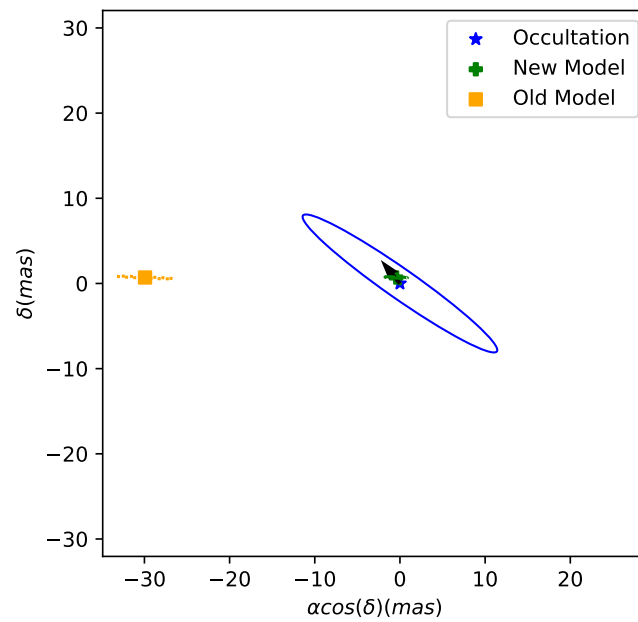


Figure 5.13: Example of event where TS20 greatly outperformed FV15, an occultation by (521) Brixia on 2011/05/27.

5.16; These correlations are to be expected, and are all connected to each other, as a larger absolute magnitude correlates with a larger diameter and brightness, making the target easier to observe, and therefore their observation database should be more complete, allowing for better orbits that are closer to the astrometric solution of the occultation.

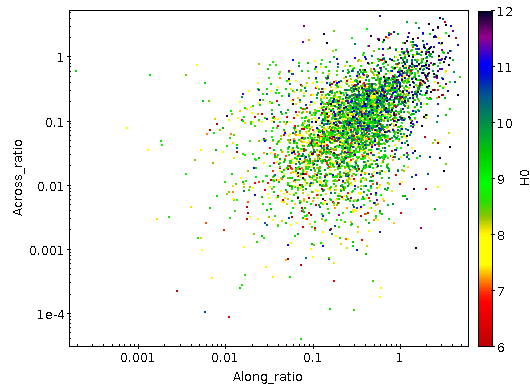


Figure 5.14: Correlation between Across and Along Track Differences (in units of diameter) and  $H_0$  magnitude of asteroid. There is a positive correlation, suggesting that the differences tend to be larger for larger magnitude asteroids, which correspond to smaller diameters.

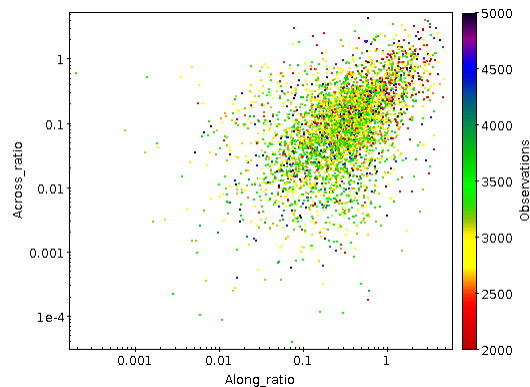


Figure 5.15: Same plot, but with Observations available for fit as auxiliary colour. There seems to be a negative correlation, as less observations can bring up the error, which is to be expected.

One important thing to check is whether the models applied create any biases on the observations. In this case, both models produced gaussian dif-

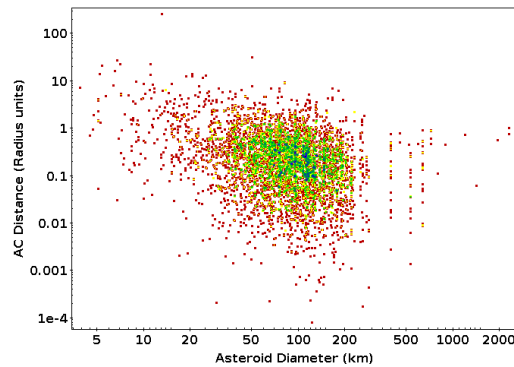


Figure 5.16: Density distribution of AC distance as a function of asteroid radius vs asteroid size, showing a negative correlation. Red means low density and green/blue high density.

ference distributions centred on 0, as seen in Figures 5.17 and 5.18, meaning none of them show any noticeable issues in this regard.

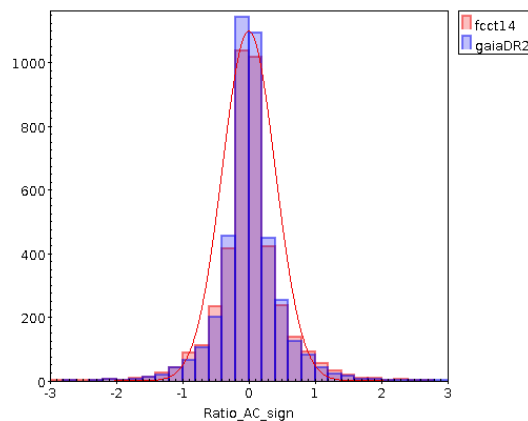


Figure 5.17: Distribution of difference to occultation solution in AC difference, in units of asteroid diameter. Both are centred on 0, and seem to display gaussian behaviour. Gaussian line is for illustration purposes.

## 5.4 Orbital Elements with Gaia

Once all of the required OrbFit files were gathered (see Appendix A for more details), a few examples were chosen to test the differences that result from

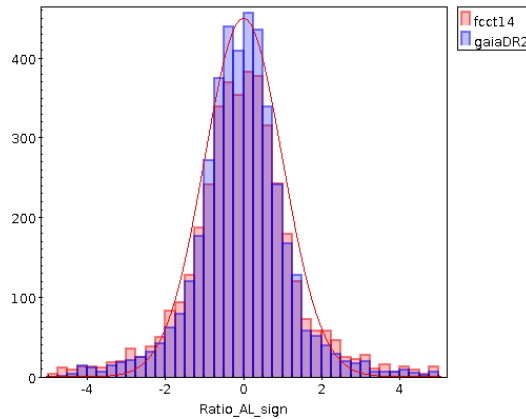


Figure 5.18: Similar plot to Figure 5.17, but for differences in AL direction. Once again, gaussian distributions centred in 0, meaning no biases are noticeable.

adding Gaia’s DR2 to the observations. For this, we chose asteroids with recent occultations, namely 2 targets observed in 2019:

1. (145) Adeona, observed on April 22<sup>nd</sup> 2019 with 17 positive chords and 2 negative;
2. (13 244) Dannymeyer on November 7<sup>nd</sup>, with only a single chord.

For each of these, a comparison was made between the astrometric solutions to the occultation, shared by Dave Herald in Occult, and to the MPC observations with and without Gaia data added.

This was done once with MPC data and once with MPC plus Gaia DR2. Once finished, the task was, once again, to check how far apart the orbital solutions were from the occultation, and whether Gaia improved the agreement between the single occultation and the rest of the data. Figures 5.19 and 5.20 show how far from the astrometric solution of the occultation we are by using or not Gaia data.

After this step, one last way of checking which of the solutions is better was to fit the position of each chord with and without Gaia, in order to not only see if the differences to the solution were consistent, but also to check if the shape was similar to the one in DAMIT, or the one constructed from the

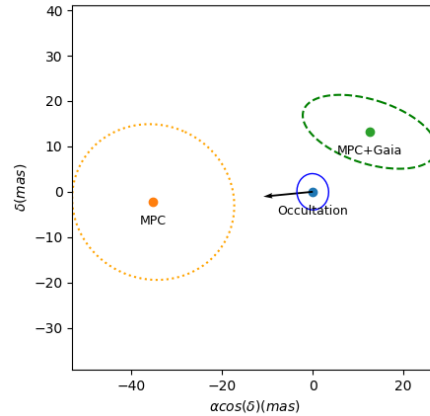


Figure 5.19: Astrometric solutions of (145) Adeona at the moment of its occultation. The origin of the plot is the position derived from the occultation, in blue. The ellipse is exaggerated, and corresponds to a 10-sigma region, and the arrow represents the velocity vector. To the left, in orange, is the fit with MPC data only. To the right, in green, the fit with MPC and Gaia combined.

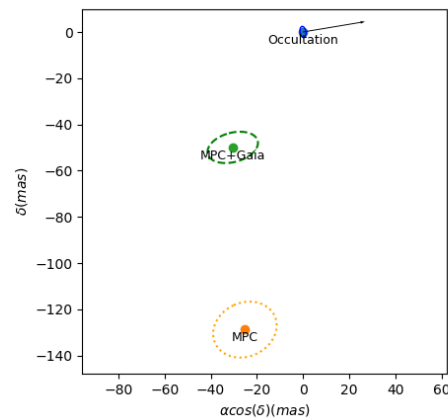


Figure 5.20: Plot similar to Figure 5.19 for (13 244) Dannymeyer, an asteroid with a single chord occultation on November 7<sup>th</sup> 2019. The discrepancy between the solutions is larger now, as this asteroid has not been observed as many times as (145) Adeona.

chords independently from this work, as exemplified in Figures 5.21<sup>15</sup>, 5.22<sup>16</sup>, 5.23<sup>17</sup> and 5.24<sup>18</sup>, where the (0,0) coordinate corresponds to the centre of mass coordinate of the occultation’s astrometric solution, and each triangle-circle-square sequence corresponds to a reported chord (triangle is start of chord, circle mid-point and square end). All shapes and orientations were consistent with those published in Euraster for these events. These events were chosen by looking at 2019 occultations to asteroids with shape models and with at least 5 positive chords.

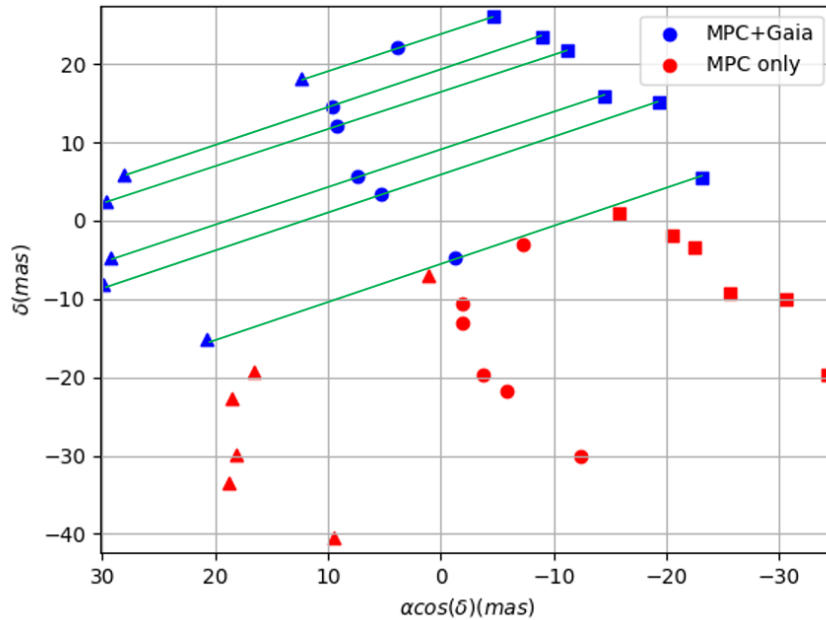


Figure 5.21: Shape solutions obtained with OrbFit for the (50) Virginia occultation. Adding Gaia data improves the agreement between orbital fit and occultation. Chords for MPC+Gaia solution show in green, to better illustrate what was observed.

In the cases of Figures 5.21 and 5.24, we see a clear improvement by adding Gaia data, while in Figures 5.22 and 5.23, the differences are marginal. This is possibly because the amount of Gaia observations are larger in the cases with

<sup>15</sup> <https://www.euraster.net/results/2019/index.html#0401-50>

<sup>16</sup> <https://www.euraster.net/results/2019/index.html#0422-145>

<sup>17</sup> <https://www.euraster.net/results/2019/index.html#0814-163>

<sup>18</sup> <https://www.euraster.net/results/2019/index.html#1012-118>

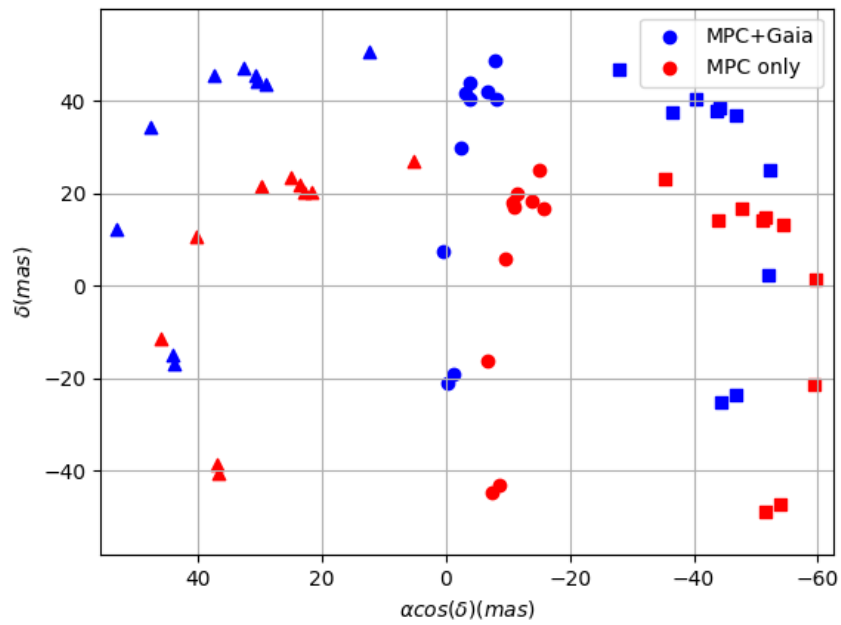


Figure 5.22: Shape solutions for (145) Adeona occultation. The orbital solution does not depend heavily on the Gaia observations, likely due to already good constraints prior to adding them, and so the results are similar.

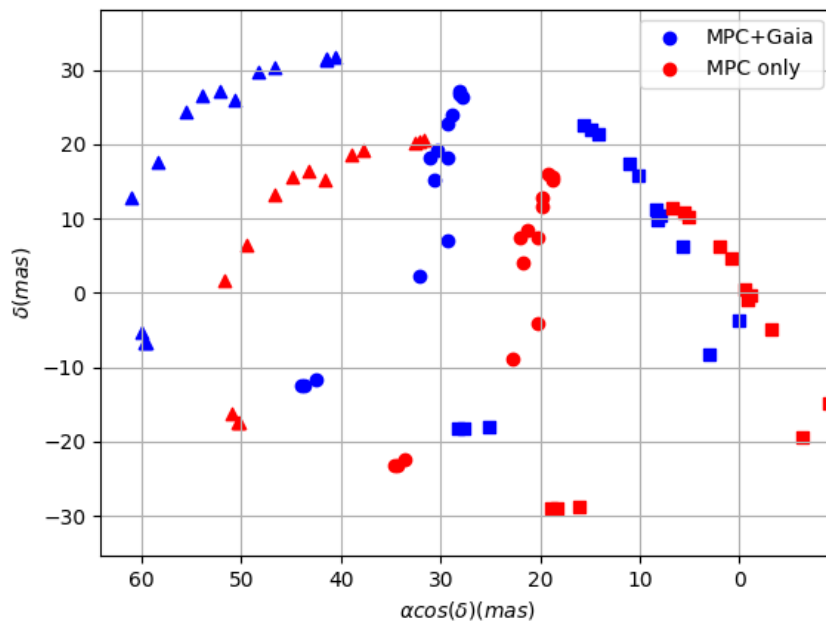


Figure 5.23: Shape solutions for (163) Erigone occultation. Once again, the orbit is relatively unchanged, with a noticeable deviation in RA from the occultation's solution.

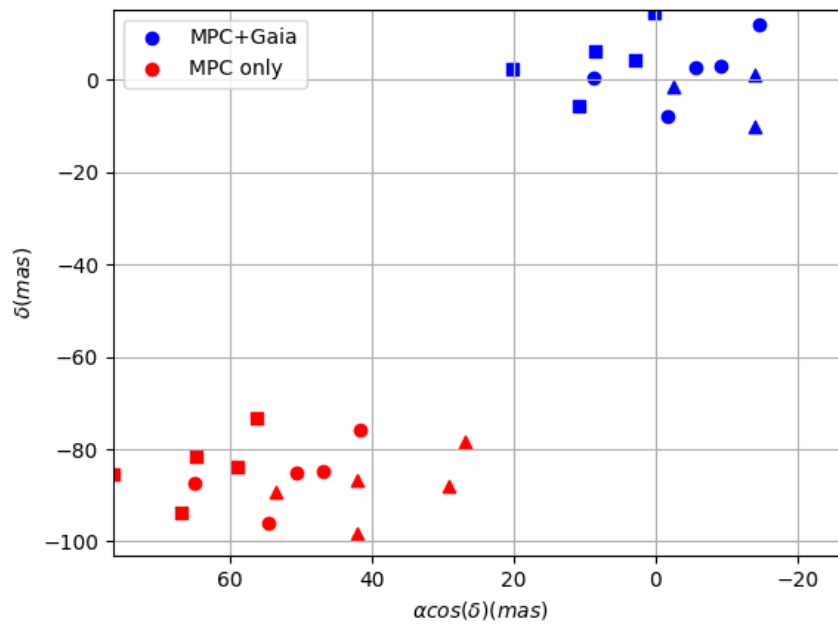


Figure 5.24: Shape solutions for (118) Peitho occultation. The most drastic change, in favour of adding Gaia data, with the difference going from almost 100 mas to less than 10 mas.

bigger improvement, or because in the marginal cases the orbit was already well established even before adding Gaia data.

### 5.4.1 Full Scale Run on DR2 Asteroids

These steps were made with some examples in order to prepare for a full-scale run, that would include all 14 099 asteroids present in DR2. A comparison was made between the FV15 and TS20 models as well. Figures 5.27 and 5.28 show us that the semi-major axis uncertainty consistently decreases by adding Gaia data, with greater decreases for larger distances, and Figure 5.29 shows that this happens for all asteroid sizes, with a noticeable increase in the improvement for larger sizes.

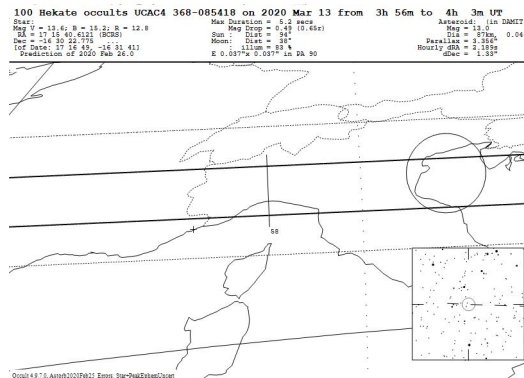


Figure 5.25: Prediction of occultation by (100) Hekate on March 13<sup>th</sup> 2020. The cross represents the site of observation at OCA. Using all MPC observations, but not Gaia, the across axis uncertainty is 37 mas, slightly smaller, but comparable, to the diameter of the object. The probability of a positive detection at our site was calculated at 33%. There were 3 009 observations to this asteroid in total, ranging from 1871 to 2020.

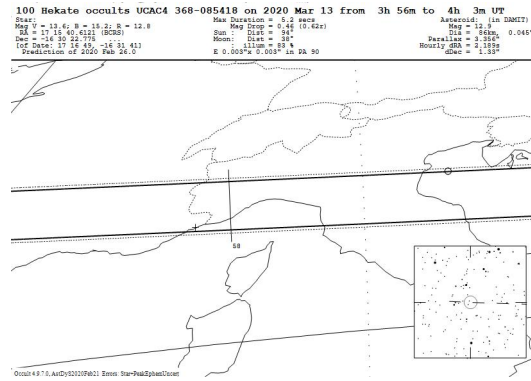


Figure 5.26: 113 observations by Gaia to (100) Hekate were added to the orbital fit. This causes a decrease on the across axis from 37 to 3 mas, our site is now inside the shadow path, and the probability raised to 91%.

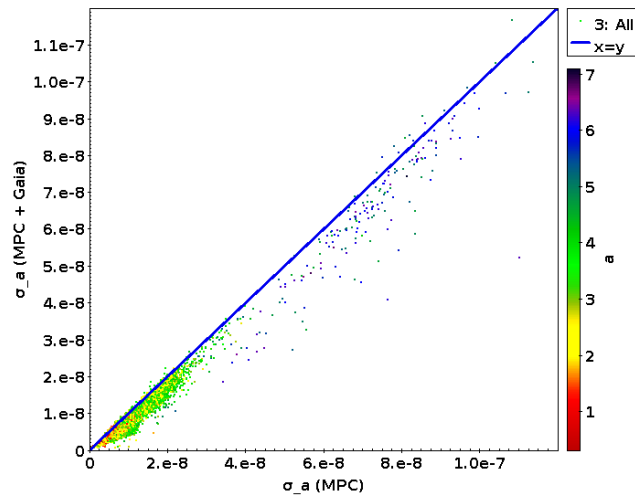


Figure 5.27: Comparison of semi-major axis uncertainty (in au) for the 14 099 asteroids in DR2 with and without Gaia data. Despite the limited number of observations (a few hundred among thousands, on average) and the small time frame of DR2 (22 months vs tens of years with other methods), there is a clear tendency for a drop of  $\sigma_a$ , with an average drop of  $\sim 17\%$ .

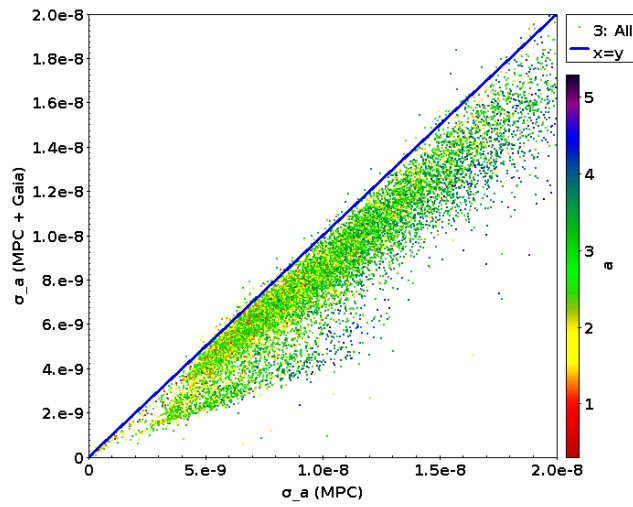


Figure 5.28: Zoomed in version of Figure 5.27, showing us that larger distances result in greater decreases, likely because these objects (Centaur) have less observations than MBA, giving Gaia a greater weight.

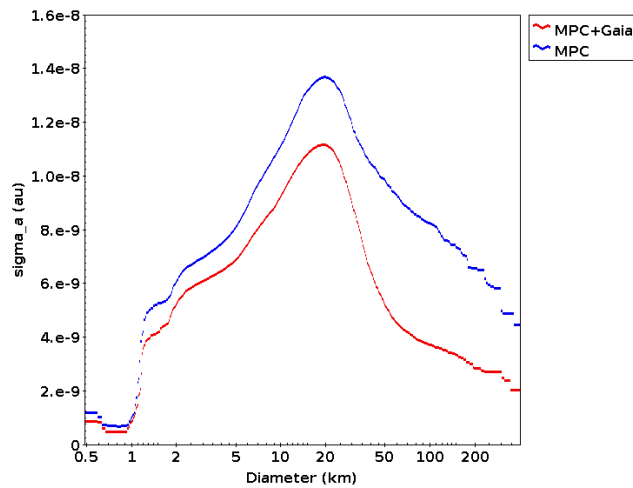


Figure 5.29: Smoothed average of semi-major axis uncertainty as a function of asteroid Diameter. We see that the uncertainty distribution lowers slightly when adding Gaia data across all sizes. For better visualization, TNO were excluded, due to their big size and semi-major axis uncertainty skewing the plot.



# Conclusions and Future Work

---

## Contents

---

<b>6.1</b>	<b>UniversCity and Robotic Telescopes . . . . .</b>	<b>177</b>
<b>6.2</b>	<b>Simulation of events . . . . .</b>	<b>178</b>
<b>6.3</b>	<b>Comparing astrometry: occultations and other sources</b>	<b>179</b>
<b>6.4</b>	<b>Future Work . . . . .</b>	<b>180</b>
6.4.1	Gaia DR3 and beyond . . . . .	180
6.4.2	Exploiting Single Chord Occultations . . . . .	181
6.4.3	NEA Events . . . . .	182

---

## 6.1 UniversCity and Robotic Telescopes

Thanks to the big leap in astrometry quality brought by Gaia (2 orders of magnitude compared to UCAC4), small and medium sized telescopes have gained a big number of viable events to observe. This viability will only increase with future data releases, not only because of the star catalogues, but because of the expected increase to the quality of asteroid orbits as well. For that reason, two strategies will become more important in the next coming years: having a team of telescopes that can be deployed for big missions to cover more ground, and having individual, robotic, telescopes that can observe and analyze several events per night. Given the cheaper nature of the second option, it should be expected to see more robotic telescopes being built for the purpose of stellar occultations. UniversCity is one of them, and once it starts working, it will be exploited according to the expected limitations, once these are verified through observations.

Since UniversCity is being built specifically for occultations, we can expect its use time to go entirely towards our field. Not accounting for poor weather conditions, I find that it will be able to observe an average of 1 viable event per night with a probability of positive detection at or above 10%, one of the typical thresholds for planned observations, a number which doubles if we go down to 5%. Such output requires automated procedures, so as to not need to have to allocate manpower to observations every night.

## 6.2 Simulation of events

Given the telescope/camera system expected for UniversCity, it was found that the limiting magnitude to reliably detect a star source at 0.1 s of exposure time should be between 13.5 and 14. This can be stretched further by increasing the exposure time, at the cost of losing timing and duration precision. Going from 0.1 to 0.5 s, for example, should allow us to see events up to magnitude 16, as long as these last longer than a fraction of a second.

By setting up and making simulations for the limit situations expected for UniversCity, we found that the performance is highly dependent on the Drop-to-Noise ratio, and less dependent on the amount of points inside the occultation. And even for most of these events, we obtained sub-sampling time precision for the timing and duration. Considering most observers report their sampling time as the precision of the event, this would represent an improvement in the majority of the reports.

It was also found that using gaussian priors, accounting for the typical uncertainties associated to predictions, helps the Bayesian Inference Method perform better than uniform priors. In particular, the uniform priors could not converge towards a unique solution 6% of the time, while gaussian priors always did. It was also found that the gaussian priors compared better with false positive signals.

The BIM also performed better than the previously used Least Squares Fit for the same light curves. Comparing it with another bayesian tool, PyOTE, showed that the BIM through the use of DIAMONDS is more user friendly, and can obtain similar results.

Finally, applying the BIM to 25 real cases showed that the sub-sampling

time precision is real, and usually an improvement upon the reported events. A mass application to past light curves could be of interest.

The practical limits expected for the use of the UniversCity telescope were:

- Magnitude 13.5 for the star;
- Duration of at least 2 sample times;
- A Drop-to-Noise Ratio (DNR) of at least 2 to get reliable sub-sample time uncertainties.

It was also found that, under these conditions, we would achieve sub-mas precision for single-chord events, with the possibility to observe hundreds of events per year, and accounting for the AL error model.

### **6.3 Comparing astrometry: occultations and other sources**

Regarding the work done in astrometry exploitation, we found that, even with a limited amount of data for asteroids in DR2, compared to the expected results in the future, we can already notice a decrease in the semi-major axis uncertainty by  $\sim 20\%$ , this being one of the commonly used indicators of the quality of an orbital fit. By adding Gaia data, the across track uncertainties of the events also improve by a big margin, though there is still work to be done before this can be fully incorporated in the commonly used prediction tools, namely making sure that the Gaia and other MPC observations don't skew the rejection rates, and checking which error model is the most appropriate to use.

Regarding the comparison of error models, encompassing a new debiasing and a new data weighting (FV15 [Farnocchia et al., 2015, Vereš et al., 2017] vs TS20, in prep.), using the full stellar occultation archive as a sample, thanks to the generally good astrometric precision of occultations, showed that the two models have a similar performance for about half of the events. The new model improved the performance for a much larger portion of the rest, with all the statistics regarding the distance between model and occultation improving

when compared to [Farnocchia et al., 2015]. These results will be published in an article, currently under preparation.

Finally, the build of a Gaia catalogue of stars up to magnitude 15.5 compatible with the Occult predictions tool allowed the increase in the number of target stars by a factor of  $\sim 5$  compared to the most common Gaia14 catalogue, which in turn allowed for a greater set of viable candidate events for specific objects of interest, such as NEA or TNO. The developer of Occult, Dave Herald, created a tool that would, from queries made to Gaia, join all resulting query object lists in a large bin file that could be used for predictions. For this end, we queried Gaia for stars up to magnitude 15.5 that had a good RUWE value. It is recommended that we use stars for which this value is lower than 1.4. This, combined with the limit of 3 million results per individual query and the limitations of the Occult tool, forced us to do queries for bands of 2 degrees in declination (the smallest regular band that the Occult tool can safely use to merge lists), until the whole catalogue had been queried. This gave us a base of about 87 million stars, approximately five times larger than the standard Gaia14.

## 6.4 Future Work

Due to the ongoing work of Gaia, and a quickly changing landscape in the field of stellar occultations, several perspectives on continuing the work of this thesis are likely. Here are listed the main possibilities.

### 6.4.1 Gaia DR3 and beyond

As mentioned throughout this work, Gaia will have further data releases. An early version of DR3 is expected by the end of the year, barring any delay, and won't bring any change in the Solar System field, being of use mostly thanks to another improvement in the star catalogue, still useful for occultations. The full DR3, on the other hand, was expected in 2021, but due to the global pandemic, this date was pushed to the first half of 2022. DR3 would bring not only an increase by 1 order of magnitude to the number of solar-system objects present, but also a quality improvement, due to the fact that, for most MBA the DR3 time scale (34 months) will encompass the majority of their orbital

period. Future data releases are expected to provide a final list with  $\sim 300\,000$  objects and 2 full orbital periods for the MBA which, with Gaia's precision, should give us unprecedented accuracy in their orbits. Further improvements to the star catalogue, mainly in the proper motion uncertainties, will also help push the limits of occultations to even shorter, fainter events. As of right now, no further Data Release dates have been announced, though DR4 should only happen a few years after DR3, and even more planned before the final release due to the mission extension of Gaia until 2020, possibly 2022.

### 6.4.2 Exploiting Single Chord Occultations

As mentioned in Chapter 5, the majority of occultations are single-chord, bringing ambiguities to the asteroid's position. The solution taken is to assume that the chord is central, and the AC uncertainty is 40% of the Diameter, with the AL uncertainty also following a rule, rather than being specific to each event. Thus, there is room for an exploitation of these events to try to improve their astrometry.

A new approach planned for these "poor" events would be to split the occultation fit in two distinct possibilities, each one centered in the estimated position of the object's diameter. Then, both fits would be fed to an orbital fit tool, and the one that fit best would be accepted as the true position of the asteroid, while the worse fit would be discarded. An example of this approach, made for TNO, can be seen in [Rommel et al., 2020].

This done to a full scale would access to data on every single chord occultation, as well as every multi-chord occultation with poor astrometric solutions, due either to bad conditions or close proximity of chords.

Assuming a circular projection and a known diameter and chord length, we could determine the distance from the chord centre to the model circumference centre of both fits, adding the value to the chord centre position in one side, and subtracting in the other, as can be seen in Equation 6.1, where  $\rho$  is the distance,  $D$  is the object's Diameter and  $L$  the chord's length:

$$\rho = \sqrt{(D)^2 - (L)^2}/2 \quad (6.1)$$

This distance is an oriented shift producing two possible astrometric posi-

tions, on opposite sides of the chord.

By having this duplicate list of solutions, the goal would be to use OrbFit to check which of the two options would best fit the orbital solution and, once this was determined, if adding the best solution would improve the orbit compared to the current standard of Dave Herald.

### 6.4.3 NEA Events

By the end of the Full Scale run on DR2 asteroids, we had built a database that could generate improved predictions to all events involving DR2 asteroids, and the differences between predictions with and without DR2 allowed tests to be made that would verify the validity of this database. Despite the limited time-span of DR2 for asteroid standards, we can see some progress made in the semi-major axis uncertainty, as can be seen in Figure 5.27

The necessary precision to start detecting the Yarkovsky effect varies with the asteroid's size, but a threshold used, for example, for asteroids smaller than 3 km is  $\sigma_a < 2 * 10^{-9}$  au [Greenstreet et al., 2019], and the amount of objects below these diameter and semi-major axis uncertainties go from 1 to 24, giving us 23 new objects that could be studied for the Yarkovsky effect, a good indicator for future Gaia Data Releases with much more extensive asteroid data [Spoto et al., 2019].

The work made with DR2 asteroids and OrbFit made possible a transition into the study of NEA. As part of the DART and HERA missions, with the end goal of a space mission to the NEA (65 803) Didymos, we built a database of other promising NEA for occultations in the near-to-mid future.

For this end, we queried MPCORB for all NEA, searching for any numbered asteroid with a semi-major axis  $a < 1.3$  au, which gave us 580 potential targets. A second query was made, this time to AstDyS-2, in order to obtain the orbital elements and respective uncertainties for each asteroid. A quality filter check ( $\sigma_a < 4 * 10^{-9}$  au) cut the number of targets to 70 (see Table 6.1 for the best NEA regarding  $\sigma_a$ ). A run was made on OrbFit to propagate their orbital elements and obtain the peak ephemeris uncertainty (PEU) value, necessary to run Occult with them.

With the NEA list complete, we could now search for interesting events. But the DR2 catalogue present in Occult, Gaia14, is limited to magnitude 14,

which can be quite limiting for such a short list. Some available catalogues go further (UCAC5, for example), but at the cost of worse precision. For that purpose, we built the Gaia15.5 catalogue. Thanks to it, even the short list of NEA could give several interesting prospects for observation in the near-future.

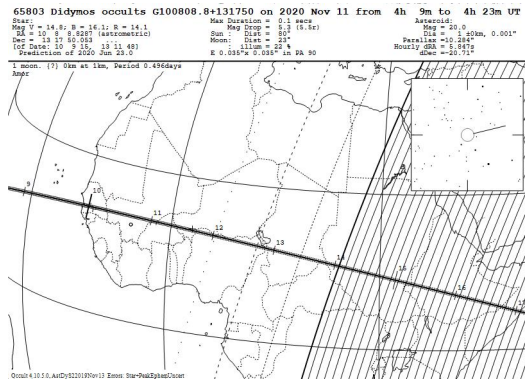


Figure 6.1: Example of occultation short term prediction of (65 803) Didymos obtained using Occult with the Gaia15.5 catalogue built for this work.

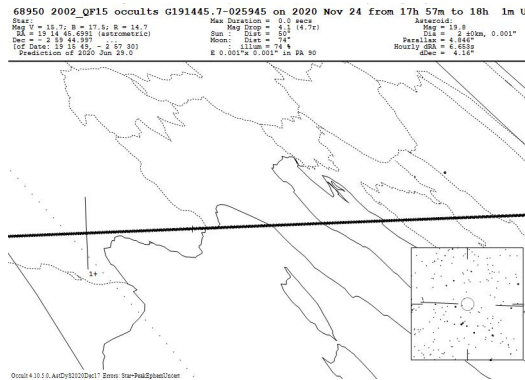


Figure 6.2: Another example, with one of the best NEA in terms of orbital precision, (68 950) 2002 QF15, theoretically visible at Calern. AC uncertainty of 15 mas.

This sort of work for NEA has already been applied for (3 200) Phaethon, resulting in predictions that allowed several observations in 2019, including the one analyzed in Chapter 4.



# Bibliography

James Baer, Steven R. Chesley, and Robert D. Matson. Astrometric Masses of 26 Asteroids and Observations on Asteroid Porosity. *Astrophysical Journal*, 141(5):143, May 2011. doi: 10.1088/0004-6256/141/5/143. (Cited on pages 15 and 38.)

F. Braga-Ribas, B. Sicardy, J. L. Ortiz, C. Snodgrass, F. Roques, R. Vieira-Martins, J. I. B. Camargo, M. Assafin, R. Duffard, E. Jehin, J. Pollock, R. Leiva, M. Emilio, D. I. Machado, C. Colazo, E. Lellouch, J. Skottfelt, M. Gillon, N. Ligier, L. Maquet, G. Benedetti-Rossi, A. R. Gomes, P. Kervella, H. Monteiro, R. Sfair, M. El Moutamid, G. Tancredi, J. Spagnotto, A. Maury, N. Morales, R. Gil-Hutton, S. Roland, A. Ceretta, S.-H. Gu, X.-B. Wang, K. Harpsøe, M. Rabus, J. Manfroid, C. Opitom, L. Vanzi, L. Mehret, L. Lorenzini, E. M. Schneiter, R. Melia, J. Lecacheux, F. Colas, F. Vachier, T. Widemann, L. Almenares, R. G. Sandness, F. Char, V. Perez, P. Lemos, N. Martinez, U. G. Jørgensen, M. Dominik, F. Roig, D. E. Reichart, A. P. Lacluyze, J. B. Haislip, K. M. Ivarsen, J. P. Moore, N. R. Frank, and D. G. Lambas. A ring system detected around the Centaur (10199) Chariklo. *Nature*, 508:72–75, April 2014. doi: 10.1038/nature13155. (Cited on pages 17, 50, 57, 58 and 59.)

J. L. Elliot. Stellar occultation studies of the solar system. *Annual Review of Astronomy and Astrophysics*, 17:445–475, January 1979. doi: 10.1146/annurev.aa.17.090179.002305. (Cited on pages 17 and 59.)

E. Høg. Astrometry Lost and Regained. *Baltic Astronomy*, 20:221–230, January 2011. doi: 10.1515/astro-2017-0286. (Cited on pages 17 and 64.)

Gaia Collaboration, F. Spoto, P. Tanga, F. Mignard, J. Berthier, B. Carry, A. Cellino, A. Dell’Oro, D. Hestroffer, K. Muinonen, and et al. Gaia Data Release 2. Observations of solar system objects. *Astronomy & Astrophysics*, 616:A13, August 2018a. doi: 10.1051/0004-6361/201832900. (Cited on pages 18, 63, 66, 67 and 144.)

- Erin Lee Ryan and Charles E. Woodward. Rectified Asteroid Albedos and Diameters from IRAS and MSX Photometry Catalogs. *The Astronomical Journal*, 140(4):933–943, October 2010. doi: 10.1088/0004-6256/140/4/933. (Cited on pages 21 and 100.)
- Joseph R. Masiero, A. K. Mainzer, T. Grav, J. M. Bauer, R. M. Cutri, J. Dailey, P. R. M. Eisenhardt, R. S. McMillan, T. B. Spahr, M. F. Skrutskie, D. Tholen, R. G. Walker, E. L. Wright, E. DeBaun, D. Elsbury, IV Gautier, T., S. Gomillion, and A. Wilkins. Main Belt Asteroids with WISE/NEOWISE. I. Preliminary Albedos and Diameters. *Astrophysical Journal*, 741(2):68, November 2011. doi: 10.1088/0004-637X/741/2/68. (Cited on pages 21, 44 and 100.)
- Peter Vereš, Davide Farnocchia, Steven R. Chesley, and Alan B. Chamberlin. Statistical analysis of astrometric errors for the most productive asteroid surveys. *Icarus*, 296:139–149, November 2017. doi: 10.1016/j.icarus.2017.05.021. (Cited on pages 34, 144, 146, 147, 154, 179 and 199.)
- Jana Tichá, Brian G. Marsden, Daniel Green, Rita M. Schulz, Michael F. A’Hearn, Julio A. Fernandez, Pamela Kilmartin, Daniela Lazzaro, Syuichi Nakano, Keith S. Noll, Lutz D. Schmadel, Viktor A. Shor, Gareth V. Williams, Donald K. Yeomans, and Jin Zhu. Division III / Wg: Committee Small Bodies Nomenclature. *Transactions of the International Astronomical Union, Series B*, 3(26B):118–119, December 2007. doi: 10.1017/S1743921308023776. (Cited on page 38.)
- F. E. DeMeo, C. M. O’D. Alexander, K. J. Walsh, C. R. Chapman, and R. P. Binzel. *The Compositional Structure of the Asteroid Belt*, pages 13–41. Asteroids IV, 2015. doi: 10.2458/azu\_uapress\_9780816532131-ch002. (Cited on page 38.)
- J. Desmars, J. I. B. Camargo, F. Braga-Ribas, R. Vieira-Martins, M. Asafin, F. Vachier, F. Colas, J. L. Ortiz, R. Duffard, N. Morales, B. Sicardy, A. R. Gomes-Júnior, and G. Benedetti-Rossi. Orbit determination of trans-Neptunian objects and Centaurs for the prediction of stellar occultations. *Astronomy & Astrophysics*, 584:A96, December 2015. doi: 10.1051/0004-6361/201526498. (Cited on pages 43, 50 and 60.)

- B. Carry. Solar system science with ESA Euclid. *Astronomy & Astrophysics*, 609:A113, January 2018. doi: 10.1051/0004-6361/201730386. (Cited on page 44.)
- Jun'ichiro Kawaguchi, Akira Fujiwara, and Tono Uesugi. Hayabusa—Its technology and science accomplishment summary and Hayabusa-2. *Acta Astronautica*, 62(10):639–647, May 2008. doi: 10.1016/j.actaastro.2008.01.028. (Cited on page 44.)
- Yuichi Tsuda, Makoto Yoshikawa, Masanao Abe, Hiroyuki Minamino, and Satoru Nakazawa. System design of the Hayabusa 2—Asteroid sample return mission to 1999 JU3. *Acta Astronautica*, 91:356–362, October 2013. doi: 10.1016/j.actaastro.2013.06.028. (Cited on page 44.)
- Dante S. Laretta. *OSIRIS-REx Asteroid Sample-Return Mission*, pages 543–567. Handbook of Cosmic Hazards and Planetary Defense, 2015. doi: 10.1007/978-3-319-03952-7\_44. (Cited on page 44.)
- Marc W. Buie, Amanda M. Zangari, Simone Marchi, Harold F. Levison, and Stefano Mottola. Light Curves of Lucy Targets: Leucus and Polymele. *Astrophysical Journal*, 155(6):245, June 2018. doi: 10.3847/1538-3881/aabd81. (Cited on page 44.)
- Andrew F. Cheng, Andrew S. Rivkin, Patrick Michel, Justin Atchison, Olivier Barnouin, Lance Benner, Nancy L. Chabot, Carolyn Ernst, Eugene G. Fahnestock, Michael Kueppers, Petr Pravec, Emma Rainey, Derek C. Richardson, Angela M. Stickle, and Cristina Thomas. AIDA DART asteroid deflection test: Planetary defense and science objectives. *Planetary Space Science*, 157:104–115, August 2018. doi: 10.1016/j.pss.2018.02.015. (Cited on page 45.)
- Derek Sears, Carl Allen, Dan Britt, Don Brownlee, Melissa Franzen, Leon Gefert, Stephen Gorovan, Carle Pieters, Jeffrey Preble, Dan Scheeres, and Ed Scott. The Hera mission: multiple near-earth asteroid sample return. *Advances in Space Research*, 34(11):2270–2275, January 2004. doi: 10.1016/j.asr.2003.05.059. (Cited on page 45.)

- Bruno Victorino Sarli, Makoto Horikawa, Chit Hong Yam, Yasuhiro Kawakatsu, and Takayuki Yamamoto. DESTINY+ Trajectory Design to (3200) Phaethon. *Journal of the Astronautical Sciences*, 65(1):82–110, March 2018. doi: 10.1007/s40295-017-0117-5. (Cited on page 45.)
- Clara Maurel, Patrick Michel, J. Michael Owen, Richard P. Binzel, Megan Bruck-Syal, and G. Libourel. Simulations of high-velocity impacts on metal in preparation for the Psyche mission. *Icarus*, 338:113505, March 2020. doi: 10.1016/j.icarus.2019.113505. (Cited on page 45.)
- G. E. Taylor. An Occultation by a Minor Planet. *Monthly Notes of the Astronomical Society of South Africa*, 11:33T, January 1952. (Cited on page 46.)
- D. S. Evans and J. Van B. Lourens. An Occultation of a Star by Pallas. *Monthly Notes of the Astronomical Society of South Africa*, 20:134, January 1961. (Cited on page 46.)
- Edwin B. Weston, Brian G. Marsden, and Brian O’Leary. The Occultation of Kappa Geminorum by Eros - A Learning Experience. *Journal of the American Association of Variable Star Observers (JAAVSO)*, 4(1):34, January 1975. (Cited on page 47.)
- M. Perryman. The history of astrometry. *European Physical Journal H*, 37:745–792, October 2012. doi: 10.1140/epjh/e2012-30039-4. (Cited on pages 47 and 62.)
- F. Colas, E. Frappa, J. Lecacheux, J. Berthier, F. Vachier, and L. Maquet. Euraster an European Network for Asteroid Stellar Occultations. In *EPSC-DPS Joint Meeting 2011*, page 1538, October 2011. (Cited on pages 47 and 62.)
- D. W. Dunham, E. Goffin, J. Manek, M. Federspiel, R. Stone, and W. Owen. Asteroidal occultation results multiply helped by Hipparcos. *Mem. Societa Astronomica Italiana*, 73:662, September 2002. (Cited on pages 47 and 62.)
- P. Tanga and M. Delbo. Asteroid occultations today and tomorrow: toward the GAIA era. *Astronomy & Astrophysics*, 474:1015–1022, November 2007. doi: 10.1051/0004-6361:20077470. (Cited on pages 47 and 73.)

- J. L. Ortiz, P. Santos-Sanz, B. Sicardy, G. Benedetti-Rossi, D. Bérard, N. Morales, R. Duffard, F. Braga-Ribas, U. Hopp, C. Ries, V. Nascimbene, F. Marzari, V. Granata, A. Pál, C. Kiss, T. Pribulla, R. Komžík, K. Hornoch, P. Pravec, P. Bacci, M. Maestripieri, L. Nerli, L. Mazzei, M. Bachini, F. Martinelli, G. Succi, F. Ciabattari, H. Mikuz, A. Carbognani, B. Gaehrken, S. Mottola, S. Hellmich, F. L. Rommel, E. Fernández-Valenzuela, A. Campo Bagatin, S. Cikota, A. Cikota, J. Lecacheux, R. Vieira-Martins, J. I. B. Camargo, M. Assafin, F. Colas, R. Behrend, J. Desmars, E. Meza, A. Alvarez-Candal, W. Beisker, A. R. Gomes-Junior, B. E. Morgado, F. Roques, F. Vachier, J. Berthier, T. G. Mueller, J. M. Madiedo, O. Unsalan, E. Sonbas, N. Karaman, O. Erece, D. T. Koseoglu, T. Ozisik, S. Kalkan, Y. Guney, M. S. Niaei, O. Satir, C. Yesilyaprak, C. Puskullu, A. Kabas, O. Demircan, J. Alikakos, V. Charmandaris, G. Leto, J. Ohlert, J. M. Christille, R. Szakáts, A. Takácsné Farkas, E. Varga-Verebélyi, G. Marton, A. Marciniak, P. Bartczak, T. Santana-Ros, M. Butkiewicz-Bąk, G. Dudziński, V. Alí-Lagoa, K. Gazeas, L. Tzouganatos, N. Paschalis, V. Tsamis, A. Sánchez-Lavega, S. Pérez-Hoyos, R. Hueso, J. C. Guirado, V. Peris, and R. Iglesias-Marzoa. The size, shape, density and ring of the dwarf planet Haumea from a stellar occultation. *Nature*, 550(7675):219–223, October 2017. doi: 10.1038/nature24051. (Cited on pages 50, 57 and 59.)
- J. Durech, B. Carry, M. Delbo, M. Kaasalainen, and M. Viikinkoski. *Asteroid Models from Multiple Data Sources*, pages 183–202. Michel, P. and DeMeo, F. E. and Bottke, W. F., 2015. doi: 10.2458/azu\_uapress\_9780816532131-ch010. (Cited on pages 54 and 60.)
- B. Sicardy, T. Widemann, E. Lellouch, C. Veillet, J.-C. Cuillandre, F. Colas, F. Roques, W. Beisker, M. Kretlow, A.-M. Lagrange, E. Gendron, F. Lacombe, J. Lecacheux, C. Birnbaum, A. Fienga, C. Leyrat, A. Maury, E. Raynaud, S. Renner, M. Schultheis, K. Brooks, A. Delsanti, O. R. Hainaut, R. Gilmozzi, C. Lidman, J. Spyromilio, M. Rapaport, P. Rosenzweig, O. Naranjo, L. Porras, F. Díaz, H. Calderón, S. Carrillo, A. Carvajal, E. Recalde, L. G. Cavero, C. Montalvo, D. Barría, R. Campos, R. Duffard, and H. Levato. Large changes in Pluto’s atmosphere as revealed by recent stellar

- occultations. *Nature*, 424:168–170, July 2003. doi: 10.1038/nature01766. (Cited on pages 57 and 59.)
- D. Farnocchia, S. R. Chesley, D. Vokrouhlický, A. Milani, F. Spoto, and W. F. Bottke. Near Earth Asteroids with measurable Yarkovsky effect. *Icarus*, 224(1):1–13, May 2013. doi: 10.1016/j.icarus.2013.02.004. (Cited on pages 59 and 60.)
- Federica Spoto, Andrea Milani, and Zoran Knezevic. Asteroid family ages. *arXiv:1504.05461 [astro-ph]*, April 2015. URL <http://arxiv.org/abs/1504.05461>. arXiv: 1504.05461. (Cited on page 59.)
- J. L. Ortiz, B. Sicardy, J. I. B. Camargo, P. Santos-Sanz, and F. Braga-Ribas. Stellar Occultations by Transneptunian objects: from Predictions to Observations and Prospects for the Future. *arXiv e-prints*, art. arXiv:1905.04335, May 2019. (Cited on page 59.)
- B. Sicardy, J. L. Ortiz, M. Assafin, E. Jehin, A. Maury, E. Lellouch, R. G. Hutton, F. Braga-Ribas, F. Colas, D. Hestroffer, J. Lecacheux, F. Roques, P. Santos-Sanz, T. Widemann, N. Morales, R. Duffard, A. Thirouin, A. J. Castro-Tirado, M. Jelínek, P. Kubánek, A. Sota, R. Sánchez-Ramírez, A. H. Andrei, J. I. B. Camargo, D. N. da Silva Neto, A. R. Gomes, R. V. Martins, M. Gillon, J. Manfroid, G. P. Tozzi, C. Harlinton, S. Saravia, R. Behrend, S. Mottola, E. G. Melendo, V. Peris, J. Fabregat, J. M. Madiedo, L. Cuesta, M. T. Eibe, A. Ullán, F. Organero, S. Pastor, J. A. de Los Reyes, S. Pedraz, A. Castro, I. de La Cueva, G. Muler, I. A. Steele, M. Cebrián, P. Montañés-Rodríguez, A. Oscoz, D. Weaver, C. Jacques, W. J. B. Corradi, F. P. Santos, W. Reis, A. Milone, M. Emilio, L. Gutiérrez, R. Vázquez, and H. Hernández-Toledo. A Pluto-like radius and a high albedo for the dwarf planet Eris from an occultation. *Nature*, 478:493–496, October 2011. doi: 10.1038/nature10550. (Cited on page 59.)
- E. Meza, B. Sicardy, M. Assafin, J. L. Ortiz, T. Bertrand, E. Lellouch, J. Desmars, F. Forget, D. Bérard, A. Doressoundiram, J. Lecacheux, J. Marques Oliveira, F. Roques, T. Widemann, F. Colas, F. Vachier, S. Renner, R. Leiva, F. Braga-Ribas, G. Benedetti-Rossi, J. I. B. Camargo, A. Dias-Oliveira, B. Morgado, A. R. Gomes-Júnior, R. Vieira-Martins,

- R. Behrend, A. Castro Tirado, R. Duffard, N. Morales, P. Santos-Sanz, M. Jelínek, R. Cunniffe, R. Querel, M. Harnisch, R. Jansen, A. Pennell, S. Todd, V. D. Ivanov, C. Opitom, M. Gillon, E. Jehin, J. Manfroid, J. Pollock, D. E. Reichart, J. B. Haislip, K. M. Ivarsen, A. P. LaCluyze, A. Maury, R. Gil-Hutton, V. Dhillon, S. Littlefair, T. Marsh, C. Veillet, K.-L. Bath, W. Beisker, H.-J. Bode, M. Kretlow, D. Herald, D. Gault, S. Kerr, H. Pavlov, O. Faragó, O. Klös, E. Frappa, M. Lavayssière, A. A. Cole, A. B. Giles, J. G. Greenhill, K. M. Hill, M. W. Buie, C. B. Olkin, E. F. Young, L. A. Young, L. H. Wasserman, M. Devogèle, R. G. French, F. B. Bianco, F. Marchis, N. Brosch, S. Kaspi, D. Polishook, I. Manulis, M. Ait Moulay Larbi, Z. Benkhaldoun, A. Daassou, Y. El Azhari, Y. Moulane, J. Broughton, J. Milner, T. Dobosz, G. Bolt, B. Lade, A. Gilmore, P. Kilmartin, W. H. Allen, P. B. Graham, B. Loader, G. McKay, J. Talbot, S. Parker, L. Abe, P. Bendjoya, J.-P. Rivet, D. Vernet, L. Di Fabrizio, V. Lorenzi, A. Magazzù, E. Molinari, K. Gazeas, L. Tzouganatos, A. Carbognani, G. Bonnoli, A. Marchini, G. Leto, R. Zanmar Sanchez, L. Mancini, B. Kattentidt, M. Dohrmann, K. Guhl, W. Rothe, K. Walzel, G. Wortmann, A. Eberle, D. Hampf, J. Ohlert, G. Krannich, G. Murawsky, B. Gährken, D. Gloistein, S. Alonso, A. Román, J.-E. Communal, F. Jabet, S. de Visscher, J. Sérot, T. Janik, Z. Moravec, P. Machado, A. Selva, C. Perelló, J. Rovira, M. Conti, R. Papini, F. Salvaggio, A. Noschese, V. Tsamis, K. Tigani, P. Barroy, M. Irzyk, D. Neel, J. P. Godard, D. Lanoiselée, P. Sogorb, D. Vérilhac, M. Bretton, F. Signoret, F. Ciabattari, R. Naves, M. Boutet, J. De Queiroz, P. Lindner, K. Lindner, P. Enskonatus, G. Dangl, T. Tordai, H. Eichler, J. Hattenbach, C. Peterson, L. A. Molnar, and R. R. Howell. Pluto's lower atmosphere and pressure evolution from ground-based stellar occultations, 1988-2016. *arXiv e-prints*, March 2019. (Cited on page 59.)
- B. Sicardy, J. Talbot, E. Meza, J. I. B. Camargo, J. Desmars, D. Gault, D. Herald, S. Kerr, H. Pavlov, F. Braga-Ribas, M. Assafin, G. Benedetti-Rossi, A. Dias-Oliveira, A. R. Gomes-Júnior, R. Vieira-Martins, D. Bérard, P. Kervella, J. Lecacheux, E. Lellouch, W. Beisker, D. Dunham, M. Jelínek, R. Duffard, J. L. Ortiz, A. J. Castro-Tirado, R. Cunniffe, R. Querel, P. C. Yock, A. A. Cole, A. B. Giles, K. M. Hill, J. P. Beaulieu, M. Harnisch,

- R. Jansen, A. Pennell, S. Todd, W. H. Allen, P. B. Graham, B. Loader, G. McKay, J. Milner, S. Parker, M. A. Barry, J. Bradshaw, J. Broughton, L. Davis, H. Devillepoix, J. Drummond, L. Field, M. Forbes, D. Giles, R. Glassey, R. Groom, D. Hooper, R. Horvat, G. Hudson, R. Idaczyk, D. Jenke, B. Lade, J. Newman, P. Nosworthy, P. Purcell, P. F. Skilton, M. Streamer, M. Unwin, H. Watanabe, G. L. White, and D. Watson. Pluto's Atmosphere from the 2015 June 29 Ground-based Stellar Occultation at the Time of the New Horizons Flyby. *Astrophysical Journal, Letters*, 819:L38, March 2016. doi: 10.3847/2041-8205/819/2/L38. (Cited on page 59.)
- J. L. Ortiz, B. Sicardy, F. Braga-Ribas, A. Alvarez-Candal, E. Lellouch, R. Duffard, N. Pinilla-Alonso, V. D. Ivanov, S. P. Littlefair, J. I. B. Camargo, M. Assafin, E. Unda-Sanzana, E. Jehin, N. Morales, G. Tancredi, R. Gil-Hutton, I. de La Cueva, J. P. Colque, D. N. da Silva Neto, J. Manfroid, A. Thirouin, P. J. Gutiérrez, J. Lecacheux, M. Gillon, A. Maury, F. Colas, J. Licandro, T. Mueller, C. Jacques, D. Weaver, A. Milone, R. Salvo, S. Bruzzone, F. Organero, R. Behrend, S. Roland, R. Vieira-Martins, T. Widemann, F. Roques, P. Santos-Sanz, D. Hestroffer, V. S. Dhillon, T. R. Marsh, C. Harlingten, A. Campo Bagatin, M. L. Alonso, M. Ortiz, C. Colazo, H. J. F. Lima, A. S. Oliveira, L. O. Kerber, R. Smiljanic, E. Pimentel, B. Giacchini, P. Cacella, and M. Emilio. Albedo and atmospheric constraints of dwarf planet Makemake from a stellar occultation. *Nature*, 491:566–569, November 2012. doi: 10.1038/nature11597. (Cited on page 59.)
- P. Tanga, B. Carry, F. Colas, M. Delbo, A. Matter, J. Hanuš, V. Alí Lagoa, A. H. Andrei, M. Assafin, M. Audejean, R. Behrend, J. I. B. Camargo, A. Carbognani, M. Cedrés Reyes, M. Conjat, N. Cornero, D. Coward, R. Crippa, E. de Ferra Fantin, M. Devogéle, G. Dubos, E. Frappa, M. Gillon, H. Hamanowa, E. Jehin, A. Klotz, A. Kryszczyńska, J. Lecacheux, A. Leroy, J. Manfroid, F. Manzini, L. Maquet, E. Morelle, S. Mottola, M. Polińska, R. Roy, M. Todd, F. Vachier, C. Vera Hernández, and P. Wiggins. The non-convex shape of (234) Barbara, the first Barbarian\*. *Monthly Notices of the Royal Astronomical Society*, 448(4):3382–3390, April 2015. doi: 10.1093/mnras/stv229. (Cited on page 60.)

- Michael K. Shepard, Bradley Timerson, Daniel J. Scheeres, Lance A. M. Benner, Jon D. Giorgini, Ellen S. Howell, Christopher Magri, Michael C. Nolan, Alessondra Springmann, Patrick A. Taylor, and Anne Virkki. A revised shape model of asteroid (216) Kleopatra. *Icarus*, 311:197–209, September 2018. doi: 10.1016/j.icarus.2018.04.002. (Cited on page 60.)
- Isao Satō, Marc Buie, Paul D. Maley, Hiromi Hamanowa, Akira Tsuchikawa, and David W. Dunham. A 3-D Shape Model of (704) Interamnia from Its Occultations and Lightcurves. *International Journal of Astronomy and Astrophysics*, 4(1):91–118, January 2014. doi: 10.4236/ijaa.2014.41010. (Cited on page 60.)
- M. Devogèle, P. Tanga, P. Bendjoya, J. P. Rivet, J. Surdej, J. Hanuš, L. Abe, P. Antonini, R. A. Artola, M. Audejean, R. Behrend, F. Berski, J. G. Bosch, M. Bronikowska, A. Carbognani, F. Char, M. J. Kim, Y. J. Choi, C. A. Colazo, J. Coloma, D. Coward, R. Durkee, O. Erece, E. Forne, P. Hickson, R. Hirsch, J. Horbowicz, K. Kamiński, P. Kankiewicz, M. Kaplan, T. Kwiatkowski, I. Konstanciak, A. Kruszewki, V. Kudak, F. Manzini, H. K. Moon, A. Marciniak, M. Murawiecka, J. Nadolny, W. Ogłóza, J. L. Ortiz, D. Oszkiewicz, H. Pallares, N. Peixinho, R. Poncy, F. Reyes, J. A. de los Reyes, T. Santana-Ros, K. Sobkowiak, S. Pastor, F. Pilcher, M. C. Quiñones, P. Trela, and D. Vernet. Shape and spin determination of Barbarian asteroids. *Astronomy and Astrophysics*, 607:A119, November 2017. doi: 10.1051/0004-6361/201630104. (Cited on page 60.)
- Xiaobin Wang, Karri Muinonen, Yibo Wang, Raoul Behrend, Rui Goncalves, Julian Oey, Pierre Antonini, Christophe Demeautis, Federico Manzini, Yasmine Damerджи, Jacques Montier, Alain Klotz, Arnaud Leroy, and Giller Ganand. Photometric analysis for the spin and shape parameters of the C-type main-belt asteroids (171) Ophelia and (360) Carlova. *Astronomy and Astrophysics*, 581:A55, September 2015. doi: 10.1051/0004-6361/201526523. (Cited on page 60.)
- W. J. Merline, J. D. Drummond, B. Carry, A. Conrad, P. M. Tamblyn, C. Dumas, M. Kaasalainen, A. Erikson, S. Mottola, J. Ďurech, G. Rousseau, R. Behrend, G. B. Casalnuovo, B. Chinaglia, J. C. Christou, C. R. Chap-

- man, and C. Neyman. The Resolved Asteroid Program - Size, shape, and pole of (52) Europa. *Icarus*, 225(1):794–805, July 2013. doi: 10.1016/j.icarus.2013.01.010. (Cited on page 60.)
- D. Herald, D. Gault, R. Anderson, D. Dunham, E. Frappa, T. Hayamizu, S. Kerr, K. Miyashita, J. Moore, H. Pavlov, S. Preston, J. Talbot, and B. Timerson. Precise astrometry and diameters of asteroids from occultations - a data-set of observations and their interpretation. *MNRAS*, 00:20, 00 2020. (Cited on pages 60, 144 and 147.)
- Gaia Collaboration, A. G. A. Brown, A. Vallenari, T. Prusti, J. H. J. de Bruijne, F. Mignard, R. Drimmel, C. Babusiaux, C. A. L. Bailer-Jones, U. Bastian, and et al. Gaia Data Release 1. Summary of the astrometric, photometric, and survey properties. *Astronomy & Astrophysics*, 595:A2, November 2016. doi: 10.1051/0004-6361/201629512. (Cited on page 63.)
- Gaia Collaboration, A. G. A. Brown, A. Vallenari, T. Prusti, J. H. J. de Bruijne, C. Babusiaux, C. A. L. Bailer-Jones, M. Biermann, D. W. Evans, L. Eyer, and et al. Gaia Data Release 2. Summary of the contents and survey properties. *Astronomy & Astrophysics*, 616:A1, August 2018b. doi: 10.1051/0004-6361/201833051. (Cited on page 63.)
- F. Spoto, P. Tanga, S. Bouquillon, J. Desmars, D. Hestroffer, F. Mignard, M. Altmann, D. Herald, J. Marchant, C. Barache, T. Carlucci, T. Lister, and F. Taris. Ground-based astrometry calibrated by Gaia DR1: new perspectives in asteroid orbit determination. *Astronomy & Astrophysics*, 607: A21, October 2017. doi: 10.1051/0004-6361/201731439. (Cited on page 63.)
- J. Durech, V. Sidorin, and M. Kaasalainen. DAMIT: a database of asteroid models. *Astronomy and Astrophysics*, 513:A46, April 2010. doi: 10.1051/0004-6361/200912693. (Cited on page 68.)
- A. Marciniak, P. Bartczak, T. Santana-Ros, T. Michałowski, P. Antonini, R. Behrend, C. Bembick, L. Bernasconi, W. Borczyk, F. Colas, J. Coloma, R. Crippa, N. Esseiva, M. Fagas, M. Fauvaud, S. Fauvaud, D. D. M. Ferreira, R. P. Hein Bertelsen, D. Higgins, R. Hirsch, J. J. E. Kajava, K. Kamiński, A. Kryszczyńska, T. Kwiatkowski, F. Manzini,

- J. Michałowski, M. J. Michałowski, A. Paschke, M. Polińska, R. Poncy, R. Roy, G. Santacana, K. Sobkowiak, M. Stasik, S. Starczewski, F. Velichko, H. Wucher, and T. Zafar. Photometry and models of selected main belt asteroids. IX. Introducing interactive service for asteroid models (ISAM). *Astronomy and Astrophysics*, 545:A131, September 2012. doi: 10.1051/0004-6361/201219542. (Cited on page 68.)
- Y. Tsapras, R. Street, K. Horne, C. Snodgrass, M. Dominik, A. Allan, I. Steele, D. M. Bramich, E. S. Saunders, N. Rattenbury, C. Mottram, S. Fraser, N. Clay, M. Burgdorf, M. Bode, T. A. Lister, E. Hawkins, J. P. Beaulieu, P. Fouqué, M. Albrow, J. Menzies, A. Cassan, and D. Dominis-Prester. RoboNet-II: Follow-up observations of microlensing events with a robotic network of telescopes. *Astronomische Nachrichten*, 330:4, January 2009. doi: 10.1002/asna.200811130. (Cited on page 74.)
- Alain Klotz and Pierre Thierry. TAROT Reunion a telescope based on the Rapido design for reliable optical observations of fast transients. *Experimental Astronomy*, 48(2-3):121–135, August 2019. doi: 10.1007/s10686-019-09638-8. (Cited on page 75.)
- D. L. Mary. A statistical analysis of the detection limits of fast photometry. *Astronomy & Astrophysics*, 452:715–726, June 2006. doi: 10.1051/0004-6361:20054425. (Cited on page 75.)
- E. Corsaro and J. De Ridder. DIAMONDS: A new Bayesian nested sampling tool. Application to peak bagging of solar-like oscillations. *Astronomy & Astrophysics*, 571:A71, November 2014a. doi: 10.1051/0004-6361/201424181. (Cited on pages 95 and 99.)
- E. Corsaro and J. De Ridder. DIAMONDS: high-Dimensional And multi-MOdal NesteD Sampling. *Astrophysics Source Code Library*, October 2014b. (Cited on pages 95 and 99.)
- F. Roques, G. Geisler, and A. Doressoundiram. *The Kuiper Belt Explored by Serendipitous Stellar Occultations*, pages 545–556. Barucci, M. A. and Boehnhardt, H. and Cruikshank, D. P. and Morbidelli, A. and Dotson, R., 2008. (Cited on page 97.)

- E. Pass, S. Metchev, P. Brown, and S. Beauchemin. Pipeline for the Detection of Serendipitous Stellar Occultations by Kuiper Belt Objects with the Colibri Fast-photometry Array. *Publications of the ASP*, 130(1):014502, January 2018. doi: 10.1088/1538-3873/aa971f. (Cited on page 97.)
- L. F. Sivia and J. Skilling. *Data Analysis: A Bayesian Tutorial*. Oxford Science, 2006. (Cited on page 99.)
- Mario Jurić, Željko Ivezić, Robert H. Lupton, Tom Quinn, Serge Tabachnik, Xiaohui Fan, James E. Gunn, Gregory S. Hennessy, Gillian R. Knapp, Jeffrey A. Munn, Jeffrey R. Pier, Constance M. Rockosi, Donald P. Schneider, Jonathan Brinkmann, István Csabai, and Masataka Fukugita. Comparison of Positions and Magnitudes of Asteroids Observed in the Sloan Digital Sky Survey with Those Predicted for Known Asteroids. *Astrophysical Journal*, 124(3):1776–1787, September 2002. doi: 10.1086/341950. (Cited on page 99.)
- Petr Pravec, Alan W. Harris, Peter Kušnirák, Adrián Galád, and Kamil Hornoch. Absolute magnitudes of asteroids and a revision of asteroid albedo estimates from WISE thermal observations. *Icarus*, 221(1):365, September 2012. ISSN 0019-1035. doi: 10.1016/j.icarus.2012.07.026. URL <https://ui.adsabs.harvard.edu/abs/2012Icar..221..365P/abstract>. (Cited on page 99.)
- J. D. Hunter. Matplotlib: A 2d graphics environment. *Computing in Science & Engineering*, 9(3):90–95, 2007. doi: 10.1109/MCSE.2007.55. (Cited on page 101.)
- R. Trotta, F. Feroz, M. Hobson, L. Roszkowski, and R. Ruiz de Austri. The impact of priors and observables on parameter inferences in the constrained MSSM. *Journal of High Energy Physics*, 12:024, December 2008. doi: 10.1088/1126-6708/2008/12/024. (Cited on page 108.)
- Ferreira, J. F., Tanga, P., Machado, P., and Corsaro, E. A survey for occultation astrometry of main belt: expected astrometric performances. *Astronomy & Astrophysics*, 641:A81, 2020. doi: 10.1051/0004-6361/202038190. URL <https://doi.org/10.1051/0004-6361/202038190>. (Cited on page 118.)

- H. Pavlov and A. Mallama. Video Technique for Observing Eclipsing Binary Stars. *Journal of the American Association of Variable Star Observers (JAAVSO)*, 43(1):80, June 2015. (Cited on page 121.)
- B. Morgado, G. Benedetti-Rossi, A. R. Gomes-Júnior, M. Assafin, V. Lainey, R. Vieira-Martins, J. I. B. Camargo, F. Braga-Ribas, R. C. Bouffleur, J. Fabrega, D. I. Machado, A. Maury, L. L. Trabuco, J. R. de Barros, P. Caccella, A. Crispim, C. Jaques, G. Y. Navas, E. Pimentel, F. L. Rommel, T. de Santana, W. Schoenell, R. Sfair, and O. C. Winter. First stellar occultation by the Galilean moon Europa and upcoming events between 2019 and 2021. *Astronomy & Astrophysics*, 626:L4, June 2019. doi: 10.1051/0004-6361/201935500. (Cited on page 136.)
- D. Farnocchia, S. R. Chesley, A. B. Chamberlin, and D. J. Tholen. Star catalog position and proper motion corrections in asteroid astrometry. *Icarus*, 245:94–111, January 2015. doi: 10.1016/j.icarus.2014.07.033. (Cited on pages 144, 145, 154, 179 and 180.)
- P. Tanga, F. Spoto, and J. F. Ferreira. Local multi-parametric debiasing of asteroid astrometry by Gaia Data Release 2. *Astronomy & Astrophysics*, 480:1015–1022, 12 2020. doi: 10.1051/0004-6361:20077470. (Cited on page 145.)
- F. L. Rommel, F. Braga-Ribas, J. Desmars, J. I. B. Camargo, J. L. Ortiz, B. Sicardy, R. Vieira-Martins, M. Assafin, P. Santos-Sanz, R. Duffard, E. Fernández-Valenzuela, J. Lecacheux, B. E. Morgado, G. Benedetti-Rossi, A. R. Gomes-Júnior, C. L. Pereira, D. Herald, W. Hanna, J. Bradshaw, N. Morales, J. Brimacombe, A. Burtovoi, T. Carruthers, J. R. de Barros, M. Fiori, A. Gilmore, D. Hooper, K. Hornoch, C. Jacques, T. Janik, S. Kerr, P. Kilmartin, Jan Maarten Winkel, G. Naletto, D. Nardiello, V. Nascimbene, J. Newman, A. Ossola, A. Pál, E. Pimentel, P. Pravec, S. Sposetti, A. Stechina, R. Szákats, Y. Ueno, L. Zampieri, J. Broughton, J. B. Dunham, D. W. Dunham, D. Gault, T. Hayamizu, K. Hosoi, E. Jehin, R. Jones, K. Kitazaki, R. Komžík, A. Marciniak, A. Maury, H. Mikuz, P. Nosworthy, J. Fábrega Polleri, S. Rahvar, R. Sfair, P. B. Siqueira, C. Snodgrass, P. Sogorb, H. Tomioka, J. Tregloan-Reed, and O. C. Winter. Stellar occultations enable milliarcsecond astrometry for Trans-Neptunian objects and

- Centaurs. *arXiv e-prints*, art. arXiv:2010.12708, October 2020. (Cited on page 181.)
- Sarah Greenstreet, Davide Farnocchia, and Tim Lister. Measuring the Yarkovsky effect with Las Cumbres Observatory. *Icarus*, 321:564–571, March 2019. doi: 10.1016/j.icarus.2018.11.032. (Cited on page 182.)
- Federica Spoto, Paolo Tanga, and Benoit Carry. Direct detections of the Yarkovsky drift with Gaia DR2. In *EPSC-DPS Joint Meeting 2019*, volume 2019, pages EPSC–DPS2019–1361, September 2019. (Cited on page 182.)
- Astropy Collaboration, Thomas P. Robitaille, Erik J. Tollerud, Perry Greenfield, Michael Droettboom, Erik Bray, Tom Aldcroft, Matt Davis, Adam Ginsburg, Adrian M. Price-Whelan, Wolfgang E. Kerzendorf, Alexander Conley, Neil Crighton, Kyle Barbary, Demitri Muna, Henry Ferguson, Frédéric Grollier, Madhura M. Parikh, Prasanth H. Nair, Hans M. Unther, Christoph Deil, Julien Woillez, Simon Conseil, Roban Kramer, James E. H. Turner, Leo Singer, Ryan Fox, Benjamin A. Weaver, Victor Zabalza, Zachary I. Edwards, K. Azalee Bostroem, D. J. Burke, Andrew R. Casey, Steven M. Crawford, Nadia Dencheva, Justin Ely, Tim Jenness, Kathleen Labrie, Pey Lian Lim, Francesco Pierfederici, Andrew Pontzen, Andy Ptak, Brian Refsdal, Mathieu Servillat, and Ole Streicher. Astropy: A community Python package for astronomy. *Astronomy & Astrophysics*, 558:A33, October 2013. doi: 10.1051/0004-6361/201322068. (Cited on page 215.)

# Asteroid Orbital Improvement

---

Here we show plots from [Vereš et al., 2017] regarding the dependency of asteroid observation residuals with parameters such as observation epoch (Figure A.1), magnitude (Figure A.2) and rate of motion (Figure A.3). The residuals tend to lower with time, due to access to better equipment and catalogues. They tend to grow with magnitude because a fainter object is more difficult to detect, and the associated uncertainties tend to be larger. And they tend to grow as well with the rate of motion due to the asteroid's movement during an observation.

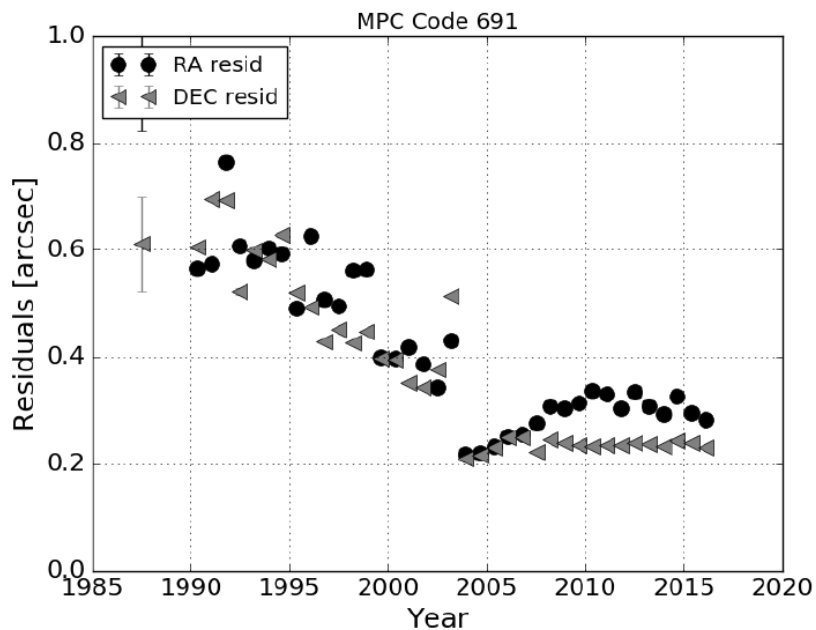


Figure A.1: Example from Veres et al. (2017) of dependence of the residuals to the year of observation for a specific site (code 691 - Spacewatch). Different observatories have different trends, so each needs its own rule. This also applies to other parameters.

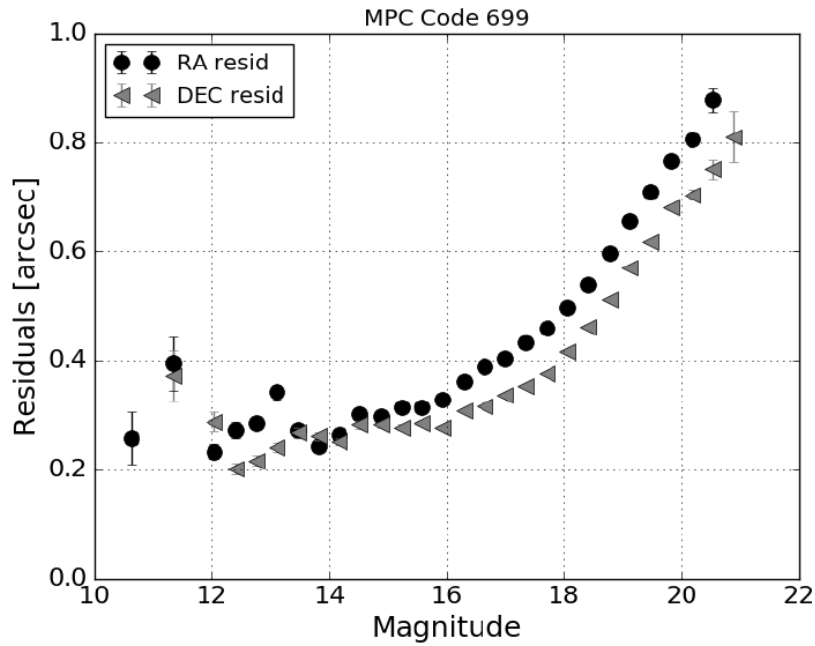


Figure A.2: Same analysis, also from Veres et al. (2017), but with dependence on object brightness (code 699 - LONEOS).

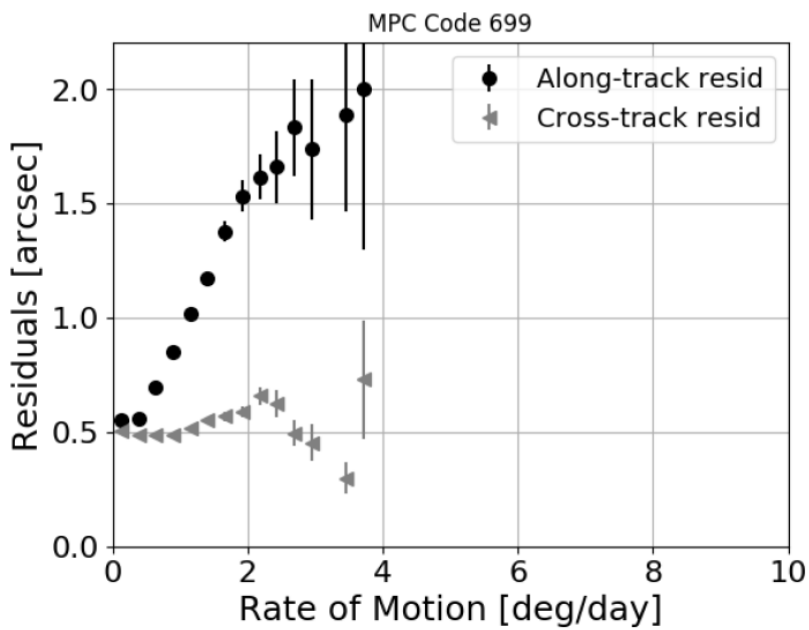


Figure A.3: Same analysis, also from Veres et al. (2017), but with dependence on object projected velocity in the sky (code 699 - LONEOS).

Looking at the residuals from the new debiasing (in preparation), we can also find some trends regarding the catalogues (Figure A.4), as well as with asteroid magnitude (Figure A.5).

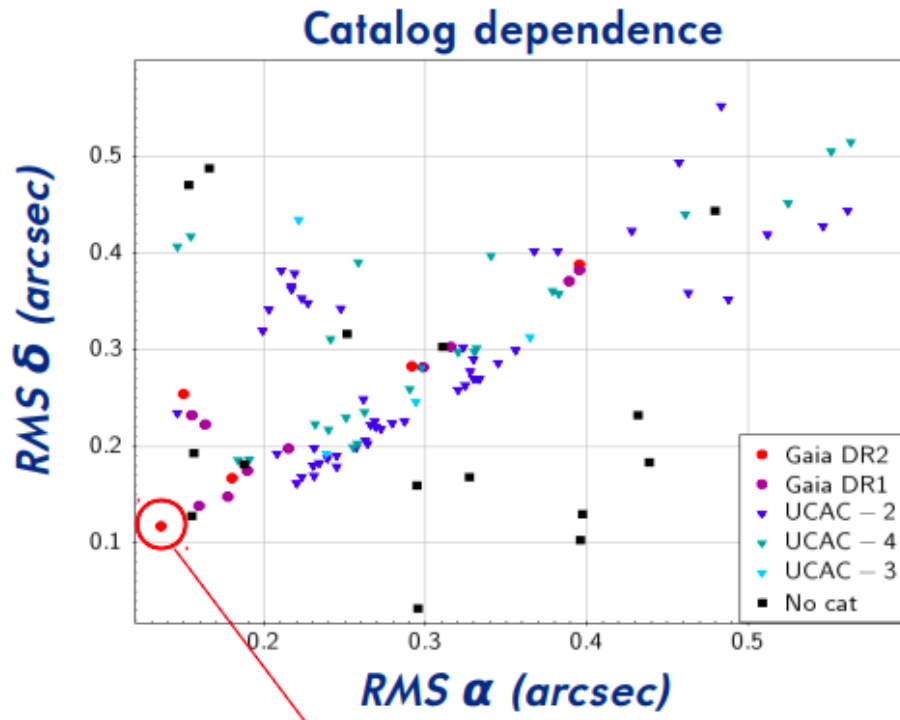


Figure A.4: Trend of residuals as a function of catalogue for RA and Dec. "No catalogue" tends to have larger residuals, Gaia DR1 and DR2 smaller, and a large scatter is seen with UCAC catalogues, especially UCAC2.

## A.1 OrbFit

### A.1.1 Software description

OrbFit consists of four main programs:

- Orbfit: batch program. It can run by giving an asteroid and having the appropriate data.
- Fitobs: interactive program. Allows the user to choose which procedures to use;

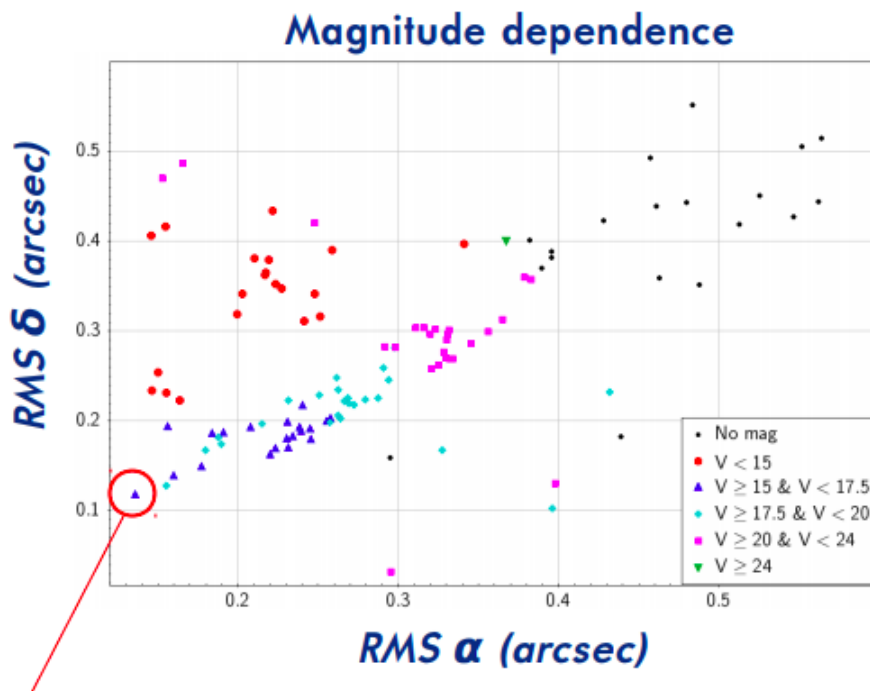


Figure A.5: Same analysis, for asteroid magnitude. "No mag" means that no magnitude is given for a certain observation, focusing only on astrometry. Observations that don't allow a magnitude estimate tend to be difficult, so these result in larger residuals. Then, there is a clear trend for larger residuals associated to larger magnitudes, similar to what was verified in FV15.

- Catpro: catalogue propagation. Moves the reference epoch of an object;
- Bineph: adds perturbations from other asteroids to the calculations. Necessary for top accuracy.

### A.1.2 Orbital elements and required data

Further uses for OrbFit include the improvement of orbits based on the combination of data in MPC and DR2 and the comparison of different debiasing and data weighting models. The following files are required:

All runs:

- MPC observations file: a file extracted from the MPC website with all the observations to an asteroid, typically several hundred to a few thousand;
- Initial orbital elements file: extracted from AstDyS, this file is the first order approximation to the orbital elements of an asteroid, which can be extracted for "mid-point" (halfway between first and last observation) or "recent" (close to the present day);
- Internal use ".fop" file, to explain to OrbFit the choices made regarding the asteroid (file number), the imported files, the models used (FV15 or TS20) and whether or not to include extra parameters, such as Yarkovsky;
- If applicable, radar observations, most common for NEA.

Additionally: Runs that include Gaia:

- Gaia observations file: extracted from the DR2 archive for solar system objects, with all the observations by Gaia to asteroids in its first 22 months. On average, this represented 200 observations per object;
- Light deflection corrections: Gaia has a light deflection correction that assumes an infinite distance to the object. Such approximation is good for stars, but for nearby objects such as asteroids, a further correction is required to get the light correction at their distance. Files given by Federica Spoto.

Runs that include the new error model:

- Updated list of international IAU Observatory Codes (e.g. 020 for Nice, 244 for occultation, 500 for geocentric observation);
- Debiasing files for each asteroid, provided by Paolo Tanga.

The typical procedure when running OrbFit includes the following steps:

- Create a file that will read the MPC and/or Gaia observations, normally named "AsteroidName.fop". By executing another file called "fitobs.x" and using the name of this .fop document, OrbFit will read the observation files, as well as the initial orbital elements and, if necessary, the light deflection correction. This will also open a menu, where the user can choose what to do with this data;
- Apply "differential corrections", which will search through the observations for the ones that can be classified as outliers, due to having abnormally high residuals, exclude them and re-fit the orbital elements all at once. OrbFit does this in a step-like procedure with a Least Squares Fit method, until no further observations are rejected. The first guess to the orbital elements is used here;
- Now that OrbFit has a new orbit calculated, we can ask for the new elements, by requesting a conversion to Keplerian coordinates, the ones typically used in prediction tools. This will give us the semi-major axis  $a$  (in au), eccentricity  $e$  (adimensional) and the inclination  $i$ , node, argument at perihelion and mean anomaly (all angles, in degrees). These values are saved in a file labeled "AsteroidName.fel", where we also have access to the covariance matrix of all these parameters;
- By choosing the date of the occultation, we can ask for the ephemerides of the asteroid. OrbFit propagates the orbit and, based on the user input, will give the ephemerides, the most important of which to us are the RA/Dec coordinates, which we will use to compare with the occultation, the velocity values, which we will use to later represent the velocity vector and the uncertainty axes, which can be looked at in greater detail with the next option;

- Finally, we ask for the uncertainty ellipse in RA/Dec coordinates by choosing the confidence level option. This will create a ".tmp" file with an arbitrary amount of points that we can use to represent the 1-sigma uncertainty around the astrometric solution of OrbFit.

Given the interactive nature of OrbFit, as well as Occult for the predictions, it was necessary to create a bash document that would launch OrbFit in a cycle for every asteroid, and then construct a "User File" which can be used in Occult for the predictions instead of the usual asteroid catalogues. This allowed us to make predictions to several thousand objects with Gaia data included for both asteroids and stars, which was not yet available before.



# Code snippets

---

## B.1 UniversCity and Linoccult

To check how many occultations would be visible from UniversCity's location, a 1-year run was made in Linoccult. Here is how we did that:

```
int StartDay 1
int StartMonth 1
int StartYear 2018
int EndDay 31
int EndMonth 12
int EndYear 2018
double MinDiameter 5.0
#double MaxDiameter 10000.0
string OutputEventsFilePath Results.bin
#string SitesFilePath /home/jferreira/Desktop/Linoccult/LinOccult_2_3_0/Nice/SitesExample.txt
#string InputEventsFilePath /home/jferreira/Desktop/Linoccult/LinOccult_2_3_0/Nice/Several.txt
#int CalculationMode 0
```

Figure B.1: Setup file for mandatory global run of events, readable by Linoccult. Dates of run are from 01/01/2018 to 31/12/2018, so one full year. "MinDiameter" is the minimum diameter of an asteroid, meaning any diameter smaller excludes the object from this run. "MaxDiameter" does the same with an upper bound, but is left unused. Results are output in a .bin file which will then be used to extract local events.

We can't make a direct run for the site we are interested in. Instead, we must first make a global run that Linoccult will subsequently scan for local data, once we set up the observer sites file.

```
# ObsName EMail OutputFiles Sort ObserverLongitude ObserverLatitude MaxDistance MaxNv MinDuration SunElev MinDrop MinProb MinCenterProb MinStarElev
# OCA
# Nice jferreira@oca.eu 1 1 43.723 7.302 1000.0 14 0.1 0.0 0.1 0.0 0.0 20.0
# Calern
Calern jferreira@oca.eu 1 1 43.753 6.921 1000.0 15 0.1 0.0 0.1 0.0 0.0 20.0
```

Figure B.2: User sites file, that Linoccult reads together with the .bin global file to assess events visible in specific locations.

This file contains all of the filter information that does not involve the date or the object's size:

- Name, e-mail and type of output file (1 means .txt, 2 to .tex and 4 to .html);
- The sort type we want (1 for date, 2 for asteroid number, 4 for magnitude drop, 8 for smallest distance to shadow-path centre, 16 for duration, 32 for probability, 64 for probability in shadow-path centre, 128 for star magnitude and 256 for uncertainty). Using a number that isn't a power of 2 means Linoccult will provide one table for each number being added (e.g. choosing 3 means a table sorted by date and a table sorted by asteroid number);
- Observer coordinates: latitude and longitude;
- Maximum allowed distance to shadow-path centre. This can be left as an arbitrarily large number to not exclude interesting events, but for distances of thousands of kilometers, the probability should always be at or near 0;
- Maximum star magnitude. Linoccult uses DR2 up to magnitude 14, but we can limit it further;
- Minimum duration allowed, 0.1 s for us;
- Maximum Sun elevation. Leaving it at 0.0 means the Sun must be set, though it should be noted that only altitudes around  $-18^\circ$  ensure no sunlight in the sky;
- Minimum magnitude drop (0.1 for us), probability at site (0.0), probability at shadow-path centre (0.0) and star altitude ( $20^\circ$ ).

Together with this site file, we used the code in Figure B.3:

## B.2 Simulations

The light curve simulations were made in C++, with cycles through magnitude, duration and magnitude drop:

```

int StartDay 1
int StartMonth 11
int StartYear 2018
int EndDay 31
int EndMonth 12
int EndYear 2018
double MinDiameter 5.0
#double MaxDiameter 10000.0
#double MinA 5.1
#double MaxA 30.1
#string OutputEventsFilePath Results.bin
string SitesFilePath /home/jferreira/Desktop/Linoccult/LinOccult_2_3_0/Nice/SitesExample.txt
string InputEventsFilePath Results.bin
int CalculationMode 0

```

Figure B.3: Local Linoccult file. "SitesFilePath" indicates where Linoccult must read the site file, "InputEventsFilePath" where to read the .bin file and "Calculation Mode 0" ensures Linoccult does not compute globally every event again, just for the local sites.

```

46 zero = 1500.0; // Value of flux to magnitude conversion using Vega scale. Do not change unless you use specific bands.
47 size = 50.0; // Telescope diameter in cm
48 area = M_PI * pow(size, 2.0) / 4.0; // Area of telescope
49 bwidth = 4100.0; // Band width in Angstrom. 4100 is visible light
50 eff = 0.75 * 0.8 * 0.5; // Efficiency of telescope-camera system
51 alt = 90.0; // Altitude in degrees of star in the sky.
52 altitude = 1200.0; // Altitude of the observation point, in meters. Reference is mean sea level.
53 airm = 1. / (cos(M_PI / 180.0 * (90.0 - alt)) + 0.50572 * pow((6.07995 + alt), 0.0 - 1.6364)) * exp(0.0 - altitude / 8000.); // Estimate for airmass
54 tin = 0.; // Initial UT time, from 0 (0h) to 86400 (24h)
55 dt = 0.1; // Time-step, or exposure time, in seconds
56 background = 7400.0; // Average background per pixel, per second and per square meter
57 pixrad = 3.5; // Pixel radius of the photometry analysis to the star
58 dark = 0.1; // Dark current factor per unit of pixel and time
59 readout = 130.0; // Readout noise factor per unit of pixel
60 eadu = 5.24; // Electron analog-to-digital conversion ratio
61 beta = 0.15 * pow(size, 0. - 2.0 / 3.0) * pow(airm, 1.75) * pow(2.0 * dt, 0.0 - 0.5);
62 background = background * dt * M_PI * pow(pixrad, 2.0) * pow(size / 104.0, 2.);
63 // magdrop - Magnitude drop during occultation
64 for(j = 10; j >= 3; j--){
65     magdrop = (double)j / 10.0;
66     magoriginal = magdrop;
67     // Uniform random distribution between -0.05 and 0.05
68     // Mag - Original magnitude of star
69     for(k = 0; k <= 10; k++){
70         mag = 11.5 + (double)k / 5.0;
71         // Occultation - Occultation duration, in seconds
72         for(z = 10; z >= 2; z--){
73             occultation = z / 10.;
74             occoriginal = occultation;
75             // Number of tests made for a specific combination of magnitude, magnitude drop and duration
76             for(tests = 1; tests <= 10; tests++){
77                 // timevalue gets a uniform distribution between -0.5 and 0.5
78                 timevalue = (double)(rand()) / (double)(RAND_MAX) - 0.5;
79                 // timevalue is normalized to the exposure time's size
80                 timevalue = timevalue * dt;

```

Figure B.4: Setting up all relevant variables for the simulation.

The variables used to calculate the flux are:

- "zero": value used for flux-to-magnitude conversion in the Vega star magnitude scale;
- Telescope area, in cm;
- Filter bandwidth, left at visible light range;
- Telescope efficiency;
- Star altitude, left at zenith;
- Site altitude, used for airmass estimate;
- Airmass estimate, to estimate how much flux is lost due to our atmosphere;
- Exposure time, set at 0.1 s;
- Values for background, readout and dark current noise;
- Cycle value of magnitude drop, magnitude, duration and test number.

All of these variables are used then to calculate the flux:

```

duration = 17. * occultation; // Simulation duration, in seconds
start = tin + 8. * occultation; // Occultation beginning, in seconds
start = start + transvalue;
fluxstar = eadu * zero * pow(2.51189, 0.02 - mag) * eff * dt * area * bwidth * pow(2.51189, 0.0 - 0.2 * airm); // Very rough estimate that 1 airmass
reg_diff = -0.8522 * log(magdrop) + 0.5147;
flux = eadu * zero * pow(2.51189, 0.02 - (mag - reg_diff)) * eff * dt * area * bwidth * pow(2.51189, 0.0 - 0.2 * airm);
fluxast = flux - fluxstar;
mag_comb = mag - reg_diff;
mag_ast = mag_comb + magdrop;
noise = pow(flux + eadu * background + pow(beta * flux, 2.) + M_PI * pow(pixrad * readout, 2.) + dark * dt * M_PI * pow(pixrad, 2.0), 0.5); // Averag
noiseast = pow(fluxast + eadu * background + pow(beta * fluxast, 2.) + M_PI * pow(pixrad * readout, 2.0) + dark * dt * M_PI * pow(pixrad, 2.0), 0.5);
separation = fluxstar; // Flux drop. Use POSITIVE values.
snr = flux / noise;
//dnr = separation / pow(noise * noise + noiseast * noiseast, 0.5);
dnr = separation / pow(noise * noise * 1.0 / 17.0 + noiseast * noiseast * 16.0 / 17.0, 0.5);
cond << dnr << " " << snr << " " << mag << " " << mag_comb << " " << magdrop << " " << mag_ast << '\n';

```

Figure B.5: Flux calculation for specific event.

## B.3 Gaia Star Query

ADQL (Astronomical Data Query Language) code used to build star catalogue from Gaia:



- The sorting of the resulting table by ascending order of declination.

The resulting files can then be read by Occult in the designated area, building the full catalogue ready to be read once we use it for predictions:

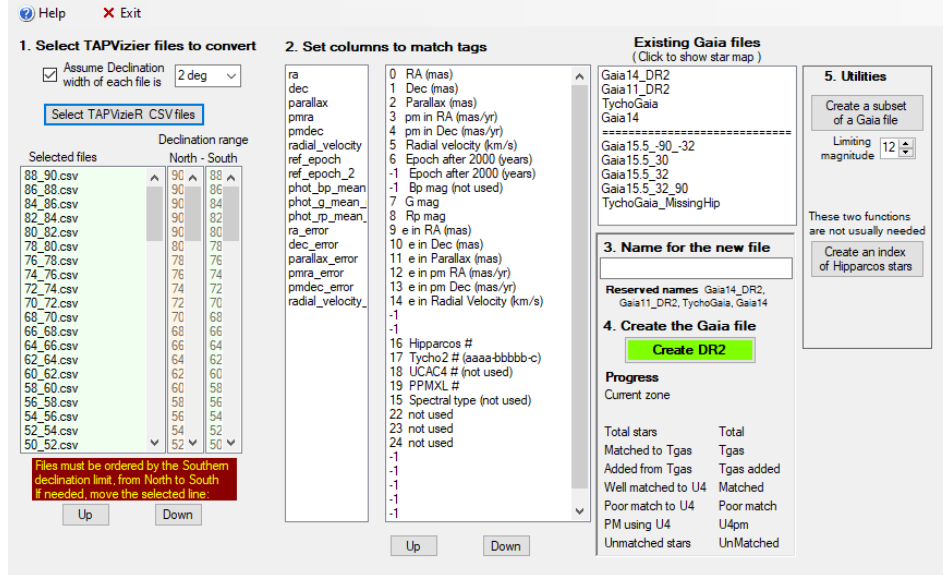


Figure B.7: Section in Occult which builds the Gaia star catalogue from our output files.

## B.4 Gaia Asteroid Query and OrbFit files

Another query to Gaia made in ADQL was for the observation files of all 14 099 asteroids present in DR2. This time, we used "gaiadr2.sso\_observation" section of the archive, and scanned it for every asteroid present.

Since we extract all information, the code is simpler:

- Grabbing every column from the "gaiadr2.sso\_observation" section;
- Specifying the asteroid we want from its MPC number;
- Ordering the observations by their epoch.

Once again, we had to make a routine to run this cycle for every asteroid present in the catalogue. The output file was later used in OrbFit.

The screenshot shows the Gaia Archive interface. At the top, there's a navigation bar with 'HOME', 'SEARCH', 'STATISTICS', 'VISUALISATION', and 'HELP'. Below that, there's a 'Basic' tab and a 'Query Results' tab. The main area contains a query editor with the following SQL query:

```
1 SELECT *
2 FROM gaiadr2.sso_observation
3 WHERE (gaiadr2.sso_observation.number_mp=8)
4 order by epoch
```

Below the query editor, there's a table of results with columns: Status, Job, Creation date, Num. rows, and Size. The table shows three jobs:

Status	Job	Creation date	Num. rows	Size
✓	15979204504660	20-Aug-2020, 11:47:30	60	11 KB
✓	15979194835420	20-Aug-2020, 11:31:23	15034	1 MB
✓	15979194485860	20-Aug-2020, 11:30:48	15034	1 MB

Figure B.8: Getting every observation from a specific asteroid made by Gaia. This example shows the query for the lowest numbered asteroid in the catalogue, (8) Flora.

Other files had to be made for all these asteroids to successfully run OrbFit, namely, files with their initial values for orbital parameters, their other recorded observations, the light bending files necessary to correct Gaia measurements and a setup file for OrbFit to read.

```
1 import urllib.request
2 import numpy as np
3
4 # Upload array with asteroid numbers from GDR2
5 numbers = np.loadtxt('numbers.txt')
6
7 asteroids = len(numbers)
8
9 for i in range(0, asteroids):
10     print(int(numbers[i]))
11     intermediate = int(numbers[i]) // 1000
12
13     # Query AstDyS for one asteroid
14     url = 'https://newton.spacedys.com/~astdys2/epoch/numbered/' + str(intermediate) + '/' + str(int(numbers[i])) + '.eq0'
15
16     # Save data in url in a .eq0 file
17     urllib.request.urlretrieve(url, 'epoch/' + str(int(numbers[i])) + '.eq0')
18
```

Figure B.9: File that queries AstDyS for the initial values of orbital parameters of every asteroid in DR2, whose MPC numbers are extracted from a source file made previously.

## B.5 Photometry

For photometry, in particular for the observations described in Chapter 4, a tool was developed to perform aperture photometry on its own, in order to

```

from astroquery.mpc import MPC

# Upload array with asteroid numbers from GDR2
numbers = np.loadtxt('numbers.txt')

asteroids = len(numbers)
splitat = 80

for i in range(0, asteroids):
    if(int(numbers[i]) > 46244):
        observations = open('mpcobs2/' + str(int(numbers[i])) + '.obs', 'w')
        print(int(numbers[i]))
        # Query MPC for observations of one asteroid, keeping the MPC file format
        obs = MPC.get_observations(int(numbers[i]), get_mpcformat=True, cache=False)
        obs2 = obs[:0].copy()
        for line in obs:
            if len(line[0]) != 80:
                line1, line2 = line[0][:splitat], line[0][splitat:]
                observations.write(line1 + '\n')
                observations.write(line2 + '\n')
            else:
                line1 = line[0][:splitat]
                observations.write(line1 + '\n')

        # ADD FILE TO WRITE OUTPUT

        observations.close()
        #obs2.write('mpcobs2/' + str(int(numbers[i])) + '.obs', format='ascii', show_name = False, show_unit = False, show_dtype = False)

```

Figure B.10: File that queries MPC for all available observations of each asteroid present in DR2.

```

!| input file for fitobs
fitobs.
! first arc
.astna0='1566'          ! full name, first arc
.ons_name=.F.          ! NEOCP
.obsdir0='mpcobs'     ! directory of observs. file, first arc
.elefi0='epoch/1566.eq0' ! epoch file
.error_model='fcct14' ! error model file name (defaults to ' ')
! bizarre control;
.ecclim= 0.9999d0     ! max eccentricity for non bizarre orbit
.samin= 0.5d0        ! min a for non bizarre orbit
.samax= 100.d0       ! max a for non bizarre orbit
.phmin= 0.001d0     ! min q for non bizarre orbit
.ahmax= 200.d0       ! max Q for non bizarre orbit
propag.
.iast=23             ! 0=no asteroids with mass n=no. of massive asteroids
.filbe='AST23'
.npoint=600         ! minimum number of data points for a deep close appr
.dmea=0.2d0         ! min. distance for control close-app. to Earth only
.dter=0.05d0        ! min. distance for control close-app. to M, V, M
.ngr_opt=.T.        !non-gravs
.det_drp=2          !only Yarko
.iyark=3            !Yarko model
reject.
.rejopp = .T.       ! reject entire oppositions
.rej_fudge= .F.    ! fudge not used
! .chi2_reject=1.0D0 ! Chi-square threshold for rejection
! .chi2_recover=0.5D0 ! Chi-square threshold for recovery
IERS.
.extrapolation=.T. ! extrapolation of Earth rotation

!

```

Figure B.11: Example of a setup file to be read by OrbFit, in this case for (1 566) Icarus. Main difference between runs is whether the error model used for the observations is the previously established one (Farnocchia - fcct14) or the new one built by Federica Spoto (gaiaDR2).

not rely on interactive programs such as Tangra once the observation output becomes larger thanks to robotic telescopes. While some of those observations were treated with Tangra, some others were verified via the use of Python's photutils<sup>2</sup> package along with Astropy [Astropy Collaboration et al., 2013]. Photutils requires that a video is split into FITS (Flexible Image Transport System) files for each frame, which are then read sequentially.

```

1 import astropy
2 from astropy.io import fits
3 from astropy.stats import mad_std
4 import numpy as np
5 import photutils
6 from photutils import datasets
7 from photutils import DAOStarFinder
8 from photutils import aperture_photometry
9 from photutils import CircularAperture
10 import ccdproc
11 import matplotlib.pyplot as plt
12 import os
13
14 results = open('data.txt', 'w')
15 results.write('#Frame Photometry x y\n')
16 for i in range(0, len(results)):
17     f = fits.open('new_rca' + str(i) + '.fits')
18     figure = f[0].data[0:1024, 0:1024].astype(float)
19     figure -= np.median(figure)
20     background_sigma = mad_std(figure)
21     daofind = DAOStarFinder(fwhm = 5.5, threshold = 5.0 * background_sigma)
22     stars = daofind(figure)
23     locations = (stars['xcentroid'], stars['ycentroid'])
24     lim = len(stars)
25     if(i==0):
26         for j in range(0, lim):
27             if (abs(float(stars['xcentroid'][j]) - 75) < 5 and abs(float(stars['ycentroid'][j]) - 106) < 5):
28                 if (abs(float(stars['peak'][j]) - 13265) < 0.5 * 13265 or abs(float(stars['flux'][j]) - 10) < 0.5 * 10):
29                     location_extra = (float(stars['xcentroid'][j]) + 251 - 46, float(stars['ycentroid'][j]) + 218 - 56)
30                     previous_x = float(stars['xcentroid'][j])
31                     previous_y = float(stars['ycentroid'][j])
32                     previous_peak = float(stars['peak'][j])
33                     previous_flux = float(stars['flux'][j])
34     else:
35         for j in range(0, lim):
36             if (abs(float(stars['xcentroid'][j]) - previous_x) < 5 and abs(float(stars['ycentroid'][j]) - previous_y) < 5):
37                 if (abs(float(stars['peak'][j]) - previous_peak) < 0.5 * previous_peak or abs(float(stars['flux'][j]) - previous_flux) < 0.5 * previous_flux):
38                     location_extra = (float(stars['xcentroid'][j]) + 251 - 46, float(stars['ycentroid'][j]) + 218 - 56)
39                     previous_x = float(stars['xcentroid'][j])
40                     previous_y = float(stars['ycentroid'][j])
41                     previous_peak = float(stars['peak'][j])
42                     previous_flux = float(stars['flux'][j])
43                 radii = CircularAperture(locations, r = 3.5)
44                 radii_extra = CircularAperture(location_extra, r = 3.5)
45                 photometry = aperture_photometry(figure, radii)
46                 photometry_extra = aperture_photometry(figure, radii_extra)
47                 results.write(str(i) + ' ' + str(location_extra[0]) + ' ' + str(location_extra[1]) + '\n')
48             results.close()

```

Figure B.12: Example of application of photutils to a stellar occultation. Target was Pluto, for an occultation on 2016/07/14 in Constância. By using a FITS file for each frame (1024 x 1024 pixels), photutils analyzes searches for sources above noise level by a certain threshold (signal 5x larger than noise in this example). Then, it lists the (x,y) pixel coordinates of each target that surpasses this threshold, and by using a first approach, we attempt to manually identify in the first frame which of these targets is the occulted star, doing aperture photometry of 3.5 pixels radius around it, the value found to have the best SNR for targets that are not very bright. Other stars, should they be above the threshold for the entire video, can be used as reference later. Once the occulted star has been found, we search its surroundings in the following frame for it. If it is not found, then we assume it remains in the same coordinates, which should be the case for stable images. This is necessary in case the drop caused by the occultation is large enough to remove the star from the list of objects above the threshold. A different approach is to use relative positions by taking a few reference stars, and using their positions to estimate the position of the lost target.

<sup>2</sup> <https://photutils.readthedocs.io/en/stable/>



# Abbreviations Used

---

**DIAMONDS**: high-Dimensional And multi-MOdal NesterD Sampling;

**DNR**: Drop-to-Noise Ratio;

**fcct14**: Farnocchia 2014, error model for asteroid orbital fitting;

**FPS**: Frames Per Second

**DR**: Gaia's Data Release (GDR can also be used);

**IOTA**: International Occultation Timing Association;

**LSF**: Least Squares Fit;

**mas**: milli-arcsecond;

**MBA**: Main Belt Asteroid;

**MPC**: Minor Planet Center;

**NEA/NEO**: Near Earth Asteroid/Object;

**Py-OTE**: Python Occultation Timing Extractor;

**TNO**: TransNeptunian Object;

**UCAC**: USNO CCD Astrogaph Catalogue (USNO stands for United States Naval Observatory and CCD stands for Charge-Coupled Device).



APPENDIX D

# Paper Published

---

# A survey for occultation astrometry of main belt: expected astrometric performances

J. F. Ferreira<sup>1,2</sup>, P. Tanga<sup>1</sup>, P. Machado<sup>2</sup>, and E. Corsaro<sup>3</sup>

<sup>1</sup> Université Côte d'Azur, Observatoire de la Côte d'Azur, CNRS, Laboratoire Lagrange, Bd de l'Observatoire, CS 34229, 06304 Nice Cedex 4, France

e-mail: [jferreira@oca.eu](mailto:jferreira@oca.eu); [Paolo.Tanga@oca.eu](mailto:Paolo.Tanga@oca.eu)

<sup>2</sup> Instituto de Astrofísica e Ciências do Espaço (IA), Universidade de Lisboa, Tapada da Ajuda, Edifício Leste, 2º Piso, 1349-018 Lisboa, Portugal

e-mail: [machado@oal.ul.pt](mailto:machado@oal.ul.pt)

<sup>3</sup> INAF–Osservatorio Astrofisico di Catania, Via S. Sofia 78, 95123 Catania, Italy

Received 17 April 2020 / Accepted 30 June 2020

## ABSTRACT

**Context.** Occultations of stars by asteroids are an efficient method to study the properties of minor bodies, and can be exploited as tools to derive very precise asteroid astrometry relative to the target star. With the availability of stellar astrometry thanks to the ESA mission *Gaia*, the frequency of good predictions and the quality of the astrometry have been strongly enhanced.

**Aims.** Our goal is to evaluate the astrometric performance of a systematic exploitation of stellar occultations, with a homogeneous data set and a given instrument setup. As a reference instrument, we adopt the example of a robotic 50 cm telescope, which is under construction at the Observatoire de la Côte d'Azur. We focus in particular on single-chord occultations.

**Methods.** We created a data set of simulated light curves, that are modelled by a Bayesian approach. To build the final statistics, we considered a list of predicted events over a long time span, and stellar astrometry from *Gaia* data release 2.

**Results.** We derive an acceptable range of observability of the events, with clear indications of the expected errors in terms of timing uncertainties. By converting the distribution of such errors to astrometric uncertainties, we show that the precision on a single chord can reach levels equivalent to the performance of *Gaia* (sub-milli-arcseconds). The errors on the asteroid position are dominated by the uncertainty on the position of the occultation chord with respect to the barycentre of the object.

**Conclusions.** The limiting factor in the use of occultation astrometry is not the light curve uncertainty, but our knowledge of the asteroid's shape and size. This conclusion is valid in a wide range of flux drops and magnitudes of the occulted star. The currently increasing knowledge of the shape, spin properties, and size, must be used to mitigate this source of error.

**Key words.** occultations – minor planets, asteroids: general – astrometry – techniques: photometric – methods: numerical

## 1. Introduction

Transit and occultation phenomena have been exploited for decades as powerful tools to infer the properties of the occulting or the occulted object. In the case of asteroids occulting a star, the main results are size and shape measurements, which are used to study specific targets (Đurech et al. 2015) or to calibrate other size-determination approaches (Shevchenko & Tedesco 2006).

For Centaurs and trans-Neptunian Objects (TNOs), stellar occultations offer the best opportunities to derive precious physical properties. Remarkable achievements include the discovery of a ring system around (10199) Chariklo (Braga-Ribas et al. 2014), the size measurement of Eris (Sicardy et al. 2011) and other TNOs, the determination of an upper threshold for the atmospheric density of Makemake (Ortiz et al. 2012), and the detection of variations in the atmosphere of Pluto (Sicardy et al. 2003; Meza et al. 2019), to mention a few.

So far, the main challenge of occultation observations resides in the accuracy of the predictions, as the uncertainty on an asteroid ephemeris usually exceeds the size of the occultation track. A first improvement in the late 1990s, brought by the HIPPARCOS astrometric mission (Perryman 2012), has allowed observers to obtain more reliable predictions for asteroids with a diameter >50 km, occulting a sample of  $\sim 10^5$  stars in the HIPPARCOS

catalogue with the best-known astrometric parameters (Colas et al. 2011; Dunham et al. 2002).

However, the *Gaia* mission by the European Space Agency (ESA) is completely changing the landscape by bringing a substantial enhancement of the prediction efficiency, thanks to the sub-mas (milli-arcseconds), precision astrometry of both target stars and asteroids.

The pre-release of star positions and proper motions appearing in the second data release (DR2) (Gaia Collaboration 2016, 2018b,a) has demonstrated the reality of the expected improvement, with successful, accurate predictions of the occultation path for several objects, including Pluto and other TNOs such as the New Horizons mission target (486958) Arrokoth (Buie et al. 2018, 2020; Porter et al. 2018; Ortiz et al. 2019).

Spoto et al. (2017) have tested the use of observed occultations as astrometric measurements, which have an accuracy comparable to that of the target star. Such an approach, if systematically applied, can give ground based observers access to ultra-precise astrometry at the level of *Gaia*, even after the mission has concluded its operations, with the uncertainty on the stellar proper motions as the only degrading factor of the measurement precision.

We recall here the importance of collecting accurate measurements of asteroid positions, at better than  $\sim 10$  mas accuracy, as this is the only way to solve some fundamental issues of

asteroid dynamics, intimately linked to our knowledge about the evolution of the Solar System. Very important in this respect is the measurement of the Yarkovsky diurnal effect, which is relevant to the delivery of asteroids in the Earth space environment, and more in general to understanding the evolution of the asteroid belt (Vokrouhlický et al. 2015). We also mention the determination of asteroid masses, as a very small number of them are unambiguously known at an acceptable accuracy (Scheeres et al. 2015).

The astrometric data set based on charge-coupled device (CCD) observations, available from the Minor Planet Center (>200 millions observations), has an average accuracy of  $\sim 400$  mas (Desmars et al. 2015). Astrometry by the HIPPARCOS mission or by stellar occultations exhibits better residuals (10–150 mas) but they represent  $\sim 0.5\%$  of the total. Radar ranging measurements have a comparable performance but, again, on a very limited sample mostly composed of near Earth asteroids (NEA) (Ostro et al. 2002; Farnocchia et al. 2015). Due to the rapid fading of the signal intensity with distance, only a few large main belt objects have been observed with this technique. In summary, the total number of measurements with an accuracy of  $\sim 10$  mas is a tiny fraction, represented by  $\sim 10\,000$  entries.

In this context, the *Gaia* DR2 asteroid data set alone, with two million astrometric positions for asteroids at  $\sim$ mas accuracy, already represents a spectacular improvement. However, the time interval over which the observations have been obtained is rather short. A joint use of DR2 with pre-*Gaia* data is then necessary to detect secular effects.

Even after the last data release by *Gaia* covering the entire operational phase (currently accepted for extension to 2022), the task of securing very accurate astrometric measurements over longer time spans will be necessary to improve Yarkovsky detections. In particular, detecting Yarkovsky directly in the main belt will be of the highest importance, to use it as a “clock” for better constraining the age of the collisions that created asteroid families (Spoto et al. 2015). As the semi-major axis change rate due to the Yarkovsky effect is stronger for smaller asteroids (going as  $D^{-1}$ ) and weaker at increasing heliocentric distance (as  $r^{-2}$ ), to reach its detection in the main belt, asteroids with a diameter of  $D \lesssim 10$  km must be targeted.

The forthcoming Legacy Survey of Space and Time (LSST) by the Vera C. Rubin observatory, will certainly contribute to this effort through the discovery and follow up astrometry of a large number of small asteroids, both in the NEA and main belt population (Ivezić et al. 2019). It will operate between 2023 and 2033, with two more years added to the mission for final data processing. Its contribution will impact all targets fainter than magnitude 16 (saturation limit of the telescope), however, the single-epoch astrometric accuracy will be limited to 10–20 mas.

The only technique capable of obtaining, at least in principle, an astrometry close to *Gaia* quality, is the observation of stellar occultations on a systematic basis, on asteroids smaller than those considered in predictions up to now. This approach will clearly disclose the possibility to extend in time the collection of the best possible astrometry and push the limits to detect subtle dynamical effects.

The expansion of the number of usable stellar targets (the *Gaia* sample is approximately complete at all magnitudes  $G < 20.5$ ) and the strong quality improvement for  $\sim 3 \times 10^5$  asteroids are at the origin of the revolution triggered by *Gaia*. While asteroid orbits improved by *Gaia* astrometry are gradually published and optimised, the number of potentially observable events increases by orders of magnitude (Tanga & Delbo 2007).

This change of perspective clearly suggests that fixed, specialised telescopes can become very efficient and observe several occultations per night. Such a systematic, massive exploitation clearly calls for automated systems to observe, process and store the collected data.

In the framework of a project named UniversCity, the Observatoire de la Côte d’Azur (OCA) is building a 50 cm robotic telescope that will start to operate at the Calern observing station in 2020.

A full description of the instrument and its operation is beyond the scope of this article. Rather, our main goal is to assess the possible astrometric performance of occultation astrometry for a large sample of main belt asteroids, when a single observing site is considered. As we discuss further below, this is difficult to obtain by exploiting the existing data set of observations. For this reason, we present an independent assessment, corresponding to constant conditions of observations, a homogeneous set of data representing occultation light curves, a given instrument, and an identical data reduction approach. Our results demonstrate the performance that can be reached under controlled, constant, and nearly ideal conditions. They can be rescaled to different instruments and observational conditions. We use them to determine which events can be considered to be observable (i.e. capable of providing usable data) and the astrometric accuracy that can be obtained from them.

We stress here that our focus is on the massive exploitation of a statistically significant amount of data obtained by a single fixed instrument, capable of exploiting the expanded domain of exploitable predictions enabled by *Gaia*. The original aspect of this work is that such an approach is clearly different from the common networked observation, in which several telescopes (usually portable ones) are deployed to cover an event by specific, high priority objects (binary asteroids, TNOs, mission targets). We will further detail the general properties of occultation observations available in the archives and their associated astrometry in the next section. Section 3 illustrates the simulations that we use to explore a homogeneous set of light curves, which are then fitted to a simple model as explained in Sect. 4. In Sect. 5 we show the results of the fit, from which a performance in the astrometry is derived (Sect. 6). The main conclusions and limitations of our approach are summarized in Sect. 7.

## 2. Properties of currently available asteroid astrometry

Stellar occultations of asteroids are being observed by networks of dedicated amateurs, with a few coordinators who compute and update predictions, collect the results, and process the data to derive information on the occulting asteroid shape, size, and astrometry. Free software is also available for the different steps of this process. Occultations present a variety of difficulties (mostly a function of target star magnitude, maximum duration, and flux drop), and are observed with a corresponding variety of instruments, ranging from small photcamera objectives to large, professional telescopes.

Since the 1990s, video and CCD cameras have become the standard tool for these observations. An accurate time reference is provided by the one-pulse-per-second (1 pps) of a global positioning system (GPS) receiver, but sometimes less accurate timing is still adopted, as provided by internal computer clocks (synchronized – or not – by external devices or by network time protocol servers). Although not completely error-free, the use of the 1 pps signal of GPS is an affordable approach that can

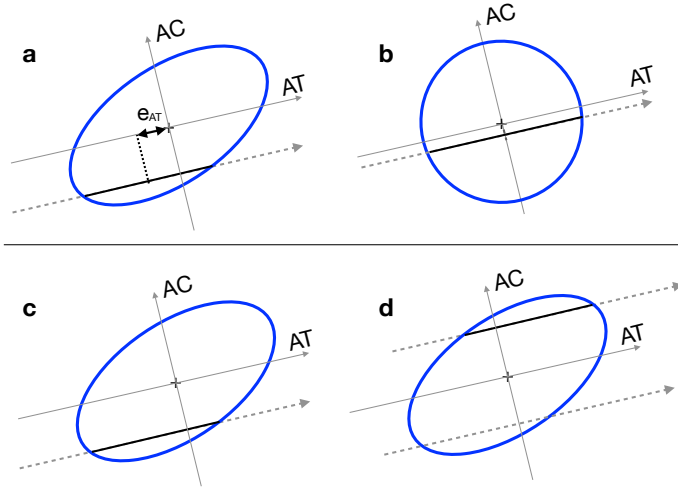


**Fig. 1.** Idealised scheme of the uncertainties involved in the astrometry derived from single chord observations of stellar occultations. We adopt as an example a very elongated ellipsoidal asteroid, projected on the fundamental plane in which the asteroid is at rest and the occulted star moves along the dashed arrows. The AC and AT axes represent the across and along-track directions, respectively. In (a) the observed chord duration (black segment) is the same as for the surface-equivalent sphere in (b). The mid-chord point corresponds to the barycentre position in (b), but not in (a), where the error on the derived astrometry  $e_{AT}$  cannot be estimated without a precise knowledge of the shape. Points (c) and (d) represent the ambiguity on the AC position of the observed chord, which can be on opposite sides of the barycentre.

easily reach an  $\sim 1$  ms accuracy when electronically coupled to the shutter signal of the acquisition camera.

The timing accuracy is very relevant to our research as the epoch of disappearance and reappearance of the occulted stars are the fundamental quantities that are obtained from the observation. As the apparent motion of the asteroid with respect to the target star can be predicted with high precision, the timings can be converted to an accurate astrometric position in the direction of the asteroid motion itself. We will call this measurement the “along track” (AT) position or astrometry.

In the direction perpendicular to the asteroid motion (i.e. “across track”, or AC), the uncertainty of the astrometry can vary, depending upon the knowledge of the physical properties (size, shape) of the asteroid. Even the ideal case of a spherical occulter can produce a large uncertainty on the AC position when its size is not well constrained, unless several occultation chords are observed from different telescope sites.

The frequent case of elongated or irregular asteroids can introduce even more uncertainty into the determination of both the AT and AC position when single occultation chords are available, unless the shape and its orientation are known.

Single-chord events, suffering from such limitations, are a majority, as they represent about 60% of the whole data set of occultations (Herald et al. 2019). As we will deal with the capabilities of a single, isolated telescope, it is important to take such shortcomings into account.

Figure 1 illustrates the errors involved in the determination of the AC and AT astrometry for a non-spherical shape, which can be mitigated (but not completely eliminated for single chords) if the shape is known.

The most common error is in fact the AC ambiguity, due to the fact that a given chord duration can occur on both sides of the occultation path (Fig. 1, panels c and d). In this case, the probability distribution of the AC position is strongly bi-modal.

Extremely elongated or irregular shapes can increase such errors, which in the worst case reach  $\sim$ half the largest extension of the asteroid silhouette. For this reason, their relevance decreases with the object size and is lower than  $\sim 10$  mas for objects of 20–30 km diameter in the main belt.

To assess the expected performance of occultation astrometry for a dedicated robotic telescope, it would be tempting to use the current data set of observed events derived from the observations that are available through the Planetary Data System base (Herald et al. 2019) or the Minor Planet Center. This data set directly provides the final astrometry, represented by the relative position between the star and the asteroid at the moment of the closest appulse, as seen from the geocentre. Its derivation is strongly model dependent, as it can involve shape fitting to the observed chords, as well as complex, approximated estimations of the uncertainties.

For these reasons, we prefer to take control of the whole process and proceed to an evaluation of the telescope performances based on simulated signals, whose properties are calibrated on real, measured quantities and known CCD camera specifications. Most importantly, this approach allows us to extend the investigation to poorly known regimes of “difficult” events (i.e. short durations, small flux drop) that are not adequately represented among past recordings. Occultation observers usually favour high-probability events that have good predictions and are not at the limit of their instruments. This approach introduces a clear bias that we intend to overcome, as a robotic telescope can more easily be programmed to spend time on less probable or difficult events.

### 3. Occultation light curves: simulations

We aim to study a reliable method to retrieve the parameters of a large number of occultation light curves, capable of operating on a variety of signal properties. To achieve this goal, we simulated a set of occultation signals, with different durations of the occultation and signal-to-noise ratios (S/N).

We simulated stellar occultation light curves as if they had been observed by imaging at visible wavelengths and as if the photometry of the occulted star, plus a reference, had been acquired by aperture photometry after the usual corrections (bias and dark frame subtraction) and normalisation (flat field).

We also consider that the asteroid flux, right before and after the event, falls within the aperture of the target star, such that at no time are the two sources resolved. Our reference for the out-of-occultation flux will thus be a luminosity level corresponding to the combination of the two sources. This is the usual situation, as their images are completely merged in the proximity of the event epoch.

Also, we consider that the Fresnel diffraction (Roques et al. 2008; Pass et al. 2018) is negligible, as the typical Fresnel length for a main belt asteroid is  $\sim 300$  m, much smaller than the asteroid size range that we consider in this article ( $> 5$  km). At the frame rate adopted in the following sections (0.1 s), time resolution is not sufficient to reveal the diffraction pattern drifting at  $10\text{--}20$  km  $\text{s}^{-1}$  over a ground-based telescope.

We can also completely neglect the apparent star size in this context, as for all stars with  $V_* > 11$  it is well below 1 mas. We have verified this assumption by using the stellar radii and parallaxes published in *Gaia* DR2. Although these have been obtained without corrections for the interstellar reddening, they are expected to be accurate enough for an estimate at  $\sim 20\%$  level (Andrae et al. 2018). In the data set, we find a maximum apparent

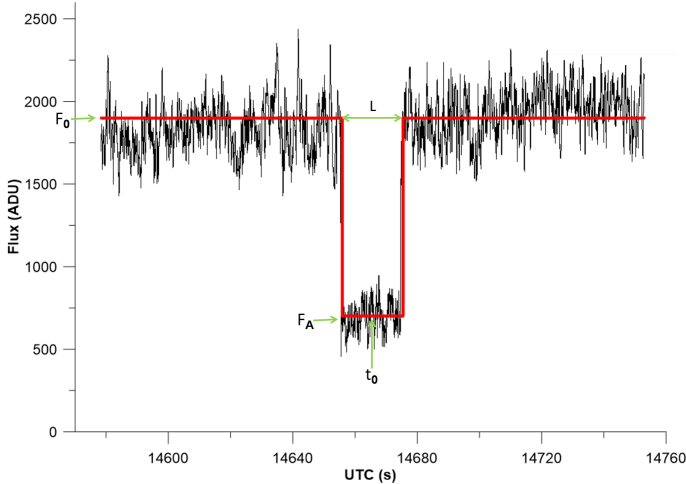


**Fig. 2.** Example of a reduced light curve with the resulting model fit (as described in Sect. 4). Asteroid (41) Daphne occulted a  $V \sim 9.3$  star on March 2, 2017. From the fit (red curve), the measured occultation duration was  $18.8 \pm 0.2$  s, and the drop 63% of the original flux, or  $1.08 \pm 0.01$  magnitudes. Data points of the flux outside the occultation extend beyond the plotted range on both sides, which contributed to the calculation of the combined flux.

diameter of  $\sim 0.2$  mas at  $V_* = 11$ , which is too small to become a serious concern.

We adopt a conservative transmission efficiency (telescope reflections, correcting optics, and camera included) of 0.3. Some observations performed at the site of the UniversCity telescope with a  $\sim 1$  m instrument, with an Andor iXON 888 camera and a Johnson-Cousin standard  $R$  filter, have allowed the determination of a typical background value used for our simulations of  $N_{\text{bg}} = 7.400 \text{ ADU s}^{-1} \text{ pixel}^{-1}$ , (ADU - analog-to-digital unit) per unit square metre of the mirror surface. These are re-scaled to the size of the UniversCity telescope, by assuming the same transmission factors, as well as the same camera and filter ( $R$ ).

By taking into account photon noise from the sources, background, read-out noise from the Andor iXON 88 camera, and scintillation noise caused by atmospheric turbulence, we find that, for an exposure time  $dt = 0.1$  s, the star’s scintillation dominates up to magnitude  $V_* \sim 9$  and the background, read-out, and dark-current noise sources take over from  $V_* > 11$ . A practical limit for a star at a low zenith distance turns out to be  $V_* \sim 13$  at  $S/N \sim 5$ . We model all the noise sources, including scintillation, following Mary (2006) to which we refer for details.

To better sample the limits of faint drops and signals ( $S/N \sim 3$ ), and to include unfiltered imaging ( $R$  filter removed) with respect to the limiting magnitude estimate above, we do not consider very bright stars (those contributing only a fraction of events in practice) and focus on the magnitude range  $V_* = 11\text{--}14$ . For this same goal, we also select events whose ratio between duration and exposure time is in the range of two to ten.

Our model for the light curves consists in a flat signal outside and inside the occultation and a sharp transition at the beginning and end of the event, and it is described (as illustrated in Fig. 2) by the following parameters:

- $F_0$ : the combined, summed flux from the asteroid,  $F_A$ , and the target star,  $F_*$ , before and after the occultation. The corresponding magnitude is defined as  $V_c$ .
- The flux drop  $F_0 - F_A = F_*$ , corresponding to a magnitude drop:  $V_{\text{drop}} = 2.5 \text{ Log} [(F_* + F_A)/F_*]$ .

- $L$ : the duration of the occultation.
- $t_0$ : the central epoch of the occultation.

The parameter ranges for our simulations are as follows:

- Star magnitude  $V_* \in [11.5, 14.0]$ .
- Magnitude drop  $V_{\text{drop}} \in [0.3, 1.0]$ .
- Duration  $L \in [0.2, 1.0]$  s.

The exposure time is considered to correspond to the sampling interval, an assumption that is valid in general for fast video cameras such as the iXON mentioned above. For this reason, hereinafter we adopt simply “exposure time”, although a read-out time must be accounted for, depending on the acquisition device.

The simulations also adopt a constant exposure time,  $dt = 0.1$  s. The mid-point  $t_0$  is assumed to fall around the centre of the simulated time span, but its exact timing is shifted with a uniform probability distribution within an interval  $\pm dt/2$ , to randomise the phase of the sampling with respect to the central epoch of the minimum. Discrete intervals of (0.2 magnitudes) were used as a distribution for  $V_*$ .

We note that magnitude drops exceeding our chosen interval are possible when faint asteroids are involved. However, larger drops are easier to observe, so their contribution to assess the limitations of our approach is minor.

Noise is added to the signal by random sampling of a Gaussian distribution, whose variance is computed from the combination of the various sources (Mary 2006).

We note that when acquiring a real signal on the sky, the flux  $F_0$  can be obtained with very high accuracy before and after the occultation, provided that the sky is photometrically stable, by measuring it on a time interval (for instance, a few minutes) much longer than the occultation event itself (a few seconds). Also, multiple reference stars can be used to minimise spurious fluctuations in the measured flux. Assuming that this procedure is validated for a specific setup, the uncertainty on  $F_0$  can be considered negligible.

We can expect that the factor dominating our capacity to retrieve the parameters of the occultation signal is related to the signature of the light drop with respect to the noise. We thus define the drop-to-noise ratio (DNR) expressed as:

$$\text{DNR} = \frac{F_0 - F_A}{\sqrt{\sigma_{(F_0)}^2 + \sigma_{(F_A)}^2}}$$

where  $\sigma_{F_0}$  and  $\sigma_{F_A}$  are the noise of the signal outside and inside the occultation. Our results in the following confirm that the DNR is the main parameter characterising the “difficulty” of the data reduction for each light curve.

To sample the parameter ranges defined above, a total of 7920 light curves were simulated. Two examples of simulated light curves that have different minima durations and DNRs are shown in Fig. 3.

In addition, we test the presence of false positives, which should start to appear when the expected DNR is very low. Our approach is to use the same parameters for the simulations exploited above, but with the elimination of the occultation signature in the data. The processed signal is thus just the constant out-of-occultation level,  $F_0$ , with its noise. We still apply priors as if the occultation was present (next section).

Eventually, we note that the discretisation of  $V_*$  in the simulation parameters, will show up in the graphic representation of our results, under the form of clusters around DNR values. We are aware of this limitation, but we will see that the conclusions are statistically robust and would not change with the adoption of a more uniform distribution.

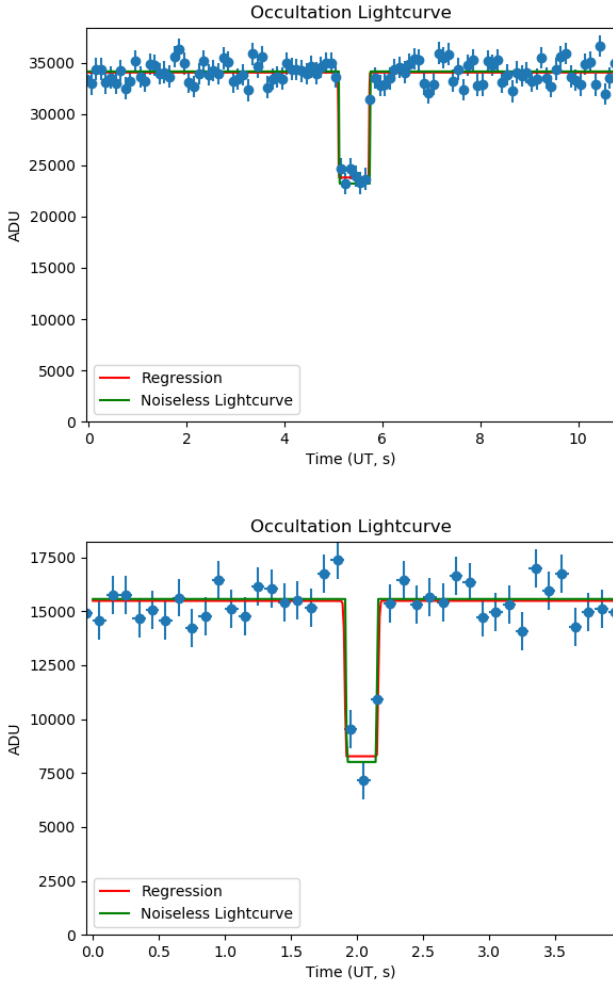


**Fig. 3.** Examples of simulated light curves (green line), sampled with our noise model at  $dt=0.1$  s (blue dots). The associated blue bars represent the one-sigma uncertainties derived from the noise model. Regression is obtained through the method explained in Sect. 5 (red). *Top panel:*  $V_* = 12.5$ , drop of 0.4 magnitudes, nine samples, DNR = 4.9. *Bottom panel:*  $V_* = 13.5$ , drop of 0.7 magnitudes and two samples, DNR = 2.1.

#### 4. Regression procedures on the simulated data

To retrieve the light curve parameters from the simulated data sets described above we adopt the Bayesian inference method (BIM) by a nested sampling Monte Carlo algorithm as implemented in the DIAMONDS<sup>1</sup> package (Corsaro & De Ridder 2014a,b; Corsaro et al. 2018).

To apply the BIM, we implement a light curve function as:

$$F(t) = F_0 - F_A S(\sigma, t_0, L) \quad (1)$$

where  $S$  is a “supergaussian” function composed of three branches:

$$S(\sigma, t_0, L) = \begin{cases} N(t, t_0 - L/2, \sigma) & t \leq t_0 - L/2 \\ 1 & t_0 - L/2 \leq t \leq t_0 + L/2 \\ N(t, t_0 + L/2, \sigma) & t \geq t_0 + L/2. \end{cases}$$

In the equation above,  $N(x, x_c, \sigma)$  is a normal distribution function of  $x$ , centred at  $x_c$ , of width  $\sigma$ . With the small value for  $\sigma$  that we adopt (1/10 of the exposure time) the supergaussian

<sup>1</sup> <https://github.com/enricocorsaro/DIAMONDS>

becomes similar to a “gate” function, but it preserves its properties of being continuous with continuous derivatives. For our specific case of occultation events, the possibility of the BIM to exploit priors is a very relevant advantage, as the predictions of occultation events provide exploitable information on the expectations for each of the light curve parameters, in particular the expected maximum duration, flux drop and centre epoch of the event.

Each simulated light curve is described by a combination ( $V_*, V_{\text{drop}}, L, t_0$ ) or equivalently in term of fluxes ( $F_0 - F_A, F_A, L, t_0$ ). These parameters are related to the observation of a hypothetical predicted event. In practical applications, the possible range of values that they can assume is constrained by the a priori knowledge conveyed by the prediction, which informs us about the brightness of the star and the asteroid, the maximum expected duration, and other factors. As a consequence, defining Bayesian priors to reduce our simulated light curves is equivalent to using the predicted parameters of an occultation event to reduce its observed light curve. The only difference is that in the case of a real event the probability distribution of the priors is constrained by the prediction; in the case of simulations, it is constrained by the nominal values used to produce each light curve. In both cases we need to make reasonable guesses about the width of the distribution, which we assume to be Gaussian.

In the case of real observations, that exploit predictions, the total flux  $F_0$  can be estimated from the brightness of the target star and the asteroid, by taking into account the properties of the instrument and the observing conditions. The flux drop  $F_0 - F_A$  can also be estimated, since the theoretical brightness of the asteroid can be affected by a rather large error (several tenths of magnitude) due both to the absolute magnitude  $H$  errors and to the viewing or illumination geometry of a possibly irregular shape.

The maximum duration  $L_{\text{max}}$  is provided in general by the prediction, but can be affected by a large uncertainty, depending both upon the uncertainty on the object size, and on the projection of its shape at the epoch of the event.

Eventually, knowledge of the absolute occultation epoch  $t_0$  is dominated by the uncertainty on the asteroid orbit and the star position. For typical multi-opposition main belt objects, the uncertainty on  $t_0$  is of the order of a few seconds. In practice, the observation always extends for a much longer time before and after  $t_0$ .

On the basis of these considerations, we define Gaussian priors whose averages are derived from the nominal parameters ( $F_0 - F_A, F_A, L, t_0$ ), and standard deviations consistent with those of the usual predictions. In particular:

- $\sigma_{F_0} = 0.5$  mag and  $\sigma_{F_*} = 0.3$  mag. This choice is done to include the discrepancy present in the prediction of asteroid brightness, which is well known to be affected by inaccurate absolute magnitude (Pravec et al. 2012), slope parameters and shape-related effects. The star magnitude is much better known in general in the current catalogues, but variability and colour effects can be present, so we prefer to be conservative.
- $\sigma_L = 0.2 \times$  the maximum duration ( $L_{\text{max}}$ ). This parameter is affected by our knowledge of asteroid size and shape. Our choice is compatible with uncertainties for asteroids of a few kilometres in diameter in the NEOWISE survey (Masiero et al. 2011; Mainzer et al. 2011a,b). This choice – while not excluding that regression from reaching a shorter duration – implicitly introduces the assumption that central chords (diametrical events) are more probable. A more sophisticated

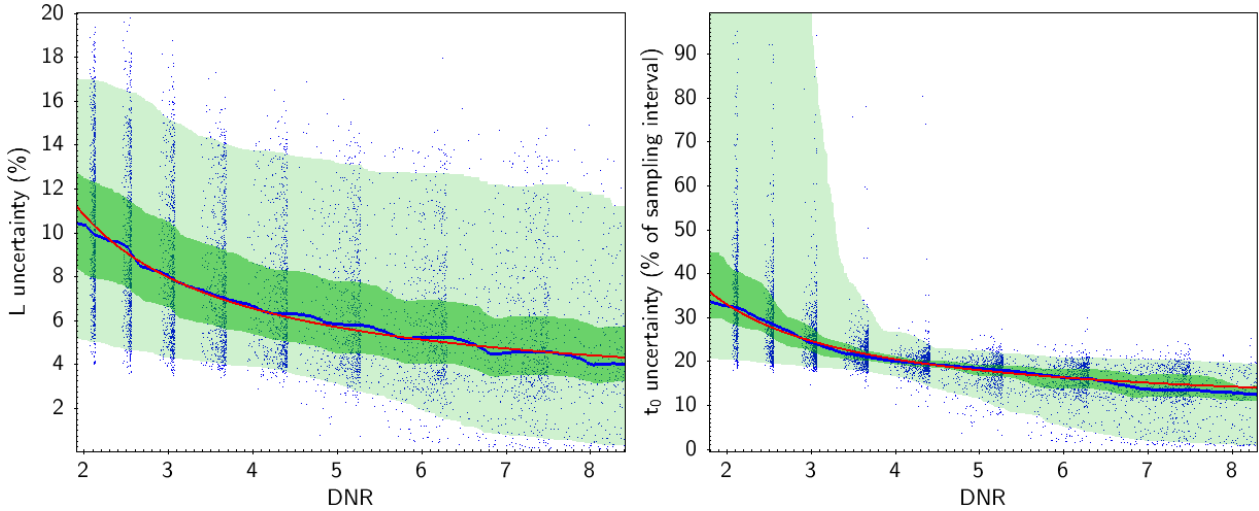


**Fig. 4.** Uncertainty on the duration  $L$  and the centre epoch  $t_0$  of the occultation, as a function of the DNR, estimated by the standard deviation of the posterior distribution, after Bayesian modelling. Each dot represents a result obtained from a simulated occultation. The continuous blue line is the smoothed average value, while the shaded areas enclose the quantiles equivalent to  $1\text{-}\sigma$  and  $2\text{-}\sigma$ . The trend  $\sim 1/\text{DNR}$ , explained in the text, is represented by the red line. The uncertainty is expressed, respectively, as percentage of duration, and of the exposure time. The clustering of the blue data points around discrete DNR values is a consequence of the choice of a discrete  $V_*$  distribution, but it does not affect the estimation of the general trend.

approach could be to impose a realistic probability distribution for the chord duration.

- $\sigma_{t_0} = 3$  s. For each prediction, by propagating the asteroid orbit errors and the error estimate on the star astrometry, an associated uncertainty on the central epoch can be computed. However, in the process, the contribution of astrometric biases on the orbit accuracy (especially those present in old asteroid astrometry) are easily underestimated. We adopt a single fixed value here, to mitigate this issue and avoid overly optimistic uncertainties.

Our choices for the definition of the priors are very general. The adoption of Gaussian priors is a compromise permitting us a first exploration of the performance of the BIM on the simulations. When applied to real observations, more complex prior distributions can be used, adjusted for the distribution of the uncertainty on the asteroid ephemeris, the star astrometry and brightness. Varying sky conditions and possible timing errors can also affect the prior shape and spread. The associated difficulty of implementing the corresponding automated processing, capable of taking them into account, are outside the scope of this article, but can be included in practical applications.

## 5. Results of the regression on the simulated light curves

The significance of the occultation can then be evaluated by comparing the Bayesian evidence of two light curve models: one containing the occultation signal  $E_{\text{occ}}$ ; the other, a constant (no occultation) function  $E_{\text{flat}}$ <sup>2</sup>. From the processing of our simulated light curve, we compute the detection probability of the occultation using the evidence ratio  $C = E_{\text{occ}}/(E_{\text{flat}} + E_{\text{occ}})$ . We consider that a model is strongly significant with respect to another if the Bayesian evidence of the former is at least five orders of magni-

<sup>2</sup> We recall here that the Bayesian evidence (or marginal likelihood) is given by the average of the likelihood distribution over the parameter space set by the priors.

tude larger than that of the latter model, yielding a  $C_{\text{crit}} \sim 0.993$ . We thus classify as “non significant” all results with  $C < C_{\text{crit}}$  (Corsaro & De Ridder 2014a,b).

In the following, we characterise the results obtained from the simulated light curves on the basis of the uncertainty (standard deviation) of the marginal distribution for the duration and the centre epoch ( $\sigma_L$  and  $\sigma_{t_0}$ ), which are the two fundamental parameters determining the observed chord length and the position of the asteroid relative to the star, in the direction of its motion. While the first quantity is related to the physical properties of the object (size, shape), the second directly defines the quality of the occultation astrometry, the seminal parameter that motivates our study.

Hereinafter,  $\sigma_L$  is expressed as a percentage of the total duration, while  $\sigma_{t_0}$  is a percentage of the exposure time. As in general the occultation minimum is sampled by several intervals, we find a smaller uncertainty for a higher DNR (Fig. 4). Interestingly, there is a clear trend of increased error dispersion for  $\text{DNR} < 3$ , implying that the determination of  $\sigma_{t_0}$  in limit conditions, despite a good average performance, can be unreliable. However, with the exception of such extreme situations, the average of  $\sigma_{t_0}$  is well below the exposure time. The overall trend of the average uncertainties is  $\sim 1/\text{DNR}$ , as expected for a trend described by a general S/N.

The fraction of false positives and non-significant solutions are additional indicators of our capabilities of retrieving the occultation parameters. We can observe in Fig. 5 that at  $\sigma_{t_0} > 100\%$  non-significant solutions start to dominate the population. However, we see that already at  $\sigma_{t_0} \sim 50\%$  about 1% of the solutions are false positives. As such a validation criterion based on a threshold for uncertainties only, can still allow for a small percentage of false positives.

A more stringent criterion comes from the detection probabilities. A comparison of the distribution of the false positives with respect to the true events, shows that false positives are systematically characterised by a low detection probability,  $C < C_{\text{crit}}$ . For the events that pass the threshold of  $C_{\text{crit}}$ , the fraction of false positives becomes negligible ( $\sim 5 \times 10^{-4}$ ).

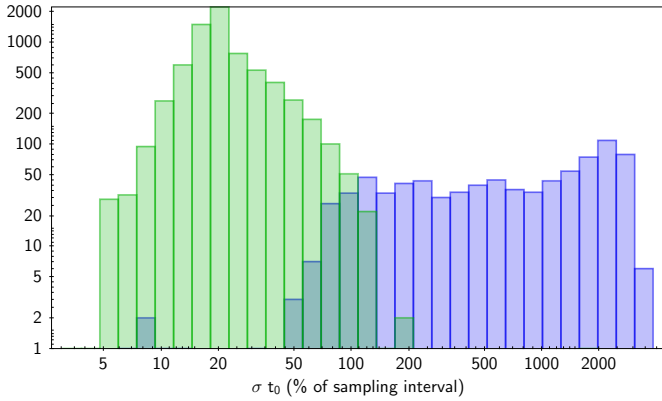


**Fig. 5.** Distribution of the significant (left, green peak) and non-significant (right, blue peak) solutions as a function of the uncertainty on the centre epoch  $t_0$ , expressed as a percentage of the exposure time. At around 100% uncertainty, the frequency of the two situations is about the same.

For completeness, we also tested the same regression on simulated light curves using a different shape of prior distribution, namely uniform probabilities, which have a constant, non-zero values within a limited interval. In this case, we obtain a worse performance. Also, while the Gaussian priors always produce a final fit, the uniform priors do not converge for 6% of the cases where the Gaussian priors are successful.

## 6. Derived uncertainty on asteroid astrometry

By a simple procedure, we can convert the precision that we expect on the centre epoch of the occultation chord (Fig. 4) to the corresponding along-track astrometric precision.

For the asteroids from the orbit database at the Minor Planet Center, we proceed by computing the predicted circumstances for occultation events from a single arbitrary site (in our case Nice observatory, MPC code 020) over a full year<sup>3</sup>. We consider a sample of *Gaia* DR2 target stars with  $V < 14$ , and include asteroids with a diameter  $> 5$  km. For each predicted event, we compute the expected DNR with our telescope configuration, and the corresponding apparent angular topocentric velocity vector  $\mathbf{v}_a$  of the asteroid, in the equatorial frame, projected on the sky.

The apparent velocity is the scale factor that allows us to convert the uncertainty on timing, given by the average shown in (Fig. 4), to an angular uncertainty on the position of the single chord relative to the occulted star, simply by the relation  $\sigma_{t_0} * \mathbf{v}_a$ .

The resulting distribution (Fig. 6) is clearly clustered towards sub-mas values, with a peak at  $\sim 0.3$  mas, showing all the potential of occultation astrometry. The colour-coded distribution also shows that chords of shorter length are in general affected by a larger uncertainty.

However, in practical application this excellent performance has to be weighed against the fact that a single chord is a poor approximation of the asteroid centre of gravity, as discussed in Sect. 2 (Fig. 1). In Fig. 6 we compare the uncertainty on the single chord to the uncertainty due to missing knowledge of the asteroid shape ( $e_{AT}$  in Fig. 1). We model  $e_{AT}$  as a fixed quantity of half the object apparent radius, computed at the epoch of each occultation event. We stress here the fact for exploiting

the astrometry in orbit computation, both AC (across-track) and AT (along-track) error sources must be included in an adequate error model, however we focus here on the AT direction, as it is the one directly linked to the timing errors that we analyse.

The along-track uncertainty,  $e_{AT}$ , dominates the error on the chord timing for objects  $> 15$  km. At the opposite end of the size range, a non-negligible fraction of small asteroids are affected by the two error sources, fit uncertainty and  $e_{AT}$ , in a more balanced way, in particular when the chord length is  $\leq 4$  sample intervals. This regime corresponds, as expected, to the rather poor sampling of the light curve minimum, which reduces the performance of the fit. By considering a typical apparent motion of a main belt asteroid ( $5\text{--}10$  mas  $\text{s}^{-1}$ ) in the inner belt (where  $\sim 1$  mas  $\sim 1$  km at opposition), and our time sampling of 0.1 s, the corresponding physical chord length is  $\sim 1.5\text{--}3$  km. This represents a practical limit, which can be overcome only by increasing the sampling frequency, if the available flux allows.

For larger objects, the overall error budget seems to be dominated by shape and size effects, increasingly for larger asteroids, and one should note that if these physical properties have been independently measured, they can be exploited to correct the astrometry derived by the occultation. Today, some thousands of shapes and rotational parameters (period, spin axis) are known, mainly from rotation light curve inversion. The largest database of asteroid sizes ( $\sim 10^5$ ), is produced by the cited NEOWISE survey. As the number of asteroids for which shape and size is known will increase in the future, the possibility to determine the position of the centre of mass with respect to the observed chords will be more and more common, permitting us to get closer to the limit represented by our single-chord astrometric accuracy.

Eventually, an evaluation of the final accuracy will be provided by the use of single-chord occultation astrometry in the improvement of orbits, where post-fit residuals can be used to evaluate anomalies in the adopted error model and to identify the outliers. This exploration, done on the data set currently available and extending Spoto et al. (2017) will be part of a separate article.

Here, we limit our comparison to some real positive events, by processing their light curve with the same approach used for the simulations. We looked for a set of events observed with video or CCD cameras over the last approximately ten years, and that have both a DNR and a duration in the appropriate range for the comparison (for instance “easy” events with very high DNR are of little interest here). For the chosen light curves, the sampling is regular and no missing data are present. This is clearly a small sample, but despite a growing number of reports, only a fraction of observers provide the photometric data and satisfy at the same time our selection criteria.

The selected sample consists of 25 events. The DNR is estimated directly from the light curve, in the absence of the required information for more accurate modelling. Drop-to-noise ratio computation shows that 18 events fall in the range of interest to us (Table A.1).

We notice (Fig. 7) that the overall trend is satisfactorily respected. A larger dispersion is present, which is probably the result of the large variety of instruments and observational conditions, certainly much less homogeneous than in our simulated sample. We consider that within the limit of this comparison our model appears to be close enough to the reality to be usable for an approximate estimate of the performance of our general survey. The lack of a clear dependence on the number of data that sample the light curve minimum, as long as there at least two or three data points, further strengthens the role of the DNR in the characterisation of the performance.

<sup>3</sup> By the asteroid occultation package “Linocult”, <http://andyplekhanov.narod.ru/occult/occult.htm>

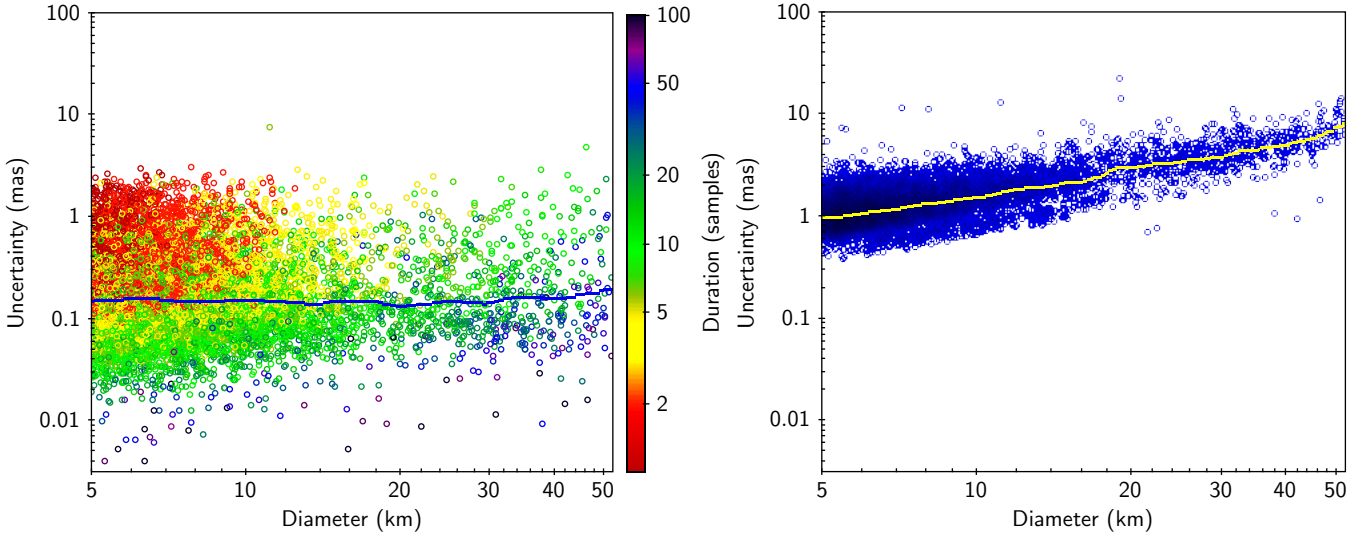


**Fig. 6.** Expected distribution of the astrometric uncertainty on the single chord estimated by our accuracy model, applied to a large set of predictions. *Left panel:* only the component of the uncertainty relative to the fit of each light curve by the BIM is taken into account. The colour corresponds to the chord length, expressed as the number of data points within the light curve minimum. *Right panel:* uncertainty including the AT error as derived from a simple model (half of the asteroid apparent radius, computed for each event). The continuous lines are the smoothed averages of the two distributions. For  $D < 10$  km and occultation duration  $< 5$  samples, the uncertainty due to asteroid size no longer dominates and the distributions overlap.

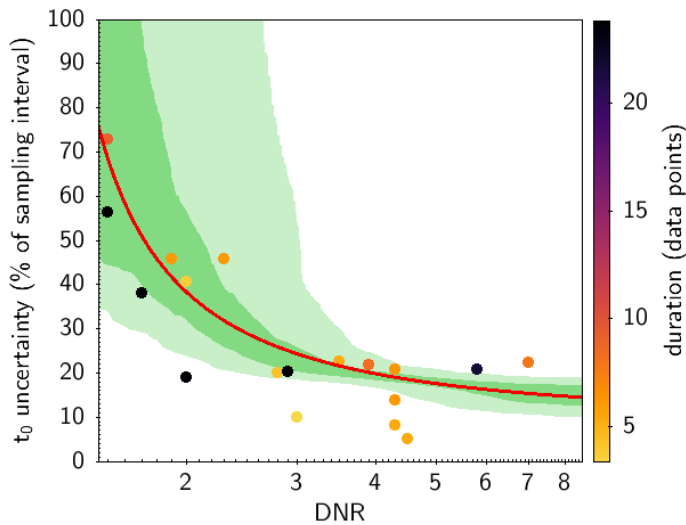


**Fig. 7.** Drop-to-noise (DNR) ratio and uncertainty on central epoch for a number of observed events similar to those adopted for the simulation. They appear as coloured circles superposed on the general trend of Fig. 4 from which we reproduce only the average (red) and the one to two sigma levels. The colour of the circles is associated to the number of data points in the occultation minimum, indicated by the scale at the right of the plot.

## 7. Conclusions

With the help of simulations, we show the capabilities of detecting and measuring occultation signals by a specific telescope setup in the idealised framework of homogeneous data quality, focusing in particular on the uncertainty on chord length ( $\sigma_L$ ) and central occultation epoch ( $\sigma_{t_0}$ ). Our statistics focus on main belt asteroids, the largest population offering both scientific challenges and the highest frequency of occultation events.

We show in quantitative terms that  $\sigma_{t_0}$  reaches a sub-sampling resolution, with a sensible degradation of the

performance for  $DNR < 3-4$ . In practice, when evaluating the results on real light curves for low DNRs, without knowing a priori the reality of a detection, only solutions with  $C > C_{crit}$  should be selected. The resulting probability of having a false positive will then be  $\sim 5 \times 10^{-4}$ .

Our results depend essentially on the DNR and (to a smaller extent) on the number of samples in the occultation minimum. The performances of other instruments and acquisition setups can be evaluated by computing the aforementioned quantities.

Another factor that we do not consider here is represented by the possible systematic effects that are not included in our noise error budget. The most important are the possible presence of time correlation in the noise (Fig. 2) and the presence of fluctuations related to unstable transparency conditions. Also, the possible effect on the light curve of stellar multiplicity (that shows up sometimes in the form of stepped light drops) can be considered in future and need a different modelling approach.

In fitting real events, another adaptation will be needed, by changing the Gaussian probability on the duration to a distribution that is less penalizing for chords that are shorter than the maximum duration, if the occultation is not central. In the context of our article this is not a limitation, as all our simulations include durations close (at noise level) to their nominal maximum values.

We also find that single-chord accuracy becomes relevant for a non-negligible fraction of occultation events involving asteroid of sizes  $D < 15$  km, for which the absolute uncertainty on the barycentre derived from a single chord becomes sensitive to size and shape. This is especially true for chords of low duration (i.e. few data points in the occultation minimum). With the improving accuracy of occultation predictions for smaller asteroids and fainter stars, an increasing fraction of observed events will fall into this domain. In particular, robotic telescopes can systematically attempt events whose probability is moderate (for instance 20–30%): these will typically fall in the above range. This is also the size range of interest for obtaining new astrometry of target candidates for the detection of the Yarkovsky effect.

We stress that we do not develop here the problem of the error model in the AC direction, which is entirely size and shape dependent and should include the ambiguities illustrated in Fig. 1. In using occultations for orbit refinement, this component must also be carefully evaluated. A recipe for the complete error model (AC, AL) and its use for orbit refinement will be detailed in a forthcoming article.

The issue of the model dependence of occultation astrometry, involving knowledge of shape, size, and rotational properties, is mitigated by the increasing knowledge that we have of them. We mention here the fact that single occultation chords will eventually contribute to the reconstruction of shapes and sizes. In fact, even isolated events have an astrometry accurate enough to improve orbits and subsequent occultation predictions. For specific objects, the prediction can become reliable enough to justify the deployment of mobile telescope arrays, thus effectively constraining the asteroid size through multiple chords. In this respect, we can conclude that the synergy between fixed telescopes hunting for single chords and traditional, multiple sites targeting specific events with improved predictions, is a very promising and fertile development in the domain of stellar occultations.

*Acknowledgements.* This research has been supported by the Pessoa program for science cooperation between Portugal and France, the Programme Nationale de Planetologie in France, the BQR programs of Laboratoire Lagrange and Observatoire de la Côte d'Azur. E.C. is funded by the European Union Horizon 2020 research and innovation program under the Marie Skłodowska-Curie grant agreement No. 664931. P.M. acknowledges project FCT 395 P-TUGA PTDC/FIS-AST/29942/2017. A special thanks to Rui Agostinho (IA) and Jean-Pierre Rivet (OCA), for their help on some critical aspects of our light curve modelling, and to the anonymous referee who helped to considerably improve the manuscript. We acknowledge the use of the Linoccul package by A. Plekhanov to compute the predictions of asteroid occultations described in Sect. 6. For this task we made use of data from the European Space Agency (ESA) mission *Gaia* (<https://www.cosmos.esa.int/gaia>), processed by the *Gaia* Data Processing and Analysis Consortium (DPAC, <https://www.cosmos.esa.int/web/gaia/dpac/consortium>). Funding for the DPAC has been provided by national institutions, in particular the institutions participating in the *Gaia* Multilateral Agreement. This research made use of Astropy (<http://www.astropy.org>), (Astropy Collaboration 2013, 2018); matplotlib (Hunter 2007); scipy (Virtanen et al. 2020).

## References

- Andrae, R., Fouesneau, M., Creevey, O., et al. 2018, *A&A*, 616, A8  
 Astropy Collaboration (Robitaille, T. P., et al.) 2013, *A&A*, 558, A33  
 Astropy Collaboration (Price-Whelan, A. M., et al.) 2018, *AJ*, 156, 123  
 Braga-Ribas, F., Sicardy, B., Ortiz, J. L., et al. 2014, *Nature*, 508, 72  
 Buie, M., Porter, S. B., Verbiscer, A., et al. 2018, *AAS/Div. Planet. Sci. Meeting Abstracts*, 50, 509.06  
 Buie, M. W., Porter, S. B., Tamblyn, P., et al. 2020, *AJ*, 159, 130  
 Colas, F., Frappa, E., Lecacheux, J., et al. 2011, *EPSC-DPS Joint Meeting 2011*, 1538  
 Corsaro, E., & De Ridder, J. 2014a, *A&A*, 571, A71  
 Corsaro, E., & De Ridder, J. 2014b, *Astrophysics Source Code Library* [record ascl:1410.001]  
 Corsaro, E., De Ridder, J., & García, R. A. 2018, *A&A*, 612, C2  
 Desmars, J., Camargo, J. I. B., Braga-Ribas, F., et al. 2015, *A&A*, 584, A96  
 Dunham, D. W., Goffin, E., Manek, J., et al. 2002, *Mem. Soc. Astron. It.*, 73, 662  
 Ďurech, J., Carry, B., Delbo, M., Kaasalainen, M., & Viikinkoski, M. 2015, *Asteroids IV*, eds. Michel, P., DeMeo, F. E., & Bottke, W. F. (Tucson, AZ: University of Arizona Press), 183  
 Farnocchia, D., Chesley, S. R., Chamberlin, A. B., & Tholen, D. J. 2015, *Icarus*, 245, 94  
 Gaia Collaboration (Brown, A. G. A., et al.) 2016, *A&A*, 595, A2  
 Gaia Collaboration (Brown, A. G. A., et al.) 2018a, *A&A*, 616, A1  
 Gaia Collaboration (Spoto, F., et al.) 2018b, *A&A*, 616, A13  
 Herald, D., Frappa, E., Gault, D., et al. 2019, *NASA Planetary Data System, Asteroid Occultations V3.0*. urn:nasa:pds:smallbodiesoccultations::3.0.  
 Hunter, J. D. 2007, *Comput. Sci. & Eng.*, 9, 90  
 Ivezić, v., Kahn, S. M., Tyson, J. A., et al. 2019, *ApJ*, 873, 111  
 Mainzer, A., Grav, T., Masiero, J., et al. 2011a, *ApJ*, 741, 90  
 Mainzer, A., Grav, T., Bauer, J., et al. 2011b, *ApJ*, 743, 156  
 Mary, D. L. 2006, *A&A*, 452, 715  
 Masiero, J. R., Mainzer, A. K., Grav, T., et al. 2011, *ApJ*, 741, 68  
 Meza, E., Sicardy, B., Assafin, M., et al. 2019, *A&A* 625, A42  
 Ortiz, J. L., Sicardy, B., Braga-Ribas, F., et al. 2012, *Nature*, 491, 566  
 Ortiz, J. L., Sicardy, B., Camargo, J. I. B., Santos-Sanz, P., & Braga-Ribas, F. 2019, *ArXiv e-prints* [arXiv:1905.04335]  
 Ostro, S. J., Hudson, R. S., Benner, L. A. M., et al. 2002, *Asteroids III* (Tucson, AZ: University of Arizona Press), 151  
 Pass, E., Metchev, S., Brown, P., & Beauchemin, S. 2018, *PASP*, 130, 014502  
 Perryman, M. 2012, *Eur. Phys. J. H*, 37, 745  
 Porter, S. B., Buie, M. W., Parker, A. H., et al. 2018, *AJ*, 156, 20  
 Pravec, P., Harris, A. W., Kušnirák, P., Galád, A., & Hornoch, K. 2012, *Icarus*, 221, 365  
 Roques, F., Georgevits, G., & Doressoundiram, A. 2008, *The Solar System Beyond Neptune*, eds. Barucci, M. A., Boehnhardt, H., Cruikshank, D. P., Morbidelli, A., & Dotson, R. (Tucson, AZ: University of Arizona Press), 545  
 Scheeres, D. J., Britt, D., Carry, B., & Holsapple, K. A. 2015, *Asteroids IV* (Tucson, AZ: University of Arizona Press), 745  
 Shevchenko, V. G., & Tedesco, E. F. 2006, *Icarus*, 184, 211  
 Sicardy, B., Widemann, T., Lellouch, E., et al. 2003, *Nature*, 424, 168  
 Sicardy, B., Ortiz, J. L., Assafin, M., et al. 2011, *Nature*, 478, 493  
 Spoto, F., Milani, A., & Knezevic, Z. 2015, *Icarus*, 257, 275  
 Spoto, F., Tanga, P., Bouquillon, S., et al. 2017, *A&A*, 607, A21  
 Tanga, P., & Delbo, M. 2007, *A&A*, 474, 1015  
 Virtanen, P., Gommers, R., Oliphant, T. E., et al. 2020, *Nat. Methods*, 17, 261  
 Vokrouhlický, D., Bottke, W. F., Chesley, S. R., Scheeres, D. J., & Statler, T. S. 2015, *The Yarkovsky and YORP Effects* (Tucson, AZ: University of Arizona Press), 509

**Appendix A: Table****Table A.1.** Observed occultation chords chosen for comparison to our model for observation accuracy.

Number	Name	Year	Month	Day	Observer	DNR
10	Hygiea	2015	5	14	Dunford	1.5
65	Cybele	2015	10	28	Kattendidt	1.5
25	Phocaea	2017	3	3	Dunford	1.7
412	Elisabetha	2016	6	20	Dunford	1.9
21	Lutetia	2016	8	13	Perello	2.0
476	Hedwig	2019	2	12	Conjat	2.0
580	Selene	2019	7	22	Haymes	2.3
131	Vala	2016	1	2	Perello	2.8
2226	Tchaikovsky	2019	1	17	Conjat	2.9
306	Unitas	2015	4	30	Bardecker	3.0
429	Lotis	2016	3	1	Gault	3.5
479	Caprera	2017	5	4	Hooper	3.9
146	Lucina	2016	11	30	Frappa	4.3
117	Lomia	2011	5	26	Gault	4.3
135	Hertha	2015	9	25	Perello	4.3
270	Anahita	2017	3	26	Hooper	4.5
3200	Phaethon	2019	10	15	Tanga	5.8
221	Eos	2015	9	26	Perello	7.0

**Notes.** Their photometric light curves data have been fitted by the model, with the same procedure adopted for the simulations.

